SURFACE ENGINEERING FOR EFFICIENT ELECTROCATALYTIC WATER SPLITTING AND NITROGEN REDUCTION

CAI LEJUAN

PhD

The Hong Kong Polytechnic University

2020

The Hong Kong Polytechnic University

Department of Applied Physics

Surface Engineering for Efficient Electrocatalytic Water Splitting and Nitrogen Reduction

CAI Lejuan

A thesis submitted in partial fulfillment of the requirements for the degree of Doctor of Philosophy

August 2019

THE HONG KONG POLYTECHNIC UNIVERSITY
香港理工大學

CERTIFICATE OF ORIGINALITY

I hereby declare that this thesis is my own work and that, to the best of my knowledge and belief, it reproduces no material previously published or written, nor material that has been accepted for the award of any other degree or diploma, except where due acknowledgement has been made in the text.

Signature:

Name of student: CAI Lejuan

Table of Content

Abstract

Energy shortage and environment pollution caused by the combustion of fossil fuels force us to seek renewable and clean energy for sustainable development. Hydrogen energy, including hydrogen and hydrogen-containing compounds is regarded as the most promising energy carrier due to its high energy efficiency and zero-emission property. Currently, the main pathway to produce hydrogen energy relies on the catalytic steam reforming and coal gasification, which still require the consumption of hydrocarbon fuels. Hydrogen energy can also be obtained through water splitting driven by renewable energy, such as light, electricity and thermal energy. Among various technologies, hydrogen energy from water electrolysis has attracted tensive attention in last decade because water electrolysis is an important method of energy conversion, which can store the renewable energy in the form of hydrogen. However, current water electrolysis is still limited to small-scale applications, large-scale hydrogen production is hindered by the great electricity consumption induced by large overpotential and poor efficiency. Thus, in this thesis, surface engineering strategy is applied to improve the electrocatalytic activity of active materials for enhanced water splitting performance and N_2 reduction activity.

For water splitting part, (1) we investigate the effect of surface functional group on hydrogen evolution reaction (HER) by studying the improved HER kinetics induced by surface hydroxyl group modification. Experimental results indicate different active materials grown on three-dimensional (3D) graphene show enhanced HER performance after crafting massive hydroxyl groups on 3D graphene. The positive role of surface hydroxyl groups on the HER performance is then explained by theoretical investigation, and increased water affinity is regarded as the main cause. Surface hydroxyl group can not only attract abundant H_2O clusters near the cathode surface to constantly supply H_2O molecular for hydrogen evolution, but also balance the

interfacial pH environment to reduce the overpotential for HER process. (2) we investigate the effect of heteroatom incorporation on water splitting performance by studying the selective water splitting behaviour of Ni_2P induced by different content of Fe dopant. According to the experimental results, enhanced water splitting performance of Ni_2P is successfully achieved when Fe dopant incorporates into Ni_2P matrix. More importantly, the activity of hydrogen evolution and oxygen evolution of Fe-doped Ni_2P can be controlled by adjusting the content of Fe dopant. Higher and lower content of Fe doping in Ni_2P matrix contribute to excellent OER performance and remarkable HER activity, respectively. Finally, the selective water splitting behavior induced by active Fe- and Ni-sites engineering is explained by the key intermediate adsorption theory. Based on above analysis, effective surface engineering strategies including functional group modification and heteroatom doping are proposed and successfully realize improved water splitting performance.

For nitrogen reduction part, (1) we optimize the *d*-electrons configuration of active transition metal (TM) center via sulfidation process to realize enhanced N_2 activation. Pt, the typical catalytic center with poor N_2 affinity, is selected to act as a model to investigate the significance of sulfidation process. Our DFT calculations predict sulfurized Pt (PtS) possesses reduced number of *d* electron, which can benefit the σ donation from N_2 molecular, realizing efficient N_2 activation. Besides, PtS shows suppressed HER performance, which may contribute to enhanced Faradaic efficiency of NRR. From the experimental results, PtS shows a reduced overpotential for NRR than Pt, and the NRR Faradaic efficiency of PtS is about 5 times as high as that of metallic Pt, showing consistent results with the theoretical analysis. (2) we propose a universal principle to construct PtS_2 supported single atom centers (SACs) for NRR process. Stability of designed catalysts, the selectivity of HER/NRR and barrier of potential limiting step

are considered to screen the most favorable electrocatalyst for NRR process. According to results, SACs with different *d* electron configurations exhibit different N* affinity, ultimately lead to differ in the energy barrier of the potential limiting step. The barrier of potential limiting step shows liner correlation with the N* binding strength, which is also liner correlated with the integral of the density of unoccupied *d* orbital states of SACs. In this part, sulfidation method and SACs construction are applied to optimize the *d* electron configuration of exposed transition metal site. After these engineering strategies, the active transition metal center can realize the combination of unoccupied *d* orbital and abundant *d* electron, which is beneficial for N_2 activation and NH_3 production.

List of Figures

List of Tables

1 Introduction

1.1 Overview of Hydrogen Economy

Hydrogen shows great potential to act as principle chemical energy carrier in future energy system due to the scarcity of fossil fuel energy and environment concerns.[1-2] Hydrogen is easy to convert into electrical energy or kinetic energy to power electric devices or vehicles. Hydrogen is producible, storable, transportable and recyclable, showing significant advantageous over the traditional energy sources. More importantly, using zero-emission hydrogen fuel is expected as one of the most promising approach to reduce the environmental pollutions, especially the green gas effect, in the long-term. In addition, hydrogen is an irreplaceable chemical feedstock in ammonia production, oil refining and methanol production. Thus, developing advanced hydrogen-related technologies, including hydrogen production and storage, is an urgent issue to support sustainable hydrogen economy.

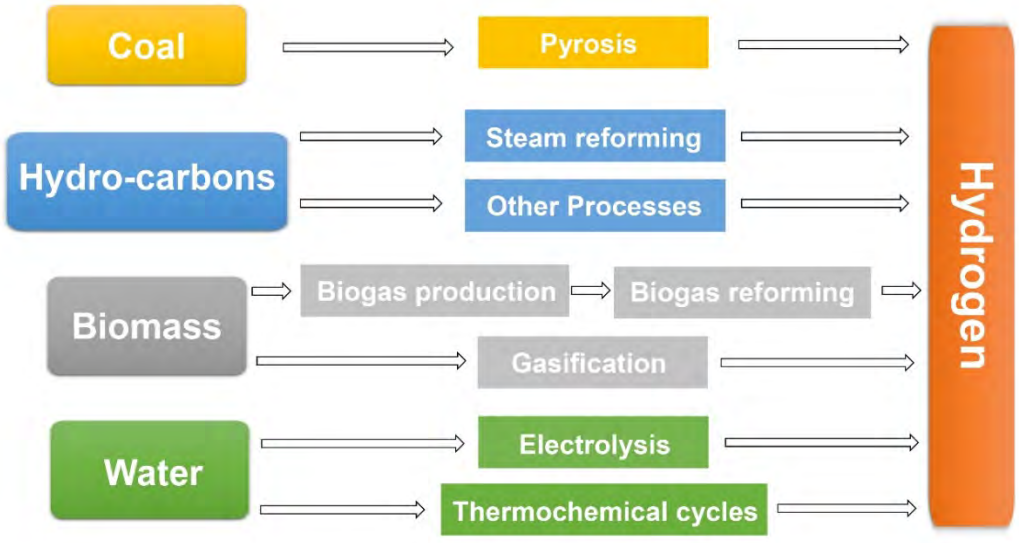

Figure 1.1. H_2 production from different routes.

From the perspectives of economic and environmental protection, separating water into H_2 and O_2 is the most desirable way to obtain H_2 fuel, because H_2 can convert back into water after combustion, which forms an entire hydrogen cycle and makes fully use of abundant water resource on earth. However, although hydrogen can be manufactured from water splitting, most of hydrogen production still lies on hydrocarbon fuels, about 95% of hydrogen production is produced via catalytic steam reforming, coal gasification and other hydrocarbons-related reactions (Figure 1.1). Hydrogen production from water electrolysis only accounts for about the proportion of 4%, which goes against the requirements of low-carbon economy in the future. To realize high-efficient hydrogen production from water splitting, various technologies have been developed, such as electrolysis, thermochemical water dissociation and photolysis.[3] Among these technologies, water electrolysis is a well-established technology that has a history of more than a century, and it also occupies the prominent position in high-purity hydrogen production.[4] Therefore, seeking for strategies to improve the efficiency of water electrolysis is of great significance for promoting the development of hydrogen economy.

1.1.1 Hydrogen Production from Electrolysis

Water electrolysis is a sustainable and renewable chemical technology to realize H_2 production by using electricity as the outer energy input.[5] Generally, the water electrolysis takes place in an electrolyzer, which consists of a cathode and an anode, separated by electrolyte (Figure 1.2). The reactions on cathode and anode varies with different electrolytes, and the corresponding reaction equations are listed as follows:

In acidic electrolytes (pH = 0):

$$\text{Oxidation at anode: } 2H_2O \rightarrow O_2 + 4H^+ + 4e^- \ (E° = +1.23 \text{ V})$$

$$\text{Reduction at cathode: } 2H^+ + 2e^- \rightarrow H_2 \ (E° = 0 \text{ V})$$

In alkaline electrolyte (pH = 14.0):

$$\text{Oxidation at anode: } 4OH^- \rightarrow O_2 + 2H_2O + 4e^- \ (E° = +0.40 \text{ V})$$

$$\text{Reduction at cathode: } 2H_2O + 2e^- \rightarrow H_2 + 2OH^- \ (E° = -0.83 \text{ V})$$

The overall reaction is: $2H_2O \rightarrow 2H_2 + O_2$

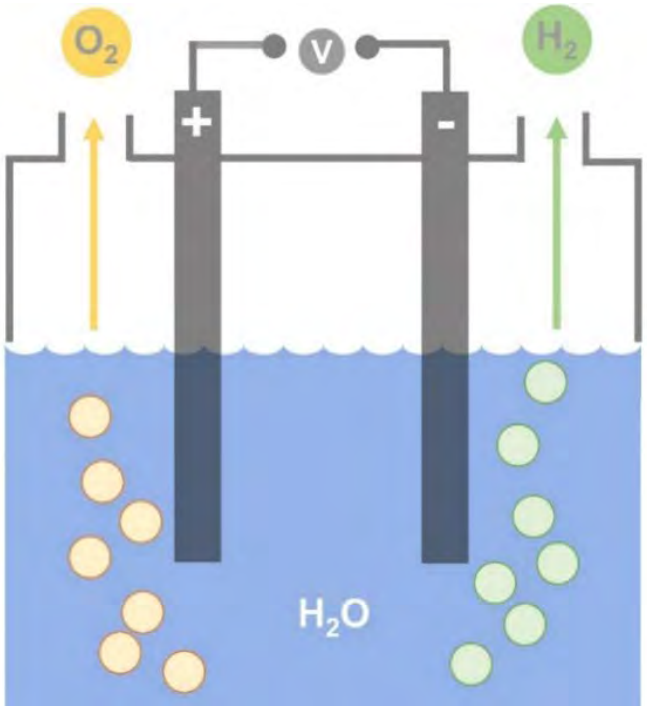

Figure 1.2. The structure of electrolyzer for water splitting.

1.1.2 The Descriptor for HER

According to the thermodynamics analysis, the standard potentials of anode and cathode reactions at standard temperature and pressure are 1.23 V and 0 V vs. reversible hydrogen electrode, respectively. The standard theoretical onset potential for H_2 and O_2 evolution under different electrolytes can be calculated by equations illustrated in Figure 1.3a. However, in real electrolysis process, it usually requires more input energy than the expected potential to drive hydrogen evolution reaction (HER) or oxygen evolution reaction (OER). The difference between theoretical potential and experimental potential is called overpotential, which represents the energy that

disappeared as useless heat (Figure 1.3b). Although the inner reasons of overpotential arise from various aspects, such as the depletion of charge-carriers, the interfacial resistance and electrode polarization, the only effective way to improve the H_2 production efficiency is reducing the overpotential, achieving optimized H_2 yield with less electricity consumption.

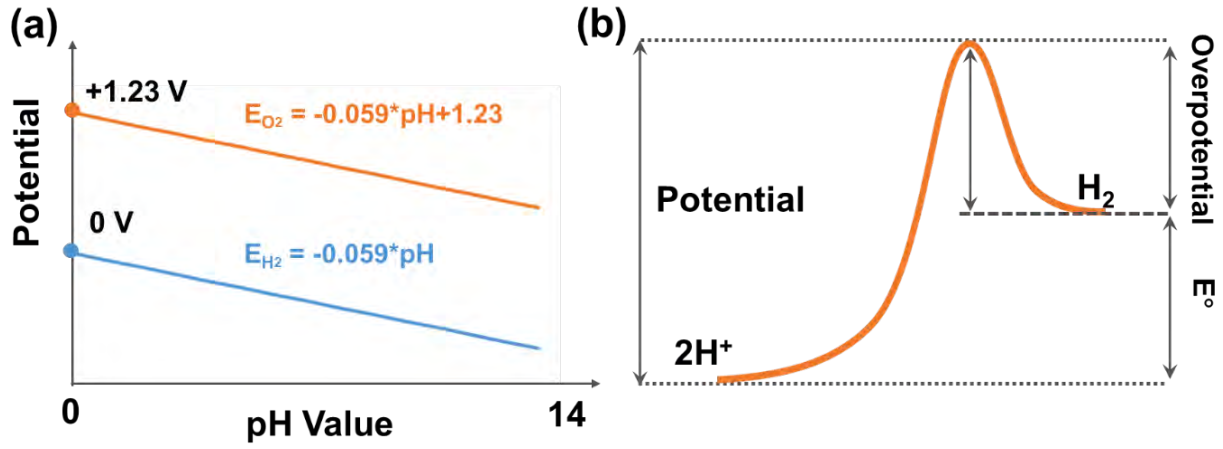

Figure 1.3. (a) Standard theoretical onset potential for H_2 and O_2 evolution under different electrolytes. (b) Schematic diagram of energy for HER reaction.

According to previous mechanism study, HER process is a two-electron transfer reaction that closely related with proton participation. The dominant HER pathway can be theoretically indicated via Tafel slope, which is also a descriptor for HER kinetics. Tafel slope represents the overpotential increment that required to increase the current density by 10 times. Small Tafel slope indicates the sharp increase of HER current density, contributing to facilitated H_2 production. As the reaction pathway shows, the first step of HER is the Volmer reaction, representing the initial discharge process. The following step has two different pathways to generate H_2, naming Heyrovsky and Tafel reactions, respectively. The detailed reaction equations and corresponding Tafel slopes calculated from Butler-Volmer theory are illustrated as follows:

Volmer step: $H^+ + e^- + * \rightarrow H^*$ (Slope = 118 $mVdec^{-1}$)

Heyrovsky step: $H^* + H^+ + e^- \rightarrow H_2 + *$ (Slope = 39 $mVdec^{-1}$)

Tafel step: $H^* + H^* \rightarrow H_2 + 2^*$ (Slope = 29.5 $mVdec^{-1}$)

From above discussion, whether it follows Volmer-Heyrovsky or Volmer-Tafel mechanism, the interaction between active sites and catalytic intermediate (H*) is the determining factor for both H adsorption and H_2 desorption processes. To quantize the interaction, hydrogen adsorption free energy ($\triangle G_{H^*}$) theory has been proposed as the descriptor of binding strength between active site and H* intermediate. As explained by Sabatier theory, the $\triangle G_{H^*}$ should show a neutral value that is close to zero, which indicates a moderate binding strength between active site and H*. When the binding strength is too weak, the active site shows poor H^+ adsorption ability, which implies great energy barrier for H* intermediate formation, leading to hindered Volmer step. If the binding strength is too strong, the energy barrier for H_2 desorption may significantly increase, the Heyrovsky/Tafel step becomes the determining step for overall HER process. Therefore, moderate binding energy can not only ensure efficient H* formation but also facilitate the desorption of generated H_2, ultimately realizing continuous water electrolysis and H_2 production.

Benefit from hydrogen adsorption free energy theory, the inner mechanism of electrocatalysts can be successfully explained by a uniform criterion, giving reasonable theoretical understanding to the intrinsic HER activities. More importantly, the criterion can help to predict promising catalytic sites for HER process and provide theory-guided strategies for HER catalysts design. Platinum (Pt) is well known as the excellent HER catalyst and achieves high hydrogen evolution rates under negligible overpotentials in acidic medium. However, the intrinsic factor that contributes to outstanding HER performance of Pt is still ambiguous until the thermo-neutral $\triangle G_{H^*}$ of Pt surface is discovered. The H* adsorption on Pt surface behaves like that on hydrogenous

and nitrogenous modes, giving a reasonable explanation for the excellent HER performance of Pt. After that, there inspires intensive search to seek for earth-abundant catalysts with appropriate H* binding strength and the value of $\triangle G_{H^*}$ is regarded as a golden rule for choosing alternative catalysts that can replace Pt.

1.1.3 Strategies for Improving Electrocatalytic HER Performance

From the microscopic point of view, the overall electrocatalytic HER process can be briefly described as four steps in Figure 1.4: (1) mass diffusion to electrode surface; (2) adsorbed H^+ gets an electron and form active H* and (3) H* combination and H_2 desorption. These steps are closely associated with the apparent HER performance, and the step with highest energy barrier dominates the rate-determining step of overall HER process. Firstly, the mass diffusion directly affects the concentration of interfacial H^+, unimpeded mass transfer can offer abundant protons for continuous H_2 production. If the mass diffusion is slow, the interfacial pH value will greatly increase as the HER reaction proceeds. Proton deficiency and increased interfacial pH environment will result in sluggish HER kinetics, leading to mass transfer limited step. Secondly, the interaction between proton and electrode surface also plays vital role in electrocatalytic HER reaction. If the electrode surface shows poor affinity to H^+ or the H^+ is difficult to accept electron to form active H*, the energy barrier of Volmer step may dramatically increase. Thus, Volmer step will becomes the rate-determining step of HER process, weakening the HER kinetics. Thirdly, the last H_2 desorption step is also important for HER kinetics because the H_2 desorption is the recovery process of active site. Only the produced H_2 releases from the catalytic site, the active site can initial the next round of HER process. If not, the catalyst will be poisoned, causing deactivation of the active sites.

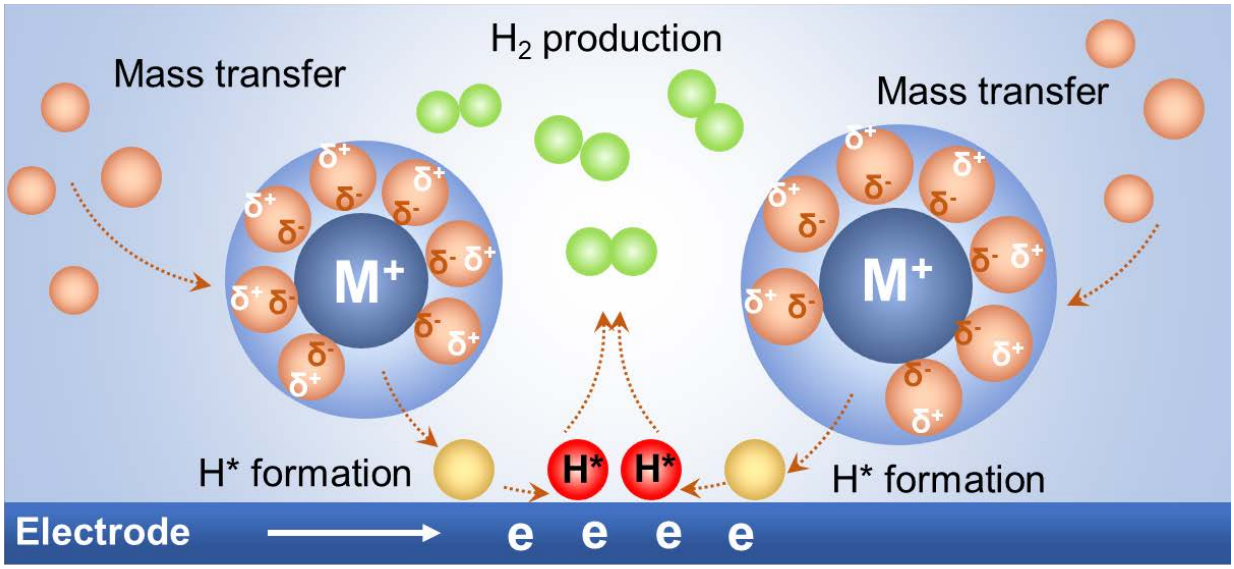

Figure 1.4. Microscopic reactions on the surface of electrode during electrocatalytic HER reaction (Volmer-Tafel mechanism).

By fully understanding the microscopic reactions involved in HER process, corresponding strategies for improving electrocatalytic HER performance can be proposed. (1) Constructing hierarchical porous structures or decreasing the interfacial resistance between electrolyte and electrocatalysts for accelerated mass transfer. (2) Engineering surface defects or surface functional groups to optimize the intrinsic H* binding strength of electrocatalysts.[6] (3) Growing electrocatalysts on three-dimensional (3D) conductive current collectors or coupling active materials with conductive species to facilitate the electron transfer. (4) Choosing electrocatalysts with weak binding strength of H_2 or keeping constantly stirring to promote the desorption of produced H_2.

1.1.4 A General View of Electrocatalysts for HER

For the past decades, a great number of non-noble metal-based catalysts have been designed based on hydrogen adsorption free energy theory, exhibiting comparable even superior HER performance than Pt surface.[7] Among these well-developed HER catalysts, the most

important HER catalyst is molybdenum disulfide (MoS_2).[8-11] Hinnemann *et al.* first discover that the edge site of MoS_2 shows a moderate $\triangle G_{H^*}$ that close to nitrogenase, breaking the conventional cognition of MoS_2 as an inactive HER catalyst. After that, researchers have performed tons of modification on nanoscale MoS_2 catalysts to engineer the active sites and electronic structures for improved the HER performance. (1) Exfoliation strategy is first proposed to convert 1H-MoS_2 into metallic 1T-MoS_2, which can expose more competitive HER activities and attain better electrical conductivity.[12-13] (2) Various porous structure of MoS_2 are well designed to increase the specific surface area and maximize the number of exposed active sites.[14-15] (3) Heteroatoms, such as Co, Ni, V and Pt, have been incorporated into the MoS_2 matrix to engineer the electronic structure and surface charge distribution of the host MoS_2, leading to optimized free energy of H* adsorption. (4) Conductive species, including graphene, carbon nanotube and carbon fiber, are introduced to couple with MoS_2 for reduced charge transfer resistance.[16]

Benefit from the intensive interests of electrocatalytic HER, the library of HER catalysts is greatly broadened, including other metal sulfides, metal nitrides and metal phosphides.[6, 17-24] For example, metallic iron-nickel sulfide nanosheets shows an overpotential of 105 mV at 10 mA/cm^2 and a reduced Tafel slope of 40 mV/dec in acidic medium. Hollow $Zn_{0.3}Co_{2.7}S_4$ exhibits superior pH-universal HER activity, requiring overpotentials of 80, 90 and 85 mV to realize current density of 10 mA/cm^2 in 0.5 M H_2SO_4, 0.1 M phosphate buffer and 1.0 M KOH solutions, respectively. Tungsten nitride nanorod array is also synthesized and regarded as an all-pH durable HER catalyst, achieving a current density of 10 mA/cm^2 under an overpotential of 198 mV. Owing to the excellent conductivity and highly active catalytic sites, metal phosphides also show great potential to act as HER catalysts in not only strong acidic solutions, but also in harsh alkaline and neutral electrolytes. Ni_2P (001) surface is successfully predicted as an active HER catalyst due to the H*

binding behavior that similar to [NiFe] hydrogenase, and the as-prepared Ni_2P nanoparticles reveal excellent HER activity that comparable to commercial Pt.[25] Carbon-Shell-Coated FeP shows a low overpotential of 71 mV at 10 mA/cm^2 and negligible activity loss after 10 000 cycles.[26] Ternary $NiCo_2P_x$ Nanowires shows remarkable pH-universal HER activity and long-term stability.[27-28] Besides, Sun *et al.* synthesize different metal phosphides grown on 3D substrates through gas-solid reaction, obtaining a large number of excellent HER electrocatalysts with reduced overpotentials and outstanding long-term stability.[29]

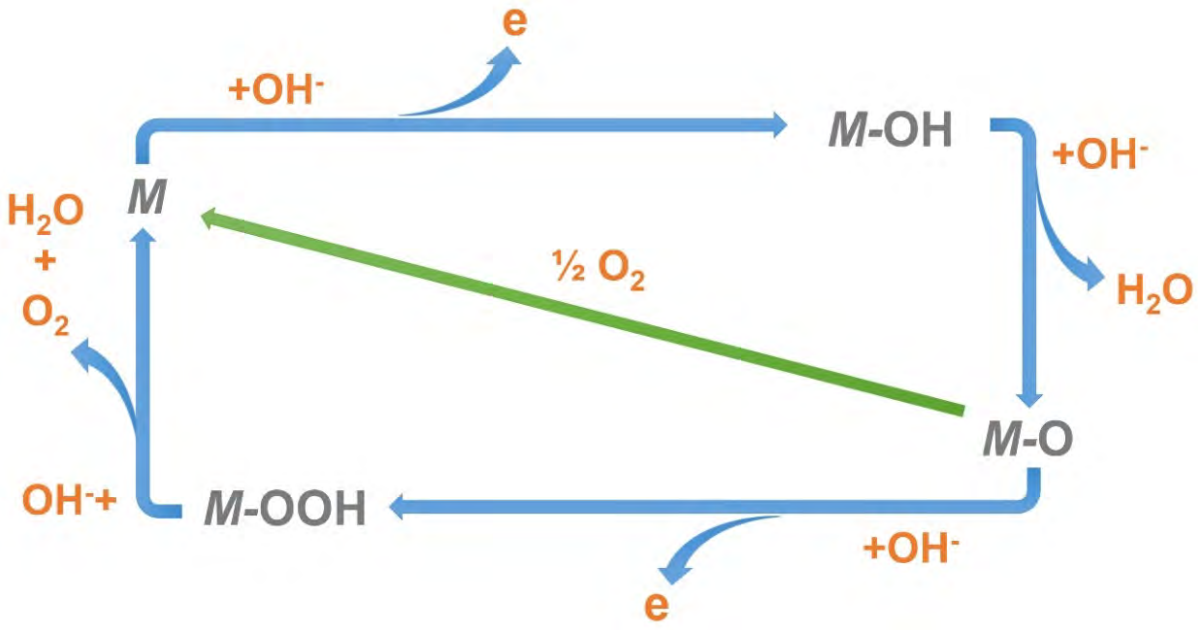

Figure 1.5. Possible OER mechanisms in alkaline medium.

1.1.5 Improved OER Performance

In addition to intrinsic properties of HER electrocatalysts and electrolyte environment, the OER kinetics occurred at the anode also has significant influence on HER performance.[30-32] As known, the total overpotential of the water electrolysis is composed of the overpotentials at the cathode and the anode, and the efficiency of anodic reaction plays important role in the overall water splitting process.[33-35] It is widely accepted that the majority of the total overpotential of water

electrolysis systems is generated from the anodic OER reaction, because the anodic OER reaction involves a sluggish proton-coupled four electrons transfer process. To overcome the efficiency-limiting step for overall water splitting, efficient OER catalysts are in demand to optimize the anode process.

The possible mechanism of OER in alkaline medium are presented in Figure 1.5, and representative active intermediates on electrode surface are denoted M-OH, M-O and M-OOH, respectively. According to the diagram of mechanism, the initial step of OER is the formation of M-OH intermediate, the energy barrier of this step is determined by OH- affinity on the surface of electrocatalysts. The next step of OER pathway is the oxidation of M-OH to produce M-O intermediate and release a H_2O molecular. Noted that two different approaches can possibly exist to form oxygen from a MO intermediate. Production of O_2 through the direct combination of 2MO or through the formation of peroxide intermediate (MOOH), followed by O_2 evolution. Detailed equations are illustrated as follows:

(1) $OH^- + M \rightarrow MOH + e$ ($\triangle G_1$)

(2) $OH^- + MOH \rightarrow MO + H_2O$ ($\triangle G_2$)

(3) $MO + MO \rightarrow O_2 + 2M$ or $MO + OH^- \rightarrow MOOH + e$ ($\triangle G_3$)

(4) $MOOH + OH^- \rightarrow M + H_2O + O_2$ ($\triangle G_4$)

The overall potential for OER (Ƞ) is determined by the largest $\triangle G$:

$$Ƞ = \triangle G_{OER} - 1.23 = \max \{\triangle G_1, \triangle G_2, \triangle G_3, \triangle G_4\} - 1.23$$

Thus, developing excellent OER catalysts with lower overpotential is of great importance for reducing the energy input of water electrolysis process, realizing improved Faradaic efficiency of hydrogen evolution.

1.2 Overview of Nitrogen Reduction

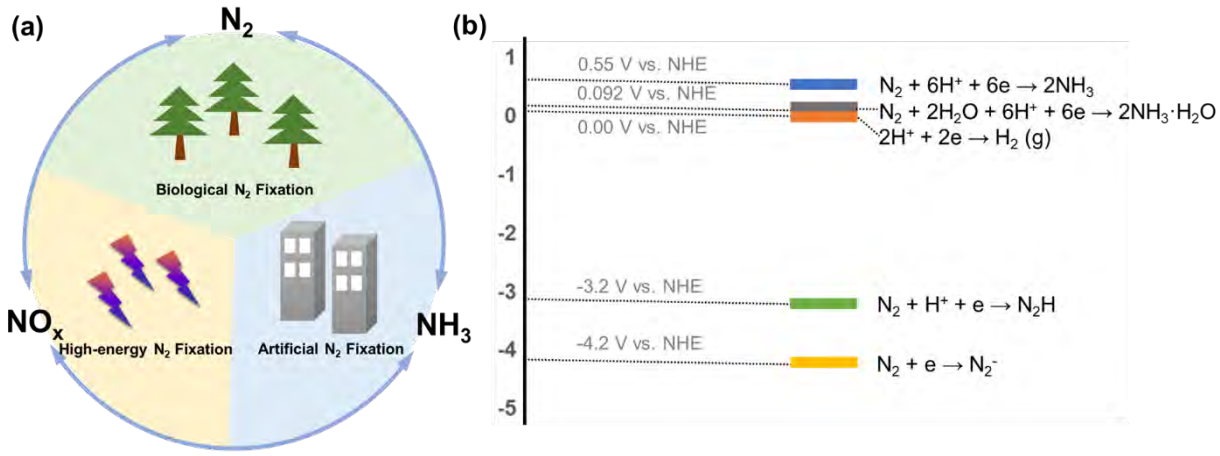

Figure 1.6. (a) Possible pathways for N_2 fixation. (b) Necessary potentials to perform N_2 reduction and H_2 evolution.

Based on the above descriptions, hydrogen energy shows great advantages to act as clean energy in sustainable society, but it still exists some shortcomings to limit its application. The largest undesirable obstacle is the transportation of hydrogen energy. According to the statistics, hydrogen energy has the highest specific density (120~142 MJ/kg), but its volume energy density is very low.[36] Therefore, to simplify the transportation process, liquefaction of hydrogen is required before hydrogen energy transportation. However, the liquefaction process needs intensive energy input and the liquid hydrogen shipping over long distance still has a lot of challenges in terms of storage and safety.

Ammonia (NH_3) possesses a volumetric hydrogen density as high as 10.7 kg_{H2}/100L and is promising to react as a convenient hydrogen carrier (liquid form at around 10 bar pressure at room temperature).[37-40] Besides, NH_3 is not only an important energy storage intermediate (liquid form, 4.32 kW h/L), it's also a key industrial chemical for both human beings and ecosystem, such as building block for the pharmaceutical synthesis, necessary fertilizer, and feedstock for

nitrogenous compounds production.[41-43] Nature exhibits outstanding nitrogen fixation ability via biological N_2 fixation and high-energy N_2 fixation, but the natural N_2 fixation hardly keep up with the sharp increase of the population (Figure 1.6a). To meet the growing demand of industry and agriculture, Haber-Bosch process was developed by Fritz Haber and Carl Bosch in the first decade of the 20th century, successfully achieving efficiently artificial nitrogen fixation process via the following equation:

$$N_2\,(g) + 3H_2\,(g) \rightleftharpoons 2NH_3\,(g)$$

During the Haber–Bosch process, atmospheric nitrogen and hydrogen can be converted into NH_3 in the presence of metal catalysts under high temperatures and pressures (400–500 °C and 15–25 MPa). Until today, Haber–Bosch process is still the main industrial method for artificial nitrogen fixation, contributing more than 50% of nitrogen elements in human body. However, intensive energy of this industrial procedure accounts for about 1% of the global energy consumption, leading to more than 1% of global CO_2 emission.[44] Therefore, the current situation of environment pollution and energy crisis call for the primary impetus to seek for technical breakthrough and improve the artificial ammonia synthesis technology.

Electrocatalytic N_2 reduction (NRR) is regarded a green and sustainable strategy for NH_3 production, since it can be driven by clean electrical energy derived from renewable solar and wind energy.[41, 45] N_2 reduction via electrolysis is also an environmentally friendly reaction, in which inert N_2 and water serve as nitrogen precursor and proton donor, respectively. Thus, electrocatalytic NRR holds great promise to realize carbon-free and sustainable NH_3 production from earth-abundant N_2 and H_2O.[46] However, sturdy N≡N triple bond has an average bond energy as high as 941 kJ/mol, the activation process of inert N_2 molecule encounters a very high energy

barrier.[46] The great energy barrier should ascribe to large energy gap between the highest occupied orbitals and lowest unoccupied orbitals of N_2 (10.82 eV) and high ionization potential of N_2 (15.8 eV). As shown in Figure 1.6b, the reduction potential to form N_2^- through $N_2 + e \rightarrow N_2^-$ is about -4.2 V versus NHE, and the first proton-coupled electron transfer reaction $N_2 + H^+ + e \rightarrow N_2H$ also requires a reduction potential of -3.2 V versus NHE. The negative electron affinity (-1.9 eV) and hindered protonation indicate the activation of N_2 molecule is thermodynamically forbidden.

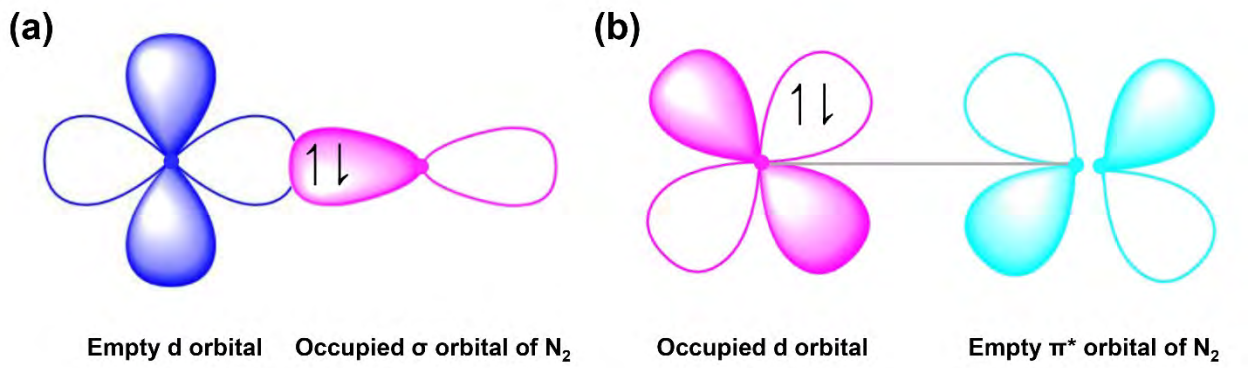

Figure 1.7. Schematic of N_2 bonding to active sites. (a) σ donation from N_2 and (b) π backdonation to N_2.

It is widely accepted that the N_2 activation efficiency is largely determined by the interaction between active site and long-pair electrons of N_2. Take transition metal (TM) active site as an example, the unoccupied *d* orbitals of TM center can accept long pair-electrons from N_2 (Figure 1.7a); and the occupied *d* orbitals of TM donate d electrons into the antibonding orbitals of N_2 molecular (Figure 1.7b), which greatly weaken the N≡N triple bond and simultaneously strengthen the bonding between TM center and nitrogen.[47-48] The combination of unoccupied *d* orbitals and spare d electrons can form bonds of σ and π symmetry, respectively, leading to effective N_2 activation and following hydrogenation process. Thus, to realize high-efficient NRR

performance, seeking for appropriate catalysts that can effectively activate N≡N triple bond is the first step.

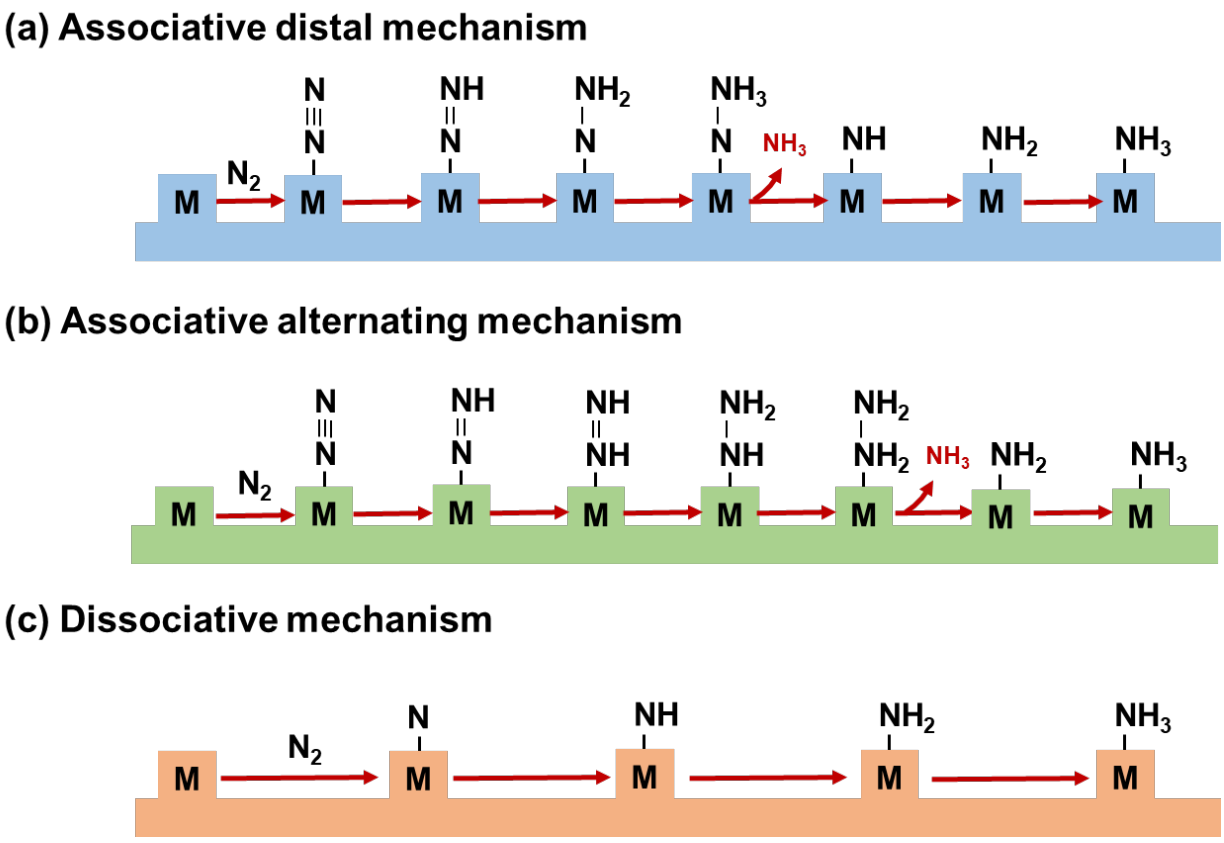

Figure 1.8. Possible NRR reaction pathways to produce NH_3.

After the initial N_2 activation, there exist three possible NRR pathways to convert N_2 into NH_3, naming associative distal mechanism, associative alternating mechanism and dissociative mechanism on the basis of N_2 dissociation and different order of hydrogen addition (Figure 1.8). In the associative mechanism, N_2 molecule first binds to the active catalytic site and then undergoes step-by-step hydrogenation process. For the end-on adsorption mode, hydrogenation prefer to occur on the N atom farther away from the active sites in the associative distal pathway. The successive hydrogenation leads to the release of first NH_3 molecule and leaving an adsorbed N atom. With the new round of hydrogenation on the other N atom, the second NH_3 molecule forms

and finally releases from the active center. In the alternating pathway, hydrogenation steps alternatively occur between the two N atoms, experiencing symmetric intermediates of diazene (HNNH) and hydrazine (H_2NNH_2), respectively. Then two NH_3 molecules forms and releases from the catalytic site in sequence, finishing the overall N_2 reduction process. As for dissociative mechanism, the triple bond of the N_2 molecule is first broken, leaving two active adsorbed N atoms on the catalyst surface. Followed by the dissociation of N_2, hydrogenation on the adsorbed N atom occurs until the NH_3 molecule formation.

To reduce the activation energy of NRR, well-designed catalysts are introduced to provide an alternative reaction mechanism with a lower activation barrier. Be spired by the active FeMo cofactor in nitrogenase (Figure 1.9), a great number of Mo- and Fe-based electrocatalyst are first synthesized and dramatically promote the efficiency of electrocatalytic NRR.[49] Defect-rich MoS_2 displays enhanced electrocatalytic N_2 reduction performance and attains a high Faradaic efficiency of 8.34% in 0.1 M Na_2SO_4.[50-51] Mo_2C nanodot embedded in ultrathin carbon nanosheet realize robust electrocatalytic NRR with a high NH_3 yield rate of 11.3 μg h^{-1} $mg^{-1}_{cat.}$ and NRR Faradaic efficiency of 7.8%.[52] Single Mo atoms on N-doped porous carbon achieves a high rate of NH_3 production and a Faradaic efficiency of about 14% in 0.1 M KOH solution.[53] Porous Fe_2O_3 nanorods grown on carbon cloth can also act as a superior electrocatalyst to convert N_2 into ammonia with a Faradaic efficiency of 7.69% in 0.1 M Na_2SO_4. Spinel Fe_3O_4 nanorod anchored on a Ti mesh exhibits outstanding and durable NRR electrocatalyst, attaining faradaic efficiency of 2.6% under ambient conditions.

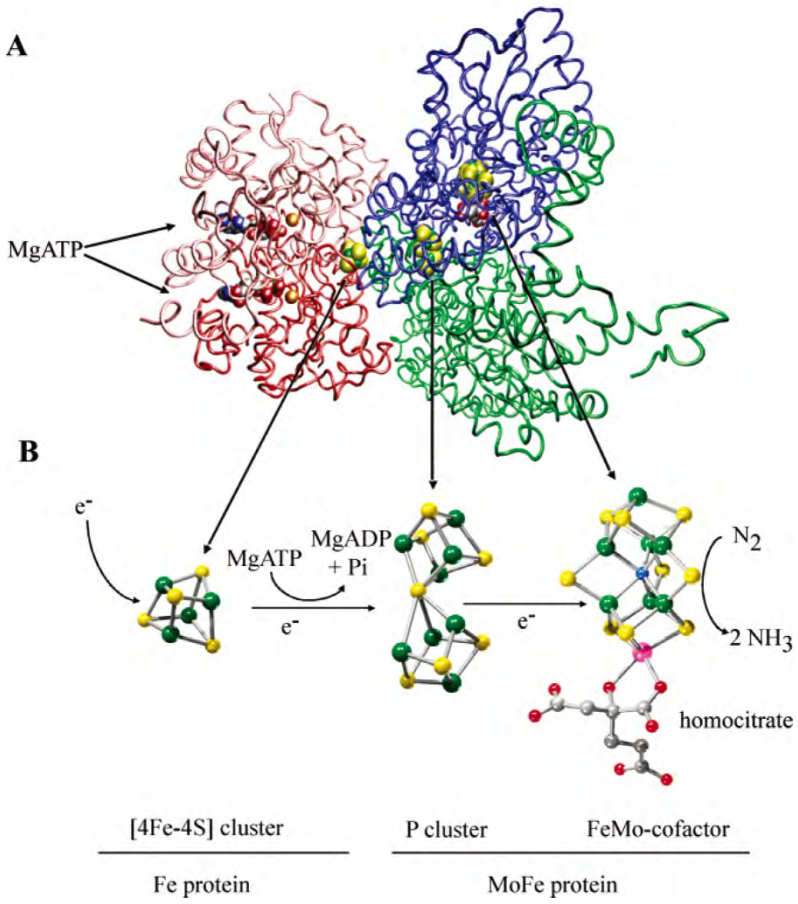

Figure 1.9. Nitrogenase component proteins and their associated metal clusters.[54]

Other electrocatalysts, including single atom electrocatalysts (SACs), carbon-based electrocatalysts and other TM-based electrocatalysts, are also designed from both of the experimental and theoretical perspectives, greatly enriching the library of NRR electrocatalysts. Single tungsten atom anchored on graphitic carbon nitride is predicted with a limiting potential of -0.35 V through associative enzymatic pathway, it also shows great potential to suppress competing hydrogen evolution reaction for improved Faradaic efficiency.[55] Ti or V single atom anchored on defective graphene requires potential determining step of 0.69 eV and 0.87 eV, respectively, indicating the advantages of single atom electrocatalysts on graphene substrate.[56] Ru single atoms on nitrogen-doped carbon achieves a NRR Faradaic efficiency of 29.6% and yield

rate of 120.9 μg_{NH3} $mg^{-}1$ h^{-1}.[57] Multishelled hollow Cr_2O_3 microspheres, as a non-noble metal electrocatalyst, show efficient and selective NRR performance for NH_3 production, achieving Faradaic efficiency of 6.78% in 0.1 M Na_2SO_4.[58] Oxygen-vacancy-rich TiO_2 grown on $Ti_3C_2T_x$ MXene also exhibits excellent NRR performance as oxygen vacancies can active the inert N_2 molecule and highly conductive $Ti_3C_2T_x$ nanosheets could not can offer unhindered electron transfer.[59] Bimetallic PdCu on reduced graphene oxide presents a synergistic effect, leading to superior electrocatalytic NRR performance.[60]

1.3 Structure of Thesis

Based on the above analysis, electrocatalytic HER and NRR are very important reactions in the field of energy conversion and utilization. The primary objective of this thesis is designing highly efficient water splitting and NRR electrocatalysts by surface and interface engineering, the detailed organization of the thesis are summarized as follows:

Chapter 1: Introduction. In this chapter, the significance and basic principles of water splitting is first introduced, followed by effective strategies for enhanced water splitting performance and current HER catalysts development. Then, the importance of nitrogen reduction is presented, and possible NRR mechanisms are also explained to deepen the understanding of NRR electrocatalysts development. Last, the context of the thesis is summarized for the guidance of the reading.

Chapter 2： Promoted interfacial H_2O supply by surface hydroxyl groups for enhanced alkaline hydrogen evolution. This chapter applies M/3D graphene modes (M = MoS_2, Pt, Fe, Ni@NiO and Co@CoO) to study the effect of interfacial H_2O supply on HER kinetics. Hydroxylated surface is then designed to facilitate the interfacial H_2O supply and boost the HER kinetics. The effect of surface hydroxyl groups on HER is investigated from both theoretical and experimental view.

Chapter 3： Active site engineering of Fe- and Ni-sites for highly efficient electrochemical overall water splitting. In this chapter, we fabricate self-supported Fe-doped Ni_2P electrocatalyst based on cost-effective 304-type SS mesh, and successfully realize selective water splitting performance by controlling the atomic content of Fe dopant. The combination of experimental and theoretical results clarifies the role of Fe dopant on bifunctional Ni-Fe-P surface.

Chapter 4: Unusual electrocatalytic nitrogen reduction of sulfurized Pt nanoparticles. This chapter demonstrates that sulfurized Pt nanoparticles plays a pivotal role in effective activation of N_2 and suppression of undesirable HER for improved electrochemical NRR efficiency. DFT calculation is first applied to predict the theoretical HER performance and NRR mechanism. PtS nanoparticles on carbon cloth are then fabricated to investigate the enhanced NRR performance of sulfurized Pt nanoparticles.

Chapter 5: Computational design of transition metal single atom electrocatalysts on PtS_2 for efficient nitrogen reduction. In this chapter, we propose computational methods to evaluate NRR performance of single atom electrocatalysts supported on PtS_2 substrate. Besides, the inner relationship among potential limiting step, binding strength of N* and unoccupied *d* orbitals of single atom center is first established, bridging the NRR activity and intrinsic electronic structure of SACs.

Chapter 6: Summary and future prospect. In this chapter, the results of this thesis are summarized, and the future prospect is also described.

2 Promoted Interfacial H_2O Supply by Surface Hydroxyl Groups for Enhanced Alkaline Hydrogen Evolution

2.1 Objective and Motivation

Robust hydrogen evolution reaction (HER) in alkaline solution using a cost-effective catalyst is still a critical challenge for industrial H_2O electrolysis. The dramatical depletion of interfacial H_2O and hindered OH^- diffusion bring about harsh interfacial environment, and thereby lead to sluggish hydrogen evolution. Here we develop heterogeneous catalysts based on the defect-rich three-dimensional graphene (M/3D graphene) and achieve promoted HER kinetics via surface hydroxyl group modification on graphene surface. Our theoretical studies suggest that the surface hydroxyl groups derived from the hydroxylation process effectively attract multi-overlayers H_2O clusters without thermodynamic barrier and form reservoir to continuously supply H_2O for catalytic sites. Electrochemical characterizations indicate the HER kinetic per active electrochemical surface area has been greatly improved after crafting abundant hydroxyl groups on 3D graphene framework, which can be attributed to sufficient proton donor and ameliorative interfacial pH environment. Benefiting from the surface hydroxyl group modification, MoS_2/3D graphene structure occurs HER at a low onset potential of 60 mV in alkaline medium and exhibits excellent durability after 3000 cycles. This surface modification strategy unveils the importance of interfacial H_2O supply on HER kinetics and provides general guidance on designing high-efficient catalysts in alkaline medium.

2.2 Introduction

The Hydrogen fuels, with zero carbon emission and high energy density, have stimulated large-scale industrial hydrogen production. Currently, electrolysis of H_2O is the principal pathway for producing large amount and high purity hydrogen in industry.[61-65] Hydrogen evolution by H_2O electrolysis in industry mainly occurs in alkaline medium instead of acidic solution. There are two major reasons for the use of alkaline solution. First, it can effectively retard the corrosion of equipment that usually occurs in acidic solution. Second, alkaline hydrogen evolution is more promising to couple with oxygen evolution reaction (OER) to accomplish electrochemical overall H_2O splitting. [66] Unfortunately, the sluggish kinetics and low efficiency of hydrogen evolution in alkaline medium prevent the wide implementations of hydrogen evolution. Even for the most efficient hydrogen evolution reaction (HER) catalyst, Pt, the HER kinetic in alkaline electrolyte is 2-3 orders of magnitude slower than that in acidic medium.[67] So far, the sluggish kinetics of alkaline HER have been generally understood from the following three aspects: (1) inert Volmer reaction ($M + H_2O + e^- \rightarrow MH_{ads} + OH^-$), which involves in H_2O dissociation and reactive Had intermediate formation, (2) high energy barrier for negatively charged hydroxide ion (OH^-) desorption and (3) harsh interfacial environment due to hindered interfacial mass transfer.[68-69]

Extensive efforts have been dedicated to design highly active catalytic centres for H_2O dissociation and choose catalysts with Gibbs free energy of adsorbed OH^- ($\triangle G_{OH-}$) that close to zero.[70-76] However, the hindered interfacial mass transfer still diminishes hydrogen evolution rate in alkaline medium. As the H_2O dissociation proceeds, the interfacial H_2O molecule dramatically depletes and lots of OH^- ions are released from the catalytic sites.[67] The abrupt depletion of H_2O and accumulation of OH^- inevitably bring about sharp increase of interfacial pH value around the active sites, which suppresses continuous catalytic reaction and leads to sluggish kinetics and

probably accounts for the poor long-term durability. Thus, aimed to ensure long-lasting efficient alkaline HER process, timely H_2O supply or rapid OH^- diffusion are required to dilute the interfacial OH^- concentration and balance the pH environment promptly.[77] In addition, the successive H_2O supply will maintain adequate proton source for continuous alkaline hydrogen evolution reaction. Unfortunately, large reorganization energy for interfacial H_2O in alkaline medium prevents the efficient OH^- transfer through electric double layer.[9] Therefore, it is important to develop effective strategies to increase the interfacial H_2O supply, and it will be more significant if the well-designed strategies can perform efficiently and sustainably in severe alkaline medium.

It is widely accepted that hydrogen bond is a desirable electrostatic attraction, and it plays a vital role in attracting H_2O clusters and realizing facilitated ionic transport in biosystems.[78] For example, [Fe-Fe] hydrogenase has been discovered with efficient proton transport pathway that composed by amino residues and H_2O clusters, where the pendant amines attract H_2O clusters via strong H-bond and forms water-rich channels for continuous proton stream supply for active catalytic centers.[79-80] Despite the superior hydrophily of amino residues, its inherent intolerance of harsh pH environment blocks the feasibility of application in alkaline medium, and the modification of amino acid on electrode surface may lead to steric effect due to its huge molecule volume, shielding the intrinsic active catalytic site. Therefore, it inspires us to seek for suitable modification methods to create alkali-tolerant electrode surface that can effectively attract H_2O clusters via strong H-bond interaction.

Surface hydroxyl group is an excellent alternative to replace amino residues because its superior hydrophilic nature and excellent stability in alkaline medium. Besides, surface hydroxyl group only occupies small space and is easy to create through mild treatment. So far, lots of

hydroxylated surfaces show enormous potential to adsorb H_2O molecules without thermodynamic barrier.[81-82] Thus, the surface with abundant surface hydroxyl groups is promising to attract free H_2O molecules for successive H_2O dissociation and relieve the sluggish HER kinetics induced by hindered interfacial mass transport. To address this challenging issue, we first demonstrate a strategy to craft defect-rich 3D self-supported graphene and realize the enhancement of HER performance by converting other surface functional groups (C-H or C=O) into surface hydroxyl groups. More importantly, the surface hydroxyl group also plays positive role in hydrogen evolution in M/3D graphene composite structures (M=MoS_2, Pt, Fe, Ni@NiO and Co@CoO), and all the structures show promoted HER kinetics after surface hydroxylation. The hydroxyl groups anchored on the 3D graphene frameworks tightly bond with free H_2O molecules via strong H-bond and form reservoir on cathode surface, offering continuous H_2O stream for catalytic active sites. The facilitated interfacial H_2O supply is conducive to sustain adequate proton donor for hydrogen evolution and balance the interfacial pH environment by diluting the interfacial OH^- concentration. Moreover, the 3D graphene skeleton provides unimpeded channels for efficient electron transfer and electrolyte transport during electrocatalytic process. In MoS_2/3D graphene structure, surface hydroxyl group, porous graphene framework and active catalytic sites synergistically collaborate, contributing to an excellent HER performance and long-term durability even in an alkaline solution of pH = 14.0.

2.3 Experimental Section

2.3.1 Synthesis and Preparation: The MoS_2/3D graphene structure synthesis was composed by two steps. At first, 0.1 g glucose, 0.1 g $(NH_4)_2MoS_4$ and 1.0 g NH_4Cl were dispersed in 20 mL ethanol by vigorous stirring to uniformly coat the glucose and $(NH_4)_2MoS_4$ on the surface of NH_4Cl. Next, the mixture was then baked on a hot plate at 65 °C under a continuous stirring to

vapor the solvent. After ethanol evaporation, grey black precursors can be collected. The grey black precursors then experienced a two-step annealing process in a tube furnace, the heating rate was 10 °C /min. The heating center temperature of the furnace was raised up to 500 °C and held at this temperature for 60 min, and was then continuous raised the temperature to 1000 °C in 100 min, followed by a constant reaction temperature of 1000 °C for 30 min. H_2 atmospheres was selected in the first-stage of annealing process to lower the decomposition temperature of $(NH_4)_2MoS_4$ and increase the content of sp^3 carbon in graphene frameworks. The second annealing was performed under Ar atmosphere, accounting for the etching interaction between H_2 and MoS_2 when the temperature was above 500 °C. Other M/3D graphene structures (M = Pt, Fe, Ni@NiO or Co@CoO) were fabricated via above annealing process except for replacing the 0.1 g $(NH_4)_2MoS_4$ with 0.021 g $H_2PtCl_6•6H_2O$, 0.062 g $FeCl_3$, 0.112 g $Ni(NO_3)_2•6H_2O$ or 0.095 g $Co(CH_3COO)_2•4H_2O$, respectively. The M/3D graphene structures (M = Pt, Fe, Ni@NiO or Co@CoO) were denoted as Pt-G, Fe-G, Ni@NiO-G or Co@CoO-G, respectively. The hydroxylated samples were obtained by treating the samples in a 1.0 M NaOH solution, then the dispersed samples in the NaOH solution was washed with DI H_2O.

2.3.2 Electrochemical Tests: A three electrodes electrochemical station was used to perform electrochemical measurements (Solartron Analytical). All alkaline tests were performed in a solution of 50 mL of 1.0 M NaOH electrolyte (pH = 14.0), the HER performances in neutral medium was performed in 0.5 M Na_2SO_4. Typically, 10 mg of sample and 20 μL Nafion solution were dispersed in 1.0 mL isopropanol solution, followed by ultrasonic treatment for 1 h to form a homogeneous ink. Then 10 μL of the dispersion was loaded onto a polished glassy carbon electrode with the diameter of 3 mm. The glassy carbon electrode loaded with sample, graphite rod and Hg/HgO were applied as working electrode, counter electrode and reference electrode,

respectively. The performance of the HER was tested using linear sweep voltammetry (LSV) with a scanning window of 0 V to -0.8 V vs RHE and a scan rate of 10 mV s^{-1}. The durability of MoS_2-G was evaluated by cycling test of 3000 times. All the LSV curves are corrected with iR compensation.

2.3.3 Electrochemical Active Surface Area: Electrochemical capacitance measurements were used to calculate the active surface area of the MoS_2-G. The applied potential was set between 0.12 to 0.22 V vs. SCE for 20 cycles at different scan rates (5, 10, 20, 30 and 50 mV/s). The capacitive currents were measured in the potential range of no faradic reactions and the current data were collected at the 0.17 V vs. SCE. Then, the capacitive currents were plotted as a function of scan rate to calculate the double layer capacitance. The EASA can be calculated based on following equation:

$$EASA=C_{dl}/C_s$$

C_{dl} is the double layer capacitance and C_s is the specific capacitance. In general, the specific capacitance for a flat surface is in the range of 0.02-0.06 mF/cm^2. In this paper, we choose the value of 0.04 mF/cm^2 in 1.0 M NaOH to calculate the EASA.

2.3.4 Characterizations: The morphology of MoS_2/3D graphene structure was characterized by scanning electron microscope and scanning transmission electron microscope (SEM, Jeol JSM-6335F & TEM, Jeol JEM-2100F). The crystal structure and composition of MoS_2/3D graphene structure were measured by X-ray Diffractometer (Rigaku SmartLab) and Raman spectroscope (Horiba HR800) with an excitation wavelength of 488 nm. The electrochemical impedance spectroscopy (EIS) of MoS_2-G before and after alkaline treatment were performed by a three-electrode configuration using CHI-660E electrochemical analyser. The surface valence state of

samples were tested by using X-ray photoelectron spectroscopy (XPS, Thermol Scientific Escalab 250Xi, Al Kα radiation). The contact angle of samples were investigated by water contact angle measurement (SDC-350).

2.3.5 Theoretical Calculations: Theoretical calculations were performed using density functional theory (DFT) as implemented in the VASP code (5.4) with exchange-correlation energy functional, which were modeled by Perdew-Burke-Ernzerhof (PBE) functional.[83-84] The cut-off energy was set to be 450 eV and all structures were relaxed to an energy convergence of 10^{-5} eV/atom and a force convergence of 0.02 eV/Å, respectively. During the geometrical optimization, 2 × 2 supercell was applied to mimic the H_2O adsorption on graphene and the k-points was 3 × 3 × 1. The thickness of vacuum in all the models was set to 30 Å to eliminate the interactions between the layers caused by the periodic boundary condition. Van der Waals (vdW) interaction correction was applied to all the structures by Grimme's DFT-D2 method. The adsorption energy of adsorbed H_2O, E_{ad}, was defined as the mean adsorption energy per H_2O molecule of the structure:

$$E_{ad} = (E_{(H_2O)/sub} - E_{sub} - n \times E_{H_2O})/n$$

The binding energy of free H_2O cluster, E_{bind}, was defined as the mean binding energy per H_2O molecule of the structure:

$$E_{bind} = (E_{cluster} - n \times E_{H_2O})/n$$

Here, $E_{(H_2O)/sub}$ is the total energy of the adsorption system, E_{sub}, $E_{cluster}$ and E_{H_2O} are energies of the substrate, free H_2O clusters and free molecules, respectively, and n is the number of H_2O molecules in the supercell.

2.4 Characterizations of catalysts and evaluation of HER activity

Figure 2.1a schematically illustrates a two-step process for the growth of MoS_2/3D graphene structure (MoS_2-G). After the two-step consecutive temperature-programmed calcination, the glucose turns into porous graphene via the blowing process induced by thermal decomposition of NH_4Cl, and $(NH_4)_2MoS_4$ simultaneously decompose into few-layered MoS_2 nanosheets decorated on the surface of 3D graphene framework.[85-86] The successful preparation of MoS_2/3D graphene is confirmed by X-ray diffraction (Figure 2.1b) and Raman spectra (Figure 2.1c). The diffraction peaks of MoS_2-G are assigned to the plane (002), (100), (102), (103), (006), (104), (105) and (110) of 2H-MoS_2 (PDF No. 87-2461), which shows similar pattern with the MoS_2 sample prepared in the same condition without glucose. A broad diffraction peak at $2\theta = 22°$ can be observed in MoS_2-G sample, which is recognized as the characteristic peak of defect-rich graphene, implying a d-spacing of 0.405 nm. Figure 2.1c illustrates the characteristic Raman peaks of MoS_2 at 380 and 405 cm^{-1}, which represent in-plane (E^1_{2g}) and out-of-plane (A_{1g}) vibrational modes, respectively.[87] The A_{1g} mode exhibits higher intensity than that of E^1_{2g} mode, indicating that the MoS_2 is edge-terminated dominated structures. The Raman peaks at 1350 cm^{-1} and 1580 cm^{-1} correspond to the D and G bands of graphene.[88-92] The D peak is associated with the size of the in-plane sp^2 (C=C) domains of graphene, and the relative intensity ratio of D peak and G peak (I_D/I_G) is an indicator of disorder degree. The I_D/I_G in our sample is approximately 0.97, suggesting that the graphene framework is rich of defects.

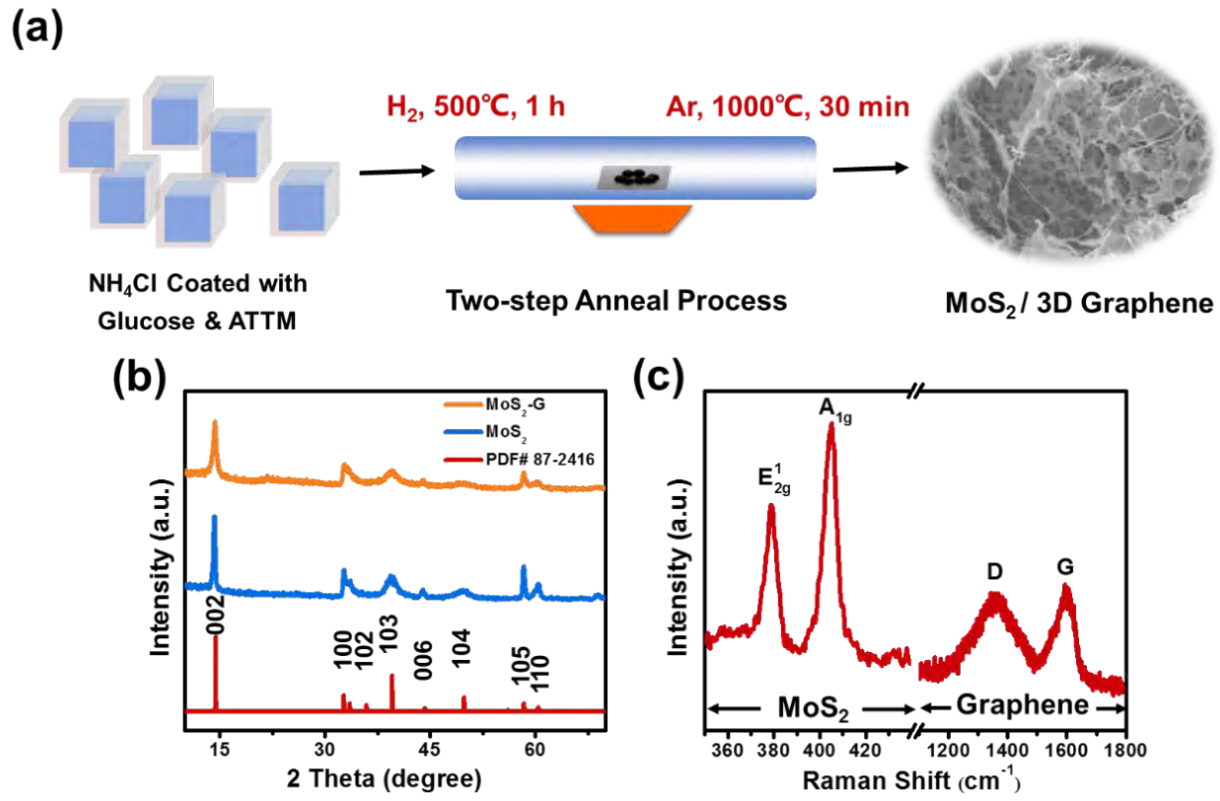

Figure 2.1. (a) Schematic illustration of the two-step thermolysis process for the fabrication of porous MoS_2-G structure. (b) X-ray diffraction spectra of the as-grown porous MoS_2-G and MoS_2 nanosheets prepared under the same anneal process. (c) Raman spectra of the porous MoS_2-G sample.

The surface chemical state is further characterized by X-ray photoelectron spectroscopy (XPS) to analyse defect types of graphene. Figure 2.2a shows XPS spectrum of the MoS_2-G. The pronounced peaks in the XPS spectrum consist of Mo, S, C and O, excluding the possibility of nitrogen-doping induced by the thermolysis of NH_4Cl. The element fraction of O in MoS_2-G is 13.14%, further confirming the oxygen-rich nature of 3D graphene. As shown in the high resolution XPS spectrum of C 1s (Figure 2.2b), the dominant carbon species in graphene framework is sp^2 carbon with a fraction of 49.71%. The high percentage of sp^2 carbon enables good conductivity for the electron transfer in MoS_2-G. Another primary carbon species existing in the graphene framework is sp^3 carbon (C-C or C-H), accounting for 31.58% in the total amount of carbon element. Minor fraction of C-O and C=O are also discovered in graphene framework,

occupying proportions of 11.06% and 7.65%, respectively. The high resolution XPS spectrum of O 1s (Figure 2.2c) demonstrates that three types of O species exist on the framework of graphene, implying the graphene surface with abundant oxygen-containing functional groups.

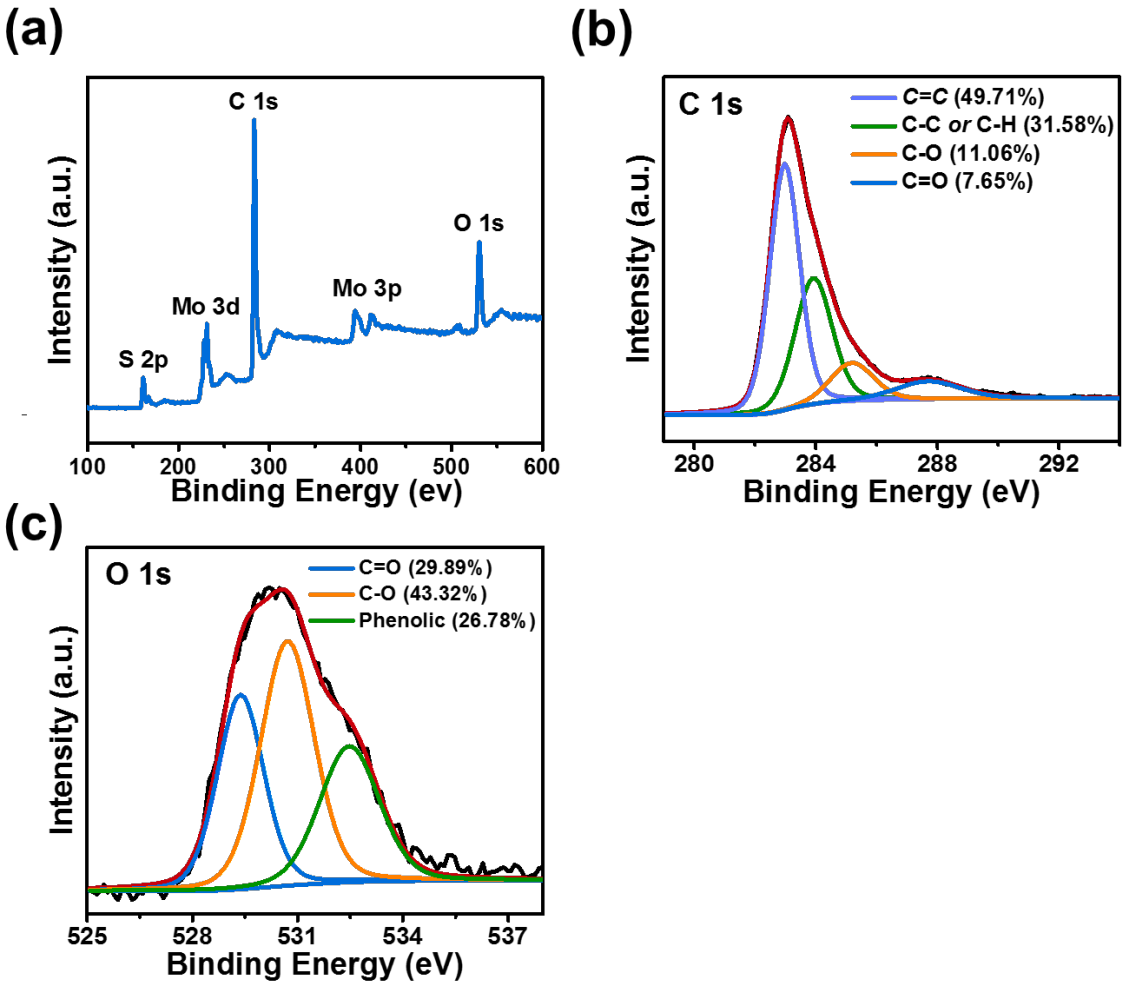

Figure 2.2. (a) XPS spectra of prepared MoS_2-G. (b) The C1s and (c) O1s XPS spectra of MoS_2-G sample.

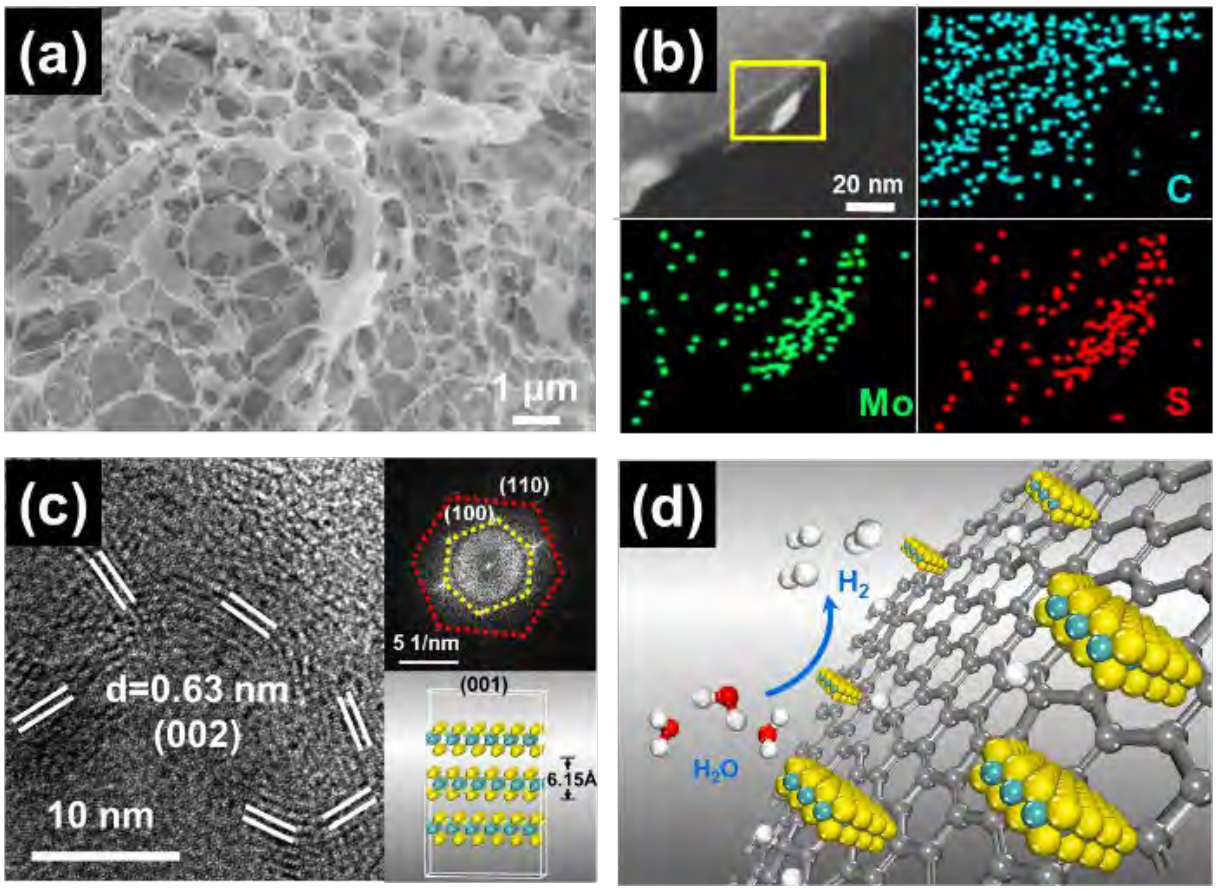

Figure 2.3. (a) SEM image of porous MoS_2-G structure. (b) STEM-EDS elemental mapping images of the MoS_2-G. (c) High-resolution TEM image for the MoS_2 nanosheet. Inset is the SAED pattern of the MoS_2 nanosheet anchored on the surface of graphene framework and the standard crystal structure of MoS_2. The d_{002} in standard PDF card is 6.15 Å, which is consistent with the HRTEM pattern. (d) The schematic diagram of H_2 evolution on the surface of MoS_2-G structure in alkaline medium.

The morphology of the MoS_2-G was investigated by scanning electron microscopy (SEM) and transmission electron microscope (TEM). As indicated in Figure 2.3a, the skeleton of MoS_2-G exhibits continuous 3D carbon membranes with micrometre-width pores. This 3D graphene framework derived from the sugar blowing technique not only provides an electrically conductive pathway for electron transfer, but also facilitates efficient electrolyte transport for electrocatalytic reaction. The TEM images (Figure 2.3b and Figure 2.4a) show that the MoS_2 nanosheets are mainly decorated on the surface of 3D graphene, and the average sheet size is 10-20 nm. As the

HRTEM image depicted in Figure 2.3c and Figure 2.4b-2.4d, the MoS_2 grown on 3D graphene framework reveals an average interlayer spacing of 0.63 nm, which is in accord with the standard (002) crystal spacing of MoS_2. The well-matching d-spacing value shows that the MoS_2 nanosheets are vertically grown on the surface of 3D graphene framework, which exposes more active sites for H_2O dissociation.[93] Thus, the microstructure of MoS_2-G can be schematically depicted as Figure 2.3d. The vertically aligned growth mode of MoS_2 not only maximizes the exposure of active catalytic sites, but also provides a regulated electron transfer in the basal plane, reducing the interlayer electron hopping resistance.[94-95]

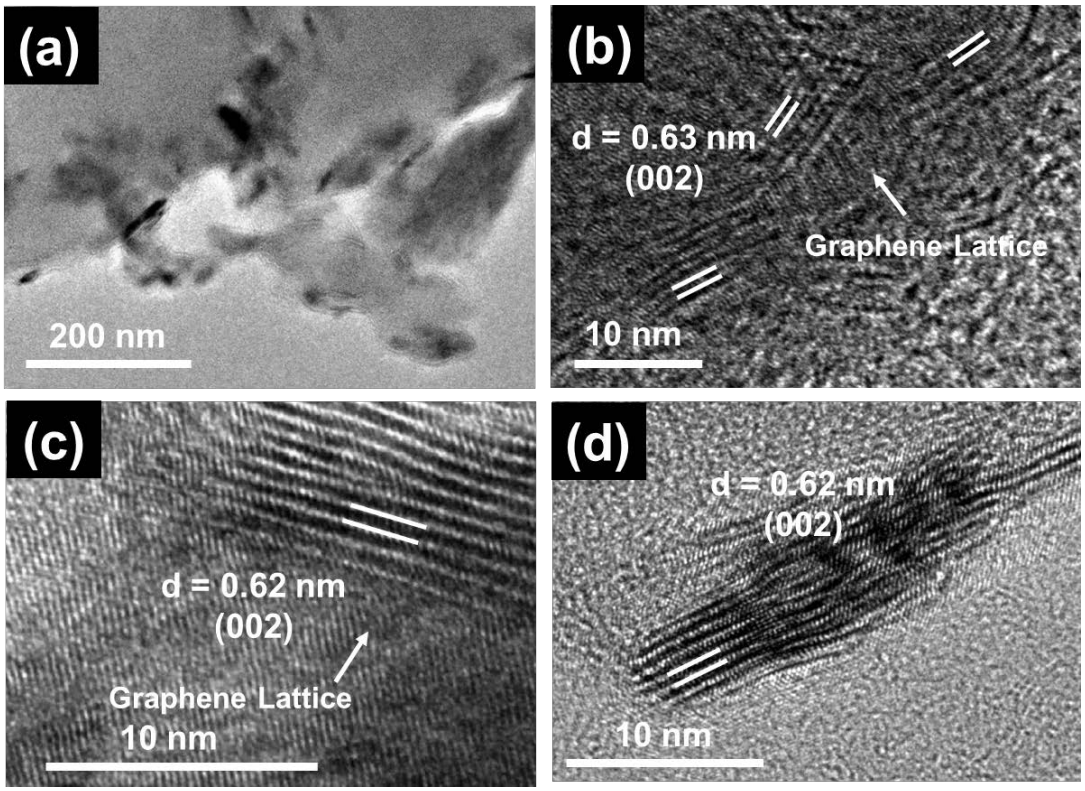

Figure 2.4. (a) TEM and (b-d) HRTEM images of the MoS_2-G heterojunctions.

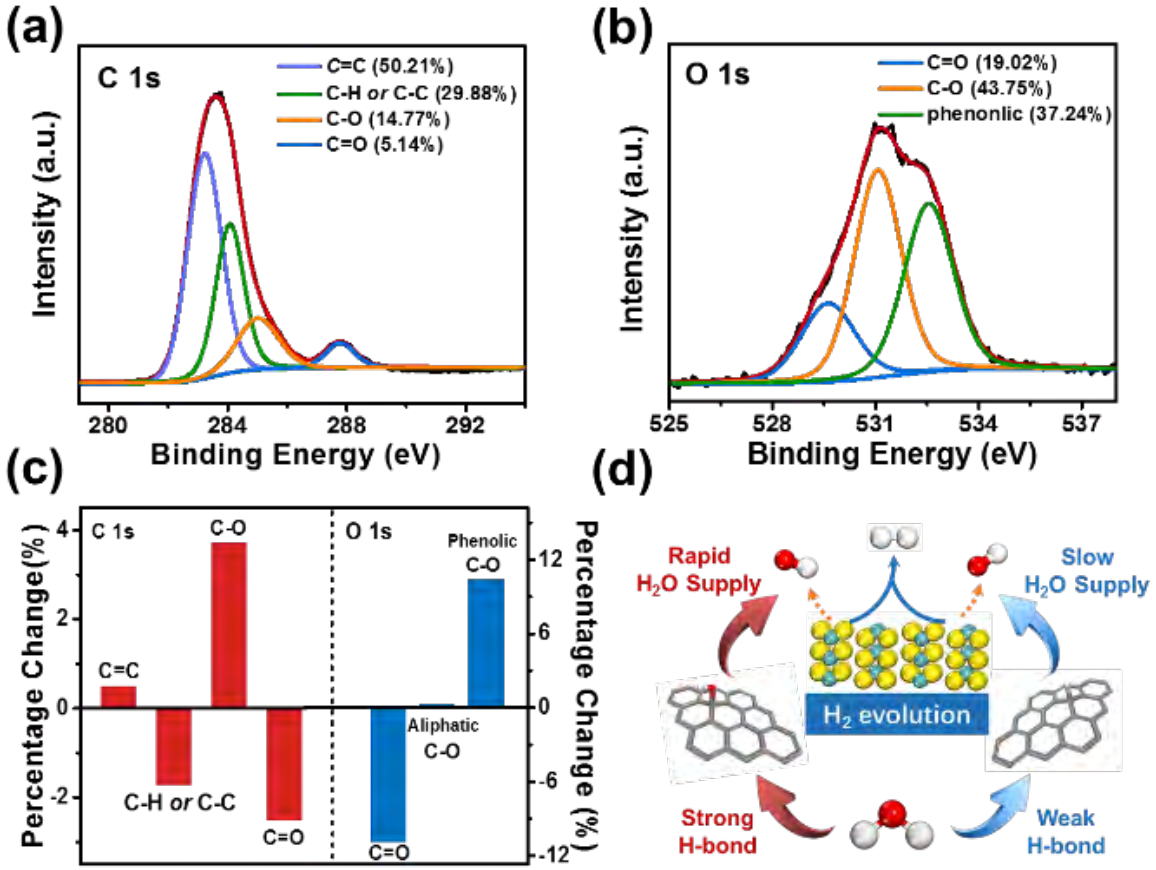

Figure 2.5. (a) The C 1s and (b) O 1s XPS spectra of MoS_2-G sample after NaOH treatment. (c) The percentage change of C and O species on the surface of MoS_2-G after NaOH treatment. (d) Schematic illustration for the difference of H_2O transfer process between the surface with C-H and C-OH surface.

To investigate the effect of surface hydroxyl group on alkaline HER performance, we applied conventional alkaline treatment to induce the functional groups conversion,[96] and used XPS to confirm the increasing concentration of surface hydroxyl groups (Figure 2.5a-2.5b). The MoS_2-G after the NaOH treatment is denoted as MoS_2-G-OH. The high resolution XPS spectra of Mo and S display negligible difference before and after alkaline treatment (Figure 2.6), indicating that MoS_2 exhibits good stability during alkaline treatment.[97] However, obvious changes of the surface functional groups on 3D graphene have been observed after the alkaline treatment. As clarified in Figure 2.5c, the fractions of sp^3 carbon and C=O of 3D graphene show obvious

reduction after the NaOH treatment, decreasing 1.7% and 2.51%, respectively. The ratios of sp^2 carbon and aliphatic C-O remain almost unchanged throughout the NaOH treatment process. In contrast, the contents of C-O in C 1s and phenolic C-O in O 1s increase, especially for phenolic C-O, greatly increasing from 26.78% to 37.24%. The increase of phenolic C-O possibly brings about abundant surface hydroxyl groups, which have potential to form reservoir and enrich interfacial H_2O molecules for continuous H_2O supply (Figure 2.5d).

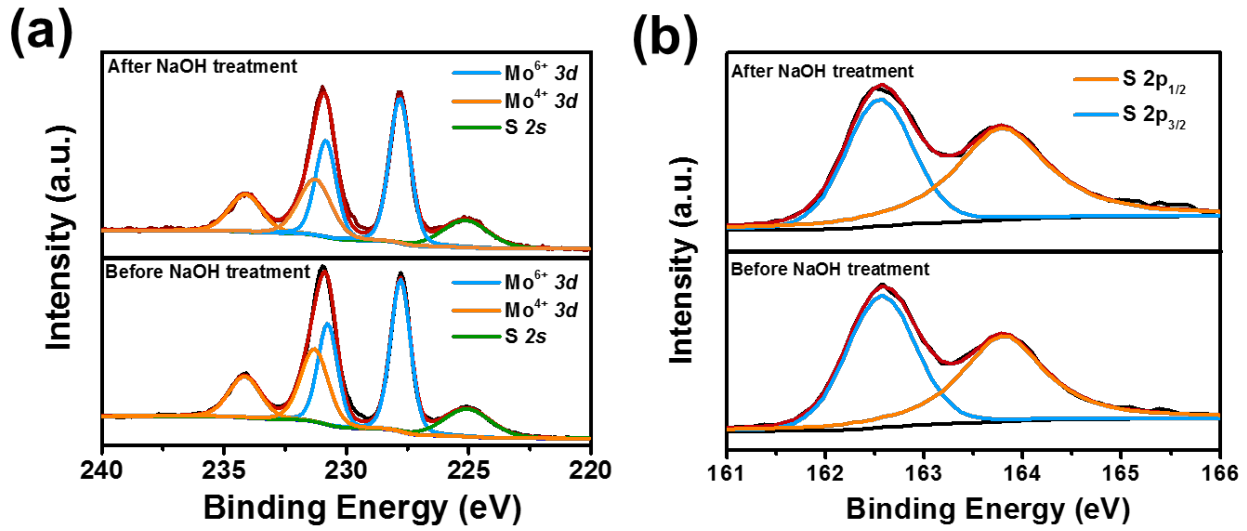

Figure 2.6. Chemical composition analysis by XPS for (a) Mo and (b) S in MoS_2-G sample before (downside) and after NaOH treatment (upside).

The enhancement of HER performance induced by surface hydroxyl group is then confirmed by comparing the electrochemical hydrogen evolution characters of MoS_2-G and MoS_2-G-OH. Neutral Na_2SO_4 solution is selected as electrolyte, because the HER mechanism in Na_2SO_4 solution is similar to that in alkaline medium and it is easier to evaluate the positive influence of hydroxyl group induced by alkaline treatment in a non-alkaline medium. As expected, hydroxyl group modification greatly promotes the electrocatalytic HER performance of MoS_2-G, giving rise to the great reduction of overpotential and sharp increase of current density, simultaneously

(Figure 2.7a). The Tafel slope of MoS_2-G before and after treatment reveals that the hydroxyl group modification leads to negligible change of HER mechanism.

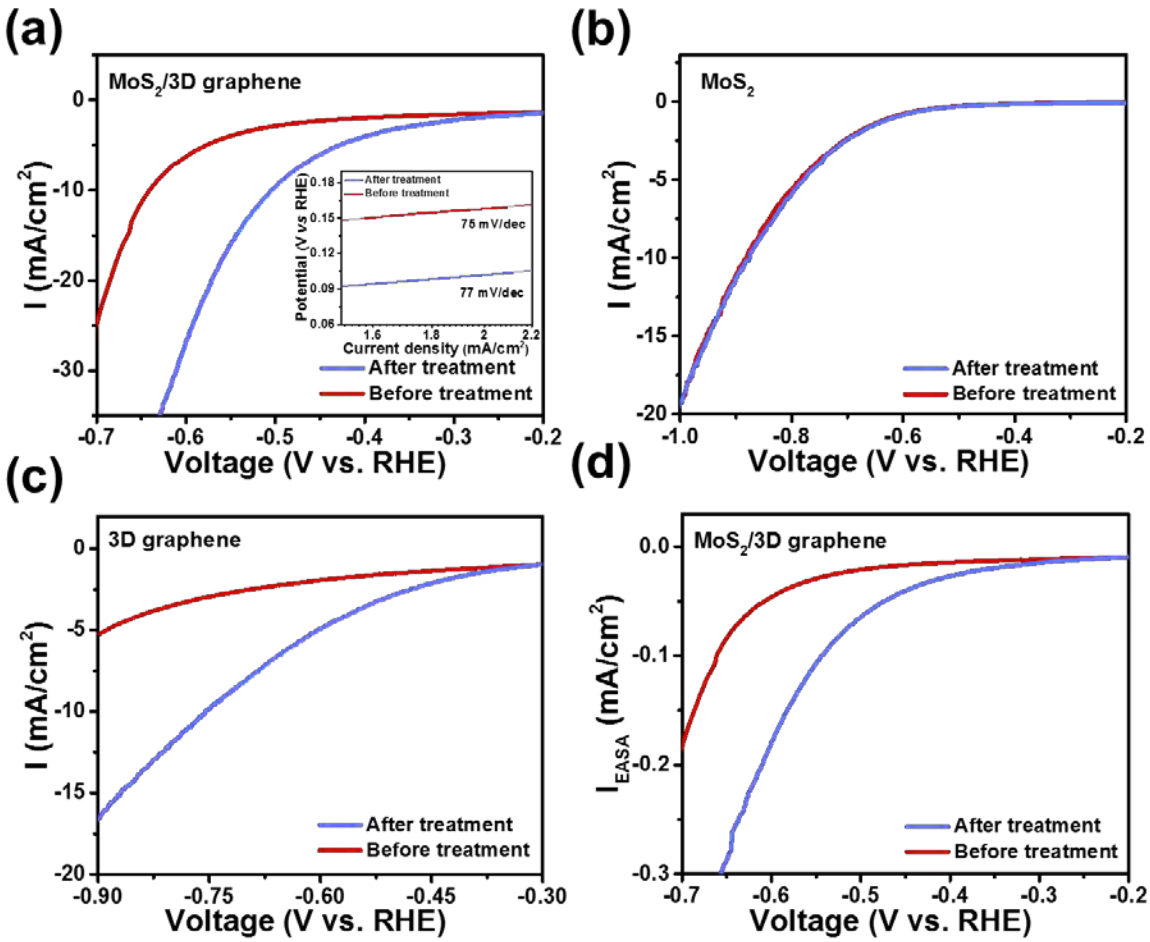

Figure 2.7. The iR-corrected LSV curves of MoS_2-G before and after NaOH treatment in 0.5 M Na_2SO_4 solution. Scan rate: 10 mV s^{-1}. Inside is the Tafel plots of MoS_2-G before and after NaOH treatment. The iR-corrected LSV curves of (b) MoS_2 and (c) 3D graphene samples before and after NaOH treatment in 0.5 M Na_2SO_4 solution. Scan rate: 10 mV s^{-1}. (d) Polarization curves of MoS_2-G normalized to the EASA before and after NaOH treatment in 0.5 M Na_2SO_4 solution. Scan rate: 10 mV s^{-1}.

Electrocatalytic HER tests are also conducted on alkaline treated 3D graphene and MoS_2 samples separately to investigate the internal cause of enhanced HER performance (Figure 2.7b-2.7c). The sharp contrast between 3D graphene and MoS_2 further verifies that the hydroxyl group modification occurred on 3D graphene framework plays a dominant role in improving HER

performance. Electrochemical impedance spectrum (EIS), contact angle and electrochemical active surface area (EASA) are then applied to investigate the inner mechanism. Figure 2.8 show the electrochemical impedance spectrum of MoS_2-G before and after alkaline and their equivalent circuit for EIS fitting. Clearly, the hydroxyl group modification brings about negligible change of charge transfer resistance (Rct) for MoS_2-G. The Rct for MoS_2-G before and after the alkaline treatment are 2.3 Ω and 2.8 Ω, respectively, the slight increase of Rct should be attributed to the increasing oxygen content induced by hydroxyl group modification. However, the solution resistance (RS) and electrolyte transfer resistance (Ret) of MoS_2-G show decreasing trend after the hydroxyl group modification, implying reduced catalysts/electrolyte interface resistance and facilitated electrolyte diffusion process.

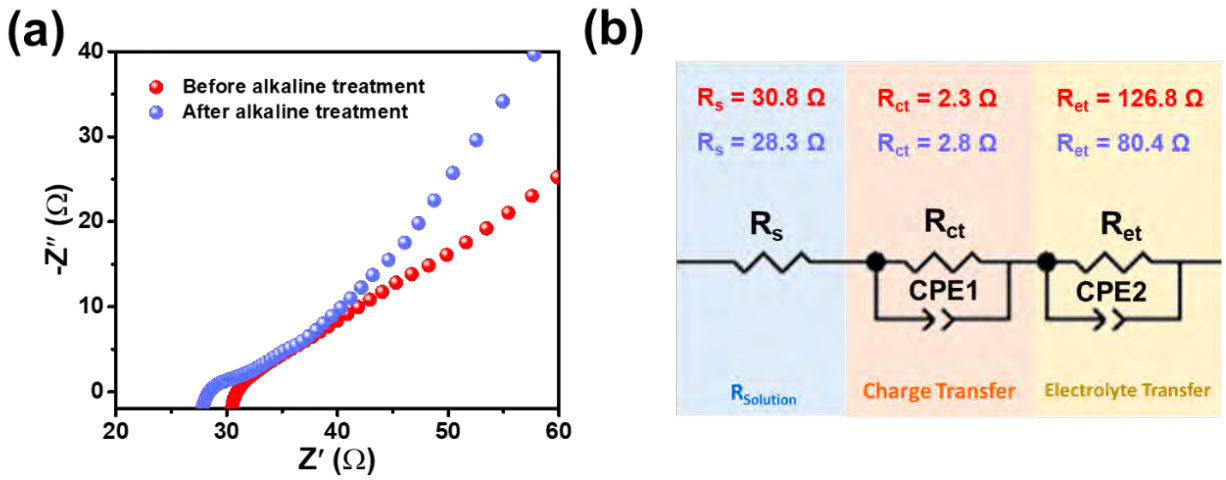

Figure 2.8. (a) The electrochemical impedance spectrum of MoS_2-G before and after alkaline treatment. (b) The equivalent circuit for EIS fitting.

Contact angles of MoS_2-G before and after alkaline treatment reveal that higher wettability can be observed after surface hydroxyl group modification, rapid interfacial interaction between electrolyte and cathode may result in smaller interfacial resistance (Figure 2.9). The EASA before and after treatment are also calculated based on the electrochemical double layer capacitance (Figure 2.10), the EASA of MoS_2-G and MoS_2-G-OH are 135.5 and 149.3 cm^{-2} EASA,

respectively. More interestingly, when normalized to the EASA (Figure 2.7d), the MoS_2-G-OH still displays much higher current density than its counterpart, which means the HER kinetic at every active catalytic site has been promoted on hydroxylated surface.

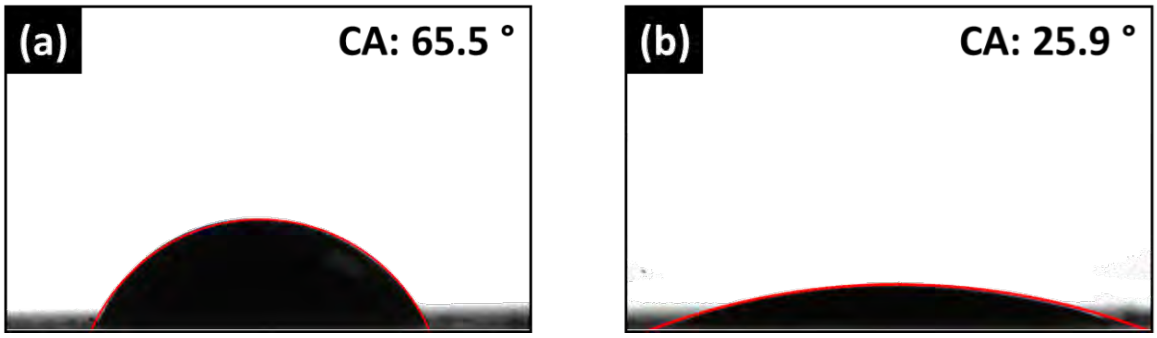

Figure 2.9. Contact angles of MoS_2-G (a) before and (b) after alkaline treatment.

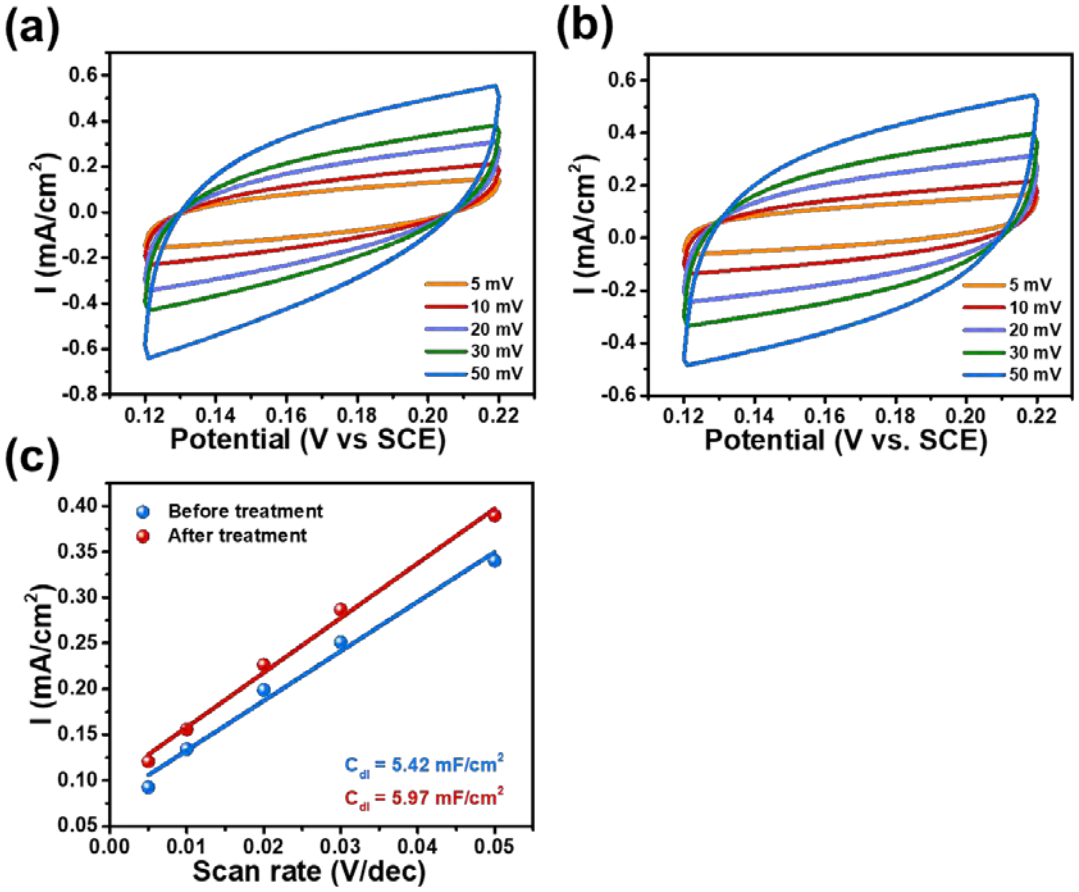

Figure 2.10. Cyclic voltammograms were tested in the non-faradaic region of 0.12–0.22 V of MoS_2-G (a) before and (b) after alkaline treatment. (c) Polarization curves of MoS_2-G normalized to the EASA before and after NaOH treatment in 0.5 M Na_2SO_4 solution. Scan rate: 10 mV s^{-1}.

Moreover, we use other active materials, such as Pt, Fe, Ni@NiO and Co@CoO to replace MoS_2 and form different M/3D graphene (M = Pt, Fe, Ni@NiO or Co@CoO) structures (Figure 2.11) to confirm the universality of enhancement mechanism induced by surface hydroxyl group. As the Figure 2.12 show, all of the M/3D graphene structures show obvious enhanced HER performance after the hydroxylation process. The dramatically increasing current densities and reduced overpotential of alkaline treated samples indicate that the HER kinetics of these M/3D graphene systems have been greatly improved. Based on the above analysis, we firmly believe that surface hydroxyl group plays a better role of improving HER kinetics than other surface functional groups (C-H or C=O), and the positive effect induced by surface hydroxyl group modification can be widely extended into different graphene-based materials.

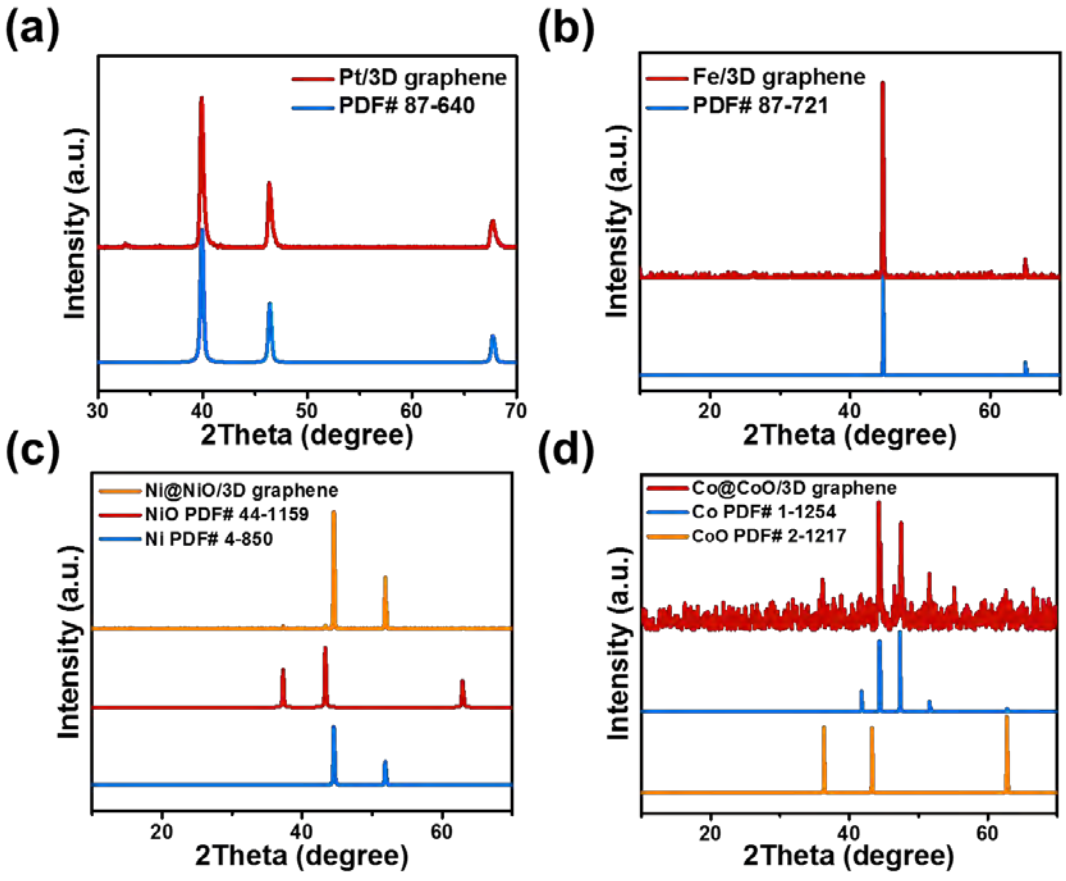

Figure 2.11. The XRD patterns of (a) Pt-G, (b) Fe-G, (c) Ni@NiO-G and (d) Co@CoO-G samples.

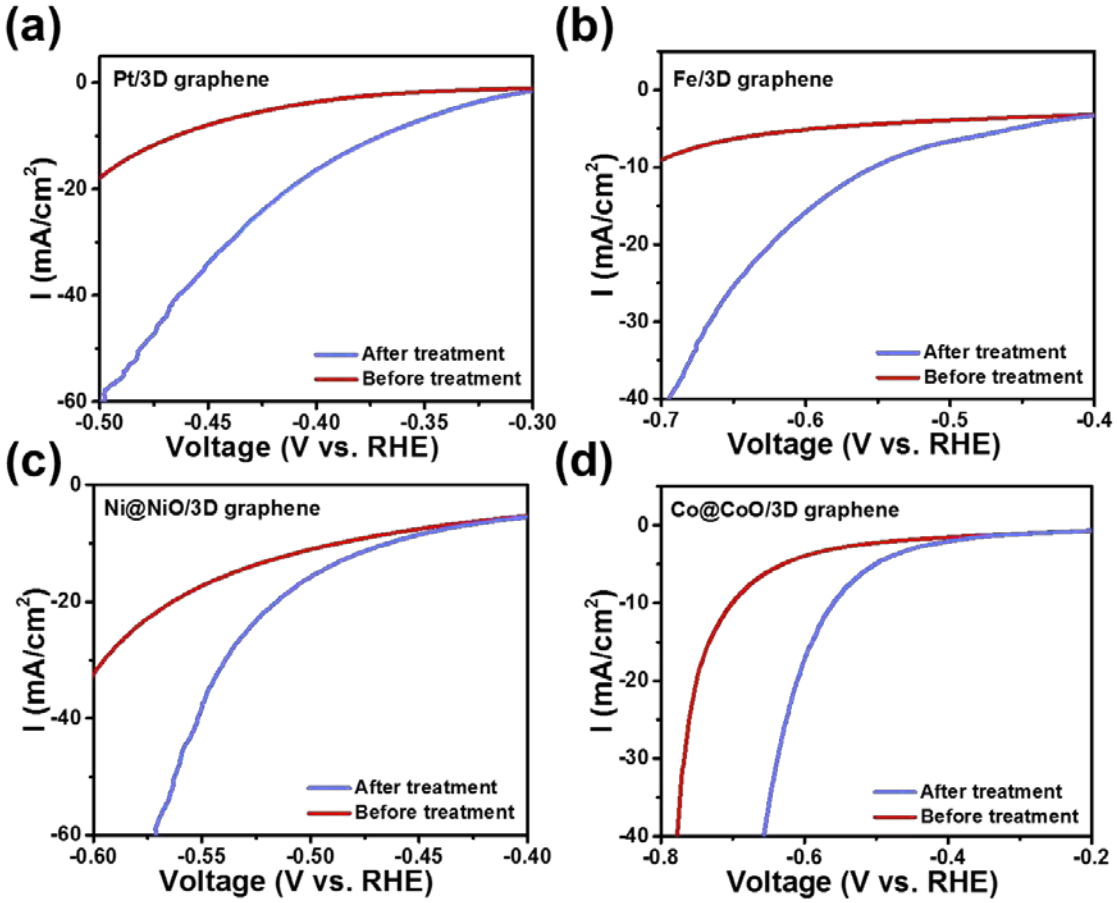

Figure 2.12. The iR-corrected LSV curves of (a) Pt-G, (b) Fe-G, (c) Ni@NiO-G and (d) Co@CoO-G samples in 0.5 M Na_2SO_4 solution before and after NaOH treatment. Scan rate: 10 mV s^{-1}.

To shed light on the advantages of surface hydroxyl group on the enhanced alkaline HER performance, we conduct first principle calculations to examine the change of electron density distribution induced by surface hydroxyl group and visualize the H-bond interaction between hydroxylated surface and H_2O molecules. C-H (G-H) and C=O (G-vac-O) terminated surfaces were selected as the control samples to compare with the hydroxylated surface, because these two functional groups may act as necessary precursors for surface hydroxyl group generation (Figure 2.13a and Figure 2.14a). The charge density contour plots reveal that surface hydroxylation intensifies the nonuniform charge distribution of graphene, and the surface hydroxyl group can confine negative electrons more effectively than G-H surface (Figure 2.13b). The electron-rich

hydroxyl group can easily attract the H_2O molecule and tend to bond with it via typical H-bond. The specific optimized geometrical configurations and corresponding H-bond parameters are described in Figure 2.13a-2.13b. The G-H surface interacts with H_2O molecule via a weak H-bond, which possesses a H-bond length of 2.13 Å.

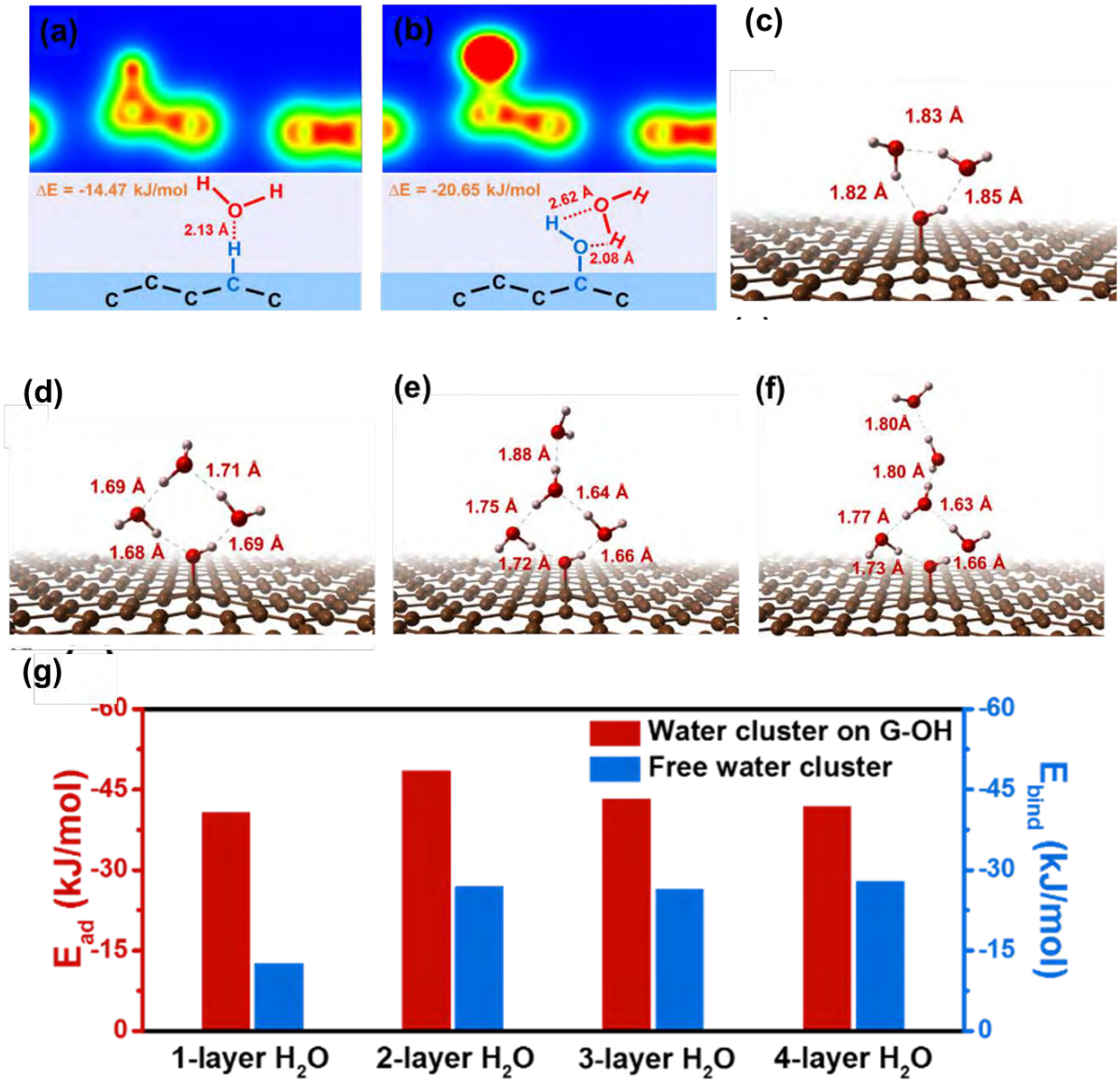

Figure 2.13. (a) Charge density contour plot (topside) of G-H and corresponding H_2O adsorption optimized configuration (downside). (b) Charge density contour plot (topside) of G-OH and corresponding H_2O adsorption optimized configuration (downside). Optimized geometrical structures of (c) one-layer (d) two-layer, (e) three-layer and (f) four-layer H_2O clusters adsorbed on G-OH. (g) The comparison of mean adsorption energies of H_2O molecule on G-OH and mean binding energies of free H_2O to form H_2O clusters.

In contrast, hydroxylated surfaces (G-OH) prefer to bond with the H_2O molecule through strong H-bond interactions. The adsorption energy of H_2O monomer adsorbed on the G-OH (-20.65 kJ/mol) is much lower than that on the G-H (-14.47 kJ/mol). In addition, although G-vac-O sample is observed with nonuniform charge distribution (Figure 2.14b), it still displays inferior capability to adsorb H_2O molecule than its counterpart (G-vac-OH), showing longer H-bond length and weaker thermodynamic feasibility. Thus, hydroxylated surface has more tendency to attract H_2O molecule and form reservoir to continuous supply H_2O molecule for catalytic sites.

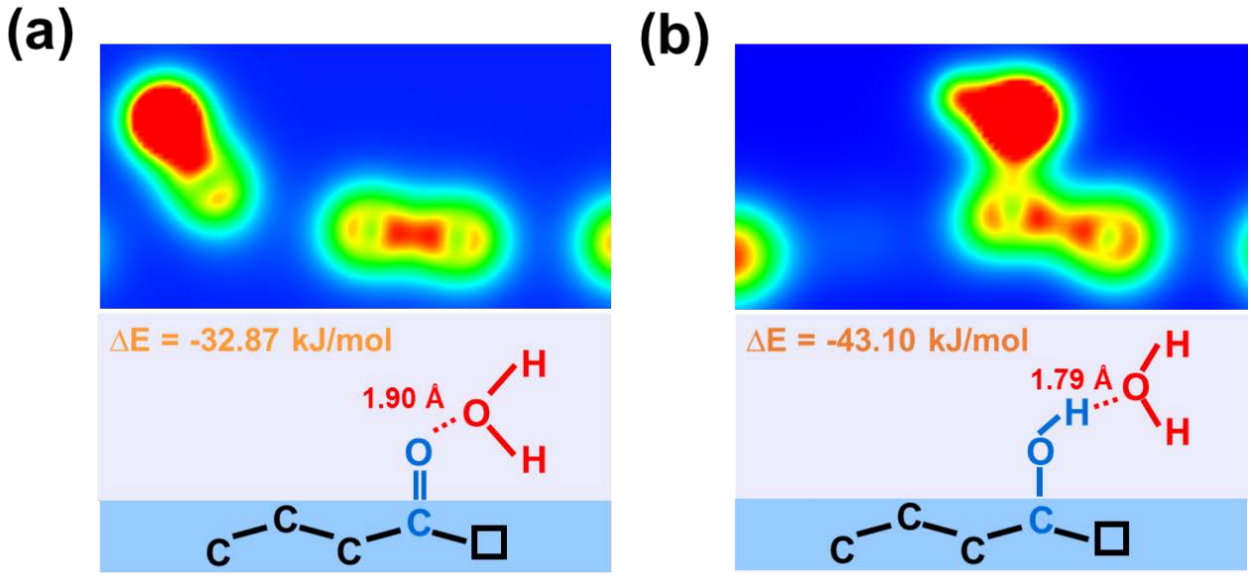

Figure 2.14. (a) Charge density contour plot (topside) of G-vac-O and corresponding water adsorption optimized configuration (downside). (b) Charge density contour plot (topside) of G-vac-OH and corresponding water adsorption optimized configuration (downside).

To estimate the capacity of hydroxylated surface to attract H_2O molecule, the adsorption modes of different overlayers H_2O clusters on hydroxylated surface are designed. Figure 2.13c-2.13f demonstrate the adsorption models of one-layer, two-layer, three-layer, and four-layer H_2O molecules, respectively. And the corresponding mean adsorption energies are depicted in Figure 2.13g. Interestingly, the G-OH surface shows bi-centre character for H_2O adsorption, two H_2O

molecules can simultaneously bind to the hydroxyl group on graphene surface via strong H-bond in the first layer, and the bond lengths are 1.82 Å and 1.85 Å, respectively (Figure 2.13c). Moreover, the two H_2O molecules in the first layer interact with each other via H-bond, thus contributing to a smaller adsorption energy (-28.14 kJ/mol) than that of H_2O monomer adsorption mode (-20.65 kJ/mol). In multi-layer adsorption modes, the H_2O molecules in upper layer forms strong H-bond to the molecules in the lower plane, and all the modes display thermodynamic feasibility with adsorption energies of about -45 kJ/mol.

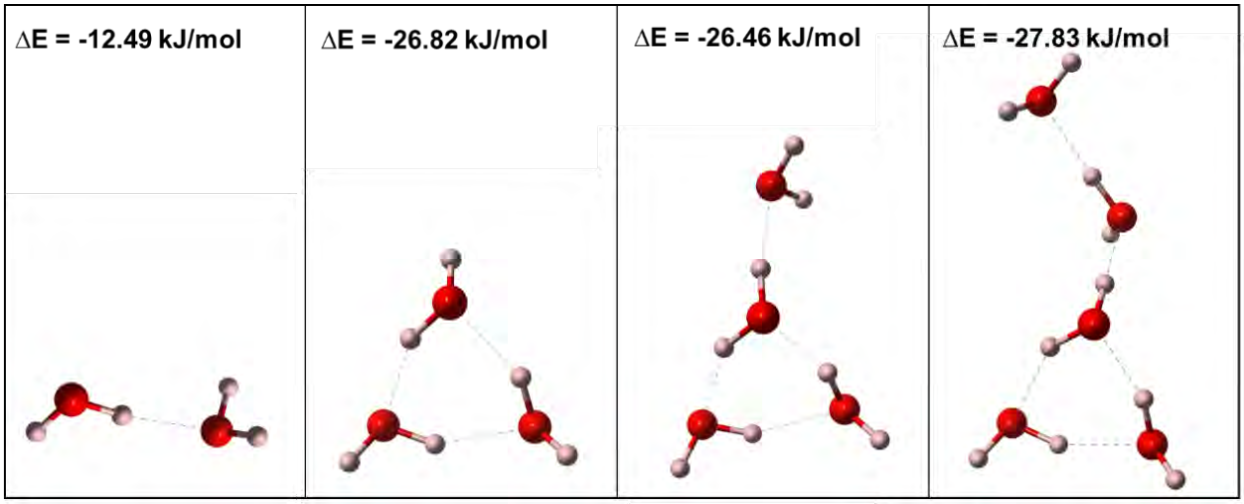

Figure 2.15. Optimized configurations and binding energies of water clusters with different number of water molecules.

In addition, the mean adsorption energy of H_2O clusters on G-OH surface is also compared with the mean binding energy of H_2O to form free clusters in Figure 2.13g and Figure 2.15. Thermodynamically, the existence of G-OH makes H_2O aggregation and adsorption more approachable. These theoretical calculation results strongly manifest that the introduction of surface hydroxyl groups is an efficient way to bond the free H_2O clusters on graphene surface without thermodynamic barrier. The strong H-bond interaction between hydroxyl groups and H_2O molecules leads to the formation of reservoir on the cathode surface. The continuous H_2O supply

for catalytic sites not only ensure sufficient proton source for hydrogen evolution but also ease the harsh interfacial pH environment by dilution method. In addition, the 3D H-bond network formed by surface hydroxyl groups and adsorbed H_2O clusters may play similar role of proton transfer pathway in [Fe-Fe] hydrogenase and facilitate the OH^- transfer during the HER performance.

To simplify the alkaline treatment process, we directly evaluate the electrocatalytic HER performance of MoS_2-G in 1.0 M NaOH solution, because in-situ surface hydroxyl group modification can be expected in alkaline medium. MoS_2-G prepared by adding precursors with weight content of 1:1 was chosen as the HER electrocatalyst due to its superior HER performance when compared to other counterparts with different weight contents (Figure 2.16). Figure 2.17a shows linear sweep voltammetry (LSV) curves within a cathodic potential window of 0 to -0.8 V versus reversible hydrogen electrode (RHE), in which MoS_2 nanosheets and 3D graphene were used as control samples. As Figure 2.17a shows, both MoS_2 nanosheets and 3D graphene display inferior HER performances, with onset potentials of 260 mV and 100 mV, respectively. Remarkably, the HER reaction of MoS_2-G occurs at an onset potential of 60 mV and shows a much lower overpotential than bare MoS_2 and 3D graphene when the cathodic current density reaches 10 mA/cm^2. The MoS_2-G sample also demonstrates a much better alkaline HER activity than MoS_2 grown on graphene-mediated 3D Ni networks, which requires a high overpotential of over 600 mV at a current density of only 4 mA/cm^2.[98] The Tafel slopes are calculated based on the Tafel equation, $\eta = b \times \log [j] + a$, where η is the overpotential, b is the Tafel slope, [j] is the current density and a is the Tafel parameter.[99] The MoS_2-G sample shows a decreased Tafel slope of 70 mV/decade (Figure 2.17b), which is significantly lower than either sole MoS_2 nanosheet (91 mV/decade) or 3D graphene (202 mV/decade). Clearly, the smaller Tafel slope implies that the HER kinetic is more favourable. With constant η, the smaller the Tafel slope is, the faster the [j].

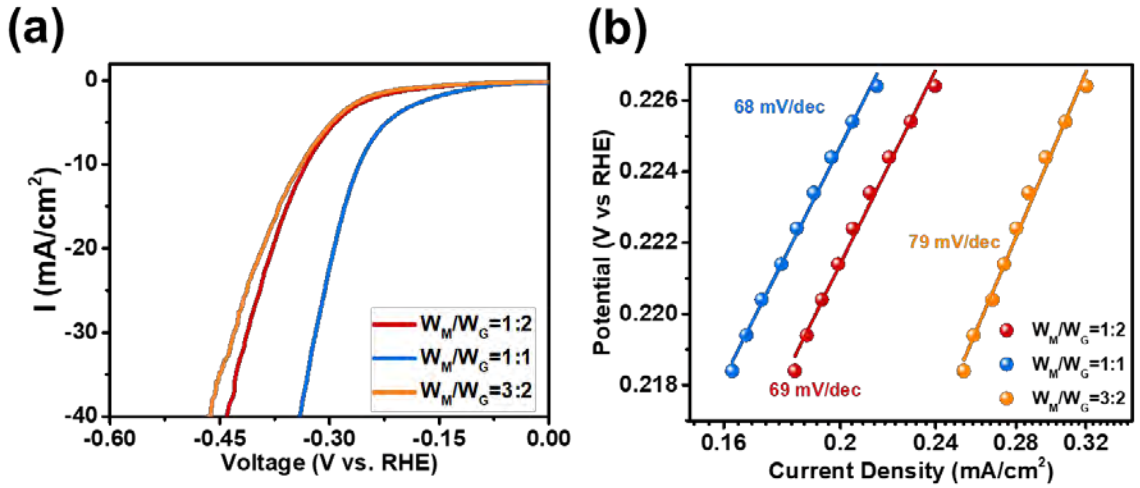

Figure 2.16. a) LSV curves and b) Tafel plots curves of MoS_2/graphene structures prepared by adding different mass ratio of W_{ATTM}:$W_{Glucose}$ = 1:2, W_{ATTM}:$W_{Glucose}$ = 1:1 and W_{ATTM}:$W_{Glucose}$ = 3:2, respectively, in 1.0 M NaOH solution.

The HER performance of our MoS_2-G sample is also compared with other Mo-based HER catalysts displaying excellent HER performance in alkaline medium (Table 2.1). We can clearly observe that MoS_2-G still exhibits a superior HER performance than most of other reported Mo-based HER catalysts. The low onset potential highlights that the HER reaction of MoS_2-G is feasible at the expense of a small bias, and the decreased Tafel slope indicates the kinetic of the water transfer in MoS_2-G is efficiently boosted. The stability of MoS_2-G is assessed by a long-term cycling test with a potential window of 0.1 V to -0.5 V. The MoS_2-G sample exhibits a favourable durability in alkaline medium. As demonstrated in Figure 2.17c, MoS_2-G only experiences slight performance degradation after 3000 cycles in 1.0 M NaOH solution and the current density shows negligible difference after long-term cycling, indicating good stability of MoS_2-G in alkaline HER process. It can be observed that the HER performance of MoS_2-G experiences slight degradation, because catalytic layers tend to peeling-off from substrate during long-term H_2 evolution. This factor is regarded as the major weakness of nano-powder electrocatalysts.

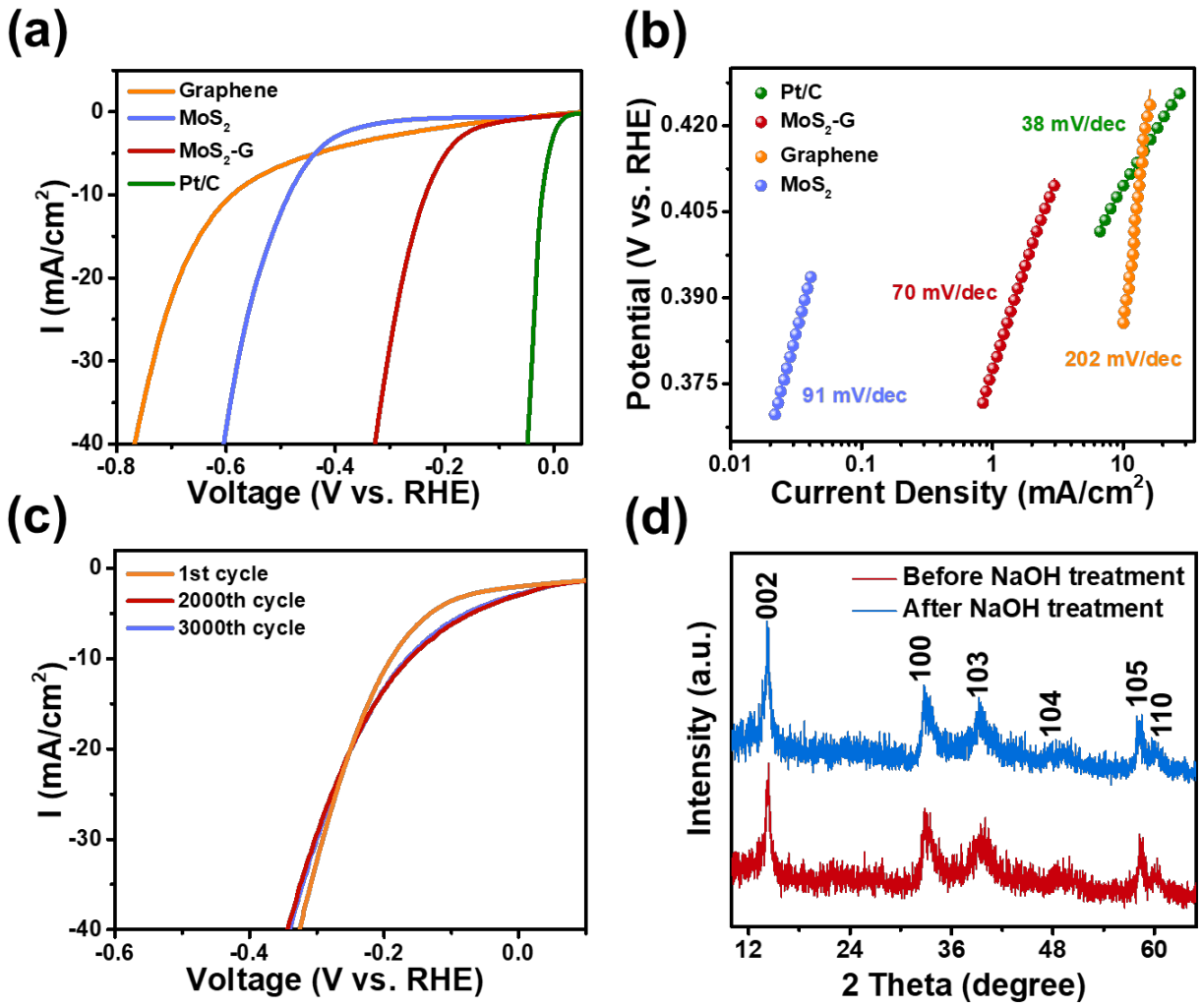

Figure 2.17. (a) LSV curves of the MoS_2-G, MoS_2, graphene and 20% Pt/C in 1.0 M NaOH solution. Scan rate: 10 mV s^{-1}. (b) Tafel plots of MoS_2-G, MoS_2, graphene and 20% Pt/C in 1.0 M NaOH solution. (c) A durability test of MoS_2-G in 1.0 M NaOH. Scan rate: 10 mV s^{-1}. (d) The X-ray diffraction spectra of MoS_2-G samples before and after immersed in 1.0 M NaOH solution for 8 hours.

Additionally, the chemical stability of the MoS_2/3D graphene is confirmed by XRD (Figure 2.17d). X-ray diffraction peaks of MoS_2-G treated in a 1.0 M NaOH solution for 8 hours shows unobvious difference with the one before the treatment, indicating good alkali-tolerance of MoS_2-G. XPS spectra is also applied to investigate the chemical stability of MoS_2-G after long-term alkaline treatment. According to the XPS results in Figure 2.18, dominant MoS_2 still retain stable elementary valence state and chemical bonding. Only minor Mo^{4+} is oxidized into Mo^{6+} due to

lone-time exposure to harsh alkaline environment. These results suggest that the MoS_2-G structure possesses a superior HER performance in alkaline solution.

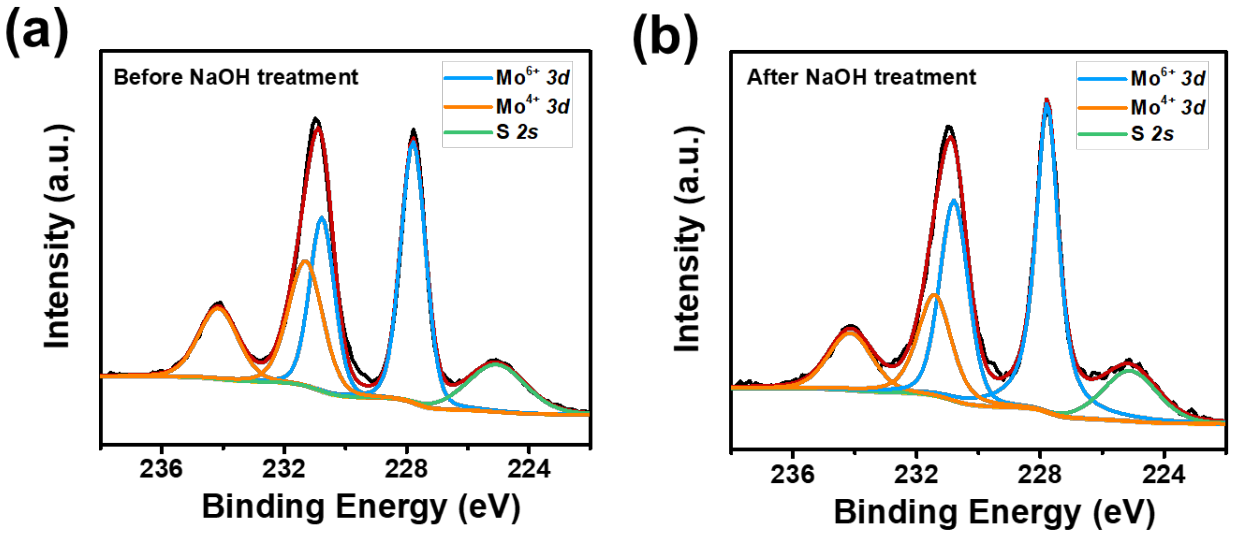

Figure 2.18. Chemical composition analysis by XPS for Mo in MoS_2-G sample (a) before and (b) after 8-hour NaOH treatment.

Table 2.1. Comparison of HER performance of various Mo-based electrocatalysts in alkaline medium.

	Onset Potential (1mA/cm^2)	Tafel Slope	Reference
Mo_2C	≈ 135 mV	54 mV/dec	[100]
MoS_2/graphene/Ni foam	≈ 300 mV	98 mV/dec	[98]
$CoMoS_x$	≈ 120 mV		[101]
MoS_2/Mo	≈ 80 mV	87 mV/dec	[102]
MoS_2/Carbon Cloth	≈ 70 mV	156.7 mV/dec	[103]
NiS_2/MoS_2	76 mV	70 mV/dec	[104]
MoS_2/Ti	≈ 70 mV	100 mV/dec	[105]
MoS_2@MoP	42 mV		[106]
Ni doped MoS_2	45 mV	60 mV/dec	[71]
MoS_2/Ni_3S_2/Ni Foam	≈ 30 mV	61 mV/dec	[107]
This Work	60 mV	70 mV/dec	

Based on these results, we can clearly see that the defect-rich 3D graphene structure is easy to evolve into a hydroxylated surface by mild alkaline treatment. The emergence of abundant surface hydroxyl group endows the structure with superior hydrophilic nature. The strong H-bond interaction between surface hydroxyl groups and H_2O clusters contributes to reservoir on cathode surface for continuous H_2O supply. Continuous H_2O supply not only provide sufficient proton resource for alkaline hydrogen evolution, but also promote the interfacial OH^- diffusion to balance the interfacial pH environment. Proton stream, relieved interfacial pH environment and highly active MoS_2 active sites cooperate with each other, contributing to robust HER kinetics and enhanced alkaline HER performance.

2.5 Conclusion

In summary, we put forward M/3D graphene mode to study the effect of interfacial H_2O supply on HER kinetics. Typical electrocatalysts, such as vertically aligned MoS_2, Pt, Fe, Ni@NiO and Co@CoO, are introduced as active materials for efficient H_2O dissociation and hydrogen evolution. More importantly, hydroxylated surface is designed to facilitate the interfacial H_2O supply and boost the HER kinetics. The effect of surface hydroxyl groups on HER is investigated from both theoretical and experimental view. Reservoir can be successfully constructed through strong H-bond interaction between free H_2O clusters and surface hydroxyl groups on graphene substrate. The water-rich surface has enormous potential to continuously supply proton donors for alkaline hydrogen evolution reaction and dilute the interfacial OH^- to balance the pH environment around catalytic sites. This work provides effective strategy to promote interfacial H_2O supply, and paves new way for realizing robust alkaline HER performance.

3 Active Site Engineering of Fe- and Ni-sites for Highly Efficient Electrochemical Overall Water Splitting

3.1 Objective and Motivation

Cost-effective, highly efficient, and durable catalyst electrodes play a critical role towards large-scale water splitting. Although bimetallic phosphides show great potential in electrocatalytic water splitting, the synergistic effect between different active sites has not been detailed investigated to date, which implies lack of effective strategy to optimize the water splitting performance in a reasonable way. Here we realize robust oxygen evolution (OER) performance with an extremely low overpotential (500 mA/cm^2 @ 255 mV), low Tafel slope (29.1 mV dec^{-1}), and superior stability by controlling the Fe sites in Ni-Fe-P surface. The prepared OER electrode exhibit superior non-noble metal catalysts for oxygen evolution and meets the commercial water electrolyzer requirements. In addition, remarkable hydrogen evolution (HER) performance with prominent stability is also achieved by reducing the content of Fe dopant. Our theoretical calculations reveal that improved O-containing intermediates chemisorption induced by Fe doping contributes to the enhanced OER performance and water molecule chemisorption, which is sensitive to the Fe content, is the primary cause to affect alkaline HER performance. This work highlights the controllable water splitting performance on Ni-Fe-P surface by precisely manipulating the surface-active Fe-sites.

3.2 Introduction

Global warming caused by the consumption of fossil fuels motivates researchers to explore clean, efficient and renewable energy.[108-109] Hydrogen energy derived from water electrolysis has shown significant potential for an ideal alternative to current fossil fuels due to its clean and

sustainable nature.[76, 110-111] To improve the efficiency of water electrolysis and realize the commercial water splitting requirement (with an overpotential below 300 mV at a current density above 500 mA/cm^2), various of noble metal-based hydrogen evolution (HER) and oxygen evolution reaction (OER) electrodes are designed for efficient overall water splitting.[31, 112-113] However, scarcity and high cost of noble metals greatly limit their large-scale practical applications. In addition, most of noble metal-based catalysts exhibit high selectivity for water reduction or oxidation. For example, IrO_2 is an excellent OER electrocatalysts with small onset potential but show poor HER performance in alkaline medium. Therefore, it is of great significance to develop high-efficient non-noble metal based bifunctional electrodes and develop effective strategies to optimize the synergistic effect of bifunctional surface for large-scale overall water splitting at the minimum cost of electricity, especially for kinetically sluggish OER process.

Recently, nickel phosphide (Ni_2P) attracts considerable attention owing to its intrinsic thermodynamic feasibility of HER property comparable to [NiFe] hydrogenase.[25, 114] Hence, Ni_2P has been applied in water splitting field to realize robust H_2 production and displays prominent HER performance in universal pH range. Moreover, Ni_2P can also act as a platform to breed bimetallic phosphides, such as, NiFe phosphides and NiCo phosphides, to achieve efficient OER performance.[9, 115-118] Especially, the incorporation of Fe atom into Ni_2P matrix not only introduces efficient active sites for OER reaction, but also modifies the electronic structure of Ni_2P, leading to high conductivity.[119] It is greatly promising to design high-efficient bifunctional electrocatalysts based on Ni_2P matrix by engineering the Fe doping levels. In addition, the fundamental understanding on the synergistic effect between active Ni- and Fe-sites is still limited, although the concept of bifunctional Ni-Fe-P surface has been proposed for a long period. Therefore, the study of Ni_2P electrocatalyst with controllable Fe doping levels provides valuable strategies to

design water splitting electrocatalysts and effective model to unveil the underlying synergetic mechanism on Ni-Fe-P surface.

From the practical perspectives, powder-like electrocatalysts show inevitable weakness due to the poor affinity between active catalysts and substrate.[74, 120] 304-type stainless steel (SS) mesh is macroporous, anticorrosive, and low-cost conductive substrate, and exhibits superior electrochemical performance in alkaline solution than other substrates, such as, nickel foam (NF) and carbon cloth (CC).[121-125] For example, Tong et al. reported that low-cost SS mesh for high-efficient and constant overall water splitting after exfoliation and heteroatom doping processes.[126] Also, SS mesh can sustain better mechanical stability than NF during post treatment, including phosphorization or selenization process, which gives rise to constant and efficient electron transfer pathway even with continuous gas bubbles emission during HER or OER process.[127-128] Thus, Ni_2P electrocatalyst with controllable Fe doping on 304-type SS mesh allows us to investigate fundamental mechanism and develop water splitting electrodes that towards practical application.

In this work, we demonstrate a scalable approach for the fabrication of Fe-doped Ni_2P grown on SS mesh by mild chemical bath deposition, followed by phosphorization process. Ni_2P with controllable Fe doping on SS mesh was successfully fabricated by controlling the deposition time. Exceptionally, the Fe-doped Ni_2P displays selective water splitting behaviors dependent on the content of atomic Fe dopant. The Fe-doped Ni_2P with high content of Fe dopant tends to drastically oxidize water into oxygen at an extremely low overpotential of 255 mV at current density of 500 mA/cm^2, which demonstrates the first-class non-noble metal catalysts for oxygen evolution and meets the commercial water electrolyzer requirements. In contrast, Fe-doped Ni_2P with lower Fe dopant exhibits remarkable HER performance, which only requires overpotential of 400 mV to realize current density of 500 mA/cm^2. Our density functional theory (DFT) calculation

reveals that the introduction of Fe site into Ni_2P can greatly decrease the adsorption energy of intermediates involved in OER process, bringing about excellent OER performance. However, water molecule chemisorption is sensitive to Fe dopant content, which is regarded as the main factor to influence HER performance. Our experimental and theoretical studies clarify the synergistic effect between Ni and Fe-sites on Ni-Fe-P surface during HER and OER process and provide us detailed OER pathways on bifunctional Ni-Fe-P surface.

3.3 Experimental section

3.3.1 Synthesis and Preparation: Fe-doped Ni_2P was synthesized directly onto SS mesh using a chemical bath deposition technique followed by phosphorization process. $Ni(NO_3)_2 \cdot 6H_2O$ (1.454 g) and NH_4NO_3 (0.2 g) were added into 35 mL of de-ionized water. Then 5 mL of 28 wt% ammonia was added into the green solution and formed dark blue nickel ammonia complex. After stirring in air for 10 min, the solution was poured into a round-bottom flask and pre-heated at 85°C for 1 h. Meanwhile, a stainless steel (SS) mesh was sequentially cleaned in isopropanol, acetone and de-ionized water, and treated with 10% HCl for 10 min before rinsed with DI water. Next, the SS was placed into the pre-heated nickel ammonia and the flask were kept at 85°C for different time duration to obtain Fe-doped $Ni(OH)_2$/SS. The iron in Fe-doped $Ni(OH)_2$/SS was derived from the substitutional reaction between $[Ni(NH_3)_6]^{2+}$ and iron in SS mesh. The $Ni(OH)_2$-HF and $Ni(OH)_2$-LF were prepared after one-hour and three-hour deposition time, respectively.

To prepare Fe-doped Ni_2P/SS, Fe-doped $Ni(OH)_2$/SS and 0.5 g NaH_2PO_2 were put in a quartz boat and NaH_2PO_2 was placed at the upstream. Subsequently, the quartz boat was transferred into a tube furnace. The heating center temperature of the furnace was raised up to 300 °C with the heating rate of 5 °C/min and held at this temperature for 120 min in an Ar flow with a flow rate of

20 sccm. The obtained Fe-doped Ni_2P on SS mesh derived from $Ni(OH)_2$-HF and $Ni(OH)_2$-LF were denoted Ni_2P-HF and Ni_2P-LF, respectively.

3.3.2 Electrochemical Tests: A three electrodes electrochemical station was used to test electrochemical performance (CHI 660D). All electrochemical tests were performed in 50 mL of 1.0 M KOH electrolyte (pH = 14.0). The prepared sample, Hg/HgO and graphite rod were applied as working electrode, reference electrode and counter electrode, respectively. The performance of the OER was tested using linear sweep voltammetry (LSV) with a scanning window of 1.2 V to 1.6 V vs RHE and a scan rate of 2 mV s^{-1}. The performance of the HER was tested using linear sweep voltammetry (LSV) with a scanning window of 0 V to -0.6 V vs RHE and a scan rate of 2 mV s^{-1}. The durability of HER and OER electrochemical performance were evaluated by time-dependent overpotential curve at a static current density of 100 mA/cm^2. All the LSV curves are corrected with iR compensation.

In Ni_2P-HF || Ni_2P-LF electrolyzer, Ni_2P-HF and Ni_2P-LF (1 cm×1 cm) were employed as anode and cathode materials, respectively. Cu electrode holder was applied to connect the working electrodes, as Cu possesses great electrical conductivety and negligible water splitting performance. LSV curves was also conducted in 1.0 M KOH solution with a scan rate of 5 mV s^{-1} between 1.0 and 1.9 V and the LSV curve was corrected with iR compensation.

3.3.3 Electrochemical Active Surface Area: The active surface area of the prepared samples was estimated by electrochemical capacitance measurements, because the current in non-faradic region is expected to be linearly proportional to the active surface area. The applied potential was set between 0.01 to 0.11 V vs. Hg/HgO for 50 cycles at different scan rates. The capacitive currents were collected at 0.98 V vs RHE. Then, the capacitive currents were plotted as a function of scan rate to calculate the double layer capacitance.

3.3.4 Characterizations: The morphology of SS and SSP samples were characterized by scanning electron microscope, scanning transmission electron microscope (SEM, Jeol JSM-6335F & TEM, Jeol JEM-2100F). The crystal structure and composition were measured by X-ray Diffractometer (Rigaku SmartLab) and Raman spectroscope (Witec Confocal Raman system) with an excitation wavelength of 532 nm. The electrochemical impedance spectroscopy (EIS) was performed in Solartron Electrochemical workstation (German) with the frequency ranging from 0.01 to 10^5 Hz. The surface valence state of sample was tested by using X-ray photoelectron spectroscopy (XPS, Thermol Scientific Escalab 250Xi, Al Kα radiation).

3.3.5 Theoretical Calculations: Theoretical calculations were performed using density functional theory (DFT) as implemented in the VASP code (5.4.3) with exchange-correlation energy functional, which were modeled by Perdew-Burke-Ernzerhof (PBE) functional.[83-84] The cut-off energy was set to be 450 eV and all structures were relaxed to an energy convergence of 10^{-4} eV/atom and a force convergence of 0.02 eV/Å, respectively. During the geometrical optimization, a (3 × 2) Ni_2P surface with exposed (1 -1 0) was applied to investigate the adsorption behavior of intermediates (including H_2O, H*, OH*, O* and OOH*) involved in HER and OER process. The k-points was 3 × 3 × 1 in slab optimization and 5 × 5 × 1 in static calculation. The thickness of vacuum in all the models was set to 30 Å to eliminate the interactions between the layers caused by the periodic boundary condition.

3.4 Characterizations of catalysts and water splitting performance

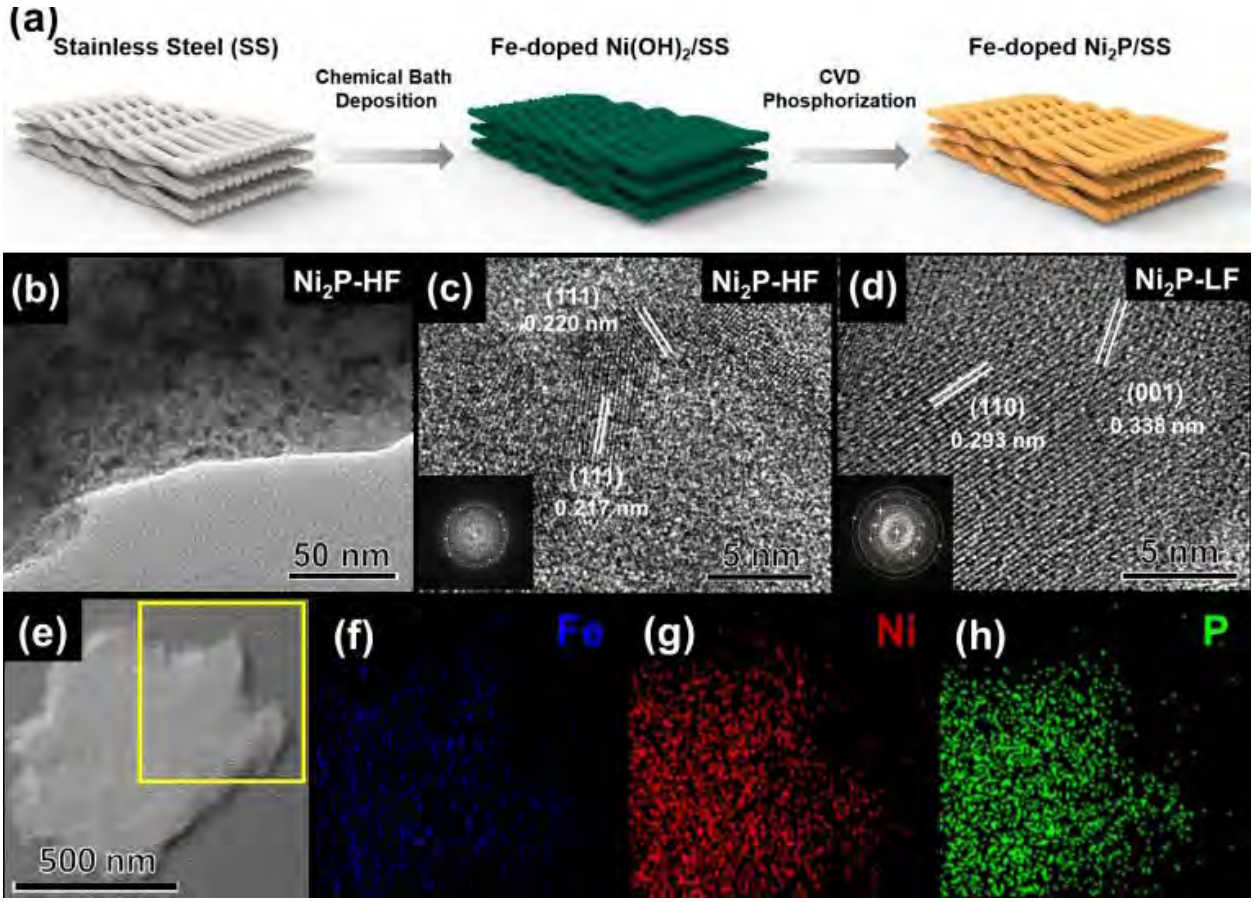

Figure 3.1. (a) Schematic illustration for the fabrication process of the Fe-doped Ni_2P on stainless steel mesh. (b) Typical TEM images of the Ni_2P-HF. (b) TEM image and (c) high-resolution TEM image of Ni_2P-HF, the inset in panel (c) is the SAED pattern of the Ni_2P-HF sample. (d) High-resolution TEM image of Ni_2P-LF, the inset in panel (d) is the SAED pattern of Ni_2P-LF. (e) Low-resolution HAADF-STEM image of the Ni_2P-LF. Corresponding elemental mapping images of (f) P, (g) Ni and (h) Fe in the Ni_2P-LF.

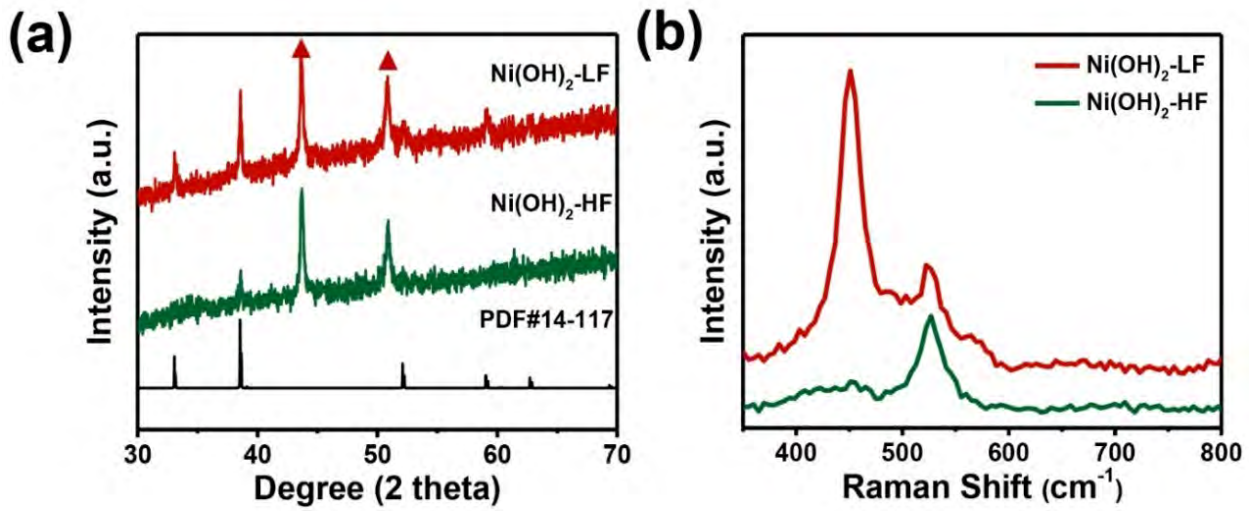

Figure 3.2. (a) XRD patterns of $Ni(OH)_2$-HF and $Ni(OH)_2$-LF on SS mesh. The typical peak of stainless steel is denoted with red triangle. (b) Raman spectrum of $Ni(OH)_2$-HF and $Ni(OH)_2$-LF collected at low wavenumber.

As schematically illustrated in Figure 3.1a, Fe-doped Ni_2P on SS mesh was synthesized by chemical bath deposition and subsequent mild phosphorization process. The Fe-doped $Ni(OH)_2$ with high and low contents of Fe ($Ni(OH)_2$-HF and $Ni(OH)_2$-LF) were first prepared via facile chemical bath deposition. Both precursors deposited from different chemical bath duration show typical diffraction peaks of $Ni(OH)_2$ (PDF# 14-117) (Figure 3.2a). The Raman spectra of $Ni(OH)_2$-HF and $Ni(OH)_2$-LF (Figure 3.2b) exhibit typical Ni-O band centered in about 450 cm^{-1} and 530 cm^{-1}, and the change of relative intensity ratio of these two peaks confirms the different level of Fe content in $Ni(OH)_2$ frameworks, which is consistent with the results reported in previous research.[129] The X-ray photoelectron spectroscopy (XPS) spectra (Figure 3.3a) verify the existence of Ni, Fe and O in $Ni(OH)_2$-HF and $Ni(OH)_2$-LF. The high resolution XPS spectra of Ni, Fe and O (Figure 3.3b-3.3d) further confirm the formation of $Ni(OH)_2$ with different contents of Fe dopant. The morphologies of $Ni(OH)_2$-HF and $Ni(OH)_2$-LF were characterized by scanning electron microscopy (SEM) (Figure $3.4a_1$-$3.4b_1$). According to the SEM images, two-dimensional (2D) $Ni(OH)_2$ nanosheet with smooth surface are densely grown on SS surface after chemical bath

deposition, and the average length of $Ni(OH)_2$-HF and $Ni(OH)_2$-LF nanosheets are approximately 1 μm and 200 nm, respectively.

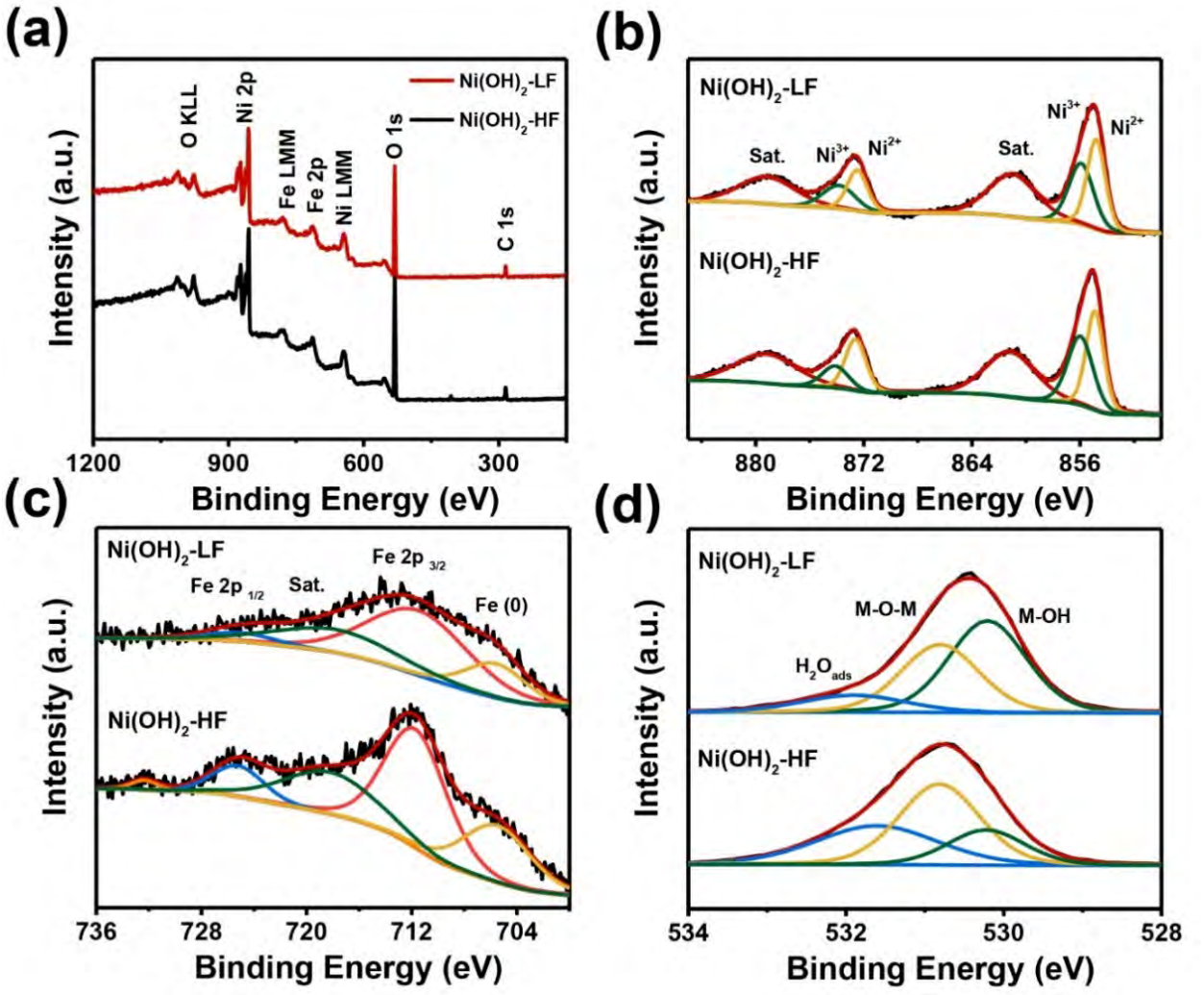

Figure 3.3. (a) XPS spectra of $Ni(OH)_2$-HF and $Ni(OH)_2$-LF. High resolution XPS spectra of (b) Ni, (c) Fe and (d) O in $Ni(OH)_2$-HF and $Ni(OH)_2$-LF, respectively.

We then conducted mild phosphorization process to convert Fe-doped $Ni(OH)_2$ into Fe-doped Ni_2P. Fe-doped Ni_2P derived from $Ni(OH)_2$-HF and $Ni(OH)_2$-LF are denoted with Ni_2P-HF and Ni_2P-LF, respectively. After the phosphorization treatment, we can obviously observe increased surface roughness of Fe-doped Ni_2P from the SEM images (*Figure 3.4*a_2-3.4b_2). Most of $Ni(OH)_2$ arrays are destroyed, and massive nanoparticles appear. Transmission electron microscopy (TEM) was then applied to further study the rough surface and generated nanoparticles.

As shown in Figure 3.1b-3.1c, the Ni_2P nanoparticles possess average diameter of 5 nm in Ni_2P-HF and show distinct lattice fringe with an interplane distances of approximately 0.220 nm, which is indexed to the (111) facet diffraction in Ni_2P.[130] In addition, Ni_2P-LF in Figure 3.1d exhibits continuous distinct lattice fringes with the interplanar spacings of 0.293 nm and 0.338 nm, corresponding to (110) and (001) plane in Ni_2P, respectively. Elemental mappings of Ni_2P-LF are displayed in Figure 3.1e-3.1h, evidencing the uniform spatial distribution of Ni, Fe and P.

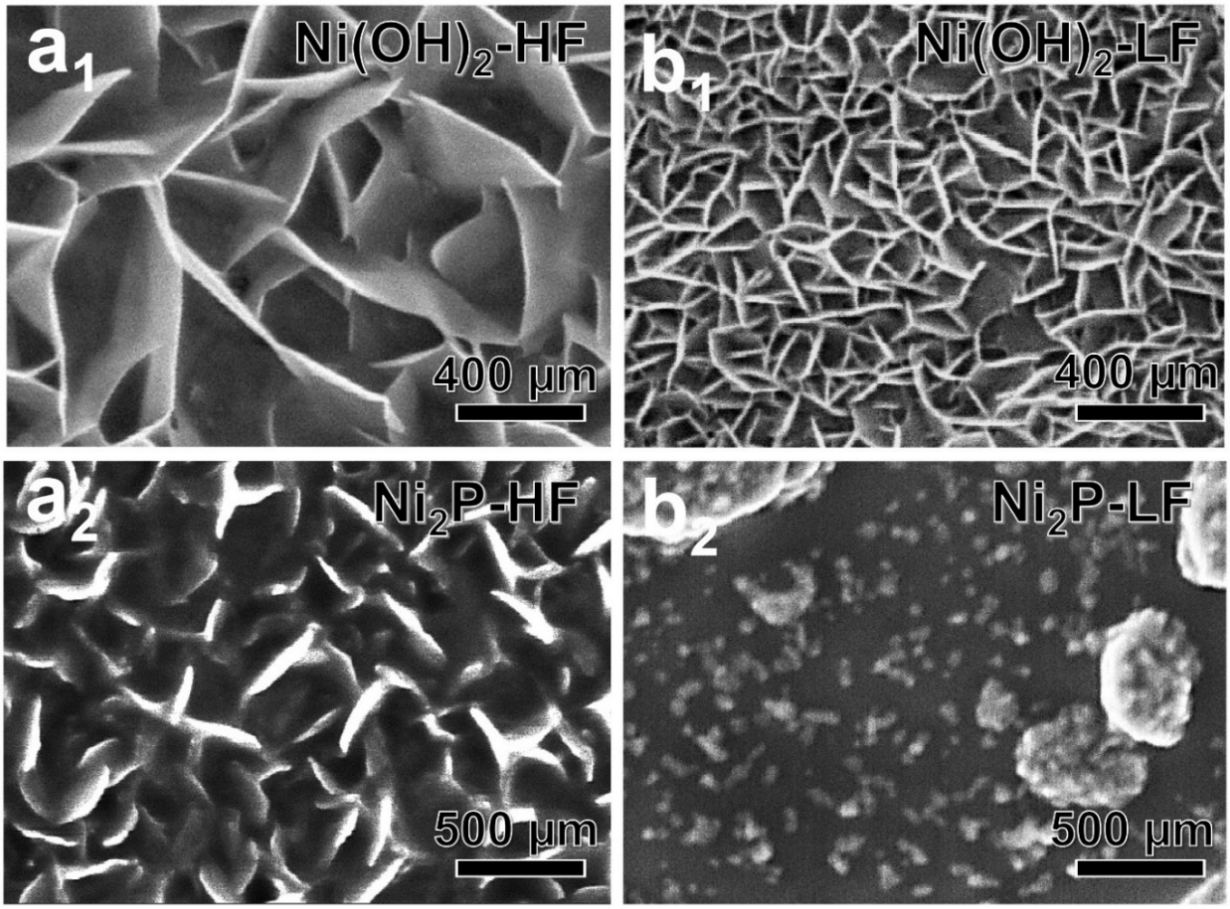

Figure 3.4. SEM images of (a_1) $Ni(OH)_2$-HF and (b_1) $Ni(OH)_2$-LF on SS mesh, respectively. SEM images of (a_2) Ni_2P-HF and (b_2) Ni_2P-LF, respectively.

We then carried out X-ray diffraction (XRD) to identify the phase structure of Fe-doped Ni_2P samples. As illustrated in Figure 3.5a, the X-ray diffraction patterns of Fe-doped Ni_2P samples show diffraction peaks at 40.7°, 44.6°, 47.4°, 54.3° and 55.0°, corresponding to the (111),

(201), (210), (300) and (211) planes of Ni_2P, respectively, which match well with standard hexagonal Ni_2P diffraction pattern (PDF#74-1385). XPS was applied to characterize the Fe-doped Ni_2P samples. Figure 3.6 demonstrates the presence of Fe, Ni, P and O elements in the Fe-doped Ni_2P samples, and obvious peaks of other elements were not detected. The XPS atomic content analysis in Table 3.1 reveals that the content of Fe in Ni_2P-HF is about 7.51%, which is twice than that of Ni_2P-LF. The Figure 3.7-Figure 3.8 indicate the EDX characterization of Ni_2P-HF and Ni_2P-LF, respectively, showing Fe/Ni atomic ratios that are in consistent with XPS elemental analysis.

In addition, the high resolution XPS spectrum of Fe 2p (Figure 3.5b) is observed with two peaks at around 712.5 and 725.2 eV, which can be assigned to the Fe 2p3/2 and Fe 2p1/2, respectively, indicating that Fe presents in the form of Fe^{3+}. More importantly, the increase of Fe dopant leads binding energy to shift towards lower energy, indicating electron interaction induced by the increase of Fe dopant. Another doublet located at 715.6 and 727.3 eV is attributed to satellite peaks of Fe 2p. The small peak with binding energy of 708.0 eV is derived from the Fe (0) in SS substrate. Figure 3.5c show the XPS peak fitting of Ni 2p, including Ni^{2+} (located at 856.3 and 874.2 eV) and Ni^{3+} (located at 858.1 and 876.0 eV).[131-132] The small peak at around 853.1 eV can be ascribed to Ni-P bond in Ni_2P. Partially charged $Ni^{\sigma+}$ in Ni_2P leads to the binding energy close to that of Ni (0).[133]

Table 3.1. Elemental composition analysis of Ni_2P-HF and Ni_2P-LF.

	Content of Fe	**Content of Ni**	**Content of P**
Ni_2P-HF	7.51%	22.46%	70.03%
Ni_2P-LF	3.37%	34.46%	62.17%

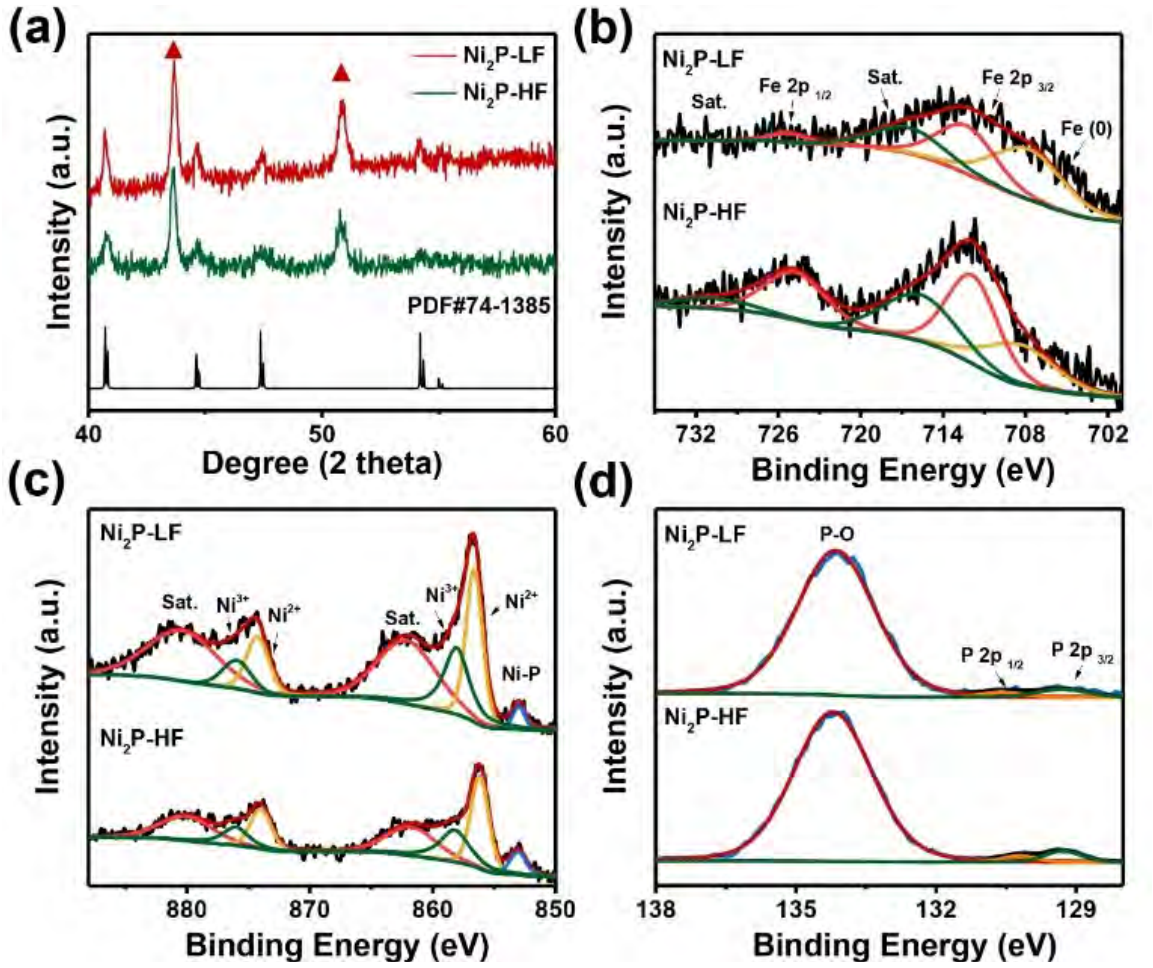

Figure 3.5. (a) XRD patterns of Ni_2P-HF and Ni_2P-LF samples on SS mesh. The typical peak of stainless steel is denoted with red triangle. High resolution XPS spectra of (b) Fe, (c) Ni and (d) P in Ni_2P-HF and Ni_2P-LF samples, respectively.

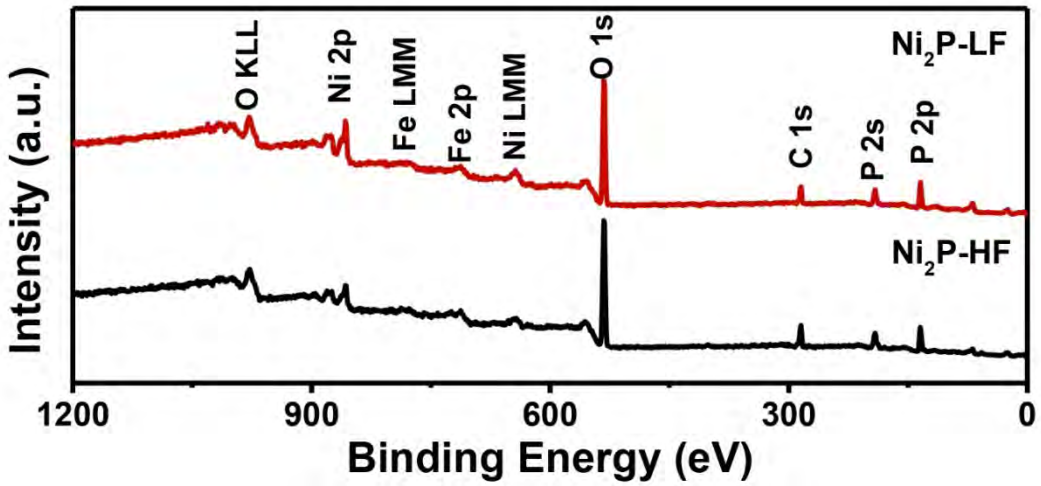

Figure 3.6. XPS spectra of Ni_2P-HF and Ni_2P-LF, respectively

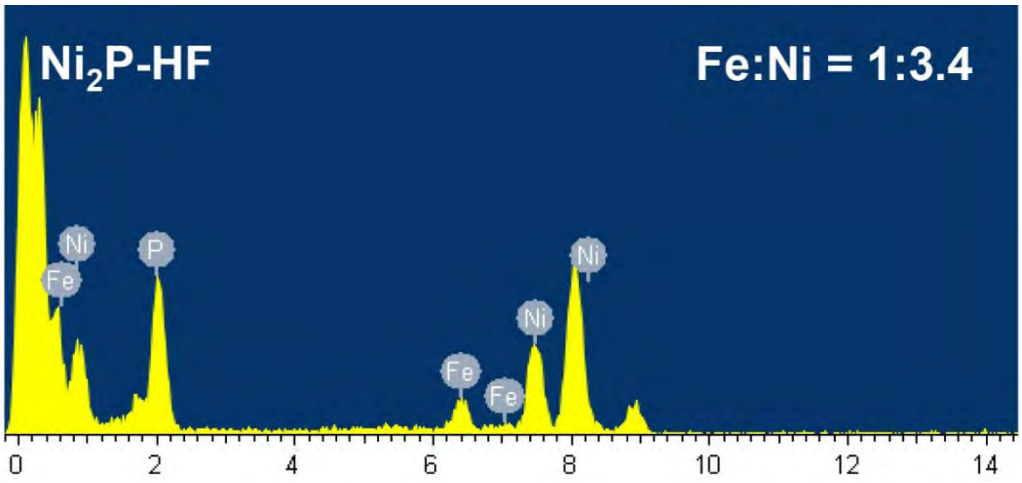

Figure 3.7. (a) EDX characterization of Ni_2P-HF sample.

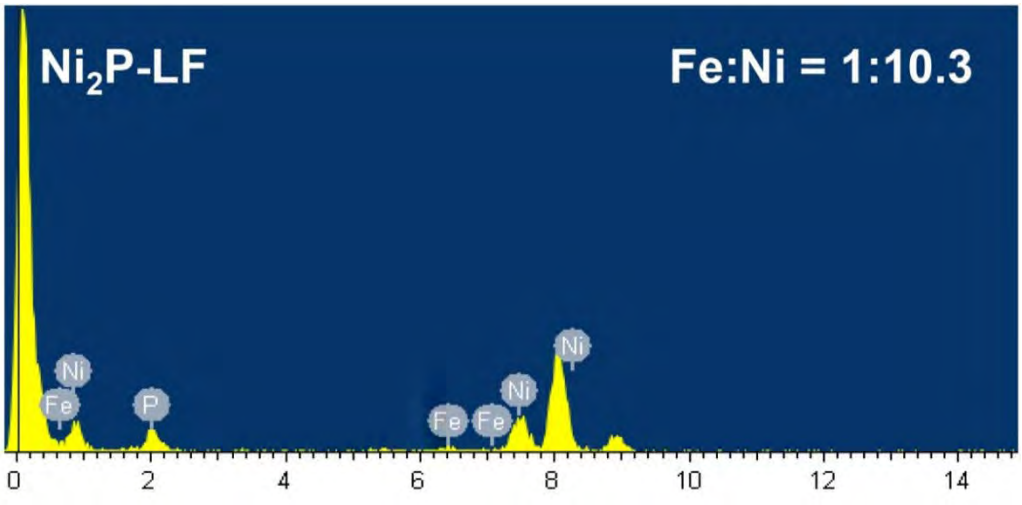

Figure 3.8. (a) EDX characterization of Ni_2P-LF sample.

The P 2p spectrum shows three main peaks at 134.3, 130.3 and 129.3 eV (Figure 3.5d). The peaks at 130.3 eV and 129.3 eV are corresponding to P $2p_{1/2}$ and P $2p_{3/2}$ signals of metal phosphides, and the peak with high binding energy arises from the oxidized metal phosphate species. The binding energy of 129.3 eV is slightly lower than P (0) species, indicating a strong bonding between metal and partial charged $P^{\sigma-}$. Moreover, the binding energy of Ni-P bond in Ni_2P-HF positively shift when compared with Ni_2P-LF, suggesting the strong electron interaction induced by increasing Fe dopant.[134] Thus, different amounts of Fe dopant will give rise to different

degrees of electron interaction, which may bring about different types of active sites and facilitate the water splitting process.

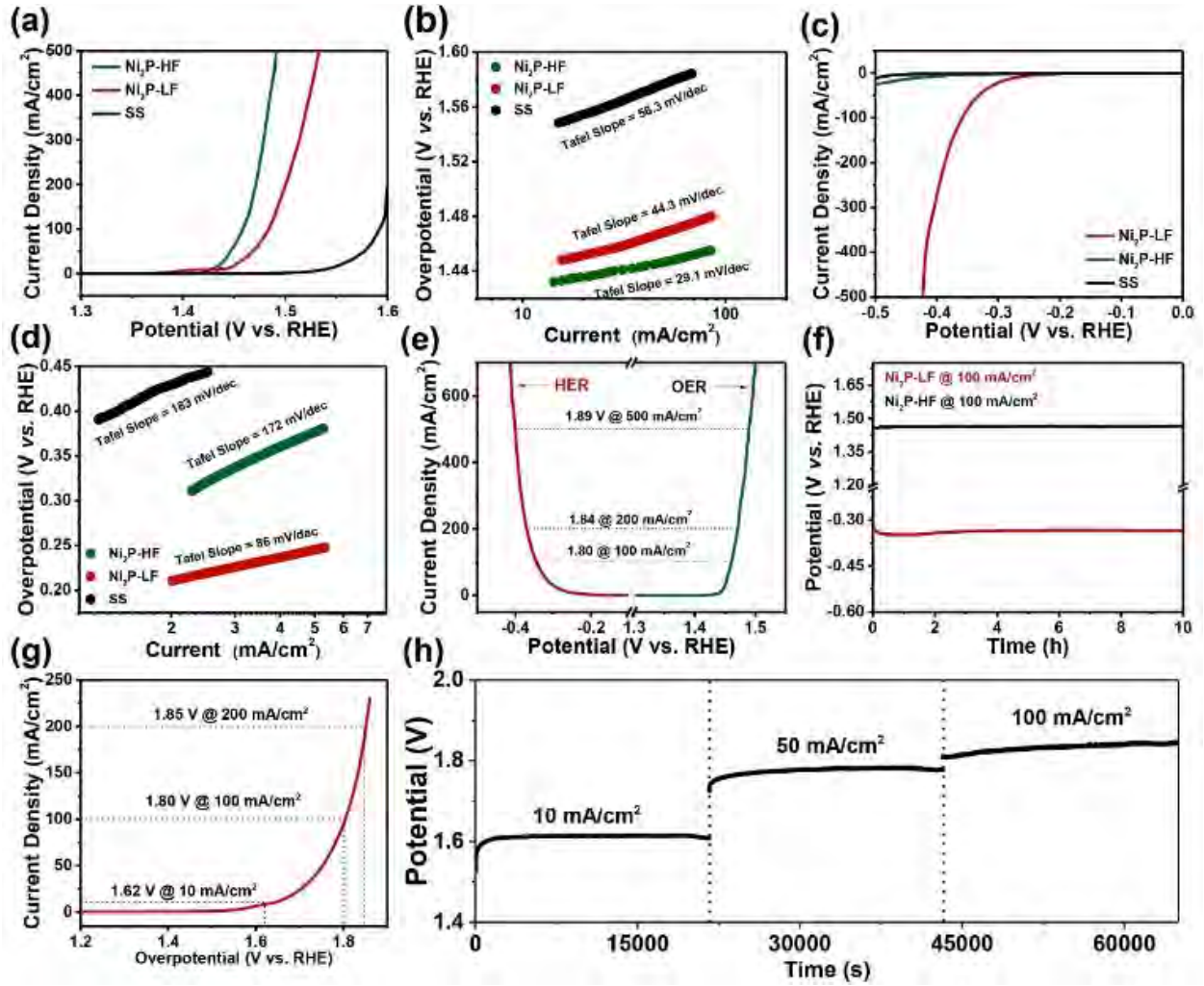

Figure 3.9. OER performance of Ni_2P-LF, Ni_2P-HF and bare SS mesh in 1.0 M KOH. (a) Polarization curves and (b) corresponding Tafel plots of Ni_2P-LF, Ni_2P-HF and bare SS mesh after iR compensation. HER performance of Ni_2P-LF, Ni_2P-HF and bare SS mesh in 1.0 M KOH. (c) Polarization curves and (d) corresponding Tafel plots of Ni_2P-LF, Ni_2P-HF and bare SS mesh after iR compensation. (e) IR-corrected LSV curves for HER (left) and OER (right) electrocatalysts when the Ni_2P-LF and Ni_2P-HF are used as cathode and anode, respectively. (f) Long-time durability of HER (red line) and OER (black line) electrocatalysts at the current density of 100 mA/cm^2. (g) IR-corrected LSV curves of Ni_2P-HF || Ni_2P-LF in a two-electrode configuration at a scan rate of 5 mV/s in 1.0 m KOH. (h) Long-time durability of Ni_2P-HF || Ni_2P-LF electrolyzer at current density of 10 mA/cm^2, 50 mA/cm^2 and 100 mA/cm^2, respectively.

To assess the performance of the prepared bifunctional electrocatalysts for practical use, the OER performance of as-fabricated Fe-doped $Ni(OH)_2$ and Fe-doped Ni_2P samples were first investigated in 1.0 M KOH by using a standard three electrodes system. Hg/HgO and graphite were applied as reference electrode and counter electrode, respectively.[135] Predictably, Fe-doped Ni_2P samples show superior OER performance than their hydroxide precursors and bare SS substrate (Figure 3.9a-3.9b and Figure 3.10a-3.10b). The polarization curves indicate that Ni_2P-HF displays the best OER performance than other samples, possessing the lowest overpotential of 255 mV at the current density of 500 mA/cm^2. The low overpotential at high current density implies great potential to construct efficient oxygen evolution system for practical applications, which requires an overpotential below 300 mV at a current density above 500 mA/cm^2. In contrast, it requires larger overpotential of 310 mV and 370 mV for Ni_2P-LF and bare SS mesh to reach the current density of 500 mA/cm^2 and 200 mA/cm^2, respectively. Notably, the Tafel slopes of Ni_2P-HF is only 29.1 mV/dec, which is much smaller than Ni_2P-LF (44.3 mV/dec) and bare SS mesh (56.3 mV/dec). The small Tafel slope indicates that increasing content of Fe dopant can facilitate the oxygen evolution kinetic of Ni_2P, which may provide valuable guidance on OER electrocatalysts design.

The excellent stability of Ni_2P-HF was confirmed by LSV curves before and after 1000 cycles in Figure 3.11a. We also compare the OER performance with other reported self-supported Fe-doped Ni phosphides in Table 2.1. The overpotential and Tafel slope of Ni_2P-HF electrodes (255 mV@500 mA/cm^2, 29.1 mV/dec) are lower than those values for other Fe-Ni phosphides electrodes, such as, $Fe(PO_3)_2/Ni_2P$/Ni foam (265 mV@500 mA/cm^2, 51.9 mV/dec), $Ni_{1.85}Fe_{0.15}P$/Ni foam (380 mV@200 mA/cm^2, 96 mV/dec), Fe-doped Ni_2P/Carbon cloth (310 mV@300 mA/cm^2, 48 mV/dec), NiFe-OH/NiFeP/Ni foam (255 mV@300 mA/cm^2, 39 mV/dec)

and metallic NiFeP (390 mV@400 mA/cm^2, 42 mV/dec).[115-116, 120, 133-134, 136-137] These detailed comparisons further prove the superior OER catalytic activity of as-fabricated Ni_2P-HF electrodes.

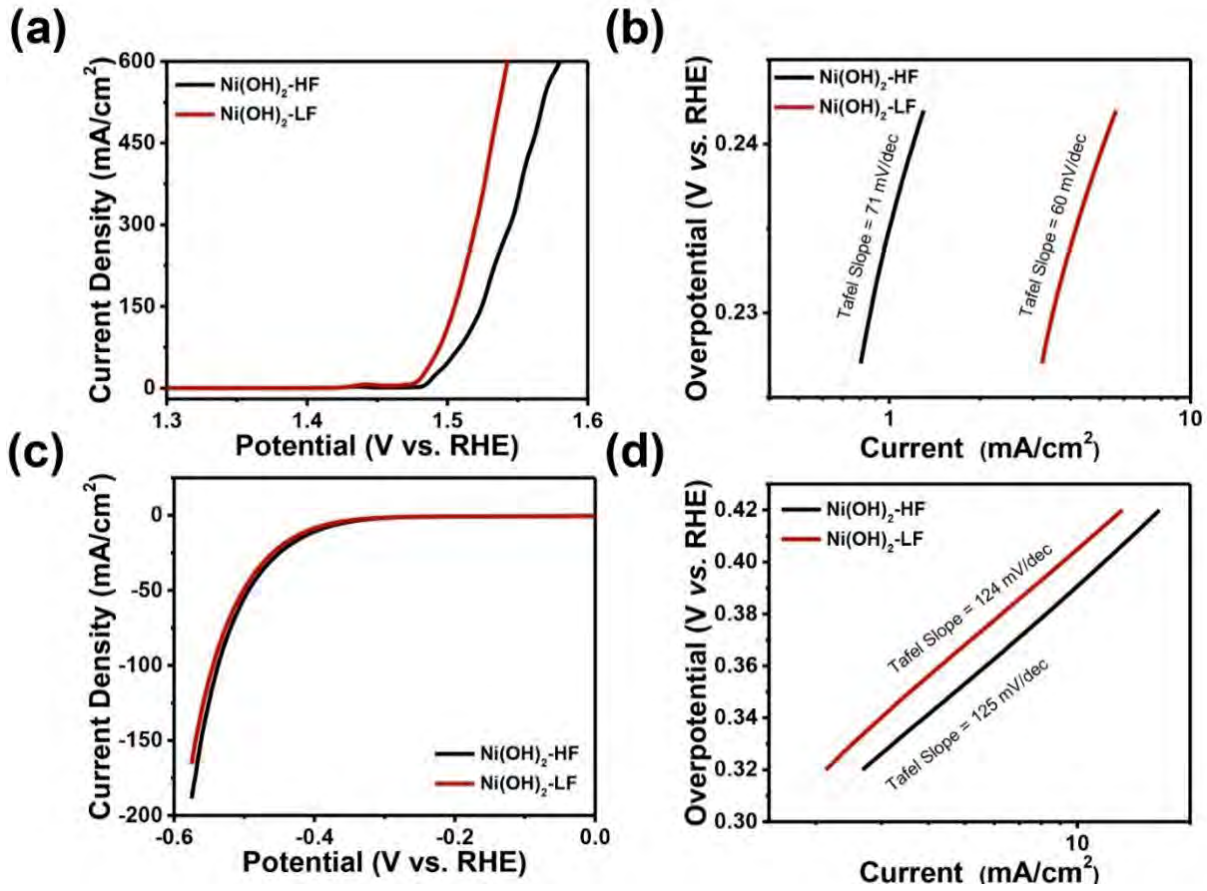

Figure 3.10. OER performance of $Ni(OH)_2$-HF and $Ni(OH)_2$-LF in 1.0 M KOH. (a) Polarization curves and (b) corresponding Tafel plots after iR compensation. HER performance of $Ni(OH)_2$-HF and $Ni(OH)_2$-LF in 1.0 M KOH. (c) Polarization curves and (d) corresponding Tafel plots after iR compensation.

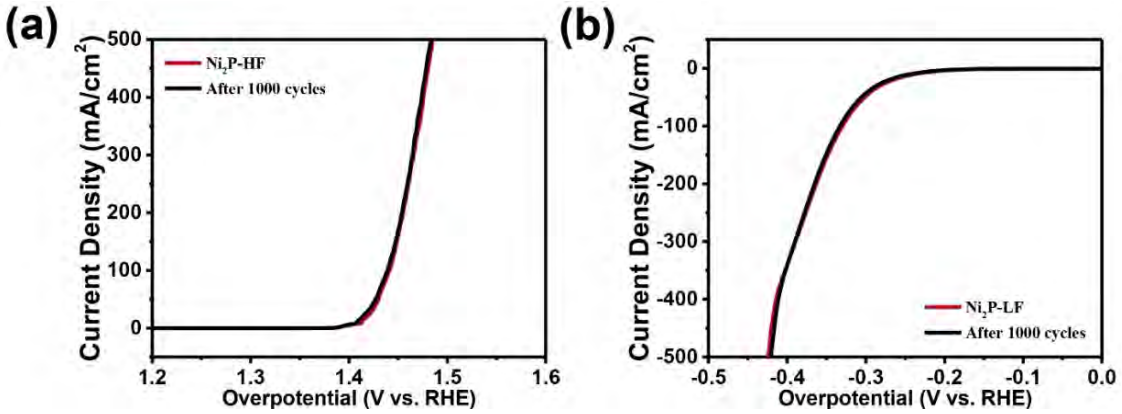

Figure 3.11. Durability tests of (a) Ni_2P-HF and (b) Ni_2P-LF in 1.0 M KOH.

Table 3.2. Comparison of OER performance of self-supported Fe-doped Nickel Phosphides.

	Overpotential for OER	**Tafel Slope**	**References**
$Ni_{1.85}Fe_{0.15}P$/Ni foam	380 mV @ 200 mA/cm^2	96 mV/dec	Wang Pengyan et al.[115]
NiFe-OH/NiFeP/Ni foam	255 mV @ 300 mA/cm^2	39 mV/dec	Liang Hanfeng et al.[133]
Amorphous Metallic NiFeP	390 mV @ 400 mA/cm^2	42 mV/dec	Hu Fei et al.[116]
Fe-doped Ni_2P/Carbon cloth	310 mV @ 300 mA/cm^2	48 mV/dec	Wang Jianmei et al.[136]
$(Fe_{0.5}Ni_{0.5})_2P$/Ni foam	260 mV @ 500 mA/cm^2	66 mV/dec	Zhang Bowei et al.[134]
$Fe(PO_3)_2/Ni_2P$ /Ni foam	265 mV @ 500 mA/cm^2	51.9 mV/dec	Zhou Haiqing et al.[120]
FeNiP/Ni foam	240 mV @ 60 mA/cm^2	76 mV/dec	Manman Qian et al.[137]
Fe-doped Ni_2P/SS	**255 mV @ 500 mA/cm^2**	**29.1 mV/dec**	**This work**

The HER activity of Fe-doped Ni_2P samples was also evaluated in 1.0 M KOH. As expected, Fe-doped Ni_2P/SS samples (Figure 3.9c-3.9d) show reduced HER overpotential than their hydroxides counterparts (Figure 3.10c-3.10d) to reach desired current densities. More interestingly, the Ni_2P-LF exhibits lowest overpotential (423 mV) to reach a current density of 500 mA/cm^2, which is much better than that of Ni_2P-HF and bare SS substrate. Moreover, the Tafel slope of the Ni_2P-LF (86 mV/dec) is exceptionally lower than Ni_2P-HF and bare SS mesh (172 mV/dec for Ni_2P-HF and 183 mV/dec for SS mesh), indicating less Fe dopant is more beneficial for HER activity. Based on the Tafel slopes, all samples follow Volmer-Heyrovsky mechanism, which is analogous to most of Ni-based materials in alkaline water medium. Besides, the stability of cathode was studied by LSV curves before and after 1000 cycles. The nearly identical LSV curves in Figure 3.11b suggest that Ni_2P-LF is an efficient HER catalysts with good durability.

The HER behavior varies with Fe content in a way totally contrary to that of OER behavior, implying Fe content is a vital factor to determine the selective water splitting performance.

We then evaluated the performance of water splitting performance by replacing the cathode and anode electrodes with Ni_2P-LF and Ni_2P-HF, respectively. According to the polarization curve in Figure 3.9e, the HER polarization curve only requires about 400 mV to reach a current density of 500 mA/cm^2, which is 23 mV lower than that with graphite as the counter electrode. The water splitting system can efficiently realize an oxidative current density of 500 mA/cm^2 with excellent durability at the overpotentials of 255 mV, which surpasses most of water splitting electrodes and meets the commercial criteria for water splitting.[138] As depicted in Figure 3.9e, the expected overall water splitting voltages are only 1.80, 1.84 and 1.89 V to achieve current densities of 100, 200 and 500 mA/cm^2, respectively.

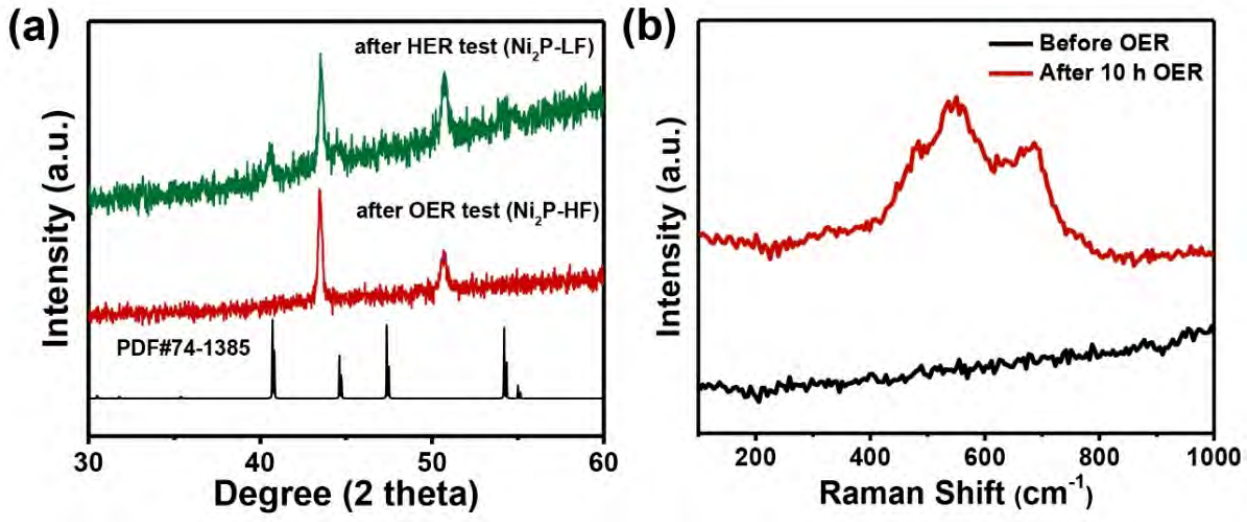

Figure 3.12. (a) XRD patterns of Ni_2P-HF and Ni_2P-LF after OER and HER test, respectively. (b) Raman spectrum of Ni_2P-HF before and after OER reaction.

Furthermore, both cathodic and anodic electrodes show remarkable water splitting performance under constant current density (100 mA/cm^2) within a considerable time, which may attribute to excellent mechanical stability and anti-corrosive character of SS mesh (Figure 3.9f).

The stability of Ni_2P-HF and Ni_2P-LF is also investigated by the XRD patterns in Figure 3.12a, Ni_2P-LF shows excellent structure stability after long-time HER reaction and amorphous state is observed on the surface of Ni_2P-HF after 10h OER test. According to Raman spectrum in Figure 3.12b, the amorphous state is oxidized Ni_2P-HF, which is regarded as the main active material for OER process. We also compare water splitting performance of as-fabricated electrodes with other reported self-supported electrodes in Table 3.3. Our designed Fe-doped Ni_2P electrodes display the best OER performance and comparable HER performance than other control electrodes, showing great potential towards practical application.[70, 72, 119, 126, 130, 139-141]

Table 3.3. Comparison of overpotentials for HER and OER reactions.

	Overpotential for HER	**Overpotential for OER**	**References**
NiP/Ni foam	185 mV @ 60 mA/cm^2	320 mV @ 100 mA/cm^2	Chen Gaofeng et al.[139]
Fe-doped Ni_2P/Ni foam	310 mV @ 200 mA/cm^2	260 mV @ 300 mA/cm^2	Li Yingjie et al.[119]
N- and P-doped SS	> 400 mV @ 100 mA/cm^2	> 600 mV @ 100 mA/cm^2	Balogun Muhammad-Sadeeq et al.[126]
Fe/Ni Phosphides on Ni foam	230 mV @ 400 mA/cm^2	290 mV @ 400 mA/cm^2	Xiao Chunhui et al.[130]
N-doped Ni_3S_2/Ni foam	250 mV @ 160 mA/cm^2	380 mV @ 400 mA/cm^2	Chen Pengzuo et al.[70]
NiFe LDH/Cu foam	192 mV @ 100 mA/cm^2	311 mV @ 500 mA/cm^2	Yu Luo et al.[72]
MoO_x/Ni_3S_2/Ni	480 mV @ 500 mA/cm^2	520 mV @ 500 mA/cm^2	Wu Yuanyuan et al.[142]
Co−Mn carbonate hydroxide/Ni foam	450 mV @ 500 mA/cm^2	400 mV @ 500 mA/cm^2	Tang Tang et al.[141]
Fe-doped Ni_2P/SS	**400 mV @ 500 mA/cm^2**	**255 mV @ 500 mA/cm^2**	**This work**

Table 3.4. Comparison of potentials for overall water splitting in two-electrode system.

	Potential	References
$Ni_{1.85}Fe_{0.15}P$/Ni foam || $Ni_{1.85}Fe_{0.15}P$/Ni foam	1.87 V @ 100 mA/cm^2	Wang Pengyan et al.[115]
IrO_2/Ni foam || Pt-C/Ni foam	1.77 V @ 100 mA/cm^2	
Ni_2P/Ni foam || Ni_2P/Ni foam	1.82 V @ 100 mA/cm^2	Menezes Prashanth W. et al.[143]
Co_3Se_4/Co foam || Co_3Se_4/Co foam	1.88 V @ 100 mA/cm^2	Li Wei et al.[144]
RuO_2/Co foam || Pt-C/Co foam	1.90 V @ 100 mA/cm^2	
NiP /Ni foam || NiP/Ni foam	1.80 V @ 40 m A/cm^2	Chen Gaofeng et al.[139]
$(Ni_{0.33}Fe_{0.67})_2P$/Ni foam || $(Ni_{0.33}Fe_{0.67})_2P$/Ni foam	1.73 V @ 100 mA/cm^2	Li Yingjie et al.[119]
$FeNiP_x$/Ni foam || $FeNiP_x$/Ni foam	1.85 V @ 100 mA/cm^2	Xiao Chunhui et al.[130]
NiCoP/Ni foam || NiCoP/Ni foam	1.83 V @ 100 mA/cm^2	Liang Hanfeng et al.[133]
N-Ni_3S_2/Ni foam || N-Ni_3S_2/Ni foam	1.82 V@ 100 mA/cm^2	Chen Pengzuo et al.[70]
Fe-doped Ni_2P (1h)/SS || Fe-doped Ni_2P (3h)/SS	**1.80 V @ 100 mA/cm^2**	**This work**

As Ni_2P-HF and Ni_2P-LF can serve as excellent OER and HER electrocatalysts in alkaline media, we design a self-supported water splitting electrolyzer based on Fe-doped Ni_2P/SS mesh. Ni_2P-HF and Ni_2P-LF were adopted as anode and cathode in the two-electrode system, respectively. According to Figure 3.9g, the electrolytic cell affords current densities of 10 mA/cm^2, 100 mA/cm^2 and 200 mA/cm^2 at 1.62V, 1.80 V and 1.85 V, respectively. To the best of our knowledge, the overall water splitting performance of Ni_2P-HF || Ni_2P-LF at high current density (e.g., 100 mA cm^{-2}) outperforms most of excellent overall water splitting electrolyzers in Table

3.4, such as, $Ni_{1.85}Fe_{0.15}P$/Ni foam || $Ni_{1.85}Fe_{0.15}P$/Ni foam (1.87 V), Ni_2P/Ni foam || Ni_2P/Ni foam (1.82 V), NiCoP/Ni foam || NiCoP/Ni foam (1.83 V), Co_3Se_4/Co foam || Co_3Se_4/Co foam (1.88 V) and $FeNiP_x$/Ni foam || $FeNiP_x$/Ni foam (1.85 V).[143-144]

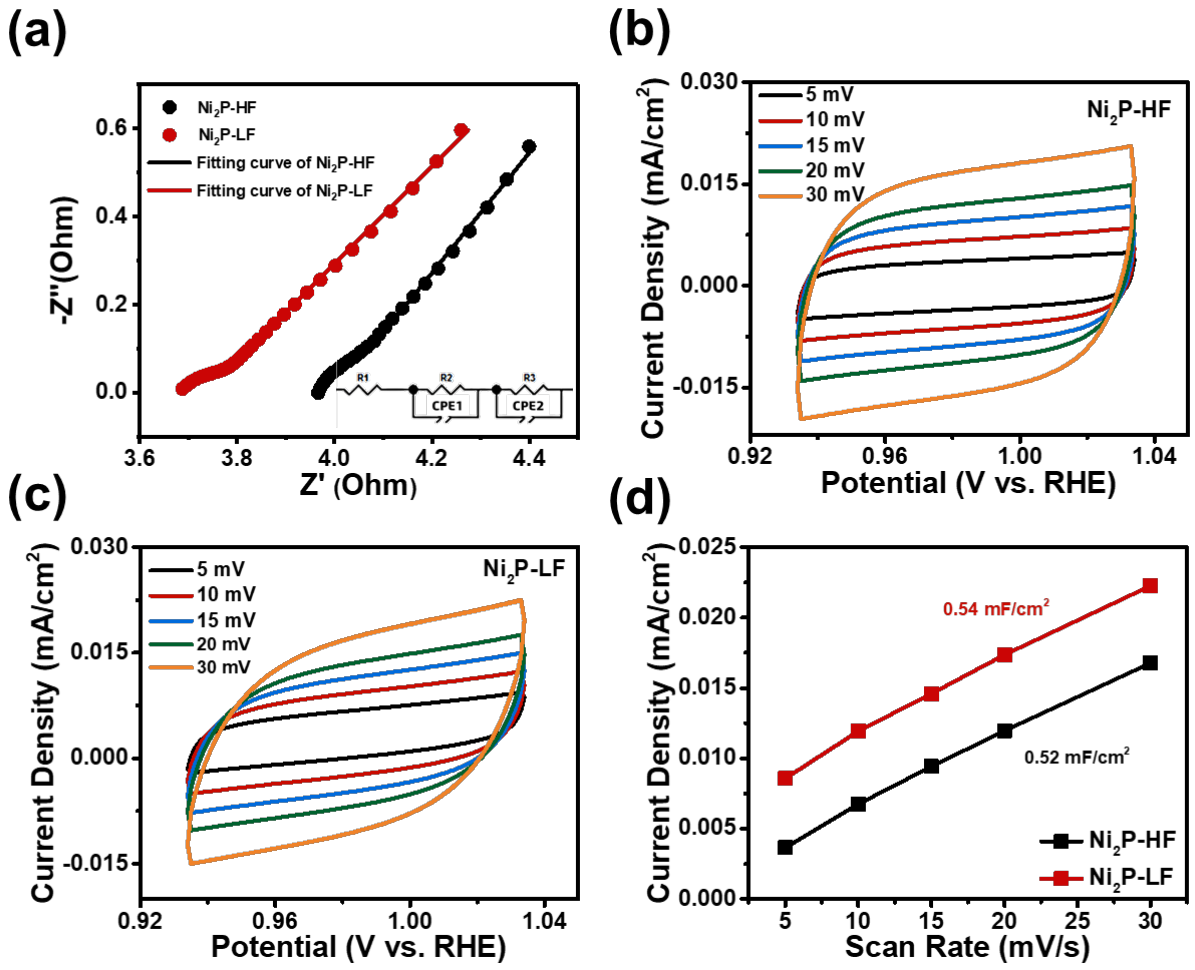

Figure 3.13. (a) Electrochemical impedance spectroscopy (EIS) Nyquist plots of Ni_2P-HF and Ni_2P-LF, the inset graph shows an electrical equivalent circuit model. Cyclic voltammograms with different scan rates obtained at non-faradaic potential region between 0.01 V and 0.11 V (vs. Hg/HgO) of (b) Ni_2P-HF and (c) Ni_2P-LF. (d) The differences in current density at 0.98 V vs RHE plotted as a function of scan rate, the slope of fitting line represents active electrochemical area of electrocatalyst.

More importantly, as shown in Figure 3.9h, the water splitting electrolyzer exhibits very good durability upon prolonged period at the current densities of 10, 50 and 100 mA cm^{-2}, respectively, showing great potential for practical application. Thus, we successfully fabricate self-

supported Fe-doped Ni_2P electrocatalysts based on SS mesh and realize prominent OER and remarkable HER performance by engineering the atomic content of Fe in Fe-doped Ni_2P. The high-efficient self-supported electrodes not only show great potential to construct overall water splitting device towards practical applications, but also provide desired model for us to clarify the synergistic effect of Fe and Ni sites during hydrogen and oxygen evolution process.

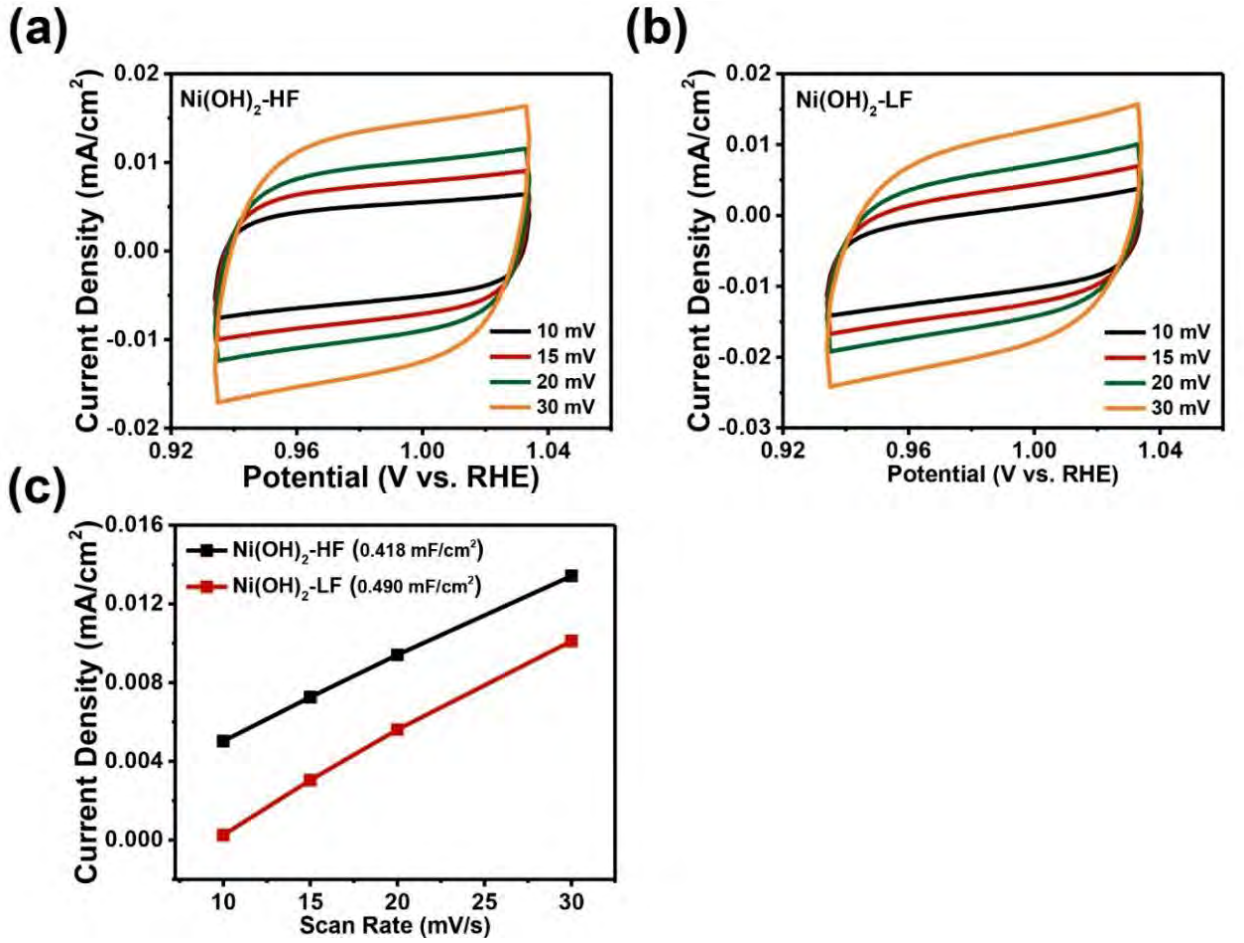

Figure 3.14**.** Cyclic voltammograms obtained at non-faradaic potential region between 0.01 V and 0.11 V (vs. Hg/HgO) of (a) $Ni(OH)_2$-HF and (b) $Ni(OH)_2$-LF samples, respectively. (c) The differences in current density at 0.98 V vs RHE plotted as a function of scan rate, the slope of fitting line represents active electrochemical area of electrocatalyst.

To verify the underlying mechanism of Fe content induced selective water splitting performance, we characterize the as-prepared electrodes by using electrochemical impedance

spectroscopy (EIS) and electrochemically active surface area (ECSA). As depicted in Figure 3.13a, the Ni_2P-LF shows a solution resistance of 3.96 Ω, which is slightly lower than Ni_2P-LF (3.67 Ω), indicating Ni_2P-HF possessing a better catalyst/electrolyte interface contact than Ni_2P-LF. In addition, the low charge resistance indicates both Ni_2P-HF and Ni_2P-LF possess good electrical conductivity and good electrical contact with substrate, which is beneficial for the electrochemical water splitting process.

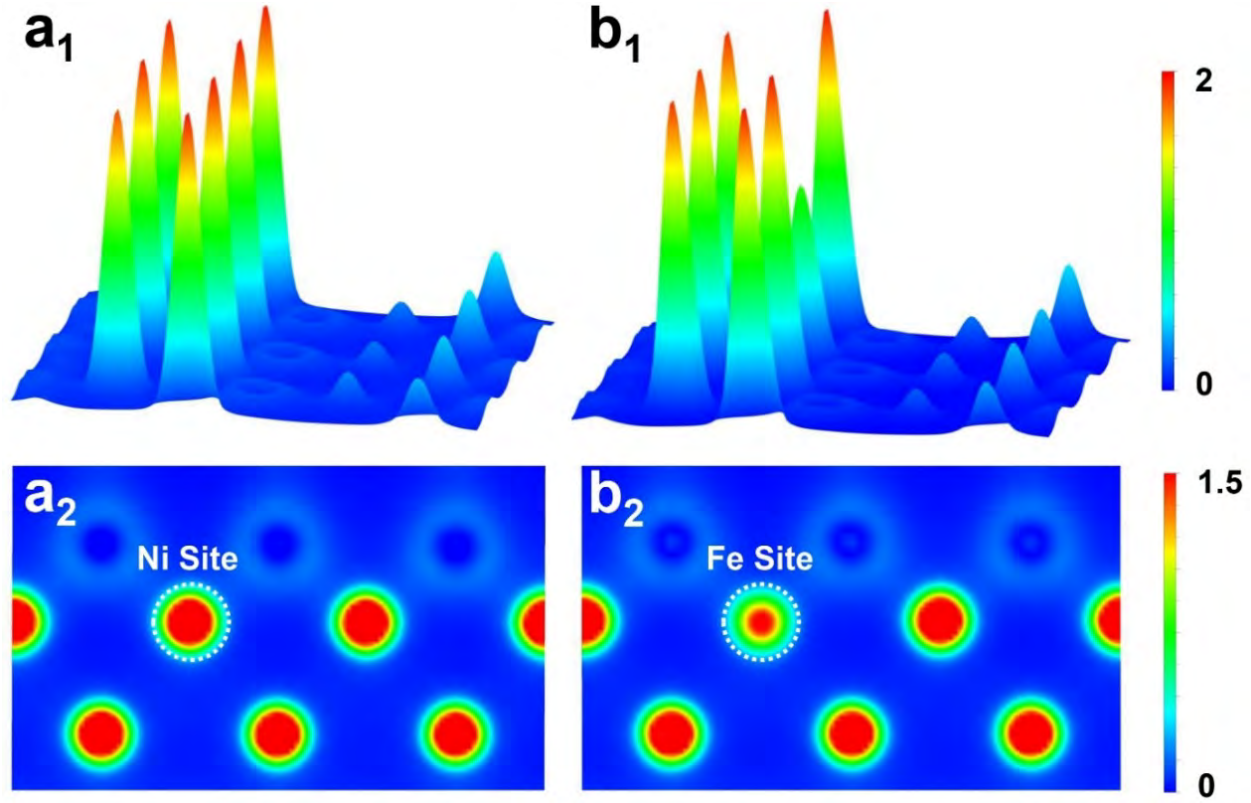

Figure 3.15. Electron density contour maps for Ni_2P surface (a_1-a_2) without and (b_1-b_2) with Fe dopant. (a_1) and (b_1) are bird's-eye view.

Typically, double-layer capacitance is characterized to estimate the active electrochemical sites of prepared Fe-doped Ni_2P samples. Figure 3.13d shows the differences of current density as a function of scan rate from the corresponding CV curves in Figure 3.13b-3.13c. The Fe-doped Ni_2P samples display larger active electrochemical area than their hydroxides counterparts (Figure 3.14). Both Ni_2P-HF and Ni_2P-LF show similar quantity of active electrochemical sites. Therefore,

the electrical conductivity and number of active electrocatalytic sites are almost irrelevant with the selective water splitting performance. The major reason for this unique behavior should ascribe to the different types of active sites resulting from different level of Fe doping.

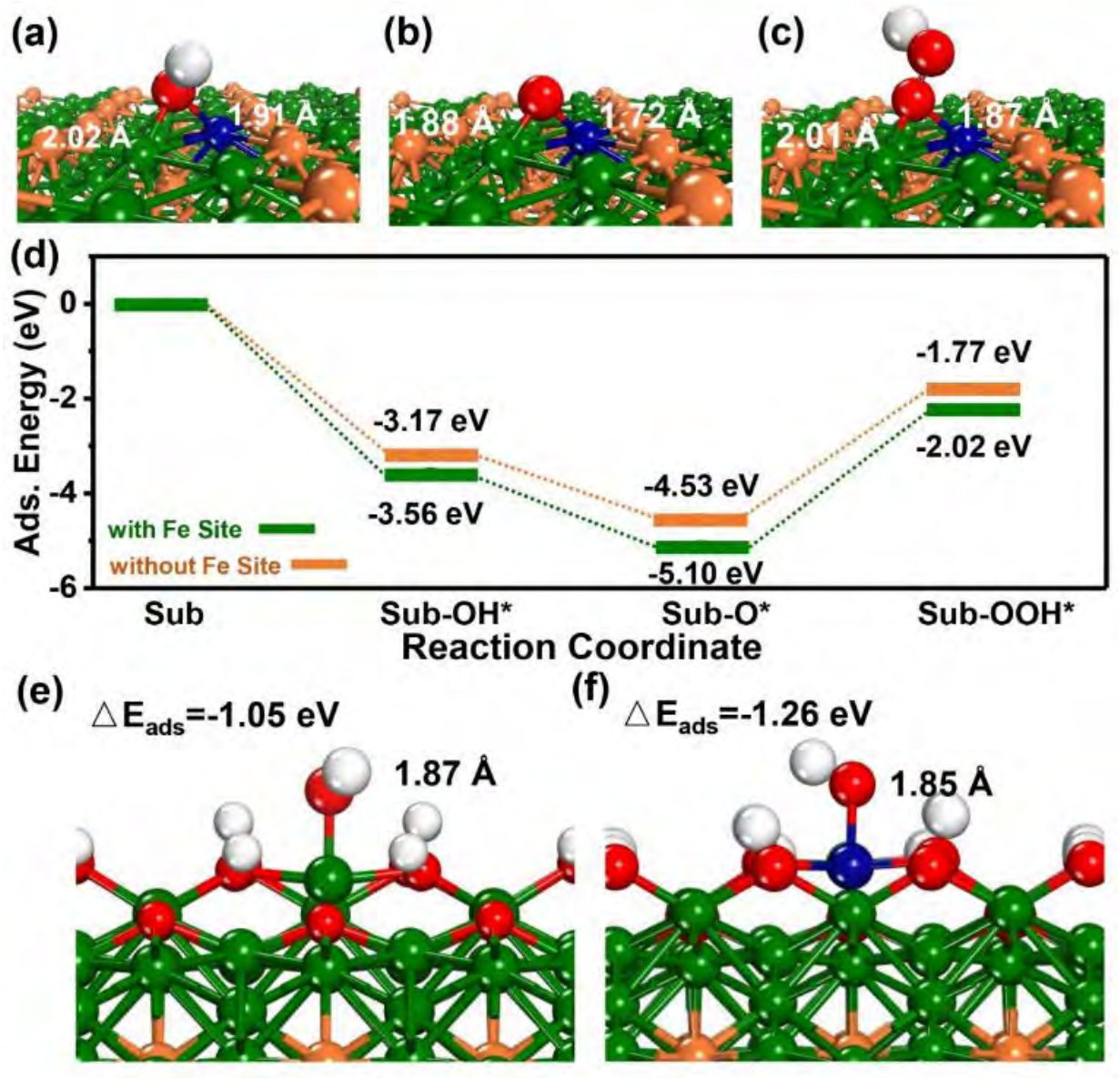

Figure 3.16. Adsorption of (a) OH*, (b) active O* and (c) OOH* intermediates on Fe-doped Ni_2P surface. For clarity, the symmetric parts of the optimized slabs at the bottom are not shown. (d) The calculated OER energy diagram of the Ni_2P surface with (green line)/without (orange line) Fe doping. Adsorption of OH* on oxidized Ni_2P surface (e) without and (f) with Fe site. The green, blue, orange, red and grey balls represent Ni, Fe, P, O and H atoms, respectively. For clarity, the symmetric parts of the optimized slabs at the bottom are not shown.

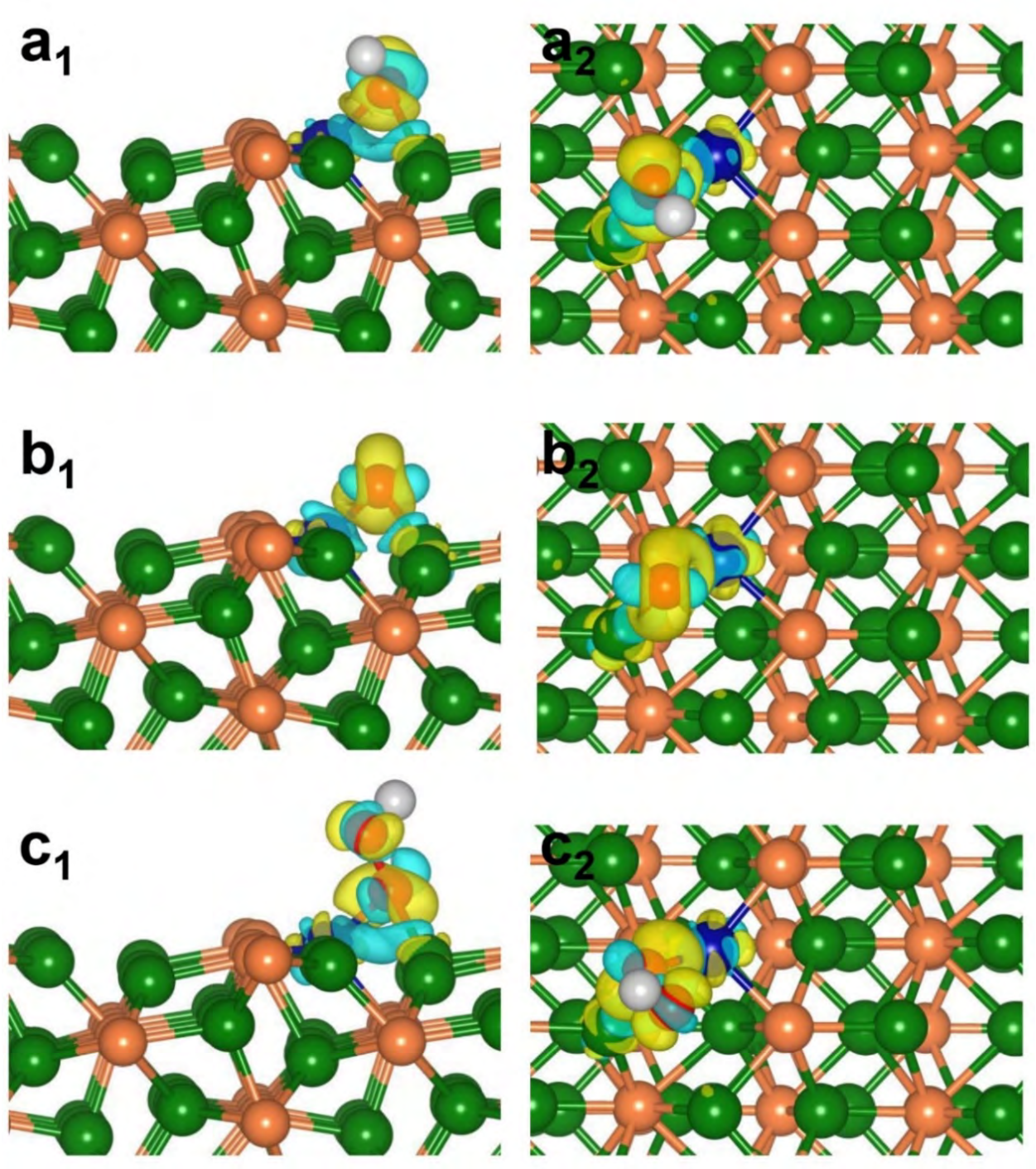

Figure 3.17. (a_1) Side view and (a_2) top view of the charge density difference of the OH*-adsorbed on Fe-doped Ni_2P surface. (b_1) Side view and (b_2) top view of the charge density difference of the O*-adsorbed on Fe-doped Ni_2P surface. (c_1) Side view and (c_2) top view of the charge density difference of the OOH*-adsorbed on Fe-doped Ni_2P surface. The yellow and blue isosurfaces represent charge accumulation and depletion, respectively. The isovalue is 0.005 au. For clarity, the symmetric parts of the optimized slabs at the bottom are not shown.

To gain insights into inherent relationship between the selective HER/OER performance and Fe dopant in Ni_2P surface, we performed DFT calculations to understand the OER and HER processes on Ni_2P surface with and without Fe dopant. Figure 3.15 shows the electron density distribution of Ni_2P surface with/without Fe doping. The introduction of Fe dopant greatly intensifies the surface charge nonuniform, and redistributes surrounding electron density, which may play positive role in O- and H-containing intermediates adsorption.

As depicted in Figure 3.16a-3.16c, the adsorption behavior of essential intermediates during OER process, including OH*, O* and OOH*, are investigated on Fe-doped Ni_2P surface. According to the optimized slabs, all the intermediates tend to bridge on the Fe site and adjacent Ni site on Fe-doped Ni_2P surface, which implies Fe site and Ni site are both necessary for OER intermediates adsorption. Furthermore, the adsorption of OH*, O* and OOH* shows distinct chemical adsorption characteristics because obvious electron transfer can be observed between the interface of adsorbates and Ni_2P substrate (Figure 3.17). The charge transfer from substrate to adsorbate may lead to effective molecule activation, which can promote succeeding O_2 evolution.

More importantly, as depicted in Figure 3.16d, the adsorption energies of OH*, O* and OOH* on Fe-doped Ni_2P surface are -3.56 eV, -5.10 eV and -2.02 eV, respectively, which are lower than those on bare Ni_2P surface, indicating feasible thermodynamic behavior of OER process on Fe-doped Ni_2P slab. In addition, we also investigated the OH* adsorption on oxidized Ni_2P surface with and without Fe doping, considering that oxidized surface is usually regarded as main active sites for OER reaction on Ni-Fe-P surface. According to Figure 3.16e-3.16f, the introduction of Fe dopant into oxidized Ni_2P surface can greatly improve the OH* adsorption and decrease the required adsorption energy from -1.05 eV to -1.26 eV. These theoretical results verify that Fe doping can enhance OER intermediates adsorption on both Ni_2P and oxidized Ni_2P surface

and greatly prompt the oxygen evolution process by reducing the adsorption energy of intermediates. Based on the experimental results and theoretical analysis, we firmly believe that the introduction of Fe dopant in Ni_2P matrix is an effective strategy for improving OER performance.

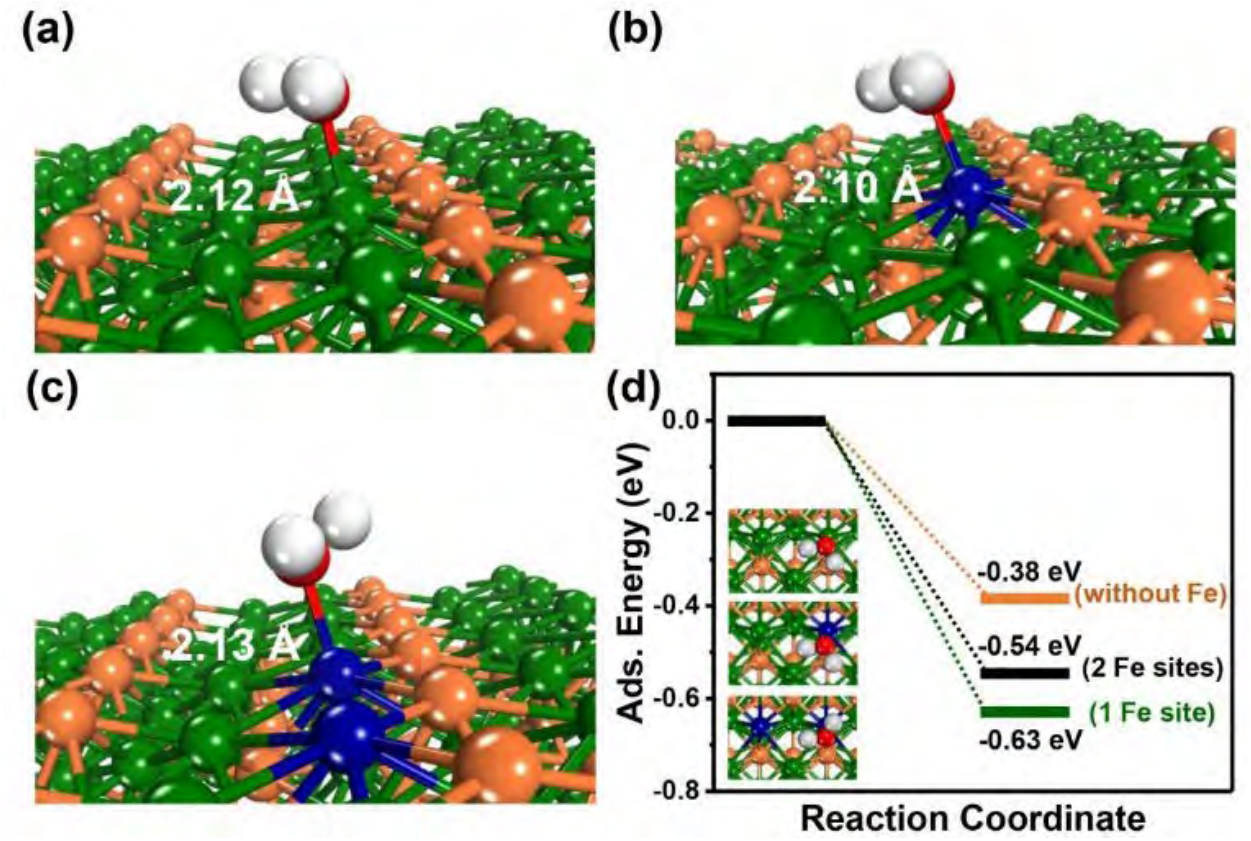

Figure 3.18**.** Adsorption of active H_2O* on (a) bare Ni_2P surface, (b) Ni_2P surface with single Fe site and (c) Ni_2P surface with bi-Fe sites, respectively. For clarity, the symmetric parts of the optimized slabs at the bottom are not shown. (d) Calculated adsorption energy of H_2O on bare Ni_2P surface (orange line), Ni_2P surface with one Fe site (green line) and Ni_2P surface with two Fe sites (black line), respectively. The green, blue, orange, red and grey balls represent Ni, Fe, P, O and H atoms, respectively.

In addition, HER mechanism on Fe-doped Ni_2P surface was also investigated. The adsorption behavior of H_2O molecule is regarded as an essential criterion to estimate alkaline HER performance.[145] As shown in Figure 3.18a-3.18c, Fe site on Ni_2P surface shows better affinity to H_2O adsorption than Ni sites, and H_2O adsorption on Fe site exhibits distinct chemical adsorption

feature. The apparent interfacial charge transfer between H_2O and Fe-doped Ni_2P surface (Figure 3.19) confirms the activation of H_2O molecule, which may be conductive to following water dissociation process. Moreover, we compare the adsorption energy of H_2O on bare Ni_2P surface and Ni_2P surface with different kinds of Fe sites to further clarify the effect of Fe content in Ni_2P matrix on HER performance. As displayed in Figure 3.18d, the introduction of Fe dopant into Ni_2P matrix can greatly decrease the adsorption energy of H_2O molecule, indicating a feasible H_2O activation and dissociation process. However, when the single Fe site is replaced by bi-Fe sites, the adsorption energy increases from -0.63 eV to -0.54 eV. The above results demonstrate Fe doping is an effective strategy to improve the H_2O adsorption on Ni_2P, and single Fe site is more active than bi-Fe site, implying the importance of Fe doping content control. Based on above analysis, H_2O adsorption is sensitive to content of Fe dopant, and only slight Fe doping can promote H_2O adsorption behaviors on Ni_2P matrix, leading to the enhanced HER performance. These theoretical results are well consistent with the electrochemical performance and deepen our understanding to the effect of Fe doping in Ni_2P on HER performance.

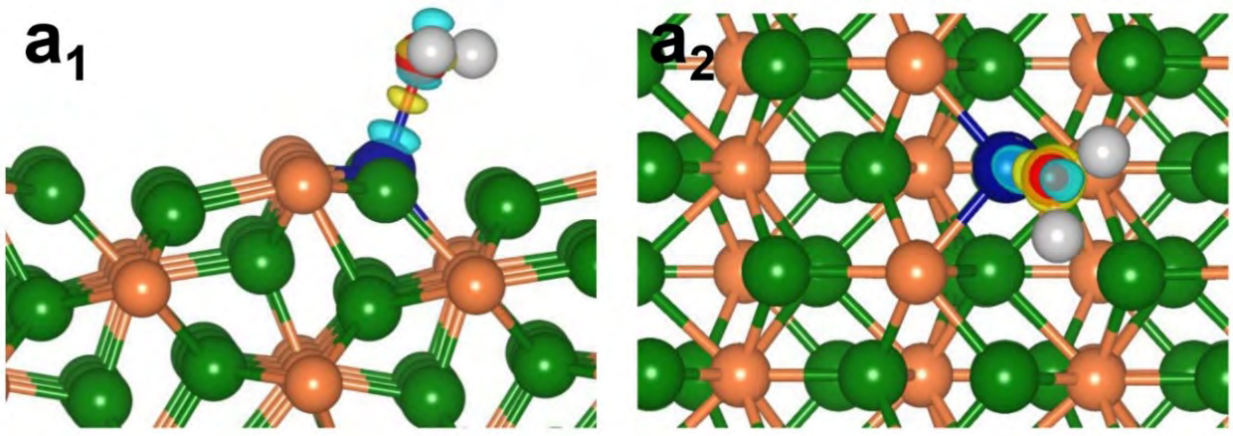

Figure 3.19. (a_1) Side view and (a_2) top view of the charge density difference of the H_2O-adsorbed on Fe-doped Ni_2P surface. The yellow and blue isosurfaces represent charge accumulation and depletion, respectively. The isovalue is 0.005 au. For clarity, the symmetric parts of the optimized slabs at the bottom are not shown.

3.5 Conclusions

In summary, we have applied cost-effective 304-type SS mesh to fabricate self-supported Fe-doped Ni_2P electrocatalyst, and successfully realize selective water splitting performance by controlling the atomic content of Fe dopant. The Ni_2P-HF with high content of Fe dopant exhibits outstanding OER performance, reaching extremely high current densities of 500 mA/cm^2 under extremely low overpotential of 255 mV. The Ni_2P-HF electrode manifests the first-class oxygen evolution performance and meets the commercial water electrolyzer requirements. The Ni_2P-LF with less Fe dopant shows comparable HER performance than other state-of-the-art non-noble metal-based counterparts in alkaline medium. Our theoretical calculations confirm that promoted intermediates adsorption induced by Fe-doping contributes significantly to enhanced OER performance. Moreover, H_2O is sensitive to the content of Fe dopant, only slight Fe dopant is beneficial for effective H_2O adsorption, which is regarded as the main reason for selective water splitting performance induced by Fe content engineering. The combination of experimental and theoretical results unambiguously clarifies the synergistic effect occurred on bifunctional Ni-Fe-P surface and deepens our understanding to the role of Fe dopant on Ni_2P surface during water splitting process. In addition, the well-designed Fe-doped Ni_2P/SS based electrolyzer can efficiently catalyze overall water splitting with low electricity consumption, which has significantly broadened the development of robust electrodes for large-scale water electrolysis.

4 Unusual Electrocatalytic Nitrogen Reduction of Sulfurized Pt Nanoparticles

4.1 Objective and Motivation

Platinum (Pt) is the most promising catalyst in chemical reduction reactions, including NO_x reduction, O_2 reduction, and reduction of aromatic nitro compounds. However, Pt has been shown as an inefficient catalyst for artificial nitrogen reduction reaction (NRR) because of the weak N_2 affinity and intrinsic competition with hydrogen evolution. Here we show that sulfurized platinum (PtS) can be used as robust electrocatalyst for nitrogen reduction owing to its optimized electron configuration. The combination of unoccupied *d* orbitals and abundant d electrons in PtS surface enables to decrease the barrier for N_2 reduction and suppress the kinetics for hydrogen evolution. Our experimental results demonstrate PtS nanoparticles on carbon cloth (PtS/CC) can greatly boost electroreduction of N_2 to NH_3, affording an NH_3 yield rate of 74 $\mu g/mg_{cat.}\cdot h$ at 0 V versus the reversible hydrogen electrode (RHE). The Faradaic efficiency of PtS/CC for NH_3 production is achieved about 10% at 0.1 V versus RHE, which is about 5 times as high as that of Pt/CC. This work not only develops an advanced electrocatalyst for N_2 reduction, but also provides an effective strategy to design NRR electrocatalysts based on noble metals.

4.2 Introduction

Ammonia (NH_3) is regarded as a carbon-free energy carrier with high energy density. The production of NH_3 from dinitrogen (N_2, the most common element form of nitrogen) is still difficult because of the stable and inert N≡N triple bond.[39, 43] In nature, nitrogen fixation is realized through the catalytic process of nitrogenases; while industrial nitrogen fixation mainly relies on the long-standing Haber-Bosch process, which requires energy-intensive input and inevitably

leads to massive greenhouse gas emissions.[40, 146-147] There exists a grand impetus to develop electrocatalytic N_2 reduction reaction (NRR) as it provides a green and sustainable approach for nitrogen fixation at the ambient conditions.[148-151] It is generally accepted that the efficiency of electrocatalytic NRR strongly depends on the active catalytic sites. Transition-metal (TM) center is the most important type of active catalytic sites for the NRR process. The roles of active TM center are mainly twofold.[48-49, 56, 152-153] (1) The interaction between active TM center and N_2 molecule determines the necessary N source for the NRR.[57, 154] (2) The interaction between active TM center and proton donors affects both desired hydrogenation process in NRR and undesirable hydrogen evolution reaction (HER). The competition between NRR and HER directly dictates the Faradaic efficiency of NRR. Therefore, it is of great significance to tune the transition metal properties for selectively improving N_2 affinity and suppressing HER activity.[155]

The well-developed NRR electrocatalysts are mainly based on TMs, especially middle group TMs, which exhibit robust N_2 reduction performance due to their featured *d*-electron configurations.[51, 140, 156-160] The unoccupied *d* orbitals of TM center enables it to accept long pair-electrons from N_2 (Figure 4.1a), forming σ donation from N_2 to TM center and ensuring the N_2 chemisorption. Meanwhile, the presence of d electrons in TM center can inject into the empty antibonding π orbitals of N_2 molecules (Figure 4.1b), which greatly weakens the N≡N triple bond and facilitates the N_2 activation.[44, 161-162] Among various TM candidates, platinum (Pt) is known as an efficient catalyst for the reduction of nitrogen-containing molecules.[163] However, Pt has been shown with inefficiency for converting N_2 to NH_3 due to the weak affinity to N_2 and intrinsic competition with hydrogen evolution.[164] The *d* orbitals of Pt is almost fully occupied, which blocks the σ donation from N_2 and show weak interaction between active site and N_2.[165-166] In addition, the moderate binding strength of Pt-H reduces the reaction barriers of hydrogen evolution process

and inevitably leads to vigorous competing reaction of hydrogen evolution.[6] Thus, it is a fundamental research interest to optimize the electron configuration and surface coordination of Pt for improved N_2 affinity and suppressed HER activity. The well-designed strategy for Pt-based NRR catalyst can also serve as an excellent reference to modify conventional inactive noble catalysts and further broaden the library of NRR catalysts.

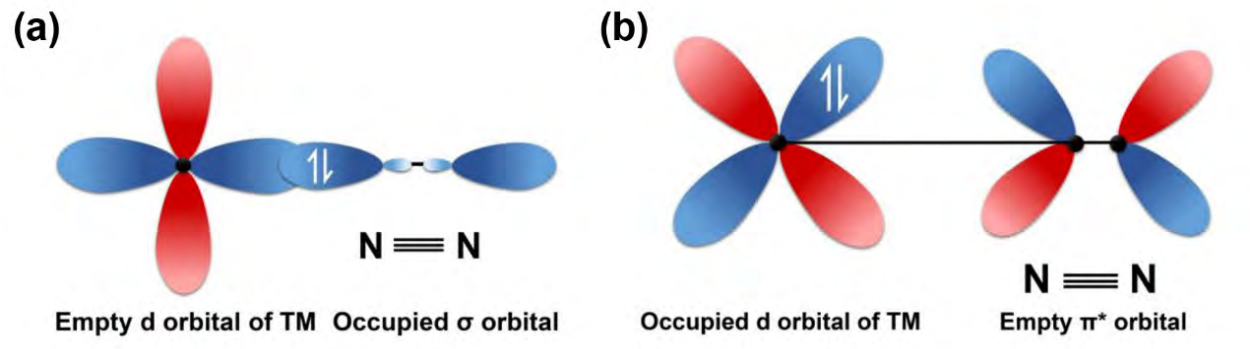

Figure 4.1. Schematic of N_2 bonding to transition metals. (a) σ donation from N_2 and (b) π backdonation to N_2.

It has been widely known that metal-sulfur cluster shows great potential for N_2 activation.[167] For example, FeMo-cofactor in nitrogenase consists of one Fe_4S_3 cluster and one $MoFe_3S_3$ cluster, showing high efficiency for N_2 fixation.[168] Moreover, the S site is active for H_2O dissociation and shows great potential to trap H* intermediates.[169] Here we demonstrate that sulfurized Pt (PtS) surface can act as an excellent NRR electrocatalysts due to the improved N_2 affinity. The Pt site in PtS shows reduced barrier of N_2 adsorption than metallic Pt surface due to rational *d*-electron configuration, and S site on PtS can effectively capture H* for subsequent hydrogenation reaction of NRR. More importantly, PtS exhibits distinct HER suppression behavior, which enables high Faradaic efficiency of electrochemical N_2 reduction. As a result, the as-synthesized PtS nanoparticles on self-supported carbon cloth (PtS/CC) achieve a superior NH_3 yield rate of 74 μg/ mg_{cat}·h at 0 V versus reversible hydrogen electrode (RHE), which is about 6

times higher than that of the Pt nanoparticles on CC (Pt/CC). In addition, PtS/CC catalyst demonstrates a Faradaic efficiency (FE) of about 10% for NH_3 production at 0.1 V versus RHE and exhibits outstanding stability for continuous N_2 reduction during long-time electrolysis.

4.3 Experimental Section

4.3.1 Treatment of Carbon Cloth: A carbon cloth (CC) (2 cm × 1 cm) purchased from CeTech Co., Ltd. was used as substrate for materials growth. The CC was treated by Piranha solution at 80 °C for 72 h, washed by deionized (DI) water, and then dried at 100 °C in oven to provide hydrophilic surface.

4.3.2 Electrodeposition of Pt Nanoparticles on CC: A standard three-electrode electrochemical cell was used for Pt nanoparticles electrodeposition. Pt nanoparticles were deposited on carbon cloth via a pulse-mode potentiostatic approach. Saturated calomel electrode (SCE) and graphite rod were used as a reference and counter electrodes, respectively. 0.5 mM $H_2PtCl_6 \cdot 6H_2O$ and 0.15 M citric acid were used as precursors. Then, Pt nanoparticle was electrodeposited at a fixed holding time of 0.2 s at −1.2 V *vs.* SCE and 2.5 s at 0 V *vs.* SCE for 100 cycles. Finally, the Pt/CC sample was washed by DI water and annealed at 500°C for 120 min.

4.3.3 Preparation of PtS Nanoparticles on CC: The PtS/CC sample was synthesized by a one-step annealing process in a tube furnace with double temperature region. The sulfur powder was put in the upstream region and the Pt/CC precursor was in the downstream section. The temperature of upstream region was set as 180 °C to evaporate the sulfur and provide sulfur source for the sulfidation process of Pt/CC. Besides, the heating center temperature of the downstream region was raised up to 700 °C and the heating rate was 10 °C /min, and the center temperature was held at 700 °C for 30 min. The sulfidation process was performed under Ar atmosphere.

4.3.4 Electrochemical Test: A three electrodes electrochemical station was used to perform electrochemical measurements. All electrochemical tests were performed in a H-cell system separated by Nafion membrane. Graphite rod and calomel electrode were used as counter electrode and reference electrode, respectively. For NRR performance test, the potentials were controlled by an electrochemical station. The N_2 electrochemical reduction was performed in N_2-saturated 0.1 M Na_2SO_4 solution at room temperature. The performance of the HER was tested using linear sweep voltammetry (LSV) with a scan rate of 2 mV s^{-1}. All the LSV curves weren't collected until the electrode surface reached electrochemical balance.

4.3.5 Determination of Ammonia: The production of ammonia was determined by the indophenol blue method. 2.2 g of NaOH, 5.0 g of salicylic acid and 5.0 g of sodium citrate was first dissolved in 100 mL DI water to form color developing reagent. 0.1 g of $C_5FeN_6Na_2O$ was dissolved in 10 mL DI water. Then, 1.48 g of NaOH and 2 mL of NaClO solution were added in 48 mL DI water to form NaClO solution with available chlorine concentration of 3.5 g/L and free alkali concentration of 0.75 mol/L. For determination, 2 mL of color developing reagent was added into 2 mL of electrolyte, followed by addition of 1 mL NaClO solution and 200 uL $C_5FeN_6Na_2O$ solution. After aging for 90 min, the absorption spectrum was measured using an UV-vis spectrophotometer and the concentration of indophenol blue was determined using the absorbance at a wavelength of 655 nm. The concentration-absorbance curve was calibrated with C = 2.093*A-0.024.

4.3.6 Determination of Hydrazine: The concentration of hydrazine in the electrolyte was estimated via the Watt and Chrisp method. The color reagent is consisted of 0.599g of para-(dimethylamino) benzaldehyde, 3mL of HCl (12 mol/L) and 30mL of ethanol. 2 mL of the

electrolyte was mixed with 2 mL of color reagent and measured the absorbance at 455 nm. The concentration-absorbance curve was calibrated with C = 0.8964*A-0.0247.

4.3.7 Characterizations: The morphology of Pt/CC and PtS/CC was characterized by scanning electron microscope (SEM, Jeol JSM-6335F) and scanning transmission electron microscope (TEM, Jeol JEM-2100F). The crystal structure and composition were measured by X-ray Diffractometer (Rigaku SmartLab). The surface valence state of Pt/CC and PtS/CC were tested by using X-ray photoelectron spectroscopy (XPS, Thermol Scientific Escalab 250Xi, Al Kα radiation). The electrochemical impedance spectroscopy (EIS) Pt/CC and PtS/CC were performed by a three-electrode configuration using Solartron Electrochemical workstation (German) with the frequency ranging from 0.01 to 10^5 Hz. The average mass loading (14.9 μg/cm^2 for Pt/CC and 16.6 μg/cm^2 for PtS/CC) of catalysts was measured with Thermo Scientific Plasma Quad 3 inductively-coupled plasma mass spectrometry (ICP-MS), and the final mass loading was determined by taking the average of three times of measurements. We performed the Pt L_3-edge X-ray absorption fine structure (XAFS) measurements at the beamline 1W1B of Beijing Synchrotron Radiation Facility (BSRF) in Beijing China. The storage ring of BSRF was operated at 2.5 GeV with the maximum stored current of 250 mA.

4.3.8 Theoretical Simulations: Theoretical calculations were performed using density functional theory (DFT) as implemented in the VASP code (5.4.3) with exchange-correlation energy functional, which were modeled by Perdew-Burke-Ernzerhof (PBE) functional.[83-84] The cut-off energy was set to be 520 eV and all structures were relaxed to an energy convergence of 10^{-4} eV/atom and a force convergence of 0.01 eV/Å, respectively. During the geometrical optimization, a (2 × 2) PtS surface with exposed (0 1 0) surface (the most stable low-index surface of PtS crystal) and (3 × 3) Pt slab with exposed (1 1 1) surface were applied to investigate the charge distribution

and adsorption behavior of NRR intermediates (including N_2*, N_2H*, N_2H_2*, HNNH*, N_2H_3*, H_2NNH*, $H_2N_2H_2$*, NH*, NH_2* and NH_3*).

The adsorption energy (E_{ads}) of H* and N-containing intermediates was determined according to the following equation: $\triangle E_{ads} = E_{total} - E_{sub} - E_{ads}$, where E_{total}, E_{sub}, and E_{ads} represent the total energies of the systems, the substrate, and the adsorbate, respectively. Change of Gibbs energy (ΔG) was calculated by the equation: $\Delta G = \Delta E + \Delta ZPE - T\Delta S$, where ΔE is the relative energy difference between the product and reactant of the NRR process; ΔZPE and ΔS are the corresponding changes of zero point energies and entropy at 298.15 K, which were estimated from the vibrational frequencies. The limiting potential for NRR is determined by $U = \max \{\Delta G_1, \Delta G_2, \Delta G_3, \Delta G_4, \Delta G_5, \ldots, \Delta G_n\}$. The k-points was 3 × 3 × 1 in slab optimization and static calculation. The thickness of vacuum in all slabs was set to 20 Å to eliminate the interactions between the layers caused by the periodic boundary condition.

Table 4.1. Calculated zero-point energies, entropy and Gibbs energy change of H* and N_2 adsorbed on PtS and Pt surface.

	E_{ZPE} (eV)	**TS (eV)**	**$\triangle G$ (eV)**
PtS(Pt)-H*	0.21	0.014	+0.36
PtS(S)-H*	0.24	0.007	-0.03
PtS-N_2*	0.15	0.050	+0.40
Pt-H*	0.20	0.018	-0.12
Pt-N_2*	0.15	0.002	+0.46

4.4 Design of catalyst and evaluation of NRR performance

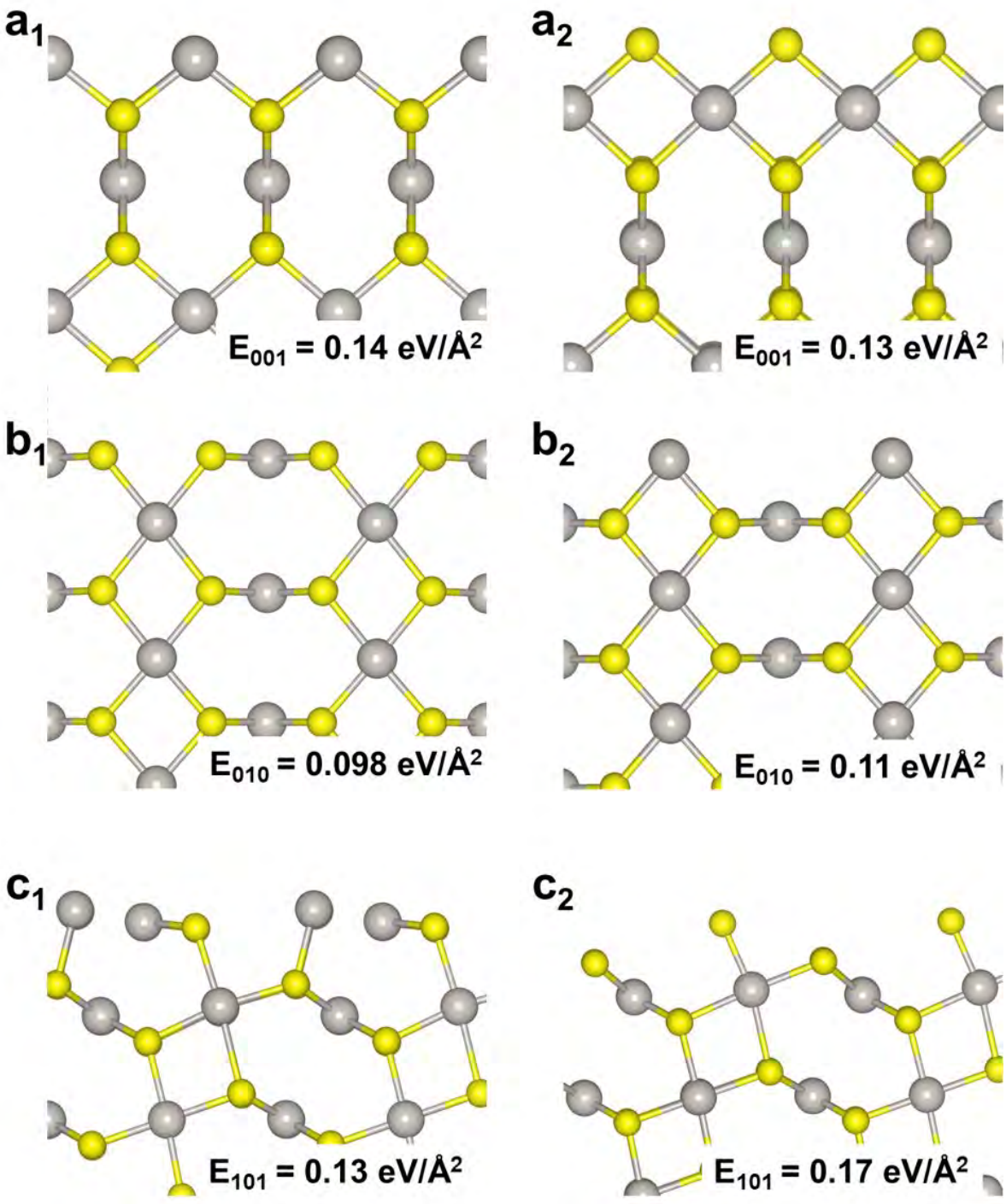

Figure 4.2. Results of surface energy test of PtS with different crystal indexes and different exposed atomic coordination. (a_1-a_2) (001) of PtS, (b_1-b_2) (010) of PtS and (c_1-c_2) (101) of PtS. Noted that owning to the crystal symmetry of PtS, the (010) of PtS is equivalent to (100).

We perform theoretical calculations to verify the outer electrons configuration and adsorption characteristics of PtS (010) surface, which is the most stable surface with the lowest surface energy (Figure 4.2). Figure 4.3 shows the calculated Bader charge of Pt atoms in Pt and PtS crystal, respectively. The average valence electron of Pt atoms decreases from 9.99 e (Pt) to 9.56 e (PtS), indicating more empty orbitals for accepting long pair-electrons from N_2 in PtS. The combination of empty *d* orbitals and abundant d electrons enables to feasible N_2 activation. Table 4.1 documents the calculated Gibbs free energy for N_2 adsorption on PtS surface.

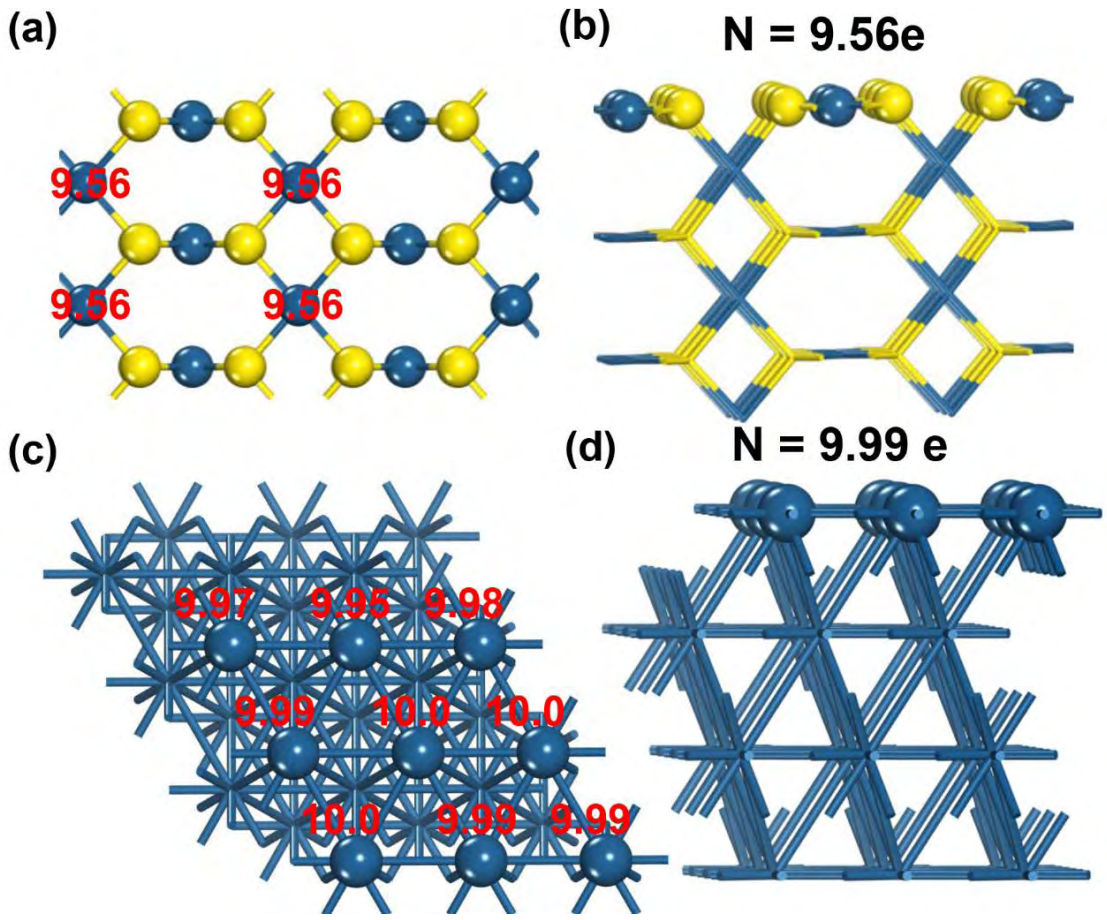

Figure 4.3. (a-b) Bader charges of surface Pt atoms in Pt crystal. The number in figure (b) is the average Bader charge of surface Pt atoms in Pt crystal. (c-d) Bader charges of surface Pt atoms in PtS crystal. The number in figure (d) is the average Bader charge of surface Pt atoms in PtS crystal.

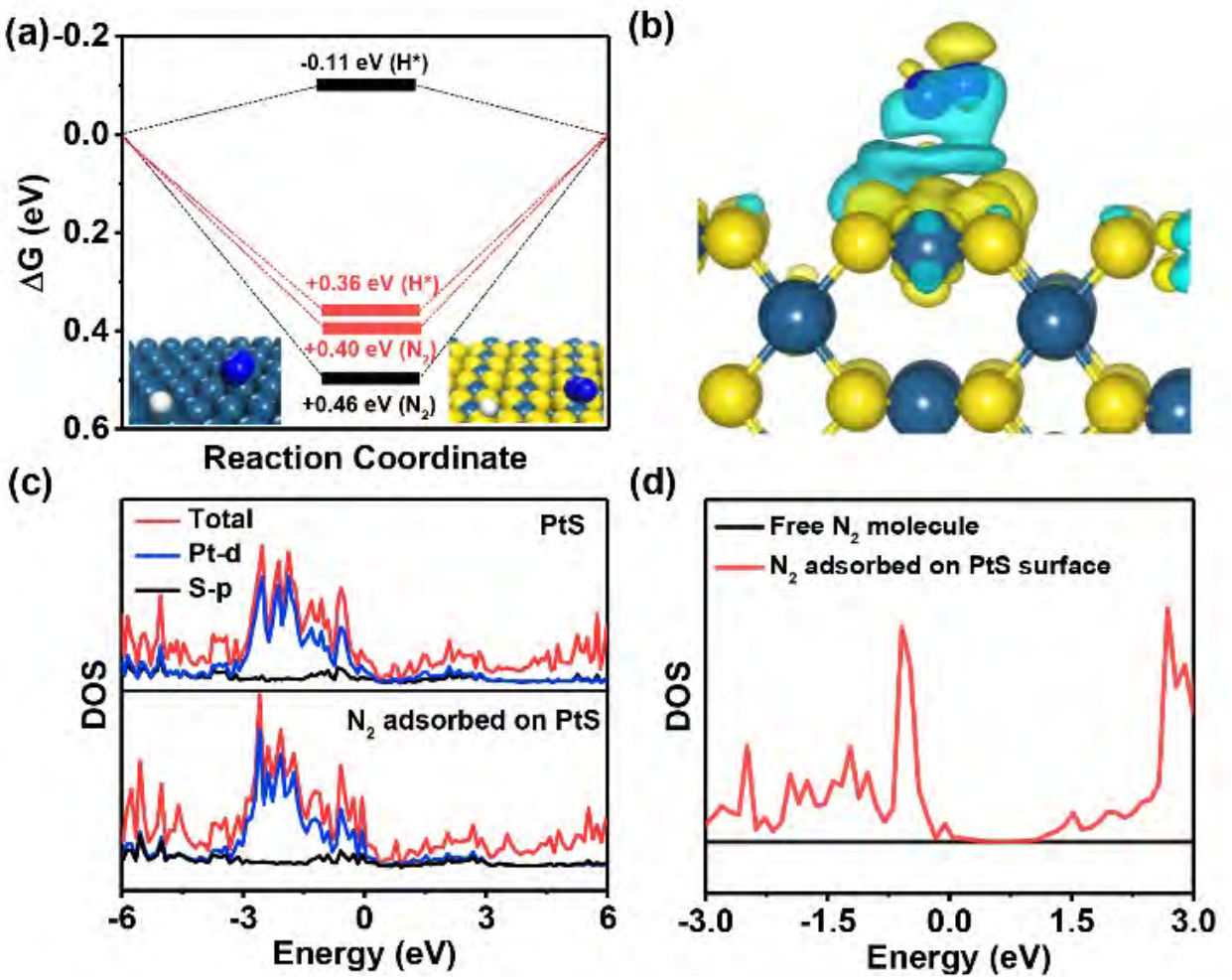

Figure 4.4. (a) Free energy diagram of H* and N_2 adsorbed on Pt (black line) and PtS (red line) surface, respectively. (b) Differential charge density of PtS with the adsorption of N_2. The yellow and cyan represent charge accumulation and charge depletion. For clarity, the symmetric parts of the optimized slabs at the bottom are not shown. Yellow, peacock blue and dark blue balls represent the S, Pt, and N atoms, respectively. (c) Calculated density of state (DOS) of PtS before and after N_2 adsorption. (d) PDOS of N_2 (2p) before and after adsorbed on PtS surface.

As shown in Figure 4.4a, N_2 adsorbed on Pt sites of PtS surface exhibits a free Gibbs energy of +0.40 eV, which is smaller than that on metallic Pt surface (+0.50 eV), suggesting the better N_2 affinity of PtS surface. The theoretical HER performance on both PtS and Pt surface are also evaluated to estimate the $*N_2/*H$ selectivity. The calculated adsorption free energy of H* ($\triangle G_{H^*}$) on PtS and Pt surface are +0.36 eV and -0.11 eV, respectively, indicating that the N_2 adsorption

on PtS is comparable to competing H* adsorption. This weaker binding strength of H* on PtS surface suggests a sluggish kinetic for H_2 formation, implying the suppressed HER performance.[109] In contrast, the metallic Pt surface shows a *H dominant character and the moderate value of $\triangle G_{H^*}$ demonstrates excellent theoretical HER performance of Pt. Hydrogen evolution is the dominant reaction at the cathode surface. Thus, compared with metallic Pt, Pt site on PtS surface shows lower probability of H* poisoning, the enhanced N_2 adsorption and suppressed HER performance may benefit the NRR efficiency on PtS surface. Additionally, the S sites of PtS surface exhibits moderate H* binding strength, suggesting that more protons can be generated on S sites and continuously delivered to adjacent Pt sites for NH_3 production (Figure 4.5).

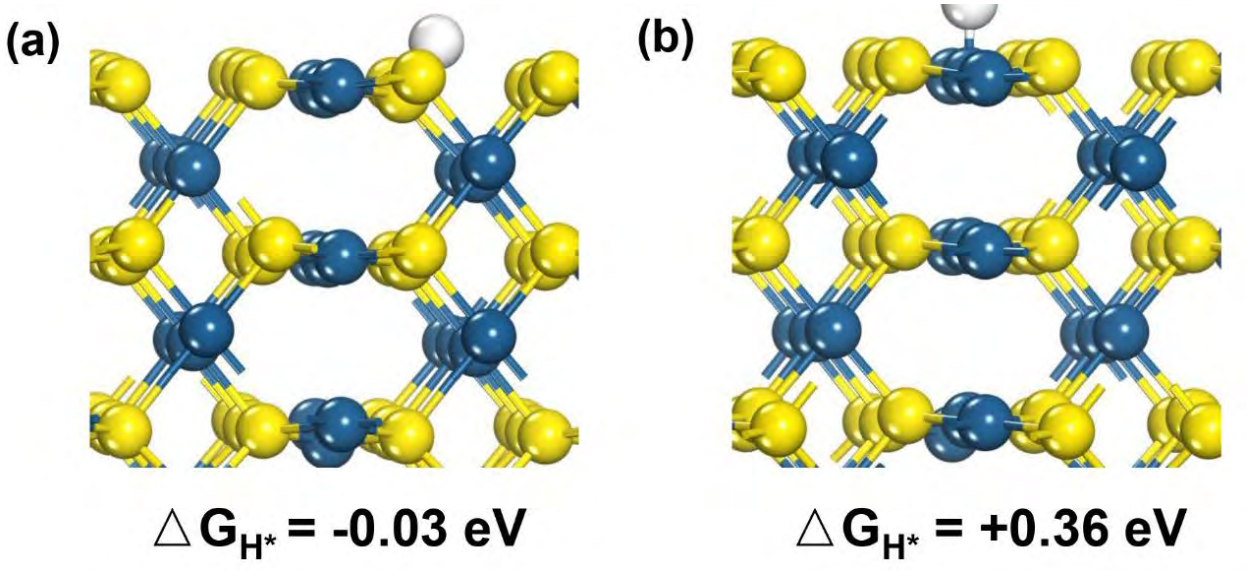

Figure 4.5. Adsorption configurations and energy of H* on (a) S site and (b) Pt site of PtS, respectively.

Interfacial charge transfer and orbitals interaction were studied to understand detailed N_2 activation process. Differential charge density (Figure 4.4b) reveals that distinct charge transfer occurs between PtS and adsorbed N_2, which weakens the inert N≡N triple bond and realizes effective N_2 activation. The density of states (DOS) intensity of PtS slab (Figure 4.4c) depicts state distribution around Fermi level, which represents rapid charge-transfer kinetic and high electron

conductivity of intrinsic PtS surface. According to the extracted Partial DOS (PDOS) of Pt *5d* orbitals (red line), the DOS at the Fermi level shows an obvious increase after the N_2 adsorption, implying that more charge carriers directly participate into the N_2 activation process. After adsorbing N_2 on PtS surface, the PDOS of N 2p is observed right below the Fermi level and overlaps with Pt *5d* orbitals (Figure 4.4d), which further reveals effective bonding between N_2 and Pt site, unveiling N_2 activation behavior on PtS surface.

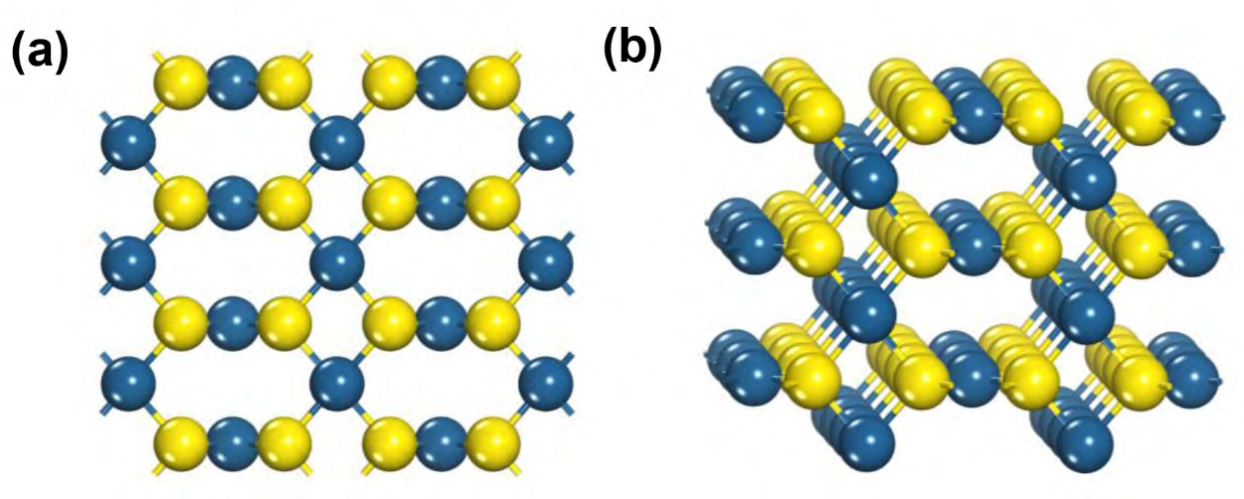

Figure 4.6. (a) Top-view and (b) side-view of PtS structure.

We also applied free energy profiles to predict possible NRR mechanisms on both PtS surface. Figure 4.6 shows the detailed structural information of optimized crystal slab. Specific calculation parameters, such as zero-point energies, entropy and Gibbs energy change, are documented in Table 4.2-Table 4.4. Figure 4.7a depicts the free energy profile and NRR intermediates adsorption configurations of distal NRR mechanism on PtS surface. As displayed in Figure 4.7a, the process of $*N_2 \rightarrow *NNH \rightarrow *NNH_2 \rightarrow *NNH_3$ on PtS surface is thermodynamically feasible. Negligible energy barrier is observed before the first NH_3 molecule formation. The potential determining step of distal mechanism on PtS surface is the desorption of $*NH_3$, requiring an energy barrier of +0.97 eV without external potential.

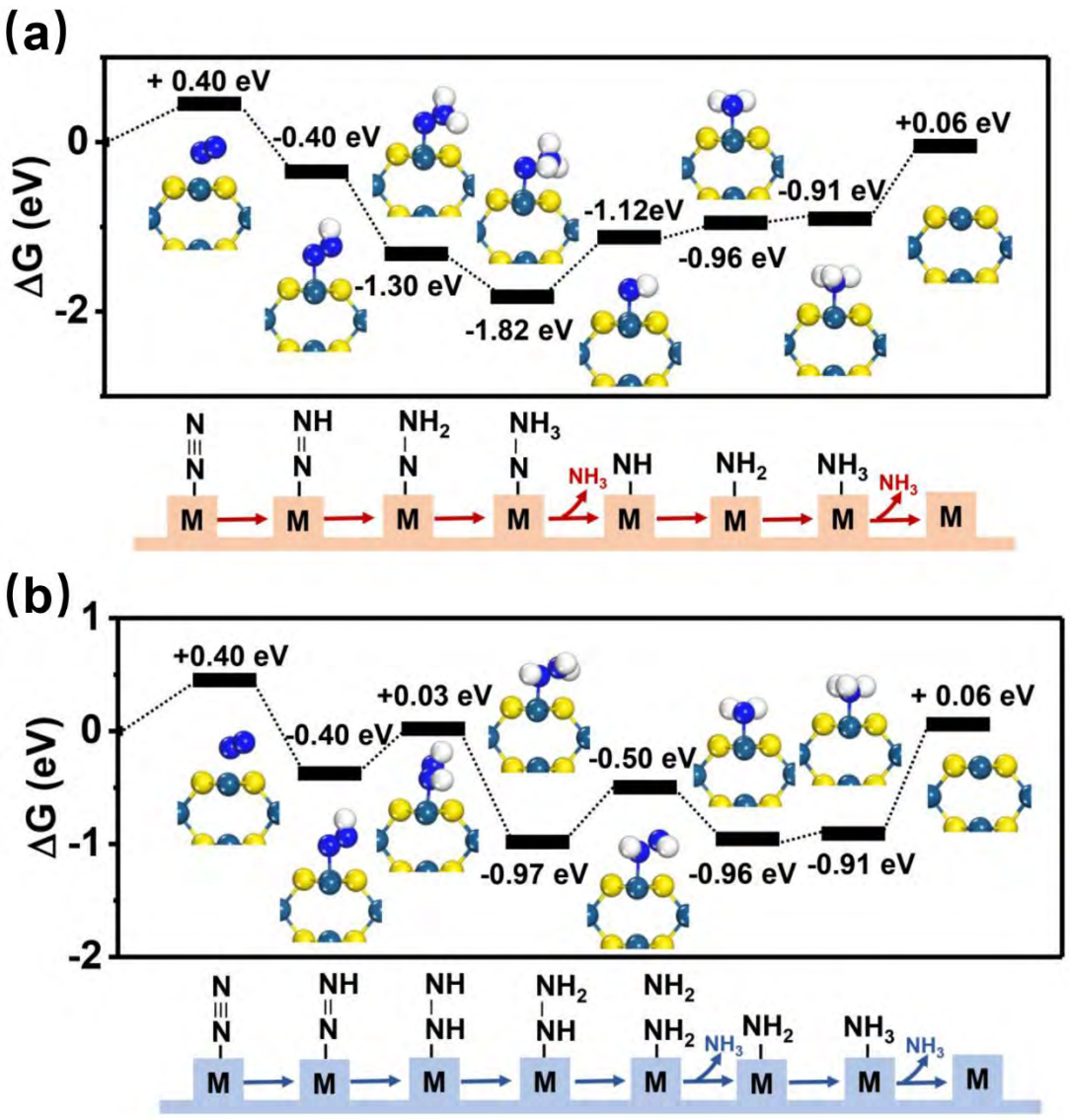

Figure 4.7. Free energy profiles of (a) distal and (b) alternating NRR mechanism on PtS surface, respectively. The produced intermediates during NRR process are corresponding to the schematic diagrams at the bottom of the figures.

In contrast, the distal mechanism on Pt surface (Figure 4.8) encounters with energy barriers of +0.46 eV for the initial N_2 activation, which may greatly hinder the subsequent hydrogenation process. The distal NRR pathway on Pt surface exhibits a potential determining step barrier of +1.56 eV, which reveals poor NH_3 desorption on Pt surface, going against the renewal of catalytic center. In addition, we investigated the alternating NRR mechanism on both PtS (Figure 4.7b) and

Pt (Figure 4.9) surfaces. PtS still shows much smaller free energy barrier to successfully convert N_2 into NH_3 molecule via alternating mechanism. The last step of NH_3 desorption is the potential determining step of alternating NRR mechanism on both PtS and Pt surface. According to these theoretical analyses, the PtS surface can reduce the energy barrier for N_2 reduction and selectively suppress the kinetics for hydrogen evolution, which is promising to realize robust NRR performance with high Faradaic efficiency.

Table 4.2. Calculated zero-point energies, entropy and Gibbs energy of different intermediates during N_2 reduction process.

	E_{ZPE} (eV)	TS (eV)	G (eV)
N_2	0.15	0.590	-13.86
H_2	0.29	0.400	-7.28
N_2H	0.34	0.001	-14.35
N_2H_2	0.70	0.054	-16.40
HNNH	0.72	0.001	-17.81
$HNNH_2$	1.04	0.012	-21.17
H_2NNH_2	1.39	0.005	-25.45
N_2H_3	1.01	0.012	-18.75
NH	0.20	0.001	-6.48
NH_2	0.53	0.040	-11.64
NH_3	0.91	0.001	-17.09

Table 4.3. Calculated zero-point energies, entropy and Gibbs energy change of adsorbed species on PtS.

	E_{ZPE} (eV)	TS (eV)	△G (eV)
PtS-NNH*	0.45	0.04	-0.37
PtS-NNH_2*	0.79	0.07	-1.30
PtS-NNH_3*	1.11	0.05	-1.82
PtS-HNNH*	0.76	0.03	0.03
PtS-$HNNH_2$*	1.14	0.06	-0.97
PtS-H_2NNH_2*	1.46	0.05	-0.50
PtS-NH*	0.31	0.03	-1.12
PtS-NH_2*	0.66	0.01	-0.96
PtS-NH_3*	0.99	0.04	-0.91

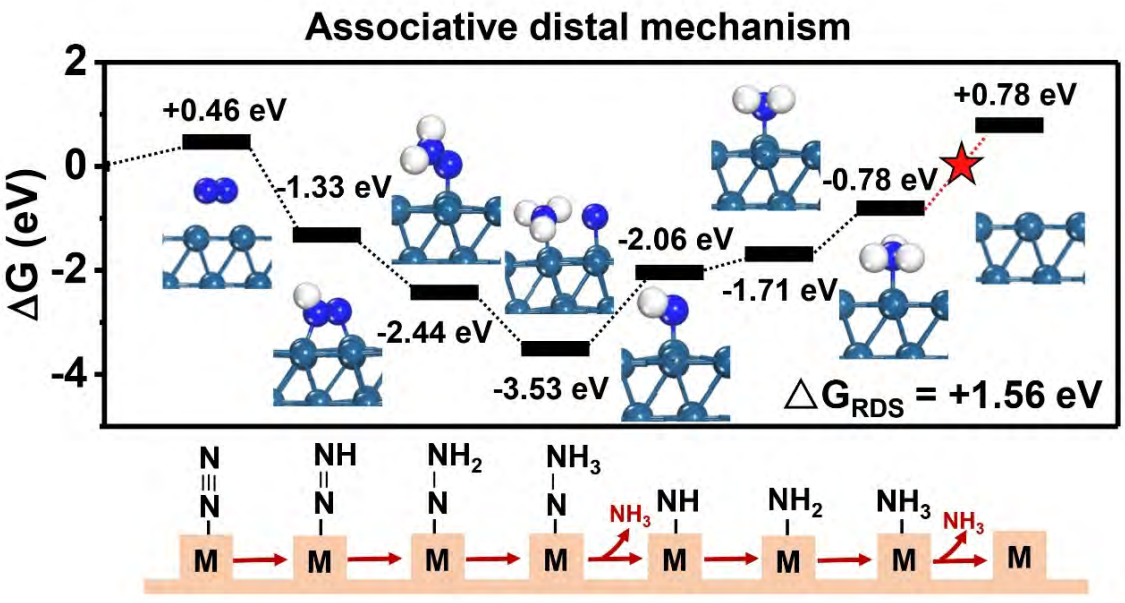

Figure 4.8. Schematic depiction of distal mechanism of NRR pathway on metallic Pt surface.

Table 4.4. Calculated zero-point energies, entropy and Gibbs energy change of different adsorption species on Pt surface.

	E_{ZPE} (eV)	TS (eV)	△G (eV)
Pt-NNH*	0.51	0.05	-1.33
Pt-NNH_2*	0.79	0.04	-2.44
Pt-NNH_3*	1.10	0.07	-3.53
Pt-HNNH*	0.83	0.06	-1.26
Pt-$HNNH_2$*	1.13	0.05	-1.43
Pt-H_2NNH_2*	1.50	0.06	-1.20
Pt-NH*	0.31	0.03	-2.06
Pt-NH_2*	0.66	0.04	-1.71
Pt-NH_3*	1.04	0.04	-0.78

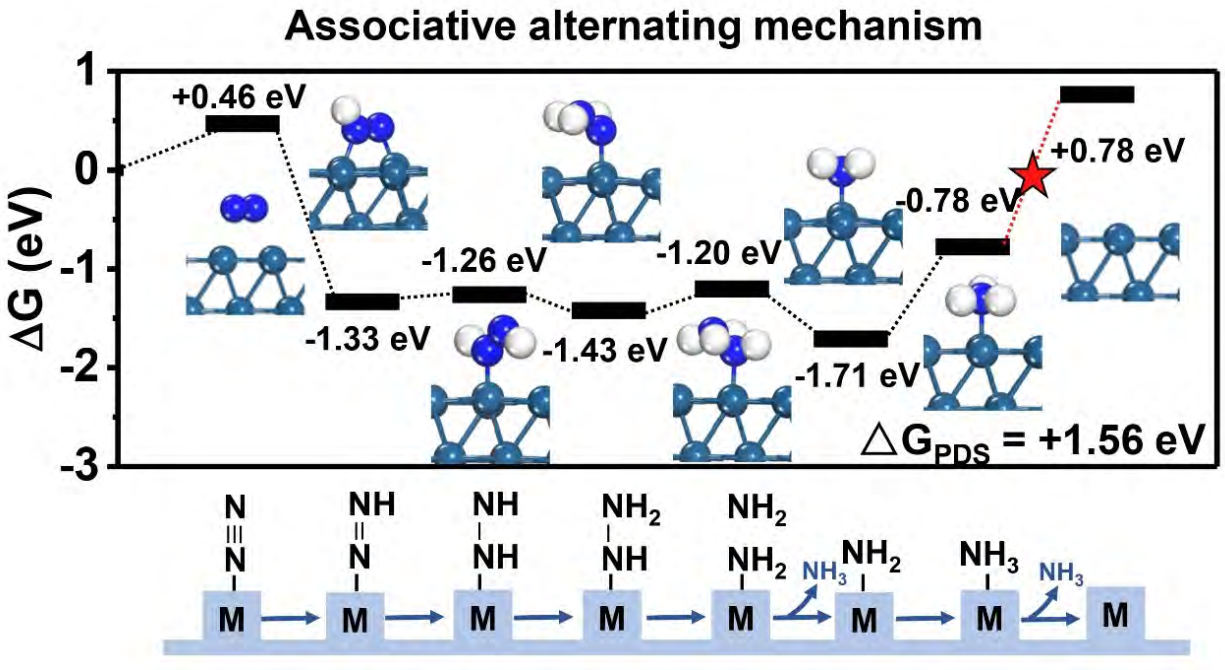

Figure 4.9. Schematic depiction of alternating mechanism of NRR pathway on Pt surface.

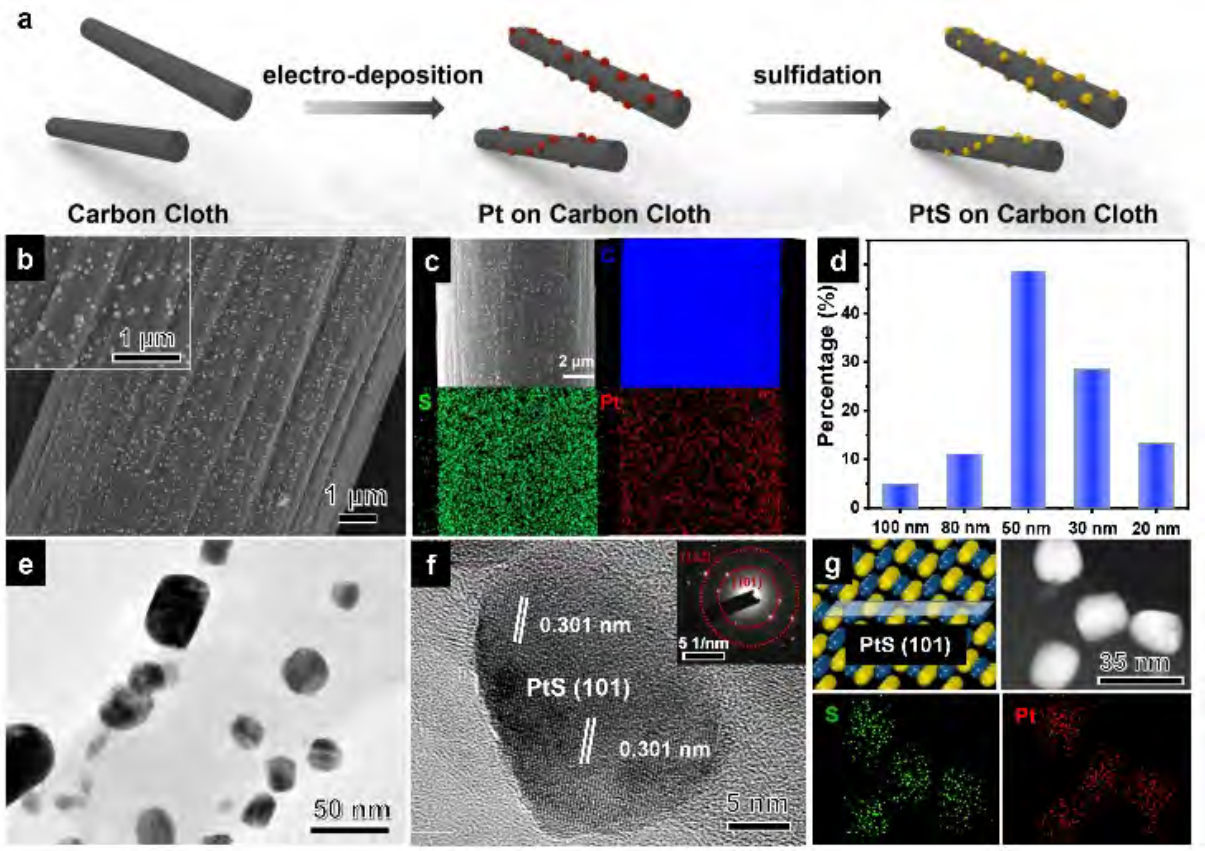

Figure 4.10. (a) Schematic of fabrication process of PtS nanoparticles on CC. (b) SEM images for PtS nanoparticles on CC. (c) EDS elemental mapping of the PtS/CC sample. (d) Particle size distribution of PtS nanoparticles on CC. (e) TEM and (f) HRTEM images of PtS nanoparticles. Insert in (f) is the corresponding Fast Fourier transformation (FFT) image. (g) HAADF-STEM image and corresponding EDX elemental mapping of S and Pt for PtS nanoparticles.

Inspired by above theoretical studies, we fabricated Pt nanoparticles on carbon cloth (CC) through the electrochemical deposition and a one-step sulfidation process (Figure 4.10a). It is noteworthy that each step throughout the fabrication process is nitrogen-free to exclude possible N contamination. The morphology characterizations (Figure 4.11) of the electrodeposition product (Pt/CC) manifests that the average diameter of Pt nanoparticles is approximately 40 nm, uniformly decorated on the surface of CC. The well-dispersed Pt nanoparticle on CC can effectively avoid the particle aggregation during catalytic process and maximize the Pt atomic utilization ratio for catalysis. After the sulfidation process, the highly dispersive morphology is well maintained

(Figure 4.10b). PtS nanoparticles are uniformly anchored on CC fibers (PtS/CC) (Figure 4.10c). The dominant particle diameter of PtS nanoparticles is approximately 50 nm (Figure 4.10d).

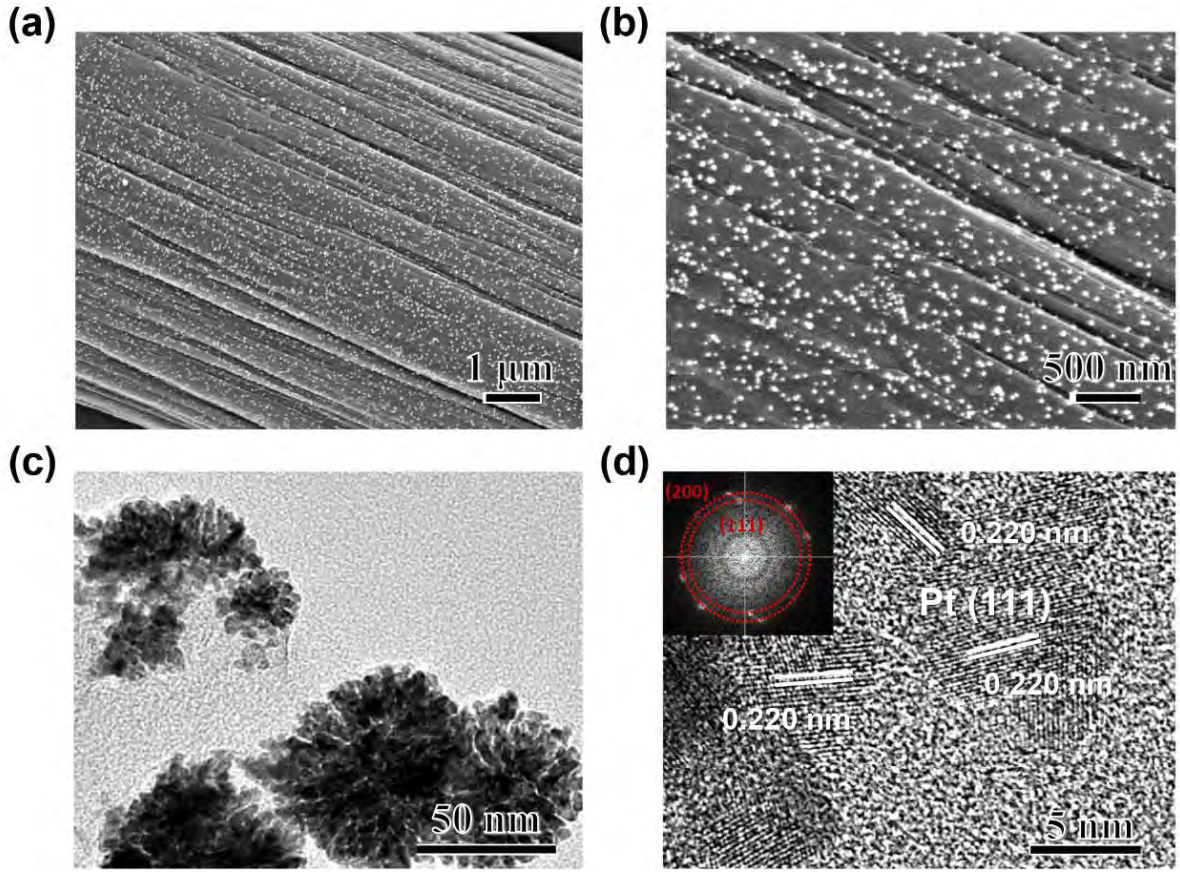

Figure 4.11. Morphological characterizations of Pt nanoparticles on carbon cloth. (a) and (b) SEM images of Pt/CC, (c) TEM and (d) HRTEM images of Pt particles, the inset in panel (d) is the corresponding SAED pattern.

Transmission electron microscopy (TEM) and high-resolution transmission electron microscopy (HRTEM) image (Figure 4.10e-10f) of the PtS nanoparticles show a lattice fringe with an interplanar spacing of 3.01 Å, corresponding to the (101) plane of PtS. The selected area electron diffraction (SAED) pattern of PtS also exhibits well-defined diffraction spots, which are well indexed to the (101) and (112) planes of PtS, respectively. Further scanning transmission electron microscopy (STEM) image and corresponding EDX mapping (Figure 4.10g) reveal that Pt and S elements are uniformly distributed throughout the whole PtS nanoparticles.

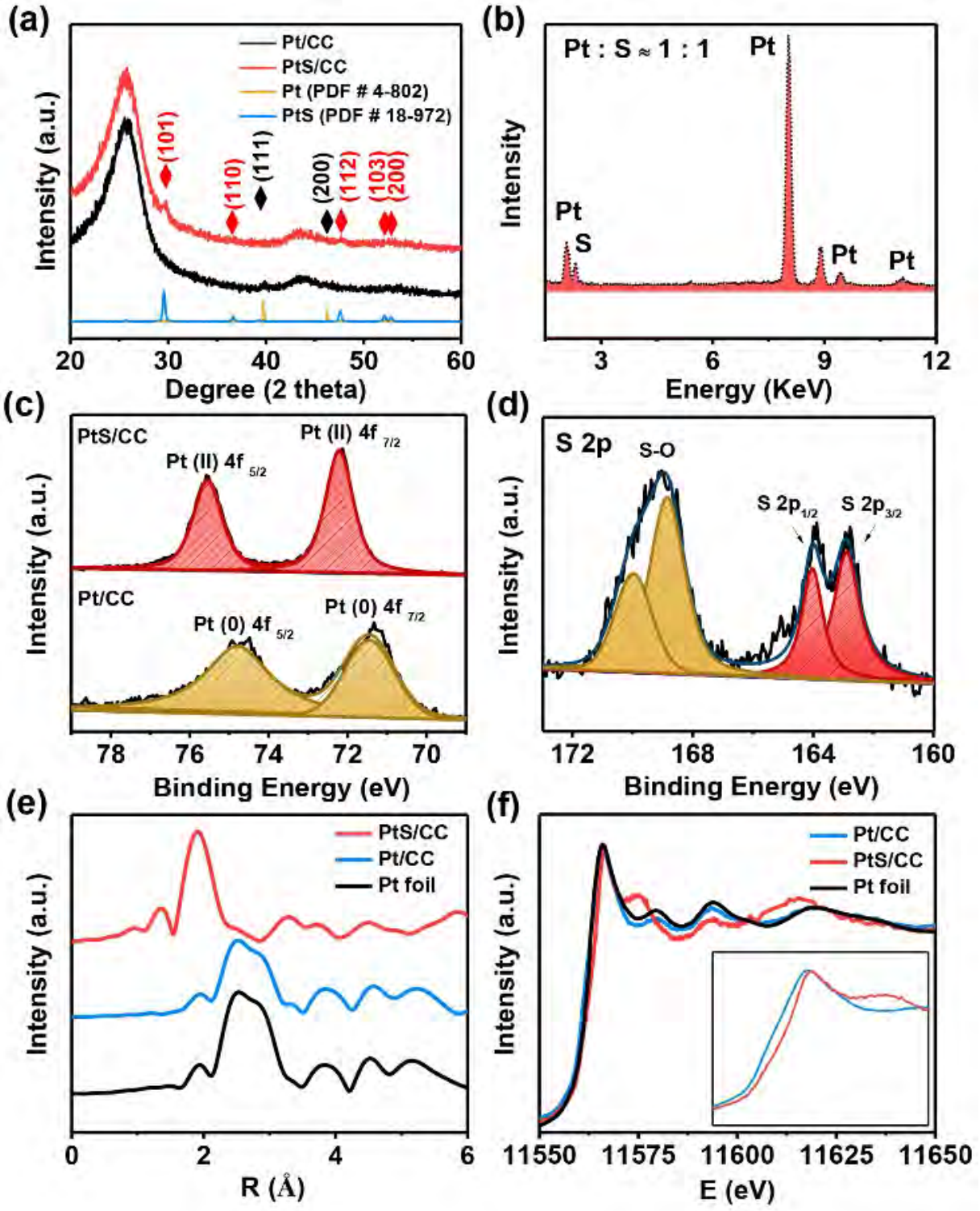

Figure 4.12. (a) XRD patterns of Pt/CC and PtS/CC, respectively. (b) EDX spectrum of PtS nanoparticles. High-resolution XPS spectrum of (c) Pt 4f and (d) S 2p spectra in Pt/CC and PtS/CC, respectively. (e) The normalized X-ray absorption near-edge structure spectra at the Pt L_3-edge and (f) k_3-weighted Fourier transform spectra from EXAFS of PtS/CC, Pt/CC and Pt foil.

X-ray diffraction (XRD), X-ray photoelectron spectroscopy (XPS) and energy-dispersive X-ray spectrum (EDX) were then applied to investigate the structures and compositions of as-prepared PtS/CC. The XRD peaks of Pt disappear in PtS/CC, suggesting that Pt nanoparticles is fully converted into PtS after the sulfidation process (Figure 4.12a). PtS/CC shows standard XRD peaks in 29.6°, 36.7° and 47.7°, corresponding to the standard (101), (110) and (112) facets of PtS (PDF # 18-972), respectively. EDX spectrum (Figure 4.12b) reveals that PtS nanoparticles possess an approximate atomic ratio of 1:1 (Pt:S). The XPS spectrum of Pt/CC and PtS/CC exhibit negligible signal of N 1s, excluding the possibility of N contamination during fabrication process (Figure 4.13 and Figure 4.14). As shown in Figure 4.12c, Pt species in Pt/CC is mainly composed by metallic Pt. The peaks at 71.5 eV and 74.9 eV are assigned to Pt (0) $4f_{7/2}$ and Pt (0) $4f_{5/2}$, respectively. After the sulfidation process, the characteristic XPS peaks of Pt (0) disappears. The dominated Pt (II) 4f peaks in PtS/CC sample locate at 72.2 eV and 75.6 eV, indicating that metallic Pt is fully converted into PtS.[170] The S 2p signal (Figure 4.12d) of PtS/CC is also clearly recorded, and the S-O peaks at 168.8 eV and 169.9 eV can be observed because of the long-time exposure to the air.

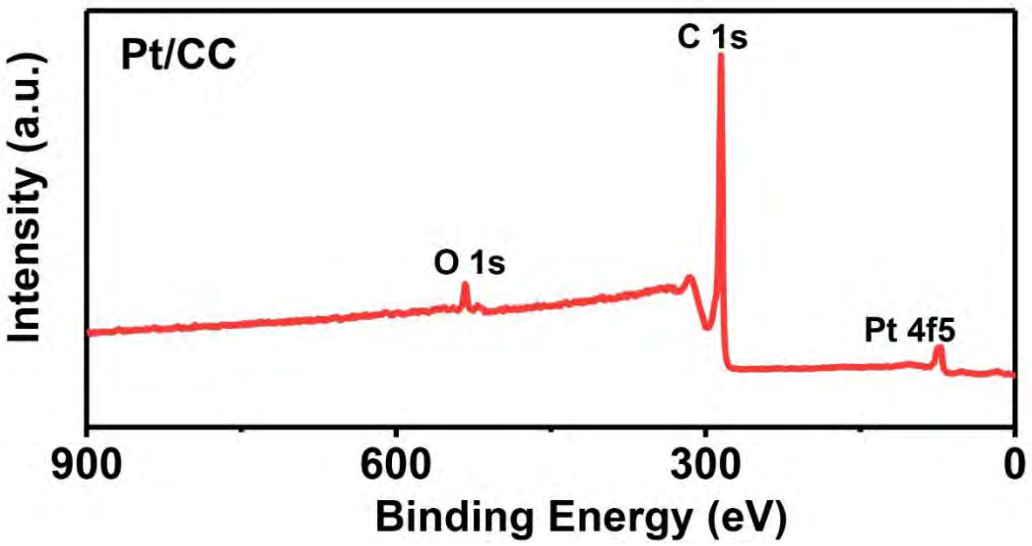

Figure 4.13. Survey spectrum of Pt nanoparticles on carbon cloth.

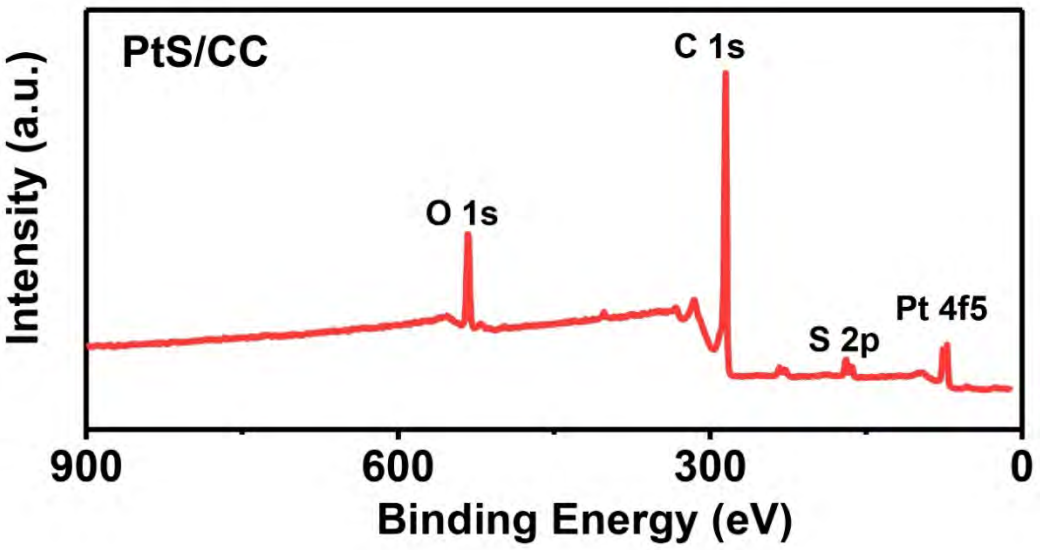

Figure 4.14. Survey spectrum of PtS nanoparticles on carbon cloth.

To further understand electronic and coordination structures of PtS nanoparticles, synchrotron radiation-based X-ray absorption fine structure (XAFS) spectroscopy of PtS were also conducted. Figure 4.12e shows the Pt L_3-edge X-ray absorption near-edge structure (XANES) profiles of PtS/CC, Pt/CC and Pt foil, respectively. Pt/CC exhibits similar white line with that of Pt foil, demonstrating the metallic Pt characteristics in Pt/CC. The white line of PtS/CC situates at more positive energy than that of Pt/CC, implying that Pt species in PtS/CC bears positive charges.[157] According to the Fourier transformed extended XAFS (EXAFS) spectra (Figure 4.12e), an apparent peak located in 1.5-2.5 Å is observed in PtS/CC, which is different from the typical peaks in Pt/CC and Pt foil (2.1-3.2 Å). For Pt/CC, the peak at 2.1-3.2 Å represents the scattering of neighboring Pt atom, agreeing well with the standard Pt foil. Besides, Pt/CC reveals a coordination number of about 9.6 and Pt-Pt bond length of 2.76 Å (Figure 4.15 & Table 4.5), which is consistent with the standard metallic Pt structure. In contrast to Pt/CC, negligible contribution from Pt-Pt is observed in PtS/CC. The peak at 1.5-2.5 Å derives from the scattering of the nearest sulfur atoms, revealing Pt atoms in PtS are chemical bonding with nearby S atoms.[171]

Besides, EXAFS fitting is also performed to further obtain the structure information of PtS/CC (Figure 4.15b). The Pt-S bond length is about 2.31 Å, and Pt species shows a coordination number of 3.1, suggesting the Pt species in PtS/CC is PtS phase (Table 4.5).

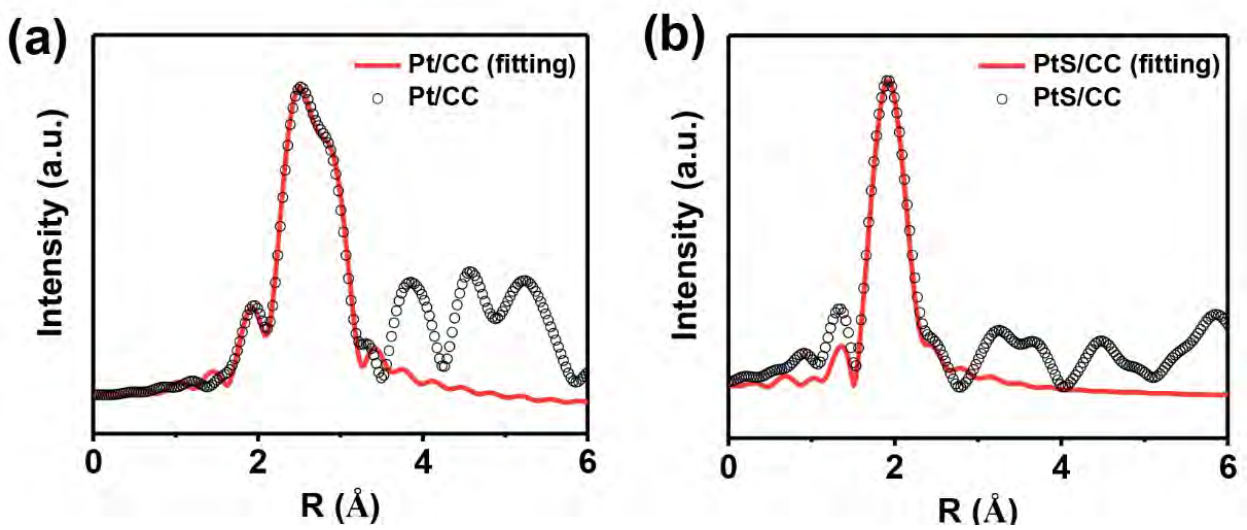

Figure 4.15**.** EXAFS fitting of Pt/CC and PtS/CC, respectively.

Table 4.5. Pt L_3-edge EXAFS fitting results of Pt/CC and PtS/CC.

	Bond	**R (Å)**	**N**	**σ^2 ($10^{-3}A^2$)**	**△E (eV)**
Pt/CC	Pt-Pt	2.76±0.01	9.6±0.7	5.5±0.5	9.9±0.5
PtS/CC	Pt-S	2.31±0.01	3.1±0.3	1.1±1.0	7.1±1.3

N, coordination number; R, the length of Pt-Pt and Pt-S bonds; σ^2, the Debye-Waller factor value; △E, inner potential correction.

We firstly performed Linear Sweep Voltammetry (LSV) in 0.1 M Na_2SO_4 solution to evaluate the hydrogen evolution performance of PtS/CC and Pt/CC, respectively. As shown in Figure 4.16, the PtS/CC requires a higher onset potential for H_2 evolution (approximately 440 mV vs. RHE) compared with Pt/CC (approximately 250 mV vs. RHE). The Tafel slope of PtS/CC

(31.4 mV/dec) is also much larger than that of Pt/CC (21.3 mV/dec), implying a sluggish HER kinetics and suppressed HER performance. NRR experiments were then performed in a compartment cell separated by Nafion membrane. N_2-saturated 0.1 M Na_2SO_4 was used as electrolyte. Figure 4.17a and Figure 4.18 show the LSV curves of PtS/CC and Pt/CC in Ar and N_2-saturated 0.1 M Na_2SO_4 solution, respectively. Different from the Pt/CC, it is clearly observed that PtS/CC exhibits a higher current density in the voltage range from 0.10 V to -0.6 V in N_2-saturated solution, indicating it is active for electrocatalytic N_2 reduction under a small overpotential of 48 mV. Small overpotential for NRR reaction can effectively prevent fierce hydrogen evolution and ultimately improve the NRR Faradaic efficiency.

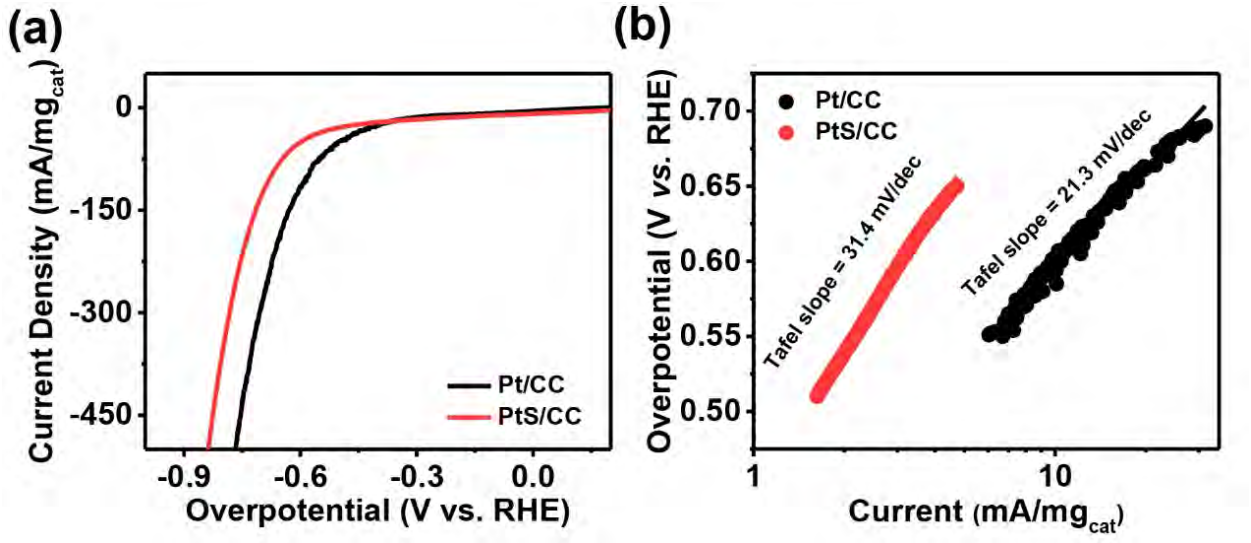

Figure 4.16. Electrochemical hydrogen evolution performance of Pt/CC and PtS/CC. Polarization curves (a) and (b) corresponding Tafel plots of Pt/CC and PtS/CC in 0.1 M Na_2SO_4 solution.

The produced NH_3 was then detected by indophenol blue method.[38, 45] Figure 4.19 shows the calibration curve. It is clearly observed that PtS/CC exhibits larger NH_3 production rate than that of Pt/CC at all applied potentials (Figure 4.17b). The NH_3 production rate of PtS/CC at 0 V vs. RHE reaches the highest value of 74 μg/ mg_{cat}·h, which is approximately 6 times than that of Pt/CC. In addition, the Faradaic efficiency of PtS/CC for NH_3 production is higher than that of

Pt/CC at all applied potentials (Figure 4.17c). Remarkably, PtS/CC shows a Faradaic efficiency of NH_3 production up to about 10% at 0.1 V vs. RHE, showing 5 times higher than that of Pt/CC. The productions of hydrazine are below the detection limit, indicating the high selectivity for NH_3 on PtS/CC surface (Figure 4.20-Figure 4.21). Therefore, PtS/CC exhibits superior NRR performance in 0.1 M Na_2SO_4 at room temperature, which should be attributed to the effects of prompted NRR kinetics and suppressed HER performance.

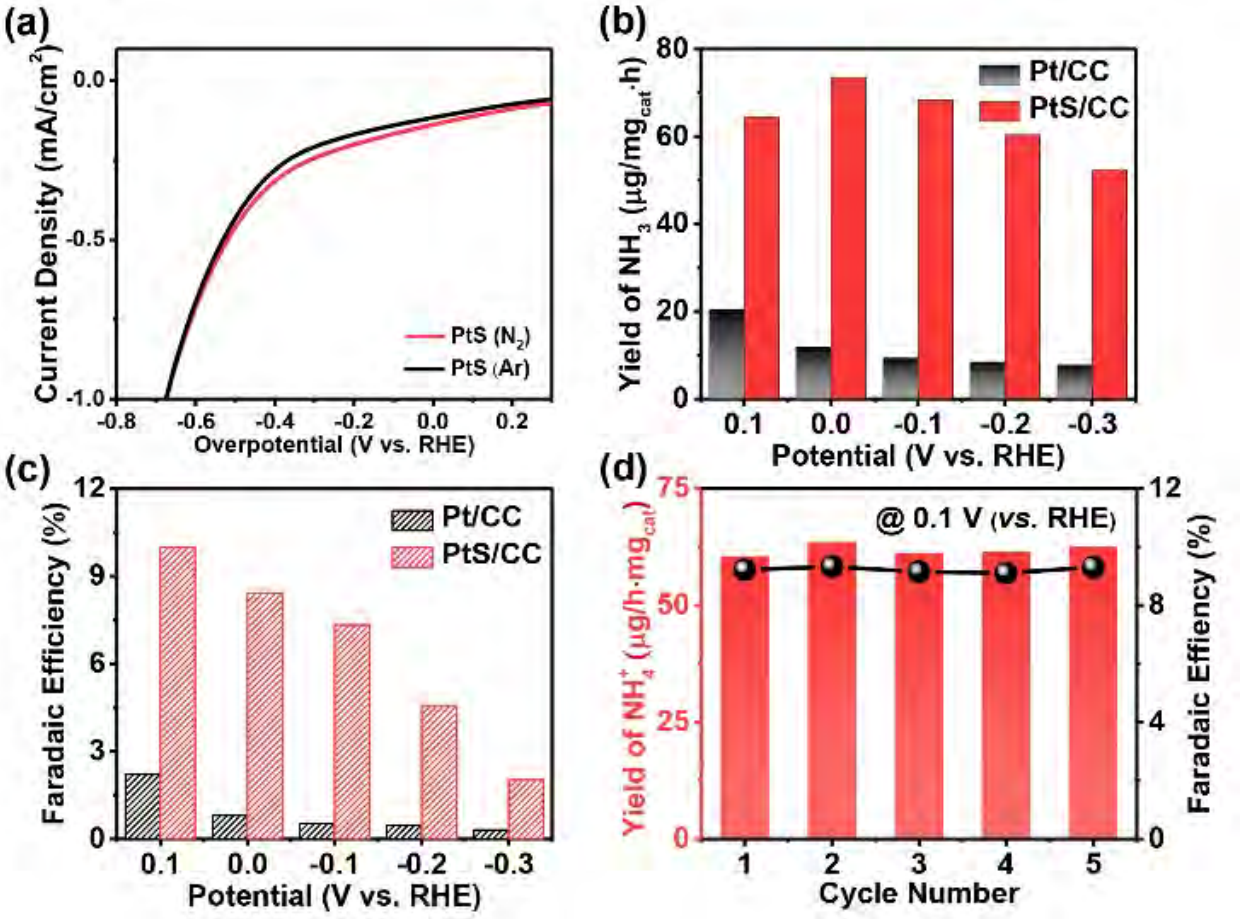

Figure 4.17. NRR performance of PtS/CC sample. (a) LSV curves of PtS/CC in Ar-saturated and N_2-saturated 0.1 M Na_2SO4 solution, respectively. (b) NH_4^+ yield rate and (c) Faradaic efficiency of both Pt/CC and PtS/CC at various potentials. (d) Cycling stability of PtS/CC at 0.1 V (vs. RHE).

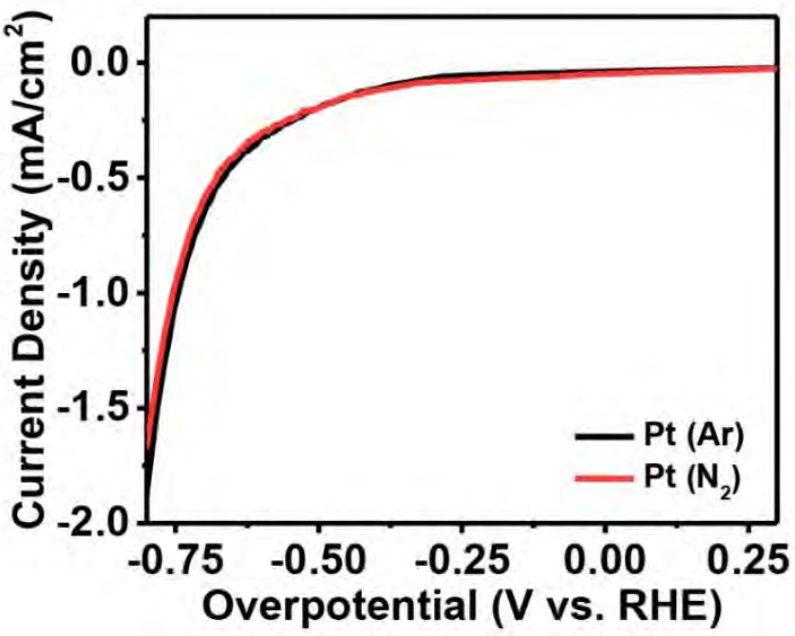

Figure 4.18. LSV curves of Pt/CC in Ar-saturated and N_2-saturated 0.1 M Na_2SO_4 solution, respectively.

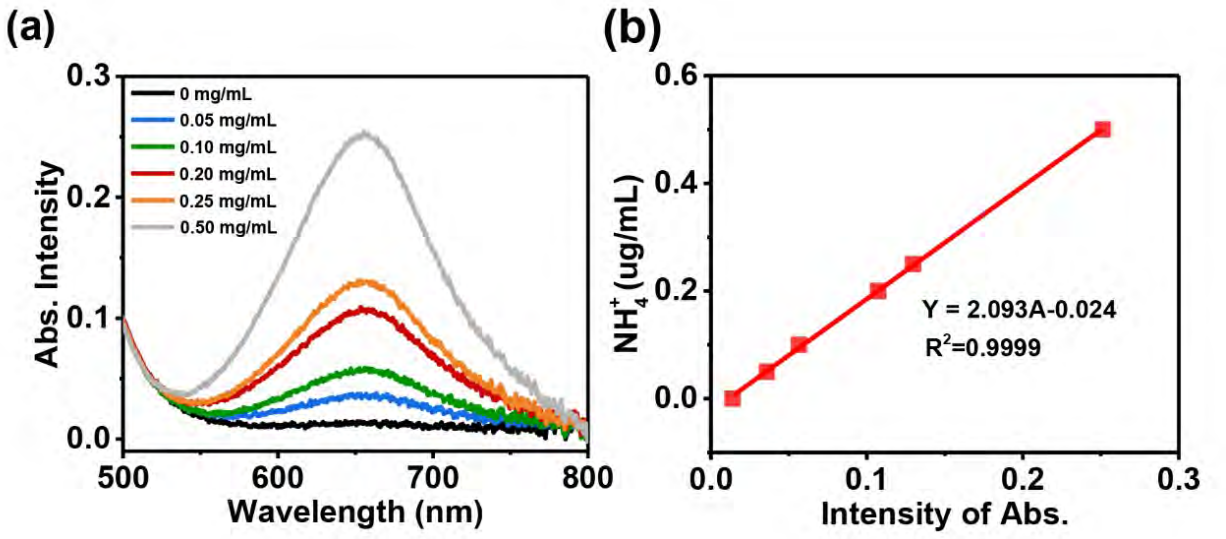

Figure 4.19. (a) UV-vis absorption spectra of various NH_4^+ ion concentration after incubated for 90 min at room temperature. (b) Calibration curve used for NH_4^+ ion production calculation.

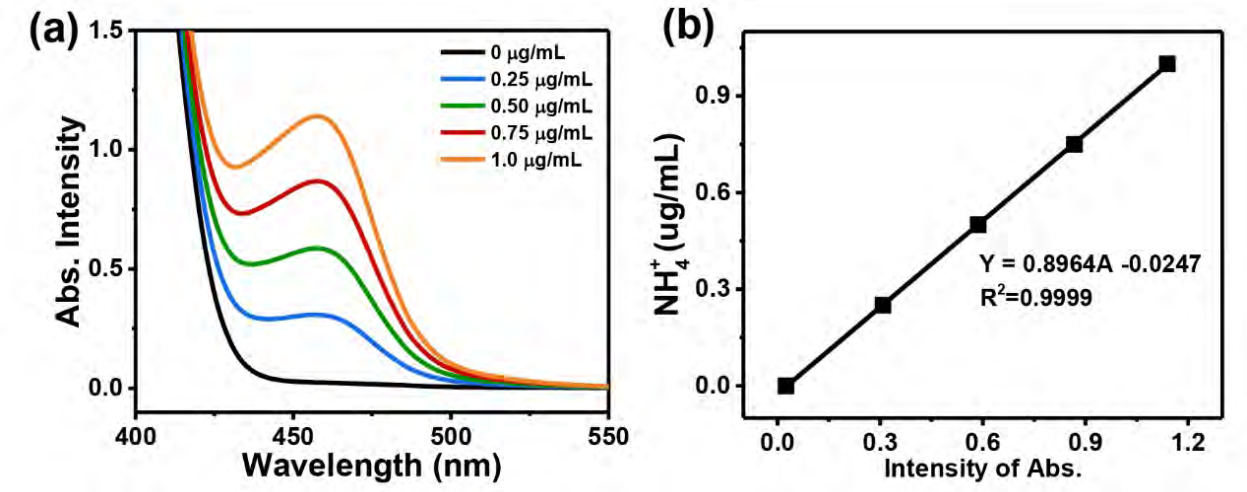

Figure 4.20. (a) UV-vis absorption spectra of various N_2H_4 concentration at room temperature. (b) Calibration curve used for N_2H_4 production calculation.

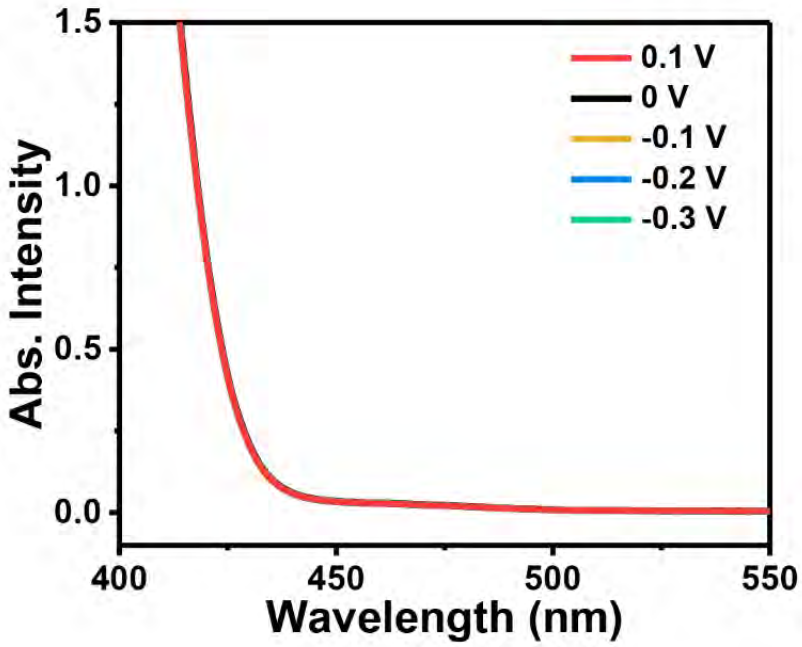

Figure 4.21. UV-visible absorption spectra of the 0.1 M Na_2SO_4 electrolytes after electrolysis at various potentials for 2 hours with PtS/CC.

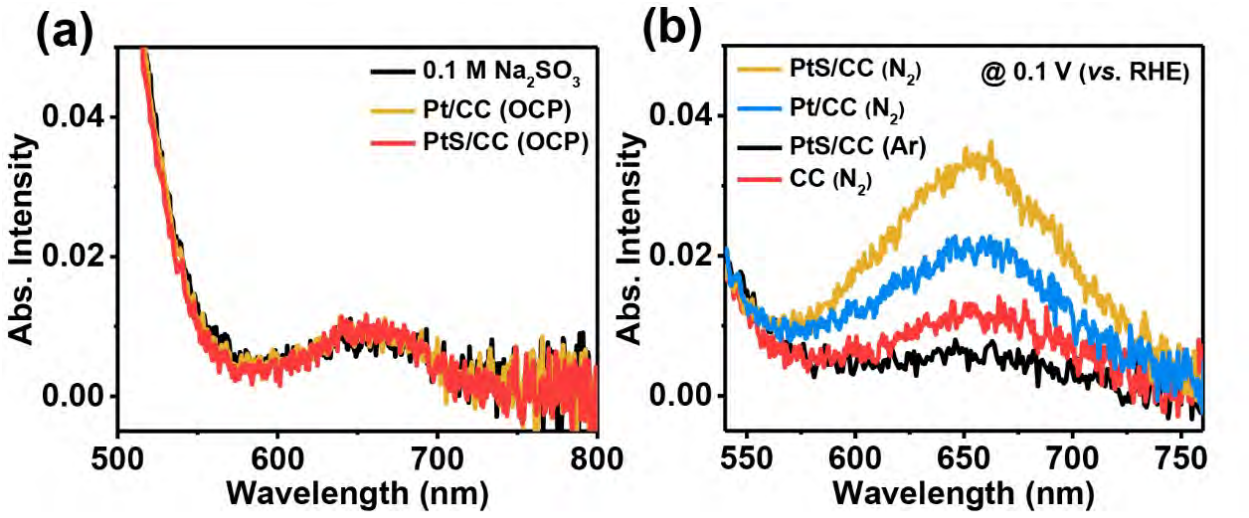

Figure 4.22. (a) UV-visible absorption spectra of the 0.1 M Na_2SO_4 electrolytes before and after electrolysis at open circuit potential (OCP) for 1 hour with PtS/CC and Pt/CC. (b) UV-visible absorption spectra of the 0.1 M Na_2SO_4 electrolytes after electrolysis at 0.1 V for 1 hour with PtS/CC in N_2 and Ar-saturated electrolyte, with Pt/CC in N_2-saturated electrolyte, and with CC in N_2-saturated electrolyte, respectively.

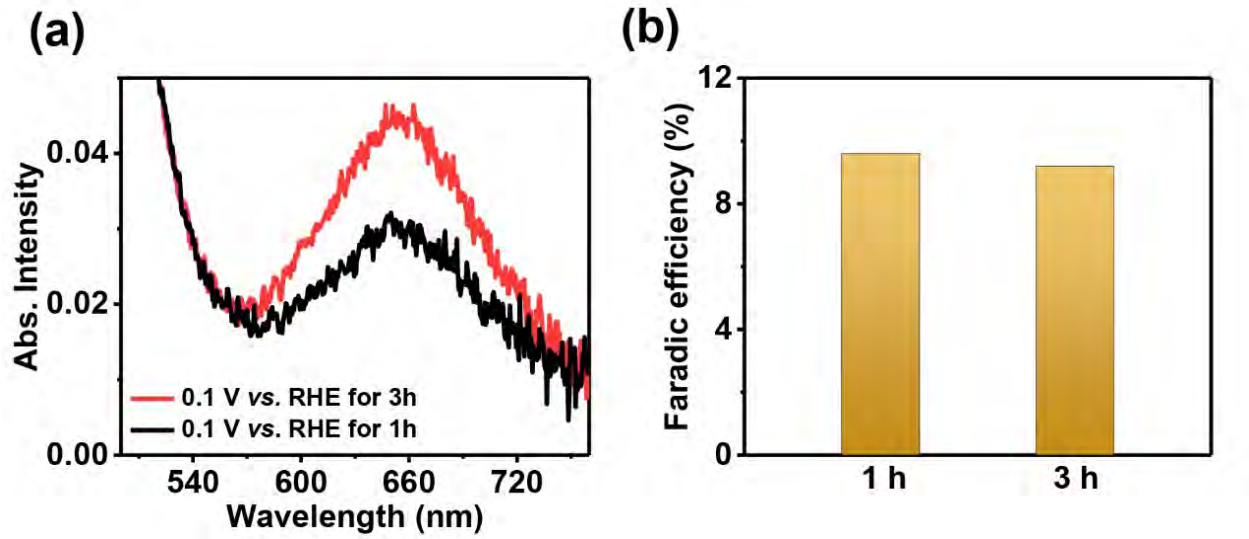

Figure 4.23. (a) UV-visible absorption spectra and (b) Faradic efficiency of the 0.1 M Na_2SO_4 electrolytes after electrolysis at 0.1 V for 1 hour and 3 hours with PtS/CC in N_2-saturated electrolyte.

To verify that the produced NH_3 originates from the electrochemical N_2 reduction process, we conducted a series of control experiments. First, negligible NH_3 are detected with PtS/CC and Pt/CC electrodes at open circuit potential, suggesting that the NH_3 is generated from the

electrochemical reduction reaction (Figure 4.22a). Second, no apparent NH_3 is detected in N_2-saturated 0.1 M Na_2SO_4 electrolyte (Figure 4.22b) when bare CC is applied as the cathode, which eliminates the contribution of substrate to nitrogen production. Third, no NH_3 is examined after replacing the electrolyte with Ar-saturated 0.1 M Na_2SO_4, further confirming that the generated NH_3 is the product of electrochemical NRR process.

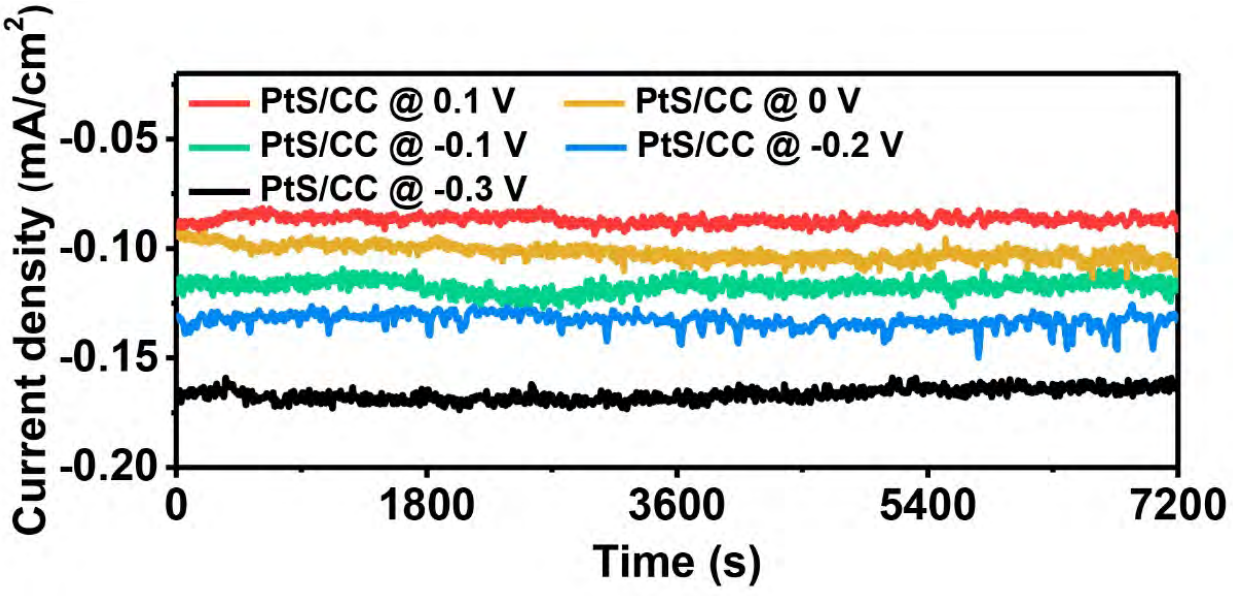

Figure 4.24. Time-dependent current density curves of PtS/CC at various potentials.

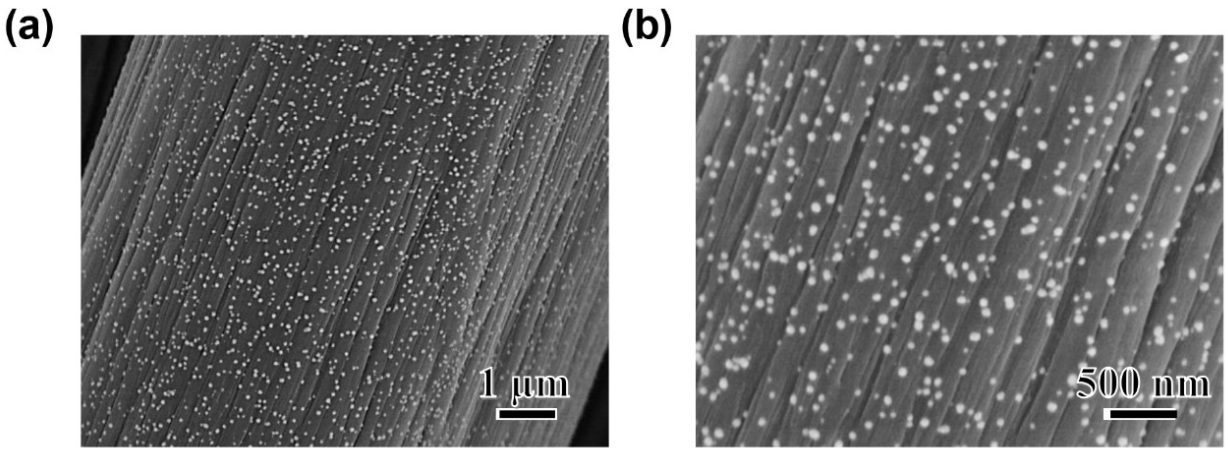

Figure 4.25. SEM images of PtS/CC after NRR stability test.

The stability of PtS/CC was evaluated by prolonging the NRR reaction time and successive recycling electrolysis at 0.1 V vs. RHE. According to the UV-visible absorption spectra (Figure 4.23a), the yield of NH_3 shows an upward trend with the prolonged electrolysis time, indicating the accumulation of NH_3 lies in the electrocatalytic NRR reaction. Additionally, the Faradaic efficiency of PtS/CC shows negligible change with the reaction time (Figure 4.23b), implying that the NRR reaction rate of PtS/CC can keep constant with the prolonged time. According to the recycling tests (Figure 4.17d), insignificant decline of the NH_3 yield rate is observed during successive 5 times recycling test. The Faradaic efficiency of PtS/CC can still maintain at approximately 10% during the recycling test at the applied potential of 0.1 vs. RHE.

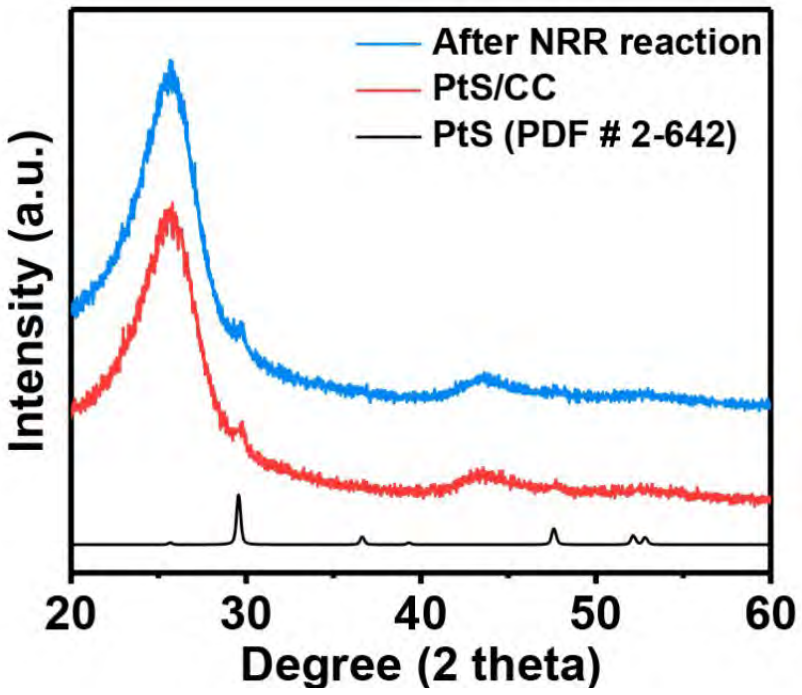

Figure 4.26. XRD patterns of PtS/CC before and after long-time NRR reaction.

The time-dependent current density curves of PtS/CC at different applied potentials further confirm the excellent stability, because we can observe negligible current density drop (Figure 4.24). The post-reaction characterization also confirms the stability of electrocatalyst. PtS/CC nanoparticles are still uniformly anchored on the CC after long-time electrolysis (Figure 4.25),

retaining the well-dispersed morphology. The XRD pattern of PtS/CC after the stability test also matches well with the standard PtS, indicating the excellent structure stability of PtS (Figure 4.26). XPS analysis on PtS/CC after the electrolysis (Figure 4.27 & Figure 4.28) further indicates the catalyst after electrolysis is still PtS/CC.

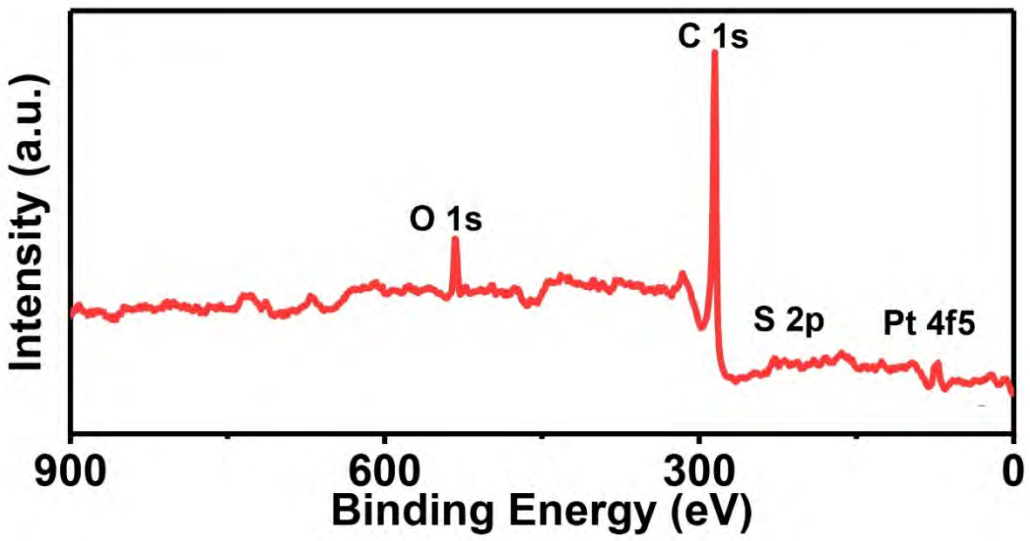

Figure 4.27. Survey spectrum of PtS/CC after long-time NRR reaction.

Furthermore, we measured the impedance of as-prepared electrodes to investigate the reaction kinetics. Although PtS/CC reveals slightly increased charge resistance (R_c) than Pt/CC (Figure 4.29), PtS/CC still shows excellent electrical conductivity, which implies good contact between active materials (PtS nanoparticles) and current collector (CC substrate). The electrochemical active surface area (EASA) of Pt/CC and PtS/CC were calculated based on the electrochemical double layer capacitance (Figure 4.30a-30b). As depicted in Figure 4.30c, the EASA of PtS/CC shows a dramatic increase when compared with its counterparts, showing a value of about 6 times as large as that of Pt/CC. The improved EASA reveals that more exposed active sites on PtS/CC can participate in the H* production and facilitate the hydrogenation kinetics during NRR process. Thus, the good electrical conductivity and increased active sites may facilitate the NRR kinetics of PtS/CC.

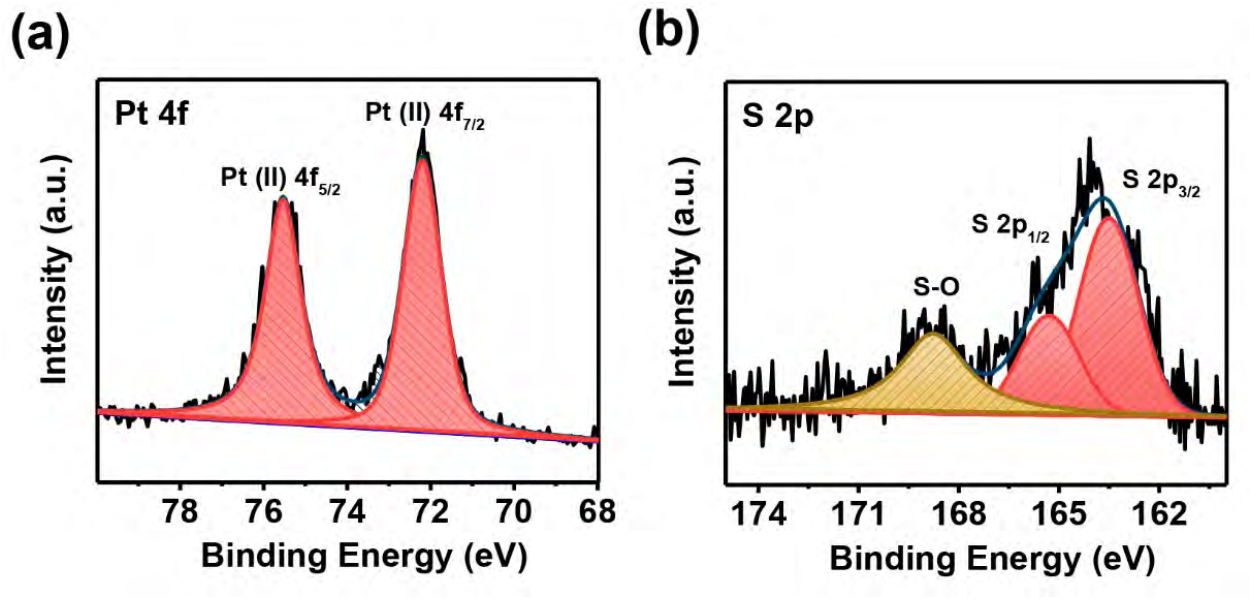

Figure 4.28. Detailed XPS analysis of PtS/CC after long-time NRR test. High-resolution XPS spectrum of (a) Pt 4f and (b) S 2p.

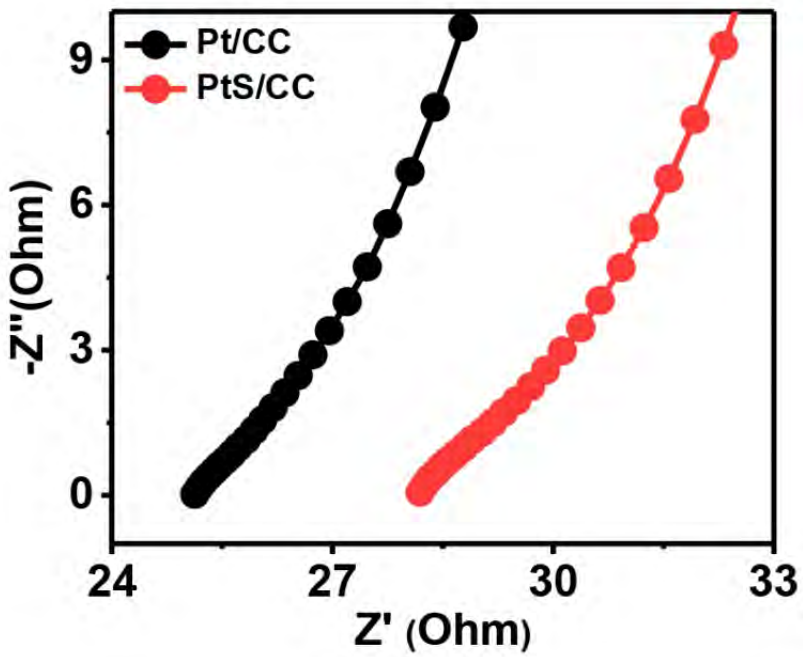

Figure 4.29. Nyquist plots of PtS/CC and Pt/CC.

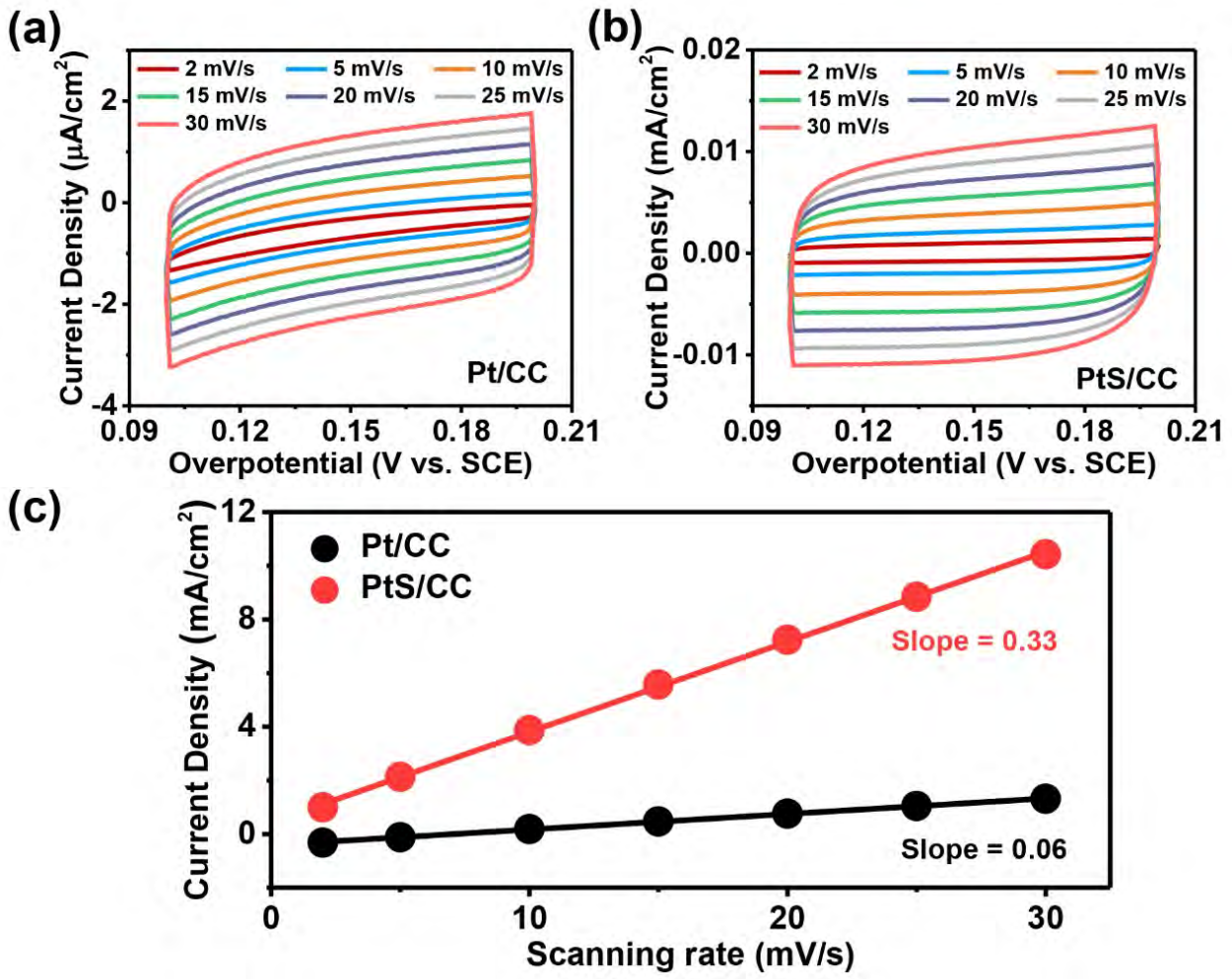

Figure 4.30**.** Electrochemical capacitance measurements for the comparison of the relative electrochemical active surface area of Pt/CC and PtS/CC. Cyclic voltammograms of (a) Pt/CC and (b) PtS/CC in the region of 0.1-0.2 V vs SCE. (c) The differences in current density at 0.15 V plotted as a function of scan rate, the slopes represent the electrochemical active surface area.

4.5 Conclusion

In summary, we demonstrate that sulfurized Pt nanoparticles plays a pivotal role in effective activation of N_2 and suppression of undesirable HER for improved electrochemical NRR efficiency. Our theoretical studies reveal that alleviated barrier for N_2 activation and thermodynamically feasible hydrogenation process can promote the conversion of N_2 to NH_3 on PtS surface. In addition, strong binding strength for H* on PtS surface indicates suppressed HER

kinetics. To confirm the theoretical predictions, we fabricated PtS nanoparticles on CC, and evaluate the NRR performance in 0.1 M Na_2SO_4. As expected, PtS/CC exhibits accelerated NH_3 yield rate and enhanced Faradaic efficiency, as well as excellent NRR durability. PtS/CC realizes a NH_3 yield rate of 74 μg/ mg_{cat}·h at 0 V versus RHE and Faradaic efficiency of about 10 % at 0.1 V versus RHE, respectively, which manifests a remarkable NRR performance in noble metal-based materials. This work provides a guideline to optimize the NRR performance of Pt-based materials and paves a new avenue to broaden the application of noble metals toward N_2 electrochemical reduction.

5 Computational Design of Transition Metal Single Atom Electrocatalysts on PtS_2 for Efficient Nitrogen Reduction

5.1 Objective and Motivation

Electrocatalytic nitrogen-to-ammonia fixation is accepted as a sustainable and environmentally friendly strategy to replace Haber-Bosch process for ammonia production. Single atom electrocatalysts hold great promise to convert N_2 into NH_3 due to its molecular catalysis property and ultrahigh atomic utilization ratio. Here, we propose a universal design principle to assess the performance of single atom electrocatalysts supported on PtS_2 substrate towards the N_2 reduction reaction. Our results demonstrate Ru single atom on PtS_2 exhibits the best NRR performance with a reduced barrier of potential limiting step, which is much smaller than the benchmark of the Ru (0001). In addition, our results demonstrate that the various barriers of limiting potential is linear correlated to the binding strength of N* ($\triangle E_{N*}$). More importantly, the $\triangle E_{N*}$ is proved to be related to the integral of the density of unoccupied *d* orbital states of the single atom center. This work proposes an intermediate parameter ($\triangle E_{N*}$) to bridge the NRR performance and intrinsic electronic structure of single atom center, which may offer effective guidance to design and screen durable and efficient single-atom electrocatalysts for NRR reaction.

5.2 Introduction

Nitrogen reduction reaction (NRR) plays a crucial role in social development, involving many aspects of modern life, such as agricultural production, chemical synthesis and biological medicine field.[41, 148, 172-174] Haber-Bosch process, as one of the most important artificial NRR processes, convert hydrogen and nitrogen to ammonia (NH_3) under high temperatures and pressures, which consumes about 1-2% of the energy supply in the whole world. Moreover, massive CO_2 emission

during Haber-Bosch process also aggravate the climate warming and other environmental problems.[44] Recently, NH_3 production driven by electricity has spurred intensive interest, because the electrochemical nitrogen reduction reaction (eNRR) process is environmentally friendly and can perform at ambient conditions.[38, 40, 146, 154, 175-176] Inspired from the MoFe-cofactor in nitrogenous, most of efficient eNRR catalysts based on transition metals (TMs) have been designed to activate inert N≡N triple bond for efficient NRR process.[177-178] However, high overpotential and unsatisfied Faradaic efficiency still hinder the eNRR development due to the high barrier for potential limiting step (PDS) and fierce competing hydrogen evolution reaction (HER).[179] Moreover, the inner mechanism that bridges the overpotential of eNRR and intrinsic property of TM center is still vague, which limits the further development of electrocatalyst for NRR reaction. Thus, it' of great significance to establish relevant theoretical cognition to give guidance for eNRR catalyst screening and modification.

Since the role of active MoFe-cofactor in biological nitrogen fixation was unveiled, functional analogues of nitrogenase based on TMs have been designed by coordinating the active mental with different ligands.[180-182] Different from the metal site in metallic state, biomimetic metal center shows properties of molecular catalysts, its unique localized electron density and surface coordination configuration are proved to be beneficial for dinitrogen reduction.[56, 183] However, majority of molecular catalysis occurs in homogeneous environment, which is not applicable in eNRR process. Recently, the emergence of single-atom catalysts (SACs) provide a platform to develop heterogeneous eNRR electrocatalysts with molecular catalysis properties.[53, 184] In SACs, the single metal center is coordinated by ligands or substrates, sharing similar structure with molecular catalysts. Besides, compared with conventional TM-based eNNR catalysts, SACs can greatly improve the atomic utilization ratio and enhance the NRR efficiency. More importantly,

SACs can act as excellent model to reveal the relationship between active metal center and overpotential of eNRR process, which is advantageous to design novel heterogeneous eNRR candidates.

So far, many theoretical studies have reported computational screening of eNRR electrocatalysts by anchoring different SACs on one specific support and selecting the most promising one with the lowest overpotential.[56, 185] For example, single Mo atom supported on defective boron nitride exhibits superior NRR performance with a very low overpotential of 0.19 V at room temperature.[152] On single W atom embedded on g-C_3N_4, N_2 molecular follows the associative enzymatic pathway and successfully convert into NH_3 with a limiting potential of −0.35 V.[55] However, rare computational work establishes the bridge between intrinsic activity of SACs and required overpotential during eNRR process. Lacking proper descriptor to describe the determining factor of NRR brings about a lot of confusion to screen the NRR candidates. In addition, the effect of supports on theoretical NRR performance of SACs is also important, as the substrate have a direct influence on the electron distribution of SACs, and the binding strength between substrate and SACs indicates the stability of eNRR catalyst.

In this work, we applied computational method to assess to theoretical NRR performance of SACs supported on PtS_2 by considering four key aspects: stability of catalysts, selectivity of HER/NRR, overpotential for NRR and electronic origins. Among various transition metal disulfide, PtS_2 was introduced as the SACs supports to construct different metal centers due to the localized charges on the surface. stability of catalysts. The formation energy of SACs-PtS_2 was first calculated to eliminate the inappropriate models with poor stability. Then, we investigated the selectivity between HER competing reaction and NRR reaction by comparing the H* and N_2 affinity of SACs-PtS_2 surface. Besides, we simulated the NRR reaction pathway on selected SACs-

PtS_2 and discovered the PDS of SACs-PtS_2 is the first protonation process. The intrinsic activity trends in terms of the barrier of PDS proved to be linear correlated to the binding strength of nitrogen atom (ΔE_{N*}). More importantly, according to relative electronic structure investigation, the variation of ΔE_{N*} on different SACs is strongly dependent on the unoccupied *d* orbitals. The integral of density of unoccupied *d* orbitals states shows a linier relationship with binding strength of N*, offering a juncture to bridge the NRR activity and intrinsic electronic structure of SACs. Based on above analysis, we propose rational strategy to design SACs supported on PtS_2 by comparing the selectivity of HER/NRR and engineering the binding strength of N* to reduce the barrier of PDS.

5.3 Experimental Section

Structure relaxation and electronic energy calculations were performed using spin-polarized density functional theory (DFT) as implemented in the VASP code (5.4.3) with exchange-correlation energy functional, which were modeled by Perdew-Burke-Ernzerhof (PBE) functional. We used the vdW2 correlation (vdW-DF2) to account for Van der Walls interactions. The cut-off energy was set to be 520 eV and all structures were relaxed to an energy convergence of 10^{-4} eV/atom and a force convergence of 0.01 eV/Å, respectively.

During the geometrical optimization, surface energies of different layers of PtS_2 were firstly tested and monolayer PtS_2 was selected as the proper slab for single atom modification. (3 × 3) PtS_2 slab with exposed (001) surface was applied to support 16 kinds of possible single atom catalysts, such as Ti, V, Cr, Mn, Fe, Co, Ni, Zr, Ni, Mo, Tc, Rh, Ru, Pd, Ir and Pt. The formation energy (E_{for}) of single transition metal (TM) atoms on monolayer PtS_2 was determined by the following equation: $\triangle E_{for} = E_{total} - E_{PtS2} - E_{atom}$, where E_{total}, E_{PtS2}, and E_{atom} represent the total energies of the SAC-PtS_2, the monolayer PtS_2 substrate, and the single TM atom, respectively. The

formation energy represents the feasibility of material design, thus V-PtS_2, Cr-PtS_2, Mn-PtS_2, Tc-PtS_2 were first excluded from the theoretical models due to the great structure distortion induced by single TM atom modification. Then, Ti-PtS_2, Zr-PtS_2, Nb-PtS_2 and Mo-PtS_2 were screened out because of the required positive barriers for N_2 adsorption.

Further charge distribution and adsorption behavior of NRR intermediates (including N_2*, N_2H*, N_2H_2*, N_2H_3*, N*, NH*, NH_2* and NH_3*) were conducted on rest of SACs-PtS_2: Co-PtS_2, Fe-PtS_2, Ni-PtS_2 and Rh-PtS_2, Ru-PtS_2, Pd-PtS_2, Ir-PtS_2 and Pt-PtS_2. The adsorption energy (E_{ads}) of H* and N-containing intermediates on SACs-PtS_2 were determined according to the following equation: $\triangle E_{ads} = E_{total} - E_{sub} - E_{ads}$, where E_{total}, E_{sub}, and E_{ads} represent the total energies of the systems, the substrates, and the adsorbates, respectively. Change of Gibbs energy (ΔG) was calculated by the equation: $\Delta G = \Delta E + \Delta ZPE - T\Delta S$, where ΔE is the relative energy difference between the product and reactant of the NRR process; ΔZPE and ΔS are the corresponding changes of zero point energies and entropy at 298.15 K, which were estimated from the vibrational frequencies.

Noted that, the computational hydrogen electrode (CHE) model was used to compute ΔG of each elementary step during NRR pathways and he chemical potential of the proton–electron pair was roughly equivalent to one-half of the chemical potential of hydrogen molecule. The selectivity of HER and NRR performance was estimated from the comparison of ΔG_{H^*} and ΔG_{N2}.The limiting potential for NRR is determined by $U = \max \{\Delta G_1, \Delta G_2, \Delta G_3, \Delta G_4, \Delta G_5, \ldots, \Delta G_n\}$. The k-points was 3 × 3 × 1 in slab optimization and 5 × 5 × 1 in static calculation, respectively. The thickness of vacuum in all slabs was set to 20 Å to eliminate the interactions between the layers caused by the periodic boundary condition.

5.4 Design of SACs and eNRR mechanism study

To determine the most suitable PtS_2 matrix for SACs-PtS_2 structures, surface energy of 1-layer, 2-layer and few-layer PtS_2 with exposed (001) surface were calculated to select the most stable substrate. As shown in Figure 5.1a, the surface energies of 1-layer, 2-layer and 3-layer PtS_2 are 0.0094 eV/Å, 0.0096 eV/Å and 0.0097 eV/Å, showing an increasing tendency with the increased layer of PtS_2. Thus, in consideration of the surface stability and simplicity of calculation, monolayer PtS_2 with exposed (001) surface is selected as the substrate for the construction of SACs-PtS_2 structures. We then calculate the formation energies of possible single metal atoms on PtS_2 monolayer to quantitatively describe their structural stabilities. Among the 18 selected TM SACs demonstrated in Figure 5.2a, V, Cr and Mn are inappropriate to act as SACs on PtS_2 monolayer because the introduction of these atoms inevitably induces great substrate distortion and leads to instable surface with high energy, which goes against the purpose for long-term uses. The formation energy of rest atoms is summarized in Figure 5.2b, all the SACs exhibit strong binding to the PtS_2 substrate, which can effectively prevent the aggregation during NRR process. Besides, SACs-PtS_2 composed by elements in the former groups, including Ti-PtS_2, Mo-PtS_2, Nb-PtS_2 and Zr-PtS_2, show stronger binding interaction than middle- and late-group elements, which may ascribe to the different electronegativity. However, further investigation of N_2 affinity on Ti-PtS_2, Mo-PtS_2, Nb-PtS_2 and Zr-PtS_2 reveal thermodynamic non-spontaneous character (Figure 5.1b), the initial N_2 adsorption on Ti-PtS_2, Mo-PtS_2, Nb-PtS_2 and Zr-PtS_2 require energy barriers of +0.25 eV, +0.15 eV, +0.48 eV and +0.49 eV, respectively. Due to the hindered initial step of NRR pathway, Ti-PtS_2, Mo-PtS_2, Nb-PtS_2 and Zr-PtS_2 are screened out from the promising NRR candidates.

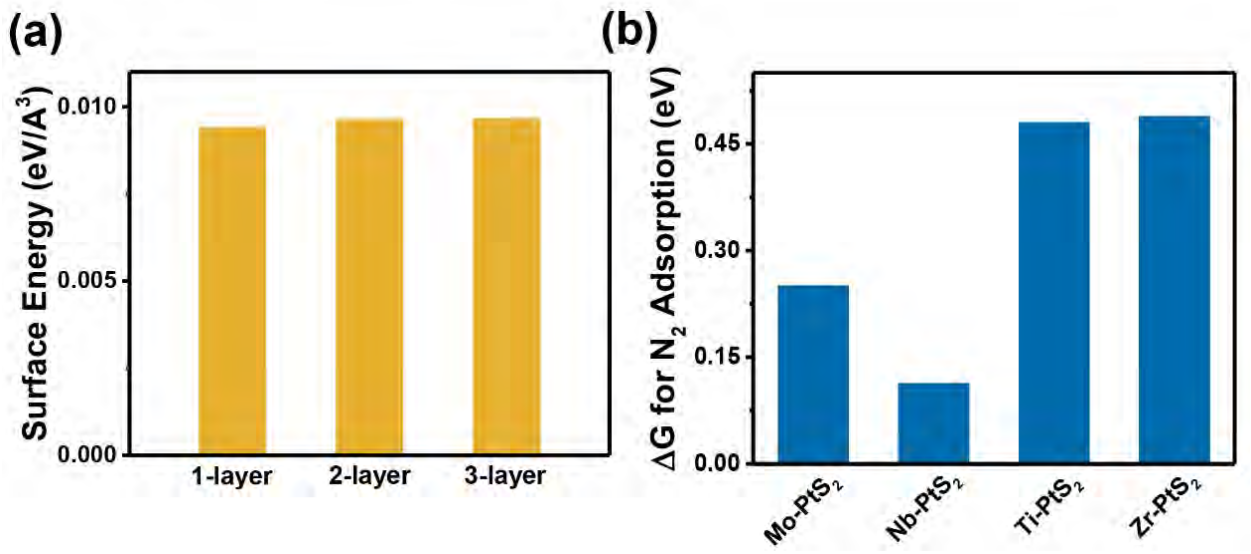

Figure 5.1. (a) Surface energy comparison of 1-layer, 2-layer and 3-layer PtS_2 slabs, respectively. (b) N_2 adsorption on Mo-PtS_2, Nb-PtS_2, Ti-PtS_2 and Zr-PtS_2, respectively.

According to the Figure 5.2b, Fe, Co, Ni, Rh, Ru, Ir and Pt single atom all exhibit moderate binding strength (-2 ~ -3 eV) with the PtS_2 substrate. The moderate interaction can not only bring about excellent stability but also reserve the unique property of single atom catalysts, which is beneficial for N_2 activation. We also study various possible adsorption sites of single atom catalysts to fully understand the formation of SACs-PtS_2 catalysts (Figure 5.3). Among various structures, the structure of SACs coordinated with three sulfur atoms and mono-sulfur atom are steady states, and partial electron transfer from PtS_2 to SACs can be observed in both of these structures. Moreover, SACs located in the cavity composed by three sulfur atoms show lower energy than that bond with mono-sulfur, and more localized electrons can be trapped on the SACs in S-S-S cavity, indicating excellent potential for N_2 activation. In addition, the Bader electron of single Pt-group atom on PtS_2 shows a value of appropriate 10, which demonstrates a fully occupied *d* orbital.

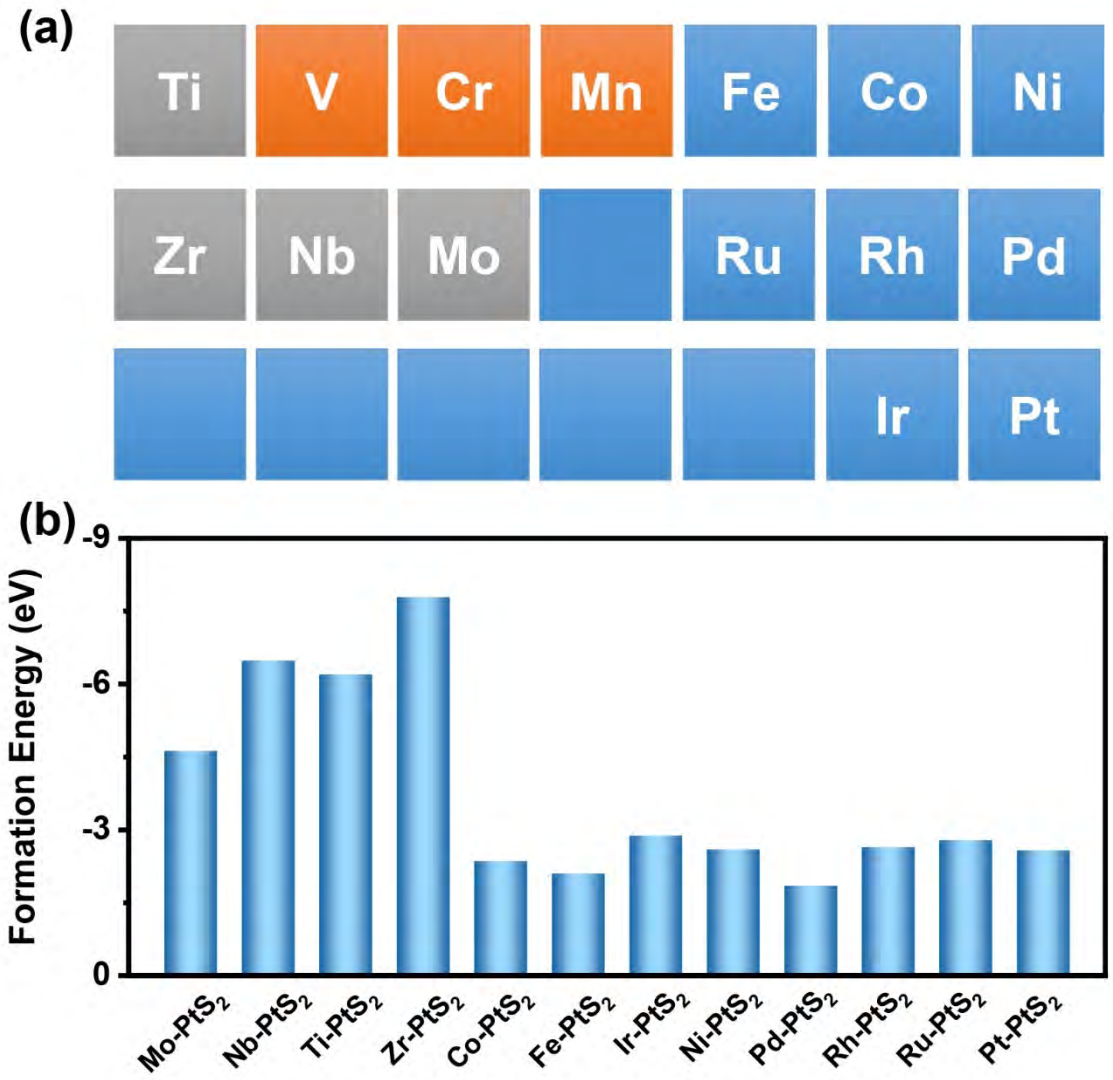

Figure 5.2**.** (a) 16 kinds of transition metals are considered to construct SACs-PtS_2. Orange shades indicate SACs-PtS_2 composed by metals that is not stable, which are not considered for further discussion. (b) Formation energy of stable SACs-PtS_2 structures.

Table 5.1. Calculated Zero-point energies, entropy and Gibbs energy of H* on SACs-PtS_2 surface.

	E_{ZPE} (eV)	TS (eV)	G (eV)
Co-PtS_2	0.17	0.03	-78.51
Fe-PtS_2	0.16	0.03	-79.86
Ir-PtS_2	0.15	0.03	-79.83
Ni-PtS_2	0.16	0.03	-77.36
Pd-PtS_2	0.17	0.03	-76.82
Pt-PtS_2	0.19	0.02	-77.22
Rh-PtS_2	0.18	0.02	-78.67
Ru-PtS_2	0.17	0.02	-79.70

Table 5.2**.** Calculated Zero-point energies, entropy and Gibbs energy of N_2 on SACs-PtS_2 surface during N_2 reduction process.

	E_{ZPE} (eV)	TS (eV)	G (eV)
Co-PtS_2	0.20	0.05	-89.33
Fe-PtS_2	0.19	0.06	-90.54
Ir-PtS_2	0.20	0.04	-89.51
Ni-PtS_2	0.19	0.06	-88.28
Pd-PtS_2	0.18	0.08	-87.84
Pt-PtS_2	0.20	0.05	-88.49
Rh-PtS_2	0.18	0.07	-89.00
Ru-PtS_2	0.19	0.05	-90.07

We compared free energy change for H* and N_2 adsorption on SACs supported on PtS_2 to determine the selectivity of NRR performance and competing HER reaction. Relative zero-point energies and entropies are documented in Table 5.1-Table 5.2. As displayed in Figure 5.4a-5.4b, H* can bond with different SACs via chemical interaction, but different SACs center shows various H* binding strength. The $\triangle G(H^*)$ of Co-PtS_2, Ni-PtS_2, Pd-PtS_2 and Pt-PtS_2 are +0.37 eV, +0.45 eV, +0.71 eV and +0.49 eV, respectively, which require external energy input to trigger H* adsorption, indicating the H* repulsive interactions. As a contrast, Ir-PtS_2 shows a $\triangle G(H^*)$ value of -0.68 eV, indicating a spontaneous and strong binding ability of H*. Strong H* binding strength suggests Ir-PtS_2 surface may have a high chance of getting "H*-poisoned", which may deactivate the SACs catalytic sites and lead to poor NRR stability. Fe-PtS_2, Rh-PtS_2 and Ru-PtS_2 exhibit moderate H* affinity and have $\triangle G(H^*)$ value that close to zero, showing $\triangle G(H^*)$ of +0.19 eV, -0.06 eV and -0.11 eV, respectively.

The free energy change of N_2 adsorption on SACs-PtS_2 were then calculated, corresponding charge density differences between before and after N_2 adsorption were also studied to unveil the interaction between SACs and N_2 molecular. Figure 5.4c shows the $\triangle G(N_2)$ on different SACs supported on PtS_2 substrate, and N_2 adsorption on all the SACs are thermodynamically feasible, revealing $\triangle G(N_2)$ of -0.23 eV, -0.27 eV, -0.15 eV, -0.25 eV, -0.09 eV, -0.18 eV, -0.26 eV and -0.56 eV on Co-PtS_2, Fe-PtS_2, Ir-PtS_2, Ni-PtS_2, Pd-PtS_2, Rh-PtS_2, Ru-PtS_2 and Pt-PtS_2, respectively. Distinct charge transfer can be observed between SACs and adsorbed N_2, which weakens the stubborn N≡N triple bond and benefits effective N_2 activation. As depicted in Figure 5.4d, the charge density of N-N bond decreases after bonding to the SACs center, and the localized charge on N atoms show great increase. In addition, the charge accumulation and depletion on SACs demonstrates effective σ donation from N_2 and π backdonation to N_2. The amount of charge

transfer on SACs and N_2 molecular are also estimated by Bader charge calculation, and the results are documented in Table 5.3. During N_2 adsorption process on Ru-PtS_2, 0.34 e is transferred from Ru single atom to N_2 molecular, which can facilitate the activation of N≡N bond and promote the succeeding hydrogenation reaction. Thus, Ru-PtS_2 holds great potential to act as excellent NRR catalysts among these candidates.

	SA-PtS_2 (structure 1)			SA-PtS_2 (structure 2)		
	Structure	Energy (eV)	Charge on SA	Structure	Energy (eV)	Charge on SA
Fe-PtS_2	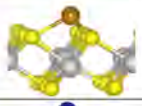	E = -76.41	Q = 7.74e	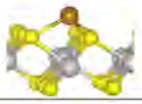	E = -76.41	Q = 7.74e
Co-PtS_2	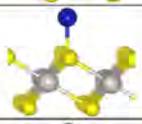	E = -74.44	Q = 8.43e	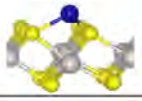	E = -75.13	Q = 8.70e
Ni-PtS_2	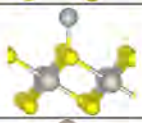	E = -73.48	Q = 9.97e	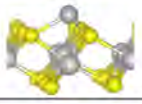	E = -74.17	Q = 10.02e
Ru-PtS_2	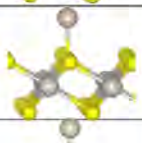	E = -75.09	Q = 7.70e	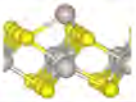	E = -75.95	Q = 7.73e
Rh-PtS_2	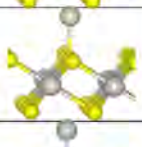	E = -74.36	Q = 8.89e	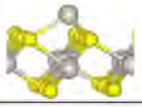	E = -74.96	Q = 8.89e
Pd-PtS_2	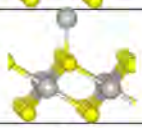	E = -73.72	Q = 9.90e	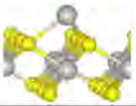	E = -73.89	Q = 10.02e
Ir-PtS_2	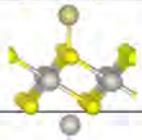	E = -74.80	Q = 8.86e	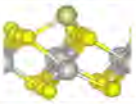	E = -75.04	Q = 9.35e
Pt-PtS_2	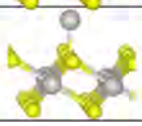	E = -74.03	Q = 9.91e	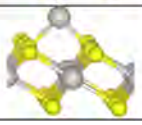	E = -74.10	Q = 10.00e

Figure 5.3. Structures of PtS_2 supported SACs with different coordination. The energies of optimized structures and localized Bader electrons on SACs are also summarized. The structure of single transition metal coordinated with three sulfur atoms is more stable than that bonds with mono-sulfur atom.

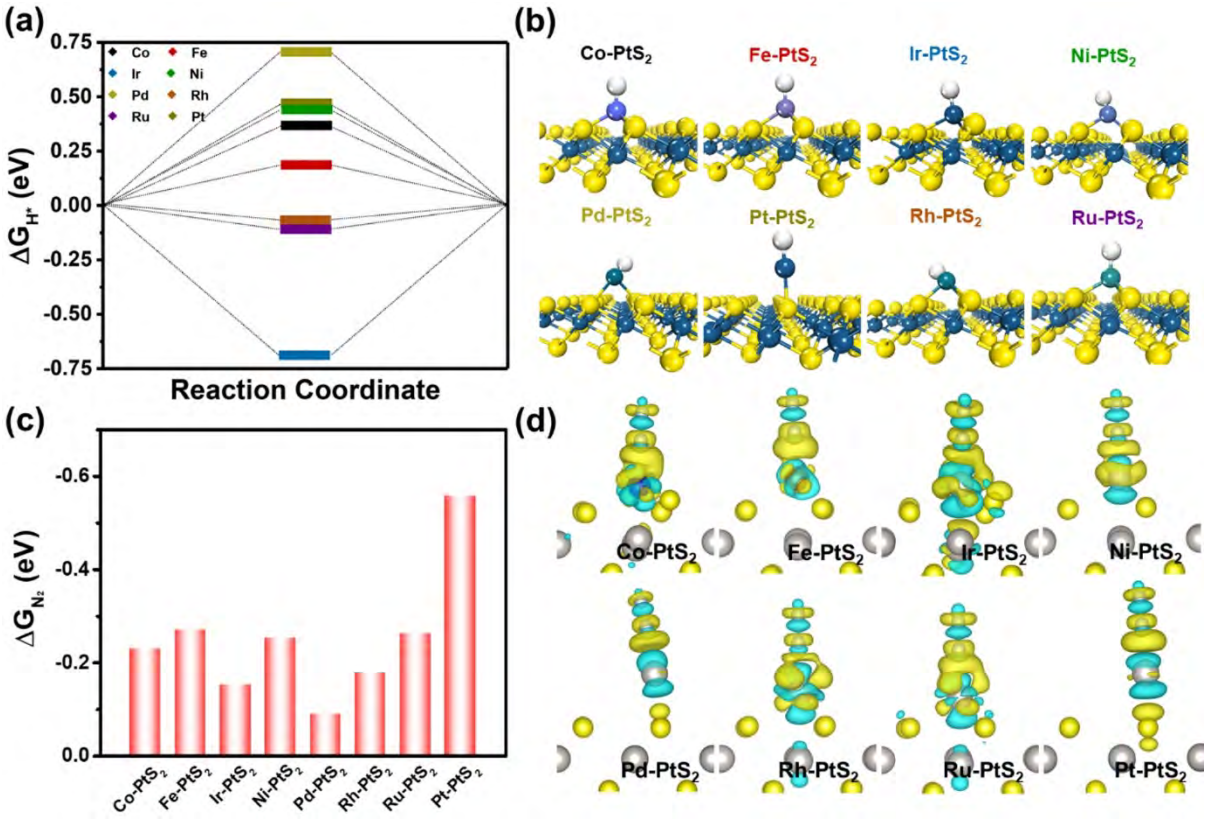

Figure 5.4. (a) Changes of Gibbs energy and (b) structures of H* adsorption on selected SACs-PtS_2. (c) Changes of Gibbs energy of N_2 adsorption on selected SACs-PtS_2. (d) Charge density differences between before and after N_2 adsorption on selected SACs-PtS_2 surfaces, respectively. The isosurface level of d is 0.003e/Å^3. The yellow and cyan represent charge accumulation and charge depletion. For clarity, the symmetric parts of the optimized slabs at the bottom are not shown.

The NRR selectivity on SACs-PtS_2 is then analyzed by detailly considering the free energy changes of *N_2 and H* adsorption processes. It is difficult to achieve high NRR efficiency when SACs have more thermodynamic advantages in binding H*. If SACs-PtS_2 show a preference of H* adsorption, the SACs center may be preoccupied by H* and leave little catalytic site for N_2 reduction. As seen in Figure 5.5, most of SACs are located in the NRR dominant region ($\Delta G(*N_2) < \Delta G(*H)$), while Ir-$PtS_2$ shows HER dominant property. For the SACs in NRR dominant region, N_2 reduction occupies a dominant position in the cathode reactions, and the Faradaic efficiency of NRR would be less hindered by the competing HER reaction under low overpotential. Thus, we

demonstrate Co-PtS_2, Fe-PtS_2, Ni-PtS_2, Rh-PtS_2, Ru-PtS_2, Pd-PtS_2 and Pt-PtS_2 are promising to serve as NRR electrocatalysts due to superior *N_2/*H selectivity.

Table 5.3. Change of amount of Bader electrons on SACs-PtS_2 and N_2 molecular after N_2 adsorption.

SA-PtS_2	**△ρ of SA**	**△ρ of S atoms near SA**	**△ρ of adsorbed N_2**
Co-PtS_2	-0.40 *e*	-0.04 *e*	+0.12 *e*
Fe-PtS_2	-0.18 *e*	-0.32 *e*	+0.16 *e*
Ir-PtS_2	-0.99 *e*	+0.37 *e*	+0.27 *e*
Ni-PtS_2	-0.14 *e*	-0.01 *e*	+0.17 *e*
Pd-PtS_2	-0.19 *e*	-0.73 *e*	+0.09 *e*
Pt-PtS_2	-0.23e	-0.16e	+0.22e
Rh-PtS_2	-0.28 *e*	-0.45 *e*	+0.22*e*
Ru-PtS_2	-0.34 *e*	+0.01 *e*	+0.34 *e*

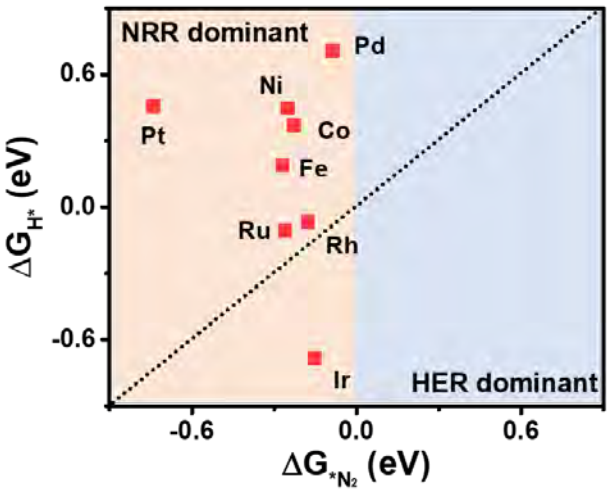

Figure 5.5. Comparison of △G(H*) and △G(*N_2) on selected SACs-PtS_2 surfaces. Light red region and light blue region indicate △G(*N_2) < 0 eV and △G(*N_2) > 0 eV, respectively. The Dashed line represents △G(H*) = △G(*N_2). SACs-PtS_2 in the △G(*N_2) < △G(H*) is NRR dominant region, and SACs-PtS_2 in the △G(*N_2) > △G(H*) is HER dominant region.

Table 5.4. Calculated Zero-point energies, entropy and Gibbs energy of $*N_2H$ on SACs-PtS_2 surface during N_2 reduction process.

	E_{ZPE} (eV)	TS (eV)	G (eV)
Co-PtS_2	0.46	0.06	-91.49
Fe-PtS_2	0.45	0.07	-92.67
Ni-PtS_2	0.44	0.07	-90.04
Pd-PtS_2	0.42	0.04	-89.40
Pt-PtS_2	0.45	0.06	-90.16
Rh-PtS_2	0.44	0.04	-91.22
Ru-PtS_2	0.47	0.05	-92.62

Table 5.5. Calculated Zero-point energies, entropy and Gibbs energy of $*N_2H_2$ on SACs-PtS_2 surface during N_2 reduction process.

	E_{ZPE} (eV)	TS (eV)	G (eV)
Co-PtS_2	0.80	0.07	-94.77
Fe-PtS_2	0.77	0.07	-95.82
Ni-PtS_2	0.79	0.04	-93.32
Pd-PtS_2	0.78	0.05	-92.58
Pt-PtS_2	0.80	0.04	-93.60
Rh-PtS_2	0.79	0.07	-94.31
Ru-PtS_2	0.79	0.07	-96.04

Table 5.6. Calculated Zero-point energies, entropy and Gibbs energy of $*N_2H_3$ on SACs-PtS_2 surface during N_2 reduction process.

	E_{ZPE} (eV)	TS (eV)	G (eV)
Co-PtS_2	1.01	0.07	-97.54
Fe-PtS_2	1.00	0.05	-99.66
Ni-PtS_2	1.10	0.04	-95.63
Pd-PtS_2	1.09	0.04	-94.81
Pt-PtS_2	1.11	0.07	-96.03
Rh-PtS_2	1.06	0.03	-98.05
Ru-PtS_2	0.97	0.01	-100.30

Table 5.7. Calculated Zero-point energies, entropy and Gibbs energy of NH* on SACs-PtS_2 surface during N_2 reduction process.

	E_{ZPE} (eV)	TS (eV)	G (eV)
Co-PtS_2	0.34	0.08	-84.49
Fe-PtS_2	0.33	0.09	-86.05
Ni-PtS_2	0.32	0.10	-83.07
Pd-PtS_2	0.29	0.03	-82.05
Pt-PtS_2	0.31	0.02	-82.93
Rh-PtS_2	0.34	0.09	-84.46
Ru-PtS_2	0.33	0.09	-86.28

Table 5.8. Calculated Zero-point energies, entropy and Gibbs energy of NH_2* on SACs-PtS_2 surface during N_2 reduction process.

	E_{ZPE} (eV)	TS (eV)	G (eV)
Co-PtS_2	0.64	0.04	-89.25
Fe-PtS_2	0.63	0.06	-90.80
Ni-PtS_2	0.64	0.04	-87.98
Pd-PtS_2	0.63	0.05	-87.08
Pt-PtS_2	0.65	0.04	-88.15
Rh-PtS_2	0.65	0.04	-88.85
Ru-PtS_2	0.65	0.03	-90.52

Table 5.9. Calculated Zero-point energies, entropy and Gibbs energy of NH_3* on SACs-PtS_2 surface during N_2 reduction process.

	E_{ZPE} (eV)	TS (eV)	G (eV)
Co-PtS_2	1.01	0.03	-93.49
Fe-PtS_2	1.01	0.03	-94.73
Ni-PtS_2	1.02	0.03	-92.48
Pd-PtS_2	1.00	0.03	-91.95
Pt-PtS_2	1.02	0.024	-92.71
Rh-PtS_2	1.01	0.03	-93.04
Ru-PtS_2	1.01	0.03	-94.09

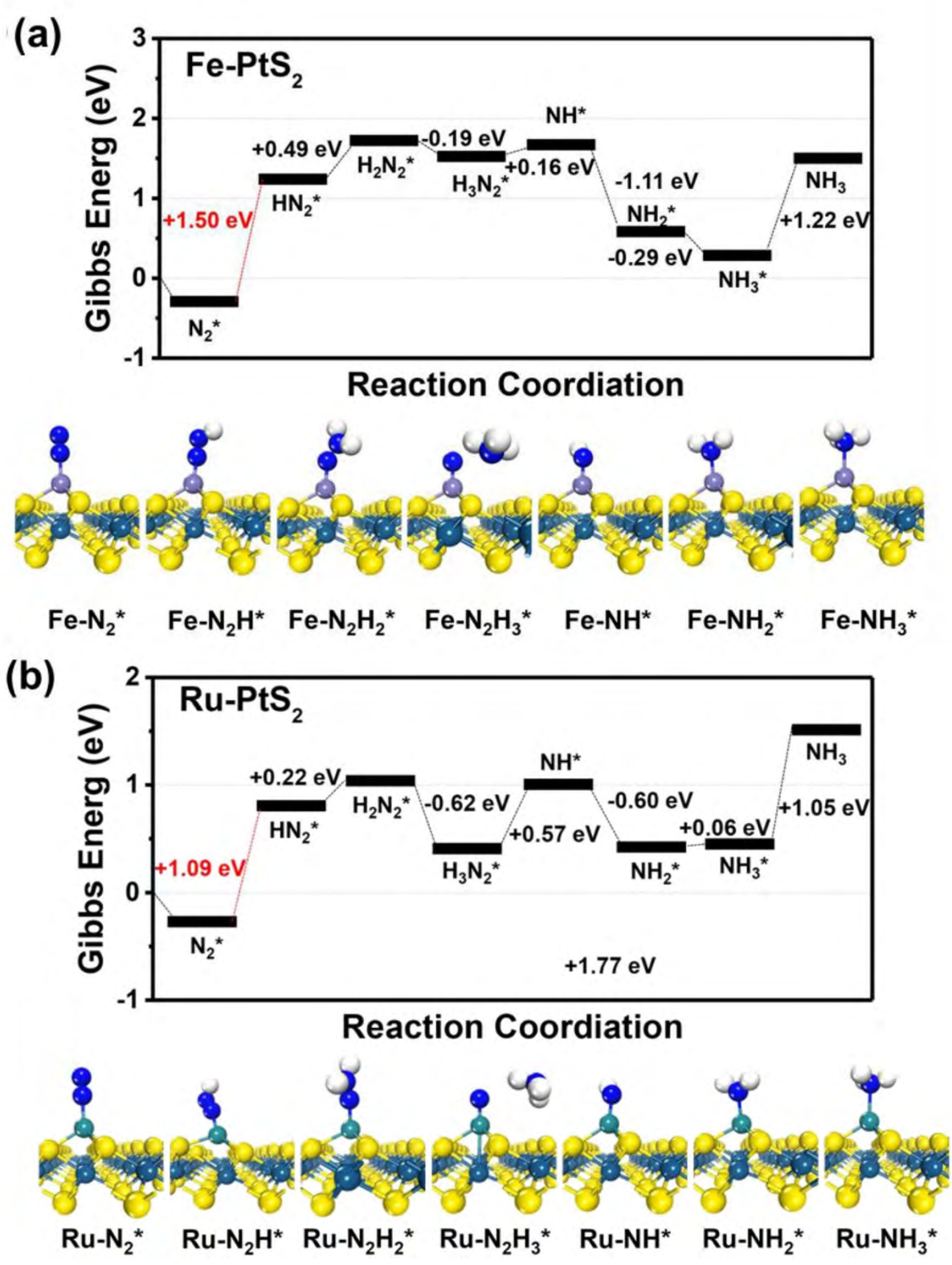

Figure 5.6. Calculated Gibbs free energy diagrams of distal NRR pathways on (a) Fe-PtS_2 and (b) Ru-PtS_2 surface, respectively. Corresponding structures are displayed at the bottom of diagrams.

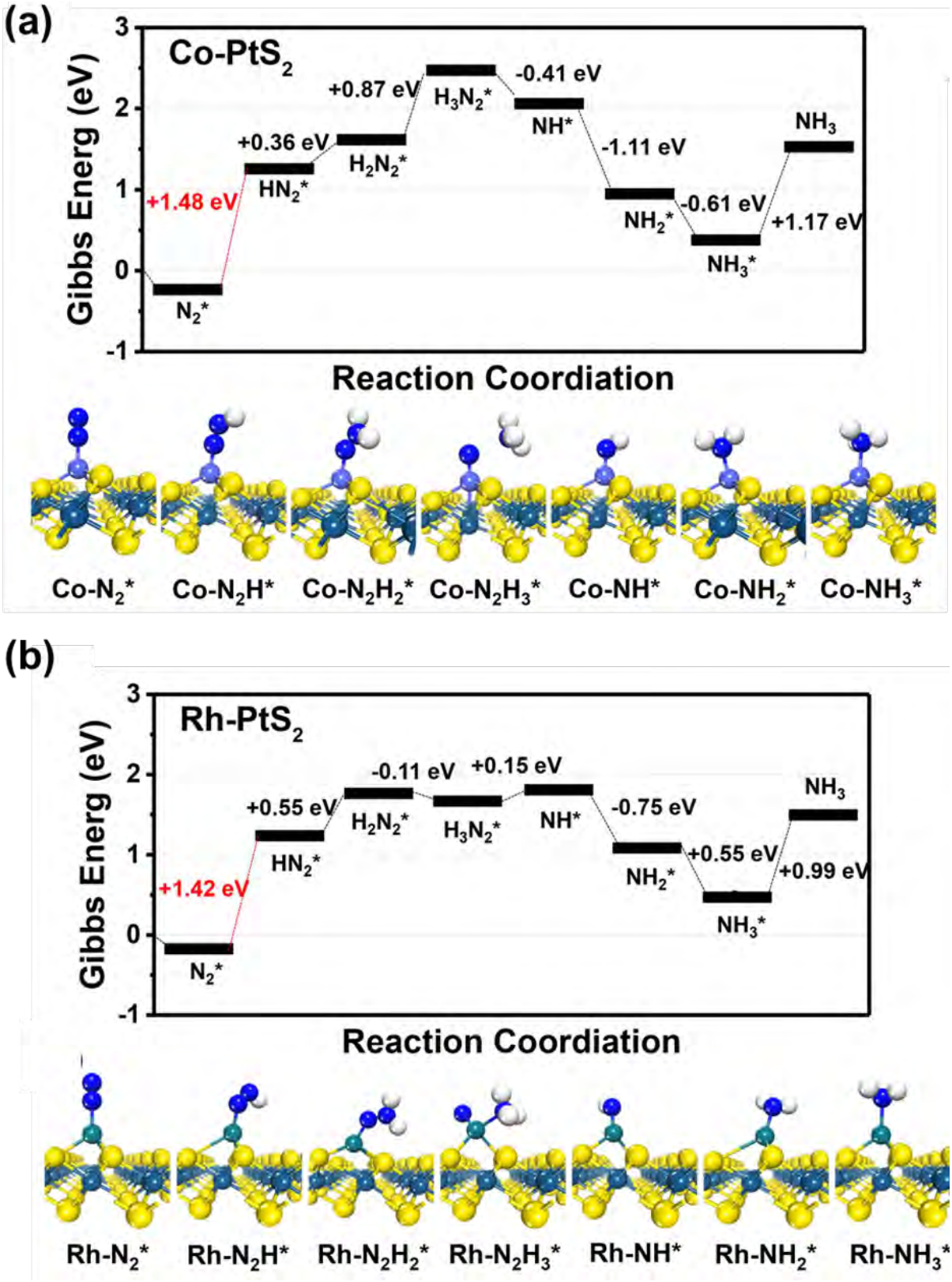

Figure 5.7. Calculated Gibbs free energy diagrams of distal NRR pathways on (a) Co-PtS_2 and (b) Rh-PtS_2 surface, respectively. Corresponding structures are displayed at the bottom of diagrams.

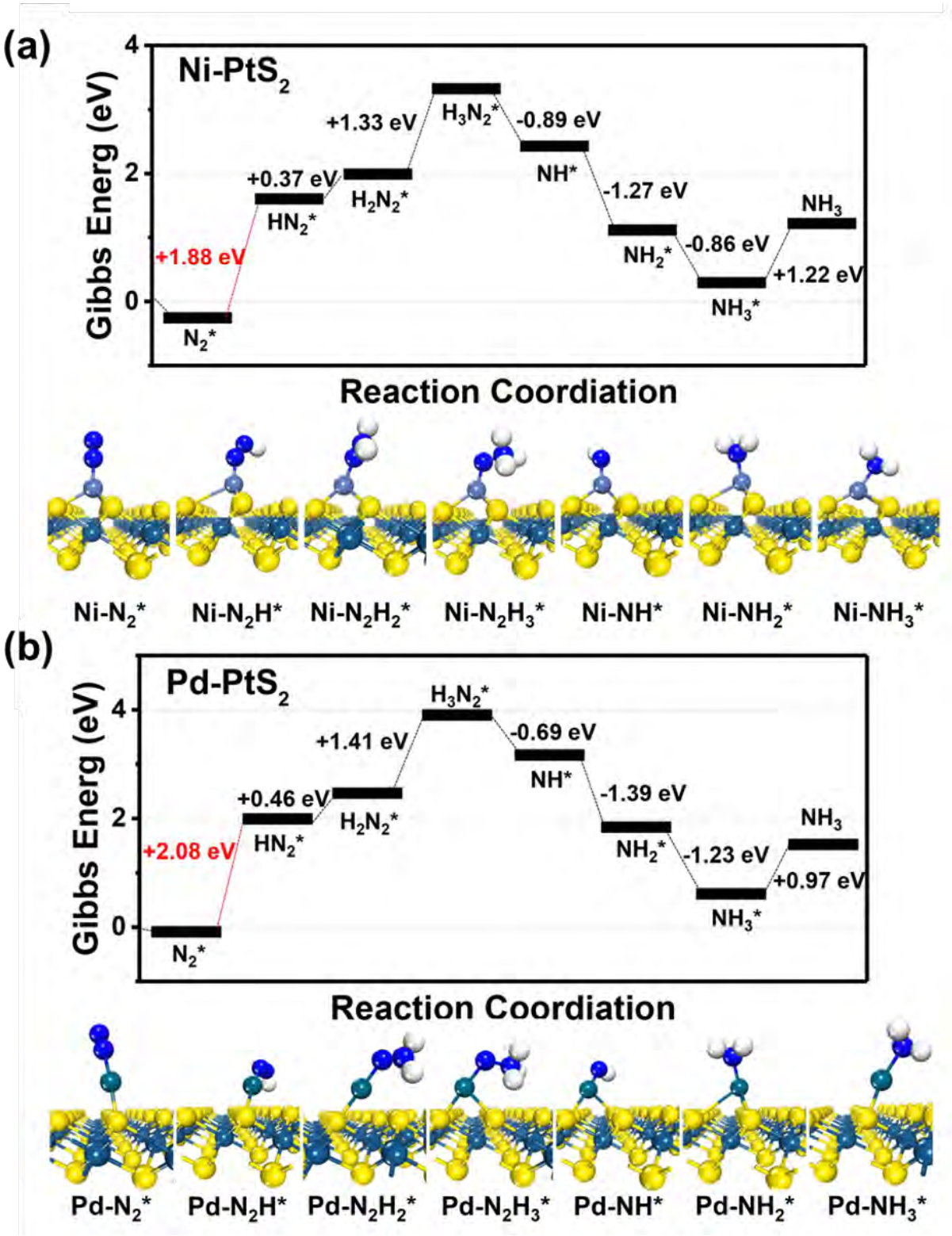

Figure 5.8. Calculated Gibbs free energy diagrams of distal NRR pathways on (a) Ni-PtS_2 and (b) Pd-PtS_2 surface, respectively. Corresponding structures are displayed at the bottom of diagrams.

To fully understand the PDS of NRR pathway and evaluate the theoretical NRR performance of selected 7 of SACs-PtS_2, the whole free energy diagrams of SACs-PtS_2 without external applied potential are investigated and corresponding structures are shown at the bottom of free energy plots. Calculated Zero-point energies, entropy and Gibbs energy of N-containing intermediates are documented in Table 5.4-Table 5.9. Figure 5.6 depicts the distal NRR pathways on Fe-PtS_2 and Ru-PtS_2 surfaces, respectively, and the SACs can sustain stable during the whole NRR process. As known, Fe and Ru have 8 outer electrons with a configuration of $4s^2\ 3d^6$ and $5s^1\ 4d^7$, respectively. The combination of occupied and unoccupied *d* orbitals shows great advantageous for N_2 activation and reduction. According to Figure 5.6, the calculated free energy on Fe-PtS_2 along distal mechanism are 1.50 eV, +0.49 eV, -0.19 eV, +0.16 eV, -1.11 eV, -0.29 eV and +1.22 eV, respectively. The calculated free energy on Ru-PtS_2 along distal mechanism are 1.09 eV, +0.22 eV, -0.62 eV, +0.57 eV, -0.60 eV, +0.06 eV and +1.05 eV, respectively. For Fe-PtS_2 and Ru-PtS_2, the steps of $*N_2 + H* \rightarrow *N_2H$ and last NH_3 desorption encounter great potential barriers (> 1.0 eV), and the first protonation step is regarded as the PDS. Ru-PtS_2 presents a PDS barrier of 1.09 eV, which is much lower than Fe-PtS_2 (1.50 eV), demonstrating Ru-PtS_2 is more favorable for NRR reaction.

Similarly, the distal NRR pathways on Co-PtS_2 ($4s^2\ 3d^6$) and Rh-PtS_2 ($5s^1\ 4d^7$) surfaces are summarized in Figure 5.7. Rh-PtS_2 shows free energies of +1.42 eV, +0.55 eV, -0.11 eV, +0.15 eV, -0.75 eV, -0.55 eV and +0.99 eV, respectively, which exhibiting a lower PDS barrier than Co-PtS_2 (1.48 eV). However, the PDS of Rh-PtS_2 is still larger than Ru-PtS_2, which may attribute to different configuration of *d* orbitals. The free energy values of Ni-PtS_2 ($4s^2\ 3d^8$), Pd-PtS_2 ($4d^{10}$) and Pt-PtS_2 ($6s^1\ 4f^{14}\ 4d^{10}$) were also detailly investigated to confirm our assumption, and corresponding free energy plots are shown in Figure 5.8 and Figure 5.9. SACs in Pt-group have

almost fully occupied *d* orbitals, Ni-, Pd- and Pt-PtS_2 require much higher PDS barriers of 1.88 eV, 2.08 eV and 1.97 eV, respectively. Among the selected 7 of SACs-PtS_2, Pd-PtS_2 has a fully occupied *d* orbitals configuration due to the Hund's rules, leading to the highest PDS barrier and sluggish NRR performance.

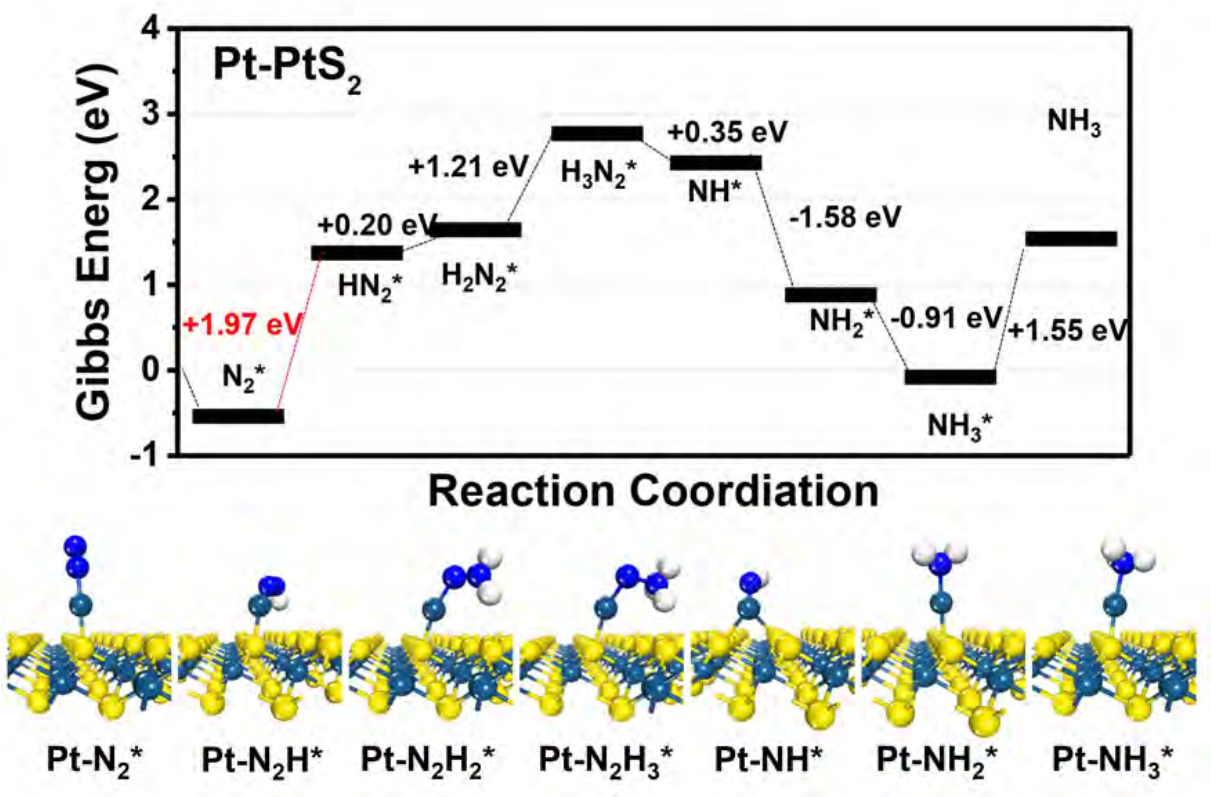

Figure 5.9. Calculated Gibbs free energy diagrams of distal NRR pathways on Pt-PtS_2 surface. Corresponding structures are displayed at the bottom of diagrams.

To present a clear understanding of the PDS step on different SAC centers, we compare the energy barriers of $*N_2 + H* \rightarrow *N_2H$ and last NH_3 desorption, which are the widely accepted PDS steps in previous study. According to Figure 5.10a, the required energy for the first step of hydrogenation is significantly larger than that for NH_3 desorption on Ni-PtS_2, Pd-PtS_2 and Pt-PtS_2. For Fe-PtS_2 and Ru-PtS_2, although the free energies of $*N_2 + H* \rightarrow *N_2H$ and NH_3 desorption show similar values, the hydrogenation step is still the PDS due to the slightly larger barrier. Thus, the

NRR limiting potential on SACs-PtS_2 is the energy barrier of the first hydrogenation step and the thermodynamic feasibility of $*N_2 + H* \rightarrow *N_2H$ reveals *d*-electron depended property, which may imply the inner connection between *d*-electronic structure and theoretical NRR performance.

Table 5.10. Calculated Zero-point energies, entropy and Gibbs energy of N* on SACs-PtS_2 surface during N_2 reduction process.

	E_{ZPE} (eV)	TS (eV)	G (eV)
Co-PtS_2	0.06	0.002	-80.17
Fe-PtS_2	0.06	0.001	-82.23
Ni-PtS_2	0.04	0.005	-78.15
Pd-PtS_2	0.03	0.007	-77.18
Pt-PtS_2	0.05	0.003	-78.63
Rh-PtS_2	0.05	0.002	-80.23
Ru-PtS_2	0.06	0.001	-82.95

To bridge the PDS on SACs-PtS_2 with the *d*-electronic configuration, we need to seek for appropriate intermediate parameter to simplify the hydrogenation process. Considering the PDS is positive correlated with the stability of N_2H* intermediate, we then applied the adsorption of N_2H* (ΔE_{N2H*}) to replace the $\triangle G$ of $*N_2 + H* \rightarrow *N_2H$. This approximation can convert the complex proton-coupled electron transfer reaction into simple adsorption behavior. To the best of our knowledge, relatively strong stabilization of N_2H* species can guarantee the reduction of the NRR overpotential. More importantly, based on previous study, N_2H* adsorption holds a good linear relation with N* affinity (ΔE_{N*}), indicating we can use ΔE_{N*} to concisely describe the PDS step of NRR reduction on SACs-PtS_2. As the SACs change, adsorption strength of all N-containing

intermediates changes too. We first confirm the relationship between ΔE_{N2H*}, ΔE_{N*} and PDS barrier by first-order linear fitting, and the fitting curve is depicted in Figure 5.10b-5.10c. Relative calculation parameters are documented in Table 5.10. For all the SACs-PtS_2, ΔE_{N2H*} and ΔE_{N*} exhibit excellent linear relationship with a R^2 of 0.93. Ru-PtS_2 possesses the best N* affinity, showing the N* adsorption energy of about -0.35 eV. The superior N* affinity of Ru-PtS_2 is beneficial for the stabilization N_2H* species (ΔE_{N2H*} = -2.4 eV), contributing to a reduced PDS barrier and favorable NRR reaction. In contrast, Ni-, Pd- and Pt-PtS_2 demonstrate poor N* affinity (ΔE_{N*} = +2.69 eV for Ni, ΔE_{N*} = +3.38 eV for Pd and ΔE_{N*} = +2.10 eV for Pt), which is regarded as the main cause for sluggish NRR pathways.

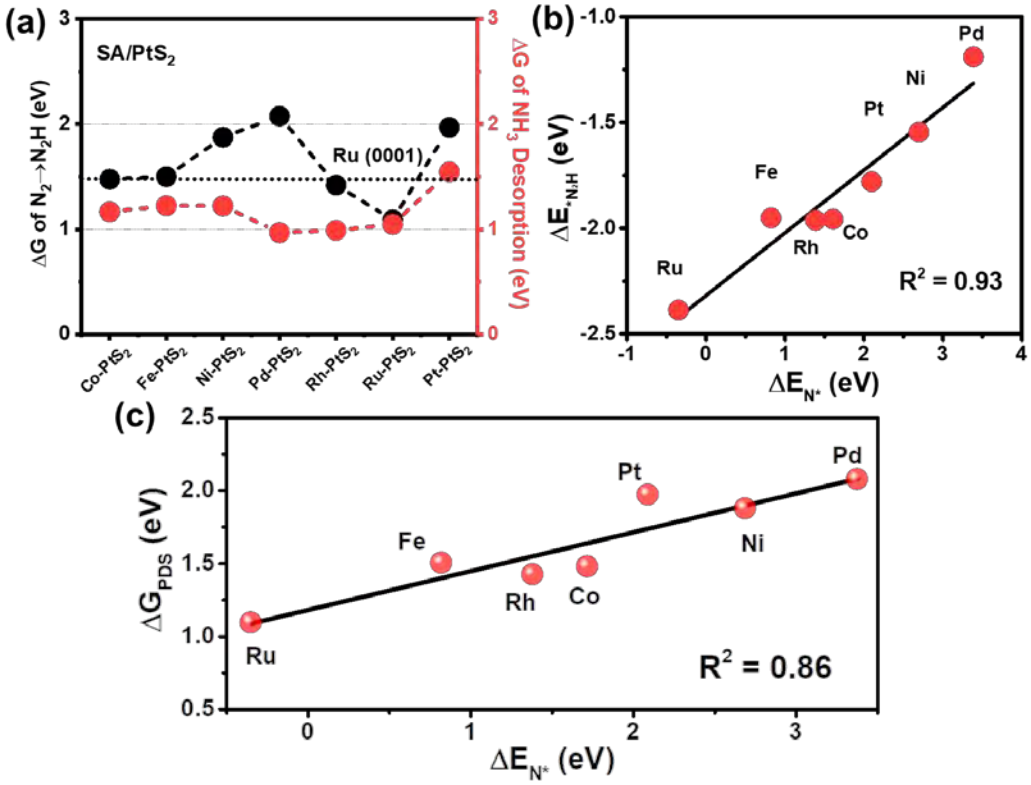

Figure 5.10. (a) Gibbs energies of *N_2 + H*→ *N_2H and NH_3 desorption on selected SACs-PtS_2 surfaces. The dashed line represents Gibbs energies change of *N_2 + H*→ *N_2H on Ru (0001), which is the PDS of NRR pathway on Ru (0001). (b) The computed adsorption energies of *N_2H ($\triangle E_{*N2H}$) as a function of the adsorption energy of N* ($\triangle E_{*N}$) on SACs-PtS_2. (c) The computed energy barriers of PDS as a function of the adsorption energy of N* ($\triangle E_{*N}$) on SACs-PtS_2.

To unveil the effect of *d*-electron configuration on N* affinity, we calculate the density of state (DOS) of N* adsorbed on SACs-PtS_2 and extract the partial density of state (PDOS) of SACs (n*d* orbitals, n = 3, 4 or 5.) and N (*2p* orbitals). According to Figure 5.11a-5.11d, Co-PtS_2, Fe-PtS_2, Rh-PtS_2 and Ru-PtS_2 show overlapped PDOS between SACs (n*d*) and N (*2p*) just below the Fermi level. The overlapped PDOS indicates SACs can interact with adsorbed N* and form strong chemical bonding, DOS intensity located at Fermi level suggests more charge can participate in the NRR process, which can greatly promote the NRR performance. In contrast, negligible DOS intensity is observed near the Fermi level when N* binds with Ni-PtS_2, Pd-PtS_2 and Pt-PtS_2, respectively (Figure 5.11e-5.11g). Moreover, the degree of orbitals overlaps between Pt-group SACs and N* is dramatically smaller than other SACs, further confirming weaker N* affinity on Ni-PtS_2, Pd-PtS_2 and Pt-PtS_2. More importantly, for all of the selected SACs-PtS_2, the orbitals overlapped regions around the Fermi level are mainly located in unoccupied *d* orbitals. Thus, we speculate the interaction between unoccupied *d* orbitals and N* (*2p*) may play an important role in N* adsorption.

We then integrate the unoccupied *d* orbitals of SACs to quantitively analyze the relationship between electronic structure of SACs center and N* affinity, which can act as impetus to explain the inner connection between *d*-electron configuration and PDS barrier of NRR. As depicted in Figure 5.12, the integral of unoccupied PDOS of SACs-PtS_2 follows an increasing trend of Pd-PtS_2 (0.67 eV) < Ni-PtS_2 (0.93 eV) < Pt-PtS_2 (1.24 eV) < Co-PtS_2 (1.97 eV) < Rh-PtS_2 (1.73 eV) < Fe-PtS_2 (2.37 eV) < Ru-PtS_2 (4.39 eV), which is in consistence with the N* affinity. Besides, the unoccupied *d* orbitals show great linear correlation with the adsorption energy of N* with a R^2 = 0.91. This linear relationship offers a quantitative explanation for the role of unoccupied *d* orbitals in determining the bonding strength of key N-containing intermediates, which is the origin

of the different PDS barriers of NRR reaction on different metal centers. Based on above analysis, we can establish a direct association from unoccupied *d* orbitals to N* affinity, N_2H stability and barrier energy of PDS, implying the amount of unoccupied *d* orbitals can act as a descriptor to predict the adsorption energy of N_2H* intermediate, ultimately speculating the PDS barrier of NRR on SACs centers.

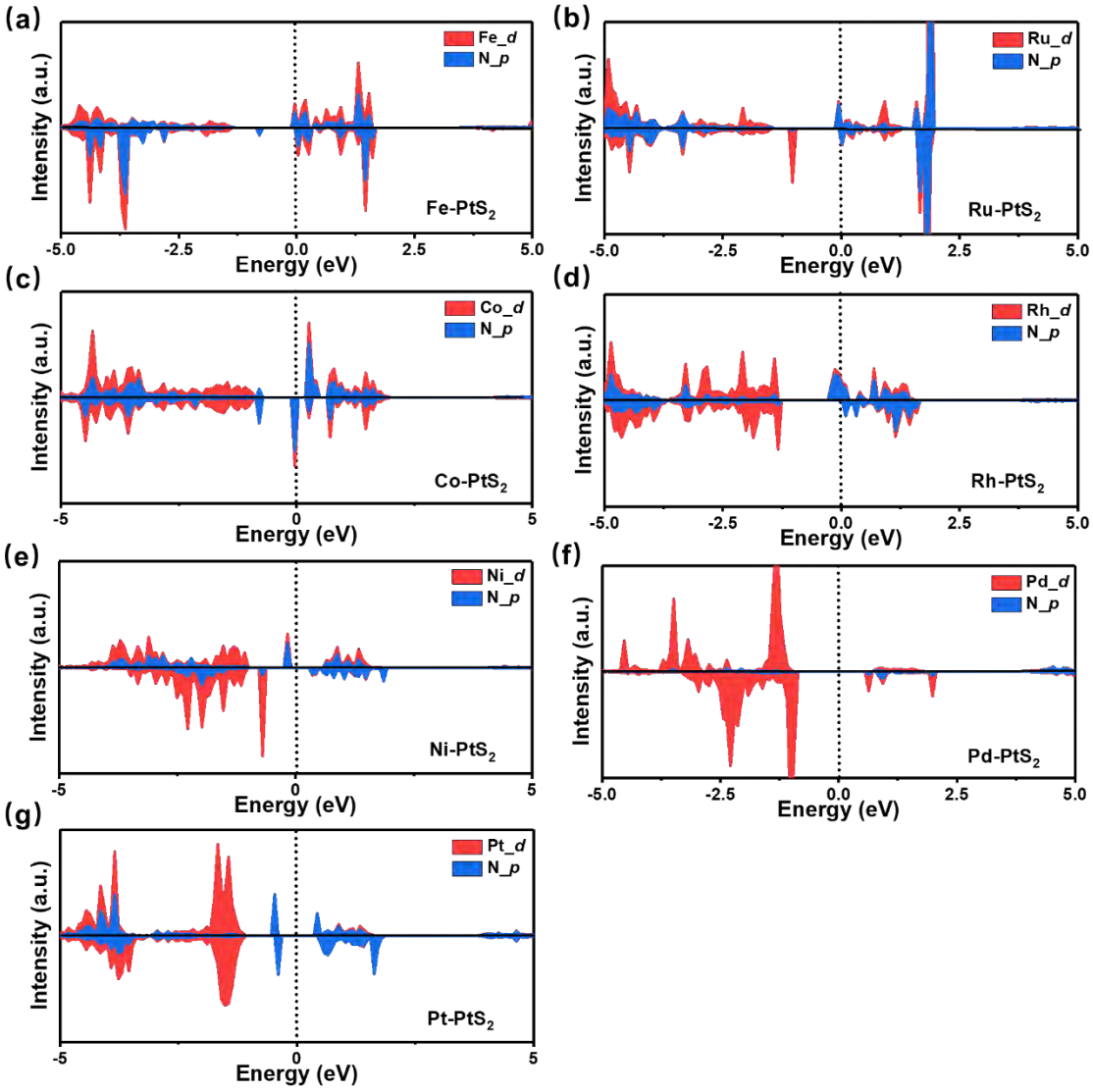

Figure 5.11. (a) The partial density of states (PDOS) of Fe (*3d* orbitals) and N (*2p* orbitals). (b) The PDOS of Ru (*4d* orbitals) and N (*2p* orbitals). (c) The PDOS of Co (*3d* orbitals) and N (*2p* orbitals). (d) The PDOS of Rh (*4d* orbitals) and N (*2p* orbitals). (e) The PDOS of Ni (*3d* orbitals) and N (*2p* orbitals). (f) The PDOS of Pd (*4d* orbitals) and N (*2p* orbitals). (g) The PDOS of Pt (*5d* orbitals) and N (*2p* orbitals).

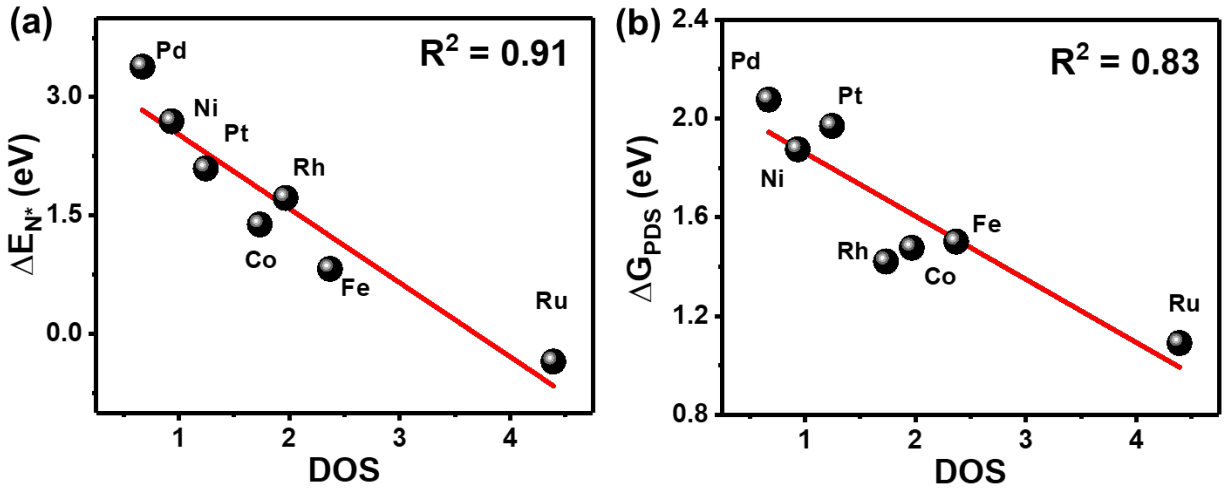

Figure 5.12. (a) The computed adsorption energy of *N ($\triangle E_{*N}$) on SACs-PtS_2 as a function of integral of DOS intensity of SACs (*nd*, n=3, 4 or 5) in the range of 0 eV-5 eV. (b) The computed energy barriers of PDS as a function of integral of unoccupied DOS intensity of SACs (*nd*, n=3, 4 or 5) in the range of 0 eV-5 eV.

5.5 Conclusion

In summary, we explored efficient SACs on PtS_2 substrate for eNRR process by setting a series of screening criteria, including binding strength of SACs to the substrate, selectivity of HER/NRR and energy barrier of potential limiting step. Among various SACs-PtS_2, Ru-PtS_2 exhibits excellent stability and better N_2 affinity, it also shows the lowest barrier (1.09 eV) to convert N_2 into NH_3, suggesting the great potential to serve as electrocatalyst for NRR performance. More importantly, we establish the inner connection between the potential barrier and intrinsic *d* electronic configuration by introducing an intermediate parameter of $\triangle_{N*}$. Based on the statistical results, the potential barrier shows linear correlation with the binding strength of N*, which is also linear correlated with the PDOS integral of the unoccupied *d* orbital of SACs.

6 Summary and perspectives

In this thesis, we demonstrate effective surface engineering strategies to enhance the electrocatalytic water splitting performance and nitrogen reduction activity. Hydrophilic functional groups modification and surface heteroatom incorporation show great potential to improve the water splitting performance. Besides, *d*-electron modulation of catalytic TM-center induced by sulfidation process plays a positive role in N_2 activation, which is significant for converting N_2 into NH_3. We further unveil the effect of *d*-orbitals of TM-center on NRR performance by comparing the NRR pathways on different single atom centers with different *d*-orbitals configuration, which is of great importance for understanding the relationship between NRR performance and intrinsic property of TM-centers.

Firstly, we synthesize defect-rich three-dimensional (3D) graphene based electrocatalysts and realize enhanced HER kinetics by increasing the amount of surface hydroxyl group of graphene. Our theoretical results confirm surface hydroxyl groups on the surface of graphene can effectively attract H_2O clusters without external energy input, forming water-rich region near the cathode surface and constantly supplying H_2O molecular for hydrogen evolution. Experimental results also indicate the HER kinetic of 3D graphene supported electrocatalysts show dramatic increase after crafting massive hydroxyl groups on 3D graphene via alkaline treatment. In addition, the increased water affinity induced by hydroxyl group modification should be the principle cause for enhanced HER performance. This surface modification strategy is beneficial to adjust interfacial pH environment and facilitate interfacial H_2O supply, contributing to outstanding HER performance.

Then, to overcome the weakness of powder-like electrocatalysts and realize efficient water splitting under high current density, we fabricate Fe-doped Ni_2P on 3D stainless steel mesh to

serve as water splitting electrode. Robust OER performance and remarkable HER performance can be realized by controlling the content of Fe dopant in Ni_2P matrix. High content of Fe dopant can bring about excellent OER electrode, meeting the requirements for commercial water electrolyzer. Ni_2P with lower Fe impurity content shows great potential to achieve remarkable HER performance with prominent stability. Theoretical results unveil the inner mechanism of controllable water splitting performance induced by Fe dopant engineering, and improved O-containing intermediates affinity induced by Fe doping is the main reason for enhanced OER performance. Interestingly, water molecule chemisorption on Ni_2P surface is sensitive to the Fe content, reduced Fe content is more favorable for HER performance. This heteroatom modification strategy highlights the importance of surface-active Fe-sites, offering valuable guidance on electrocatalysts design towards water splitting.

In addition, we manipulate the *d*-electrons configuration of active Pt sites via one-step sulfidation process and successfully realize high-efficient NRR performance. The DFT calculations predict, compared with metallic Pt surface, sulfurized Pt can greatly reduce the barrier for N_2 activation and suppress the competing HER reaction. Our experimental also indicates the HER kinetics on PtS is more sluggish than metallic Pt, leading to reduced competing hydrogen evolution. More importantly, PtS can perform the NRR reaction under a lower overpotential than Pt, which is consistent with the theoretical analysis. This work not only reports an efficient electrocatalyst towards NRR reaction, but also proposes an effective strategy to modify the d-orbitals of group-10 TM-centers for enhanced NRR performance.

Finally, we propose a universal principle to screen NRR electrocatalysts by building up a picture of single atom electrocatalysts supported on PtS_2 substrate. Binding strength of single atom on PtS_2 substrate is the first criteria to evaluate the stability of designed eNRR catalyst. To predict

the competing cathode reaction, the selectivity of HER/NRR is then estimated by comparing the Gibbs energy of N_2 adsorption and H* adsorption, respectively. Then, the NRR pathways of selected SACs-PtS_2 are detailly investigated and corresponding barriers for limiting potential are also calculated. Ru-PtS_2 is regarded as the most promising eNRR due to the excellent selectivity and reduced overpotential. We also establish the connection between NRR performance and intrinsic electronic structure of single atom center by introducing an intermediate parameter of N* binding strength of ($\triangle E_{N*}$). The limiting potential of NRR on SACs-PtS_2 is linear correlated to $\triangle E_{N*}$, which is also proved to be closely related to the integral of density of unoccupied *d* orbitals states of the single atom center. This work provides an effective guidance to screen and design efficient single-atom electrocatalysts for NRR reaction.

Based on above results, surface engineering strategies, including surface functional group modification, surface heteroatom incorporation, sulfidation treatment and construction of single atom electrocatalysts, are proposed in this thesis. Although efficient water splitting performance and enhanced NRR reduction can be successfully achieved, there is still some aspects to be improved. The efficiency of overall water splitting still needs to be optimized to meet the demand of practical application. Besides, the resistance to corrosion of electrode is also required to improve to apply the electrolysis technology into electrocatalytic seawater splitting. Finally, although the NRR performance exhibit dramatically promotion, the Faradaic efficiency of NRR is still low, which calls for more effective strategies to optimize the structure of cathode electrode for enhanced NRR efficiency.

7 List of Publications

1. **L. J. Cai**, Z. Y. Lin, M. Y. Wang, F. Pan, J. W. Chen, Y. Wang, X. P. Shen, and Y. Chai*. *Journal of Materials Chemistry A*, **2017**, 5, 24091.

2. **L. J. Cai**, B. C. Qiu, Z. Y. Lin, Y. Wang, S. N. Ma, M. Y. Wang, Y. H. Tsang, and Y. Chai*. *Journal of Materials Chemistry A*, **2018**, 6, 21445.

3. B. C. Qiu,# **L. J. Cai**,# Y. Wang, Z. Y. Lin, Y. P. Zuo, M. Y. Wang, and Y. Chai*. *Advanced Functional Materials*, **2018**, 28, 1706008. (Joint first author)

4. B. C. Qiu,# **L. J. Cai**,# Y. Wang, S. N. Ma, Y. H. Tsang*, and Y. Chai*. *Materials Today Energy*, **2019**, 11, 89. (Joint first author)

5. B. C. Qiu,# **L. J. Cai**,# Y. Wang, X. Y. Guo, S. N. Ma, Y. Zhu, Y. H. Tsang, Z. J. Zheng, R. K. Zheng, and Y. Chai*. Small, 2019, 1904507. (Joint first author)

6. J. Y. Lu,# **L. J. Cai**,#, N. Zhang, B. C. Qiu and Y. Chai*. *ACS Appl. Mater. Inter.* **2019**, 11, 44214. (Joint first author)

7. M. Y. Wang, **L. J. Cai**, Y. Wang, F. C. Zhou, K. Xu, X. M. Tao, and Y. Chai*. *Journal of the American Chemistry Society*, **2017**, 139, 4144.

8. Z. Y. Lin, **L. J. Cai**, W. Lu, and Y. Chai*. *Small*, **2017**, 13, 170051.

9. Y. Wang, S. Y. Su, **L. J. Cai**, B. C. Qiu, C. Yang, X. M. Tao*, and Y. Chai*. *Energy Storage Materials*, **2019**, 20, 315.

10. Y. Wang, S. Y. Su, **L. J. Cai**, B. C. Qiu, N. Wang, J. Xiong, C. Yang, X. M. Tao*, and Y. Chai*.*Advanced Energy Materials*, **2019**, 9, 1900037.

11. S. N. Ma, H. Y. Yuan, **L. J. Cai**, X. Y. Wang, H. Long, Y. Chai, and Y. H. Tsang*. *Materials Today Chemistry*, **2018**, 9, 133.

12. M. Y. Xing, Y. Zhou, C. Y. Dong, **L. J. Cai**, L. X. Zeng, B. Shen, L. H. Pan, C. C. Dong, Y. Chai, J. L. Zhang*, and Y. D. Yin*. *Nano Letters*, **2018**, 18, 3384.

13. B. C. Qiu, C. Wang, N. Zhang, **L. J. Cai**, Y. J. Xiong and Y. Chai*. *ACS Catalysis*, **2019**, 9, 6484.

14. M. Y. Wang, Y. P. Zuo, J. L. Wang, Y. Wang, X. P. Shen, B. C. Qiu, **L. J. Cai**, F. C. Zhou, S. P. Lau, and Y. Chai*. *Advanced Energy Materials*, **2019**, 1901801.

8 Acknowledgements

Our life is composed of a series of fantastic choices. Each choice can bring us about a unique journey, during which we make new friends, accumulate valuable experience and firm our goals. Good journey gradually makes you to be who you want to be; good journey makes you know the most real happiness in life; good journey makes you see the whole world from the scenery along the way.

Three years ago, I started a three-year journey as a PhD candidate in the Hong Kong Polytechnic University, where we can learn how to open the mind and shape our future. During my PhD period, I enjoyed the professional level, vigorous vitality and realistic attitude of the school. Advanced instruments and convenient facilities here not only give me much support in academic study and scientific research but also enrich my daily life. Here, I'd like to extend my sincere gratitude to my alma mater.

I am deeply indebted to my supervisor Prof. Yang Chai for his enlightening guidance and continuous support during the whole process. His strong sense of responsibility and high enthusiasm for scientific research inspire me to persevere in striving for my goal. I am also deeply impressed by his constant encouragement, which greatly strengthens my courage to overcome the difficulties on the academic road.

Secondly, I would give my thanks to all the technicians who supported me during my doctoral period. I'd like to appreciate Dr. Vincent Chan, Dr. Wei Lu, Dr. Hardy Lu, Ms. Henrietta Ho and Mr. Tsz Lam Chan for their guidance and help. I'd like to thank Prof. Li Song and Dr. Shuangming Chen for their cooperation in our collaborative research work. I also feel grateful to all of my group members, Dr. Yuda Zhao, Dr. Mengye Wang, Dr. Bocheng Qiu, Dr. Ning Zhang, Dr. Feichi Zhou, Dr. Yang Wang, Dr. Jingli Wang, Dr. Yanghui Liu, Dr. Fang Yuan, Dr. Yao Guo,

Dr. Jingkai Qin, Mr. Ziyuan Lin, Mr. Jiewei Chen, Mr. Xinpeng Shen, Mr. Kang Xu, Mr. Feng Pan, Mr. Yi Wang, Mr. Yunpeng Zuo, Ms. Cong Wang, and Mr. Tsz Hin Choy. Their kindness and happiness comfort my heart, and our friendship is the wealth of my life.

Thirdly, I would like to express my gratitude to Dr. Jingsi Qiao, Ms. Sainan Ma, Ms. Yongxin Lye, Dr. Wei Xu, Dr. Yan Liu, Dr. Li Chen, Mr. Shuoguo Yuan, Mr. Zehan Wu, Dr. Yanyong Li, Dr. Shenghuang Lin, Dr. Gongxun Bai, Dr. Wenjing Jie, Dr. Ying Fu, Dr. Ran Ding, Mr. Siqi Li, Mr. Longhui Zeng and Mr. Hong Tan. Thank all of you for helping me to adapt to the life in Hong Kong, and I enjoy the three years in Hong Kong because of your company and support.

Last but not the least, I'd like to give my sincere gratitude to my parents, parents-in-law and my beloved husband. They always care about my health, joys and sorrows, trying to understand and support every decision I made. Their selfless love and forever respect are the inexhaustible power to push me forward. When people care about how strong I can be, they are always the ones who care about whether I am happy. Home is the paradise, home is the harbor of love, and home is where the heart is. Thank all of you for giving me such a sweet home, I love you.

9 References

1. Tee, S. Y.; Win, K. Y.; Teo, W. S.; Koh, L. D.; Liu, S.; Teng, C. P.; Han, M. Y., Recent Progress in Energy-Driven Water Splitting. *Adv. Sci.* **2017,** *4*, 1600337.

2. Ding, Q.; Song, B.; Xu, P.; Jin, S., Efficient Electrocatalytic and Photoelectrochemical Hydrogen Generation Using MoS_2 and Related Compounds. *Chem* **2016,** *1*, 699.

3. Chen, Y. Y.; Zhang, Y.; Zhang, X.; Tang, T.; Luo, H.; Niu, S.; Dai, Z. H.; Wan, L. J.; Hu, J. S., Self-Templated Fabrication of $MoNi_4/MoO_{3-X}$ Nanorod Arrays with Dual Active Components for Highly Efficient Hydrogen Evolution. *Adv. Mater.* **2017,** *29*, 1703311.

4. Ma, Y. Y.; Wu, C. X.; Feng, X. J.; Tan, H. Q.; Yan, L. K.; Liu, Y.; Kang, Z. H.; Wang, E. B.; Li, Y. G., Highly Efficient Hydrogen Evolution from Seawater by a Low-Cost and Stable CoMoP@C Electrocatalyst Superior to Pt/C. *Energ. Environ. Sci.* **2017,** *10*, 788.

5. Li, X. M.; Hao, X. G.; Abudula, A.; Guan, G. Q., Nanostructured Catalysts for Electrochemical Water Splitting: Current State and Prospects. *J. Mater. Chem. A* **2016,** *4*, 11973.

6. Li, G.; Zhang, D.; Yu, Y.; Huang, S.; Yang, W.; Cao, L., Activating MoS_2 for pH-Universal Hydrogen Evolution Catalysis. *J. Am. Chem. Soc.* **2017,** *139*, 16194.

7. Duan, H.; Li, D.; Tang, Y.; He, Y.; Ji, S.; Wang, R.; Lv, H.; Lopes, P. P.; Paulikas, A. P.; Li, H.; Mao, S. X.; Wang, C.; Markovic, N. M.; Li, J.; Stamenkovic, V. R.; Li, Y., High-Performance Rh_2P Electrocatalyst for Efficient Water Splitting. *J. Am. Chem. Soc.* **2017,** *139*, 5494.

8. Cai, X.; Luo, Y.; Liu, B.; Cheng, H. M., Preparation of 2D Material Dispersions and Their Applications. *Chem. Soc. Rev.* **2018,** *47*, 6224.

9. Wang, Y.; Kong, B.; Zhao, D. Y.; Wang, H. T.; Selomulya, C., Strategies for Developing Transition Metal Phosphides as Heterogeneous Electrocatalysts for Water Splitting. *Nano Today* **2017,** *15*, 26.

10. Deng, D.; Novoselov, K. S.; Fu, Q.; Zheng, N.; Tian, Z.; Bao, X., Catalysis with Two-Dimensional Materials and Their Heterostructures. *Nat. Nanotechnol.* **2016,** *11*, 218.

11. Hong, J.; Jin, C.; Yuan, J.; Zhang, Z., Atomic Defects in Two-Dimensional Materials: From Single-Atom Spectroscopy to Functionalities in Opto-/Electronics, Nanomagnetism, and Catalysis. *Adv. Mater.* **2017,** *29*, 1606434.

12. Deng, S.; Zhong, Y.; Zeng, Y.; Wang, Y.; Yao, Z.; Yang, F.; Lin, S.; Wang, X.; Lu, X.; Xia, X.; Tu, J., Directional Construction of Vertical Nitrogen-Doped 1T-2H $MoSe_2$/Graphene

Shell/Core Nanoflake Arrays for Efficient Hydrogen Evolution Reaction. *Adv. Mater.* **2017,** *29*, 1700748.

13. Kappera, R.; Voiry, D.; Yalcin, S. E.; Branch, B.; Gupta, G.; Mohite, A. D.; Chhowalla, M., Phase-Engineered Low-Resistance Contacts for Ultrathin MoS_2 Transistors. *Nat. Mater.* **2014,** *13*, 1128.

14. Zhang, J.; Wang, T.; Pohl, D.; Rellinghaus, B.; Dong, R.; Liu, S.; Zhuang, X.; Feng, X., Interface Engineering of MoS_2/Ni_3S_2 Heterostructures for Highly Enhanced Electrochemical Overall-Water-Splitting Activity. *Angew. Chem. Int. Ed. Engl.* **2016,** *55*, 6702.

15. Chen, Y. C.; Lu, A. Y.; Lu, P.; Yang, X.; Jiang, C. M.; Mariano, M.; Kaehr, B.; Lin, O.; Taylor, A.; Sharp, I. D.; Li, L. J.; Chou, S. S.; Tung, V., Structurally Deformed MoS_2 for Electrochemically Stable, Thermally Resistant, and Highly Efficient Hydrogen Evolution Reaction. *Adv. Mater.* **2017,** *29*, 1703863.

16. He, R.; Hua, J.; Zhang, A.; Wang, C.; Peng, J.; Chen, W.; Zeng, J., Molybdenum Disulfide-Black Phosphorus Hybrid Nanosheets as a Superior Catalyst for Electrochemical Hydrogen Evolution. *Nano Lett.* **2017,** *17*, 4311.

17. Qin, F.; Zhao, Z.; Alam, M. K.; Ni, Y.; Robles-Hernandez, F.; Yu, L.; Chen, S.; Ren, Z.; Wang, Z.; Bao, J., Trimetallic NiFeMo for Overall Electrochemical Water Splitting with a Low Cell Voltage. *ACS Energy Lett.* **2018,** *3*, 546.

18. Wang, W.; Xu, X.; Zhou, W.; Shao, Z., Recent Progress in Metal-Organic Frameworks for Applications in Electrocatalytic and Photocatalytic Water Splitting. *Adv. Sci.* **2017,** *4*, 1600371.

19. Duan, J.; Chen, S.; Zhao, C., Ultrathin Metal-Organic Framework Array for Efficient Electrocatalytic Water Splitting. *Nat. Commun.* **2017,** *8*, 15341.

20. Yan, L. T.; Cao, L.; Dai, P. C.; Gu, X.; Liu, D. D.; Li, L. J.; Wang, Y.; Zhao, X. B., Metal-Organic Frameworks Derived Nanotube of Nickel-Cobalt Bimetal Phosphides as Highly Efficient Electrocatalysts for Overall Water Splitting. *Adv. Funct. Mater.* **2017,** *27*, 1703455.

21. Zhou, H.; Yu, F.; Sun, J.; Zhu, H.; Mishra, I. K.; Chen, S.; Ren, Z., Highly Efficient Hydrogen Evolution from Edge-Oriented $WS_{2(1-x)}Se_{2x}$ Particles on Three-Dimensional Porous $NiSe_2$ Foam. *Nano Lett.* **2016,** *16*, 7604.

22. Hu, C.; Zhang, L.; Zhao, Z. J.; Li, A.; Chang, X.; Gong, J., Synergism of Geometric Construction and Electronic Regulation: 3D Se-$(NiCo)S_x$ /$(OH)_x$ Nanosheets for Highly Efficient Overall Water Splitting. *Adv. Mater.* **2018,** *30*, e1705538.

23. Yang, L.; Guo, Z.; Huang, J.; Xi, Y.; Gao, R.; Su, G.; Wang, W.; Cao, L.; Dong, B., Vertical Growth of 2D Amorphous $FePO_4$ Nanosheet on Ni Foam: Outer and Inner Structural Design for Superior Water Splitting. *Adv. Mater.* **2017,** *29*, 1704574.

24. Huang, S. C.; Meng, Y. Y.; He, S. M.; Goswami, A.; Wu, Q. L.; Li, J. H.; Tong, S. F.; Asefa, T.; Wu, M. M., N-, O-, and S-tridoped Carbon-Encapsulated Co_9S_8 Nanomaterials: Efficient Bifunctional Electrocatalysts for Overall Water Splitting. *Adv. Funct. Mater.* **2017,** *27*, 1606585.

25. Liu, P.; Rodriguez, J. A., Catalysts for Hydrogen Evolution from the [NiFe] Hydrogenase to the Ni_2P (001) Surface: The Importance of Ensemble Effect. *J. Am. Chem. Soc.* **2005,** *127*, 14871.

26. Chung, D. Y.; Jun, S. W.; Yoon, G.; Kim, H.; Yoo, J. M.; Lee, K. S.; Kim, T.; Shin, H.; Sinha, A. K.; Kwon, S. G.; Kang, K.; Hyeon, T.; Sung, Y. E., Large-Scale Synthesis of Carbon-Shell-Coated FeP Nanoparticles for Robust Hydrogen Evolution Reaction Electrocatalyst. *J. Am. Chem. Soc.* **2017,** *139*, 6669.

27. Tang, C.; Gan, L.; Zhang, R.; Lu, W.; Jiang, X.; Asiri, A. M.; Sun, X.; Wang, J.; Chen, L., Ternary $Fe_xCo_{1-x}P$ Nanowire Array as a Robust Hydrogen Evolution Reaction Electrocatalyst with Pt-like Activity: Experimental and Theoretical Insight. *Nano Lett.* **2016,** *16*, 6617.

28. Zhang, R.; Wang, X.; Yu, S.; Wen, T.; Zhu, X.; Yang, F.; Sun, X.; Wang, X.; Hu, W., Ternary $NiCo_2P_x$ Nanowires as pH-Universal Electrocatalysts for Highly Efficient Hydrogen Evolution Reaction. *Adv. Mater.* **2017,** *29*, 1605502.

29. Tang, C.; Zhang, R.; Lu, W.; He, L.; Jiang, X.; Asiri, A. M.; Sun, X., Fe-Doped CoP Nanoarray: A Monolithic Multifunctional Catalyst for Highly Efficient Hydrogen Generation. *Adv. Mater.* **2017,** *29*, 1602441.

30. Hunter, B. M.; Gray, H. B.; Muller, A. M., Earth-Abundant Heterogeneous Water Oxidation Catalysts. *Chem. Rev.* **2016,** *116*, 14120.

31. Suen, N. T.; Hung, S. F.; Quan, Q.; Zhang, N.; Xu, Y. J.; Chen, H. M., Electrocatalysis for the Oxygen Evolution Reaction: Recent Development and Future Perspectives. *Chem. Soc. Rev.* **2017,** *46*, 337.

32. Liu, W.; Liu, H.; Dang, L. N.; Zhang, H. X.; Wu, X. L.; Yang, B.; Li, Z. J.; Zhang, X. W.; Lei, L. C.; Jin, S., Amorphous Cobalt-Iron Hydroxide Nanosheet Electrocatalyst for Efficient

Electrochemical and Photo-Electrochemical Oxygen Evolution. *Adv. Funct. Mater.* **2017,** *27*, 1603904.

33. Yu, J. H.; Cheng, G. Z.; Luo, W., Hierarchical NiFeP Microflowers Directly Grown on Ni Foam for Efficient Electrocatalytic Oxygen Evolution. *J. Mater. Chem. A* **2017,** *5*, 11229.

34. Chen, Z.; Kronawitter, C. X.; Yeh, Y. W.; Yang, X. F.; Zhao, P.; Yao, N.; Koel, B. E., Activity of Pure and Transition Metal-Modified CoOOH for the Oxygen Evolution Reaction in an Alkaline Medium. *J. Mater. Chem. A* **2017,** *5*, 842.

35. Jia, Y.; Zhang, L.; Gao, G.; Chen, H.; Wang, B.; Zhou, J.; Soo, M. T.; Hong, M.; Yan, X.; Qian, G.; Zou, J.; Du, A.; Yao, X., A Heterostructure Coupling of Exfoliated Ni-Fe Hydroxide Nanosheet and Defective Graphene as a Bifunctional Electrocatalyst for Overall Water Splitting. *Adv. Mater.* **2017,** *29*, 1700017.

36. Giddey, S.; Badwal, S. P. S.; Munnings, C.; Dolan, M., Ammonia as a Renewable Energy Transportation Media. *ACS Sustain. Chem. Eng.* **2017,** *5*, 10231.

37. Cao, N.; Zheng, G., Aqueous Electrocatalytic N_2 Reduction under Ambient Conditions. *Nano Res.* **2018,** *11*, 2992.

38. Cui, X. Y.; Tang, C.; Zhang, Q., A Review of Electrocatalytic Reduction of Dinitrogen to Ammonia under Ambient Conditions. *Adv. Energy Mater.* **2018,** *8*, 1800369.

39. Chen, J. G.; Crooks, R. M.; Seefeldt, L. C.; Bren, K. L.; Bullock, R. M.; Darensbourg, M. Y.; Holland, P. L.; Hoffman, B.; Janik, M. J.; Jones, A. K.; Kanatzidis, M. G.; King, P.; Lancaster, K. M.; Lymar, S. V.; Pfromm, P.; Schneider, W. F.; Schrock, R. R., Beyond Fossil Fuel-Driven Nitrogen Transformations. *Science* **2018,** *360*, eaar6611.

40. Jiao, F.; Xu, B., Electrochemical Ammonia Synthesis and Ammonia Fuel Cells. *Adv. Mater.* **2018,** e1805173.

41. Zhao, S.; Lu, X.; Wang, L.; Gale, J.; Amal, R., Carbon-Based Metal-Free Catalysts for Electrocatalytic Reduction of Nitrogen for Synthesis of Ammonia at Ambient Conditions. *Adv. Mater.* **2019,** *31*, e1805367.

42. Schlogl, R., Catalytic Synthesis of Ammonia-a "Never-Ending Story"? *Angew. Chem. Int. Ed. Engl.* **2003,** *42*, 2004.

43. Service, R. F., Liquid Sunshine. *Science* **2018,** *361*, 120.

44. Li, H.; Shang, J.; Ai, Z.; Zhang, L., Efficient Visible Light Nitrogen Fixation with BiOBr Nanosheets of Oxygen Vacancies on the Exposed {001} Facets. *J. Am. Chem. Soc.* **2015,** *137*, 6393.

45. Guo, C.; Ran, J.; Vasileff, A.; Qiao, S.-Z., Rational Design of Electrocatalysts and Photo(Electro)Catalysts for Nitrogen Reduction to Ammonia (NH_3) under Ambient Conditions. *Energ. Environ. Sci.* **2018,** *11*, 45.

46. Han, J.; Ji, X.; Ren, X.; Cui, G.; Li, L.; Xie, F.; Wang, H.; Li, B.; Sun, X., MoO_3 Nanosheets for Efficient Electrocatalytic N_2 Fixation to NH_3. *J. Mater. Chem. A* **2018,** *6*, 12974.

47. Wang, X.-G.; Zhang, Q.; Zhang, X.; Wang, C.; Xie, Z.; Zhou, Z., Promoting Nitrogen Electroreduction on Mo_2C Nanoparticles Highly Dispersed on N-Doped Carbon Nanosheets toward Rechargeable Li-N_2 Batteries. *Small Methods* **2019,** *3*, 1800334.

48. Martirez, J. M.; Carter, E. A., Thermodynamic Constraints in Using AuM (M = Fe, Co, Ni, and Mo) Alloys as N_2 Dissociation Catalysts: Functionalizing a Plasmon-Active Metal. *ACS Nano* **2016,** *10*, 2940.

49. Suryanto, B. H. R.; Wang, D.; Azofra, L. M.; Harb, M.; Cavallo, L.; Jalili, R.; Mitchell, D. R. G.; Chatti, M.; MacFarlane, D. R., MoS_2 Polymorphic Engineering Enhances Selectivity in the Electrochemical Reduction of Nitrogen to Ammonia. *ACS Energy Lett.* **2018,** *4*, 430.

50. Li, X.; Li, T.; Ma, Y.; Wei, Q.; Qiu, W.; Guo, H.; Shi, X.; Zhang, P.; Asiri, A. M.; Chen, L.; Tang, B.; Sun, X., Boosted Electrocatalytic N_2 Reduction to NH_3 by Defect-Rich MoS_2 Nanoflower. *Adv. Energy Mater.* **2018,** 1801357.

51. Zhang, L.; Ji, X.; Ren, X.; Ma, Y.; Shi, X.; Tian, Z.; Asiri, A. M.; Chen, L.; Tang, B.; Sun, X., Electrochemical Ammonia Synthesis Via Nitrogen Reduction Reaction on a MoS_2 Catalyst: Theoretical and Experimental Studies. *Adv. Mater.* **2018,** *30*, e1800191.

52. Cheng, H.; Ding, L. X.; Chen, G. F.; Zhang, L.; Xue, J.; Wang, H., Molybdenum Carbide Nanodots Enable Efficient Electrocatalytic Nitrogen Fixation under Ambient Conditions. *Adv. Mater.* **2018,** *30*, e1803694.

53. Han, L.; Liu, X.; Chen, J.; Lin, R.; Liu, H.; Lu, F.; Bak, S.; Liang, Z.; Zhao, S.; Stavitski, E.; Luo, J.; Adzic, R. R.; Xin, H. L., Atomically Dispersed Molybdenum Catalysts for Efficient Ambient Nitrogen Fixation. *Angew. Chem. Int. Ed. Engl.* **2019,** *58*, 2321.

54. Santos, P. C. D.; Dean, D. R.; Hu, Y.; Ribbe, M. W., Formation and Insertion of the Nitrogenase Iron−Molybdenum Cofactor. *Chem. Rev.* **2004,** *104*, 1159.

55. Chen, Z.; Zhao, J.; Cabrera, C. R.; Chen, Z., Computational Screening of Efficient Single-Atom Catalysts Based on Graphitic Carbon Nitride (G-C_3N_4) for Nitrogen Electroreduction. *Small Methods* **2018**, 1800368.

56. Choi, C.; Back, S.; Kim, N.-Y.; Lim, J.; Kim, Y.-H.; Jung, Y., Suppression of Hydrogen Evolution Reaction in Electrochemical N_2 Reduction Using Single-Atom Catalysts: A Computational Guideline. *ACS Catal.* **2018,** *8*, 7517.

57. Geng, Z.; Liu, Y.; Kong, X.; Li, P.; Li, K.; Liu, Z.; Du, J.; Shu, M.; Si, R.; Zeng, J., Achieving a Record-High Yield Rate of 120.9 ug_{NH3} $mg_{cat.}^{-1}$ h^{-1} for N_2 Electrochemical Reduction over Ru Single-Atom Catalysts. *Adv. Mater.* **2018,** e1803498.

58. Zhang, Y.; Qiu, W.; Ma, Y.; Luo, Y.; Tian, Z.; Cui, G.; Xie, F.; Chen, L.; Li, T.; Sun, X., High-Performance Electrohydrogenation of N_2 to NH_3 Catalyzed by Multishelled Hollow Cr_2O_3 Microspheres under Ambient Conditions. *ACS Catal.* **2018,** *8*, 8540.

59. Fang, Y.; Liu, Z.; Han, J.; Jin, Z.; Han, Y.; Wang, F.; Niu, Y.; Wu, Y.; Xu, Y., High-Performance Electrocatalytic Conversion of N_2 to NH_3 Using Oxygen-Vacancy-Rich TiO_2 in Situ Grown on $Ti_3C_2T_x$ Mxene. *Adv. Energy Mater.* **2019,** *9*, 1803406.

60. Shi, M.-M.; Bao, D.; Li, S.-J.; Wulan, B.-R.; Yan, J.-M.; Jiang, Q., Anchoring PdCu Amorphous Nanocluster on Graphene for Electrochemical Reduction of N_2 to NH_3 under Ambient Conditions in Aqueous Solution. *Adv. Energy Mater.* **2018**, 1800124.

61. Dresselhaus, M. S.; Thomas, I. L., Alternative Energy Technologies. *Nature* **2001,** *414*, 332.

62. Miao, M.; Pan, J.; He, T.; Yan, Y.; Xia, B. Y.; Wang, X., Molybdenum Carbide-Based Electrocatalysts for Hydrogen Evolution Reaction. *Chemistry* **2017,** *23*, 10947.

63. Roger, I.; Shipman, M. A.; Symes, M. D., Earth-Abundant Catalysts for Electrochemical and Photoelectrochemical Water Splitting. *Nat. Rev. Chem.* **2017,** *1*, 0003.

64. Ong, W. J.; Tan, L. L.; Ng, Y. H.; Yong, S. T.; Chai, S. P., Graphitic Carbon Nitride (G-C_3N_4)-Based Photocatalysts for Artificial Photosynthesis and Environmental Remediation: Are We a Step Closer to Achieving Sustainability? *Chem. Rev.* **2016,** *116*, 7159.

65. Cai, L. J.; Lin, Z. Y.; Wang, M. Y.; Pan, F.; Chen, J. W.; Wang, Y.; Shen, X. P.; Chai, Y. Improved Interfacial H_2O Supply by Surface Hydroxyl Groups for Enhanced Alkaline Hydrogen Evolution, *J. Mater. Chem. A* **2017**, *5*, 24091.

66. Zeng, K.; Zhang, D. K., Recent Progress in Alkaline Water Electrolysis for Hydrogen Production and Applications. *Prog. Energ. and Combust.* **2010,** *36*, 307.

67. Ooka, H.; Figueiredo, M. C.; Koper, M. T. M., Competition between Hydrogen Evolution and Carbon Dioxide Reduction on Copper Electrodes in Mildly Acidic Media. *Langmuir* **2017,** *33*, 9307.

68. Danilovic, N.; Subbaraman, R.; Strmcnik, D.; Stamenkovic, V. R.; Markovic, N. M., Electrocatalysis of the HER in Acid and Alkaline Media. *J. Serb. Chem. Soc.* **2013,** *78*, 2007.

69. Tong, Y.; Guo, Y.; Mu, K.; Shan, H.; Dai, J.; Liu, Y.; Sun, Z.; Zhao, A.; Zeng, X. C.; Wu, C.; Xie, Y., Half-Metallic Behavior in 2D Transition Metal Dichalcogenides Nanosheets by Dual-Native-Defects Engineering. *Adv. Mater.* **2017,** *29*, 1703123.

70. Chen, P.; Zhou, T.; Zhang, M.; Tong, Y.; Zhong, C.; Zhang, N.; Zhang, L.; Wu, C.; Xie, Y., 3D Nitrogen-Anion-Decorated Nickel Sulfides for Highly Efficient Overall Water Splitting. *Adv. Mater.* **2017,** *29*, 1701584.

71. Zhang, J.; Wang, T.; Liu, P.; Liu, S. H.; Dong, R. H.; Zhuang, X. D.; Chen, M. W.; Feng, X. L., Engineering Water Dissociation Sites in MoS_2 Nanosheets for Accelerated Electrocatalytic Hydrogen Production. *Energ. Environ. Sci.* **2016,** *9*, 2789.

72. Yu, L.; Zhou, H. Q.; Sun, J. Y.; Qin, F.; Yu, F.; Bao, J. M.; Yu, Y.; Chen, S.; Ren, Z. F., Cu Nanowires Shelled with NiFe Layered Double Hydroxide Nanosheets as Bifunctional Electrocatalysts for Overall Water Splitting. *Energ. Environ. Sci.* **2017,** *10*, 1820.

73. Voiry, D.; Yang, J.; Chhowalla, M., Recent Strategies for Improving the Catalytic Activity of 2D TMD Nanosheets toward the Hydrogen Evolution Reaction. *Adv. Mater.* **2016,** *28*, 6197.

74. Balogun, M. S.; Qiu, W. T.; Yang, H.; Fan, W. J.; Huang, Y. C.; Fang, P. P.; Li, G. R.; Ji, H. B.; Tong, Y. X., A Monolithic Metal-Free Electrocatalyst for Oxygen Evolution Reaction and Overall Water Splitting. *Energ. Environ. Sci.* **2016,** *9*, 3411.

75. Zhou, H. Q.; Yu, F.; Liu, Y. Y.; Sun, J. Y.; Zhu, Z. A.; He, R.; Bao, J. M.; Goddard, W. A.; Chen, S.; Ren, Z. F., Outstanding Hydrogen Evolution Reaction Catalyzed by Porous Nickel Diselenide Electrocatalysts. *Energ. Environ. Sci.* **2017,** *10*, 1487.

76. Zhang, J.; Wang, T.; Liu, P.; Liao, Z.; Liu, S.; Zhuang, X.; Chen, M.; Zschech, E.; Feng, X., Efficient Hydrogen Production on $MoNi_4$ Electrocatalysts with Fast Water Dissociation Kinetics. *Nat. Commun.* **2017,** *8*, 15437.

77. Botti, A.; Bruni, F.; Imberti, S.; Ricci, M. A.; Soper, A. K., Ions in Water: The Microscopic Structure of Concentrated NaOH Solutions. *J. Chem. Phys.* **2004,** *120*, 10154.

78. Fontecilla-Camps, J. C.; Volbeda, A.; Cavazza, C.; Nicolet, Y., Structure/Function Relationships of [NiFe]- and [FeFe]-Hydrogenases. *Chem. Rev.* **2007,** *107*, 4273.

79. Hambourger, M.; Gervaldo, M.; Svedruzic, D.; King, P. W.; Gust, D.; Ghirardi, M.; Moore, A. L.; Moore, T. A., [FeFe]-Hydrogenase-Catalyzed H_2 Production in a Photoelectrochemical Biofuel Cell. *J. Am. Chem. Soc.* **2008,** *130*, 2015.

80. Cornish, A. J.; Gartner, K.; Yang, H.; Peters, J. W.; Hegg, E. L., Mechanism of Proton Transfer in [FeFe]-Hydrogenase from Clostridium Pasteurianum. *J. Biol. Chem.* **2011,** *286*, 38341.

81. Stankovich, S.; Dikin, D. A.; Piner, R. D.; Kohlhaas, K. A.; Kleinhammes, A.; Jia, Y.; Wu, Y.; Nguyen, S. T.; Ruoff, R. S., Synthesis of Graphene-Based Nanosheets Via Chemical Reduction of Exfoliated Graphite Oxide. *Carbon* **2007,** *45*, 1558.

82. Ma, X. S.; Wang, D. H.; Cui, Y. Z.; Tao, F. R.; Wang, Y. T.; Li, T. D., A Novel Hydrophilic Conjugated Polymer Containing Hydroxyl Groups: Syntheses and Sensing Performance for NACs in Aqueous Solution. *Sensors Actuat. B-Chem.* **2017,** *251*, 851.

83. Bucko, T.; Hafner, J.; Lebegue, S.; Angyan, J. G., Improved Description of the Structure of Molecular and Layered Crystals: Ab Initio DFT Calculations with Van der Waals Corrections. *J. Phys. Chem. A* **2010,** *114*, 11814.

84. Perdew, J. P.; Burke, K.; Ernzerhof, M., Generalized Gradient Approximation Made Simple. *Phys. Rev. Lett.* **1996,** *77*, 3865.

85. Liu, K. K.; Zhang, W.; Lee, Y. H.; Lin, Y. C.; Chang, M. T.; Su, C. Y.; Chang, C. S.; Li, H.; Shi, Y.; Zhang, H.; Lai, C. S.; Li, L. J., Growth of Large-Area and Highly Crystalline MoS_2 Thin Layers on Insulating Substrates. *Nano Lett.* **2012,** *12*, 1538.

86. Wang, X.; Zhang, Y.; Zhi, C.; Wang, X.; Tang, D.; Xu, Y.; Weng, Q.; Jiang, X.; Mitome, M.; Golberg, D.; Bando, Y., Three-Dimensional Strutted Graphene Grown by Substrate-Free Sugar Blowing for High-Power-Density Supercapacitors. *Nat. Commun.* **2013,** *4*, 2905.

87. Fei, L.; Lei, S.; Zhang, W. B.; Lu, W.; Lin, Z.; Lam, C. H.; Chai, Y.; Wang, Y., Direct Tem Observations of Growth Mechanisms of Two-Dimensional MoS_2 Flakes. *Nat. Commun.* **2016,** *7*, 12206.

88. Qiu, B. C.; Xing, M. Y.; Zhang, J. L., Stober-Like Method to Synthesize Ultralight, Porous, Stretchable Fe_2O_3/Graphene Aerogels for Excellent Performance in Photo-Fenton Reaction and Electrochemical Capacitors. *J. Mater. Chem. A* **2015,** *3*, 12820.

89. Zhao, Y. D.; Liu, Z. J.; Sun, T. Y.; Zhang, L.; Jie, W. J.; Wang, X. S.; Xie, Y. Z.; Tsang, Y. H.; Long, H.; Chai, Y., Mass Transport Mechanism of Cu Species at the Metal/Dielectric Interfaces with a Graphene Barrier. *Acs Nano* **2014,** *8*, 12601.

90. Qiu, B.; Deng, Y.; Du, M.; Xing, M.; Zhang, J., Ultradispersed Cobalt Ferrite Nanoparticles Assembled in Graphene Aerogel for Continuous Photo-Fenton Reaction and Enhanced Lithium Storage Performance. *Sci. Rep.* **2016,** *6*, 29099.

91. Wang, M.; Cai, L.; Wang, Y.; Zhou, F.; Xu, K.; Tao, X.; Chai, Y., Graphene-Draped Semiconductors for Enhanced Photocorrosion Resistance and Photocatalytic Properties. *J. Am. Chem. Soc.* **2017,** *139*, 4144.

92. Qiu, B.; Xing, M.; Zhang, J., Mesoporous Tio2 Nanocrystals Grown in Situ on Graphene Aerogels for High Photocatalysis and Lithium-Ion Batteries. *J. Am. Chem. Soc.* **2014,** *136*, 5852.

93. Ghuman, K. K.; Yadav, S.; Singh, C. V., Adsorption and Dissociation of H_2O on Monolayered MoS_2 Edges: Energetics and Mechanism from Ab Initio Simulations. *J. Phys. Chem. C* **2015,** *119*, 6518.

94. Yu, Y.; Huang, S. Y.; Li, Y.; Steinmann, S. N.; Yang, W.; Cao, L., Layer-Dependent Electrocatalysis of MoS_2 for Hydrogen Evolution. *Nano Lett.* **2014,** *14*, 553.

95. He, H.; Lin, J.; Fu, W.; Wang, X.; Wang, H.; Zeng, Q.; Gu, Q.; Li, Y.; Yan, C.; Tay, B. K.; Xue, C.; Hu, X.; Pantelides, S. T.; Zhou, W.; Liu, Z., MoS_2/TiO_2 edge-on Heterostructure for Efficient Photocatalytic Hydrogen Evolution. *Adv. Energy Mater.* **2016,** *6*, 1600464.

96. Lee, D.; Seo, J., Three-Dimensionally Networked Graphene Hydroxide with Giant Pores and Its Application in Supercapacitors. *Sci. Rep.* **2014,** *4*, 7419.

97. Li, G.; Zhang, D.; Qiao, Q.; Yu, Y.; Peterson, D.; Zafar, A.; Kumar, R.; Curtarolo, S.; Hunte, F.; Shannon, S.; Zhu, Y.; Yang, W.; Cao, L., All the Catalytic Active Sites of MoS_2 for Hydrogen Evolution. *J. Am. Chem. Soc.* **2016,** *138*, 16632.

98. Geng, X.; Wu, W.; Li, N.; Sun, W.; Armstrong, J.; Al-hilo, A.; Brozak, M.; Cui, J.; Chen, T.-p., Three-Dimensional Structures of MoS_2 Nanosheets with Ultrahigh Hydrogen Evolution Reaction in Water Reduction. *Adv. Funct. Mater.* **2014,** *24*, 6123.

99. Shinagawa, T.; Garcia-Esparza, A. T.; Takanabe, K., Insight on Tafel Slopes from a Microkinetic Analysis of Aqueous Electrocatalysis for Energy Conversion. *Sci. Rep.* **2015,** *5*, 13801.

100. Vrubel, H.; Hu, X., Molybdenum Boride and Carbide Catalyze Hydrogen Evolution in Both Acidic and Basic Solutions. *Angew. Chem. Int. Ed. Engl.* **2012,** *51*, 12703.

101. Staszak-Jirkovsky, J.; Malliakas, C. D.; Lopes, P. P.; Danilovic, N.; Kota, S. S.; Chang, K. C.; Genorio, B.; Strmcnik, D.; Stamenkovic, V. R.; Kanatzidis, M. G.; Markovic, N. M., Design of Active and Stable Co-Mo-S_x Chalcogels as pH-Universal Catalysts for the Hydrogen Evolution Reaction. *Nat. Mater.* **2016,** *15*, 197.

102. Pu, Z. H.; Liu, Q.; Asiri, A. M.; Luo, Y. L.; Sun, X. P.; He, Y. Q., 3D Macroporous MoS_2 Thin Film: In Situ Hydrothermal Preparation and Application as a Highly Active Hydrogen Evolution Electrocatalyst at All pH Values. *Electrochim. Acta* **2015,** *168*, 133.

103. Zhu, W. X.; Tang, C.; Liu, D. N.; Wang, J. L.; Asiri, A. M.; Sun, X. P., A Self-Standing Nanoporous MoP_2 Nanosheet Array: An Advanced pH-Universal Catalytic Electrode for the Hydrogen Evolution Reaction. *J. Mater. Chem. A* **2016,** *4*, 7169.

104. An, T.; Wang, Y.; Tang, J.; Wei, W.; Cui, X.; Alenizi, A. M.; Zhang, L.; Zheng, G., Interlaced NiS_2-MoS_2 Nanoflake-Nanowires as Efficient Hydrogen Evolution Electrocatalysts in Basic Solutions. *J. Mater. Chem. A* **2016,** *4*, 13439.

105. Shi, J. L.; Hu, J. M., Molybdenum Sulfide Nanosheet Arrays Supported on Ti Plate: An Efficient Hydrogen-Evolving Cathode over the Whole Ph Range. *Electrochim. Acta* **2015,** *168*, 256.

106. Wu, A.; Tian, C.; Yan, H.; Jiao, Y.; Yan, Q.; Yang, G.; Fu, H., Hierarchical MoS_2@MoP Core-Shell Heterojunction Electrocatalysts for Efficient Hydrogen Evolution Reaction over a Broad pH Range. *Nanoscale* **2016,** *8*, 11052.

107. Yang, Y.; Zhang, K.; Lin, H.; Li, X.; Chan, H. C.; Yang, L.; Gao, Q., MoS_2-Ni_3S_2 Heteronanorods as Efficient and Stable Bifunctional Electrocatalysts for Overall Water Splitting. *ACS Catal.* **2017,** *7*, 2357.

108. Montoya, J. H.; Seitz, L. C.; Chakthranont, P.; Vojvodic, A.; Jaramillo, T. F.; Norskov, J. K., Materials for Solar Fuels and Chemicals. *Nat. Mater.* **2016,** *16*, 70.

109. Seh, Z. W.; Kibsgaard, J.; Dickens, C. F.; Chorkendorff, I.; Norskov, J. K.; Jaramillo, T. F., Combining Theory and Experiment in Electrocatalysis: Insights into Materials Design. *Science* **2017,** *355*, eaad4998.

110. Chen, G.; Wang, T.; Zhang, J.; Liu, P.; Sun, H.; Zhuang, X.; Chen, M.; Feng, X., Accelerated Hydrogen Evolution Kinetics on NiFe-Layered Double Hydroxide Electrocatalysts by Tailoring Water Dissociation Active Sites. *Adv. Mater.* **2018,** *30*, 1706279.

111. Cai, L. J.; Qiu, B. C.; Lin, Z. Y.; Wang, Y.; Ma, S. N.; Wang, M. Y.; Tsang, Y. H.; Chai, Y. Active Site Engineering of Fe- and Ni-sites for Highly Efficient Electrochemical Overall Water Splitting, *J. Mater. Chem. A* **2018**, 6, 21445.

112. Qiu, B.; Xing, M.; Zhang, J., Recent Advances in Three-Dimensional Graphene Based Materials for Catalysis Applications. *Chem. Soc. Rev.* **2018,** *47*, 2165.

113. Ding, J. B.; Shao, Q.; Feng, Y. G.; Huang, X. Q., Ruthenium-Nickel Sandwiched Nanoplates for Efficient Water Splitting Electrocatalysis. *Nano Energy* **2018,** *47*, 1.

114. Hansen, M. H.; Stern, L. A.; Feng, L.; Rossmeisl, J.; Hu, X., Widely Available Active Sites on Ni_2P for Electrochemical Hydrogen Evolution-Insights from First Principles Calculations. *Phys. Chem. Chem. Phys.* **2015,** *17*, 10823.

115. Wang, P.; Pu, Z.; Li, Y.; Wu, L.; Tu, Z.; Jiang, M.; Kou, Z.; Amiinu, I. S.; Mu, S., Iron-Doped Nickel Phosphide Nanosheet Arrays: An Efficient Bifunctional Electrocatalyst for Water Splitting. *ACS Appl. Mater. Interfaces* **2017,** *9*, 26001.

116. Hu, F.; Zhu, S.; Chen, S.; Li, Y.; Ma, L.; Wu, T.; Zhang, Y.; Wang, C.; Liu, C.; Yang, X.; Song, L.; Yang, X.; Xiong, Y., Amorphous Metallic Nifep: A Conductive Bulk Material Achieving High Activity for Oxygen Evolution Reaction in Both Alkaline and Acidic Media. *Adv. Mater.* **2017,** *29*, 1606570.

117. Qiu, B. C.; Cai, L. J.; Wang, Y.; Lin, Z. Y.; Zuo, Y. P.; Wang, M. Y.; Chai, Y., Fabrication of Nickel-Cobalt Bimetal Phosphide Nanocages for Enhanced Oxygen Evolution Catalysis. *Adv. Funct. Mater.* **2018,** *28*, 1706008.

118. Liang, H.; Gandi, A. N.; Anjum, D. H.; Wang, X.; Schwingenschlogl, U.; Alshareef, H. N., Plasma-Assisted Synthesis of NiCoP for Efficient Overall Water Splitting. *Nano Lett.* **2016,** *16*, 7718.

119. Li, Y. J.; Zhang, H. C.; Jiang, M.; Zhang, Q.; He, P. L.; Sun, X. M., 3D Self-Supported Fe-Doped Ni_2P Nanosheet Arrays as Bifunctional Catalysts for Overall Water Splitting. *Adv. Funct. Mater.* **2017,** *27*, 1702513.

120. Zhou, H.; Yu, F.; Sun, J.; He, R.; Chen, S.; Chu, C. W.; Ren, Z., Highly Active Catalyst Derived from a 3D Foam of $Fe(PO_3)_2/Ni_2P$ for Extremely Efficient Water Oxidation. *Proc. Natl. Acad. Sci. USA* **2017,** *114*, 5607.

121. Chen, J. S.; Ren, J.; Shalom, M.; Fellinger, T.; Antonietti, M., Stainless Steel Mesh-Supported NiS Nanosheet Array as Highly Efficient Catalyst for Oxygen Evolution Reaction. *ACS Appl. Mater. Interfaces* **2016,** *8*, 5509.

122. Schafer, H.; Beladi-Mousavi, S. M.; Walder, L.; Wollschlager, J.; Kuschel, O.; Ichilmann, S.; Sadaf, S.; Steinhart, M.; Kupper, K.; Schneider, L., Surface Oxidation of Stainless Steel: Oxygen Evolution Electrocatalysts with High Catalytic Activity. *ACS Catal.* **2015,** *5*, 2671.

123. Liu, X.; You, B.; Sun, Y. J., Facile Surface Modification of Ubiquitous Stainless Steel Led to Competent Electrocatalysts for Overall Water Splitting. *ACS Sustain. Chem. Eng.* **2017,** *5*, 4778.

124. Schafer, H.; Chevrier, D. M.; Zhang, P.; Stangl, J.; Muller-Buschbaum, K.; Hardege, J. D.; Kuepper, K.; Wollschlager, J.; Krupp, U.; Duhnen, S.; Steinhart, M.; Walder, L.; Sadaf, S.; Schmidt, M., Electro-Oxidation of Ni_{42} Steel: A Highly Active Bifunctional Electrocatalyst. *Adv. Funct. Mater.* **2016,** *26*, 6402.

125. Zhang, Q.; Zhong, H.; Meng, F.; Bao, D.; Zhang, X.; Wei, X., Three-Dimensional Interconnected $Ni(Fe)O_xH_y$ Nanosheets on Stainless Steel Mesh as a Robust Integrated Oxygen Evolution Electrode. *Nano Res.* **2018,** *11*, 1294.

126. Balogun, M. S.; Qiu, W.; Huang, Y.; Yang, H.; Xu, R.; Zhao, W.; Li, G. R.; Ji, H.; Tong, Y., Cost-Effective Alkaline Water Electrolysis Based on Nitrogen- and Phosphorus-Doped Self-Supportive Electrocatalysts. *Adv. Mater.* **2017,** *29*, 1702095.

127. Zhong, H.; Wang, J.; Meng, F.; Zhang, X., In Situ Activating Ubiquitous Rust Towards Low-Cost, Efficient, Free-Standing, and Recoverable Oxygen Evolution Electrodes. *Angew. Chem. Int. Ed. Engl.* **2016,** *55*, 9937.

128. Schafer, H.; Sadaf, S.; Walder, L.; Kuepper, K.; Dinklage, S.; Wollschlager, J.; Schneider, L.; Steinhart, M.; Hardege, J.; Daum, D., Stainless Steel Made to Rust: A Robust Water-Splitting Catalyst with Benchmark Characteristics. *Energ. Environ. Sci.* **2015,** *8*, 2685.

129. Louie, M. W.; Bell, A. T., An Investigation of Thin-Film Ni-Fe Oxide Catalysts for the Electrochemical Evolution of Oxygen. *J. Am. Chem. Soc.* **2013,** *135*, 12329.

130. Xiao, C. H.; Zhang, B.; Li, D., Partial-Sacrificial-Template Synthesis of Fe/Ni Phosphides on Ni Foam: A Strongly Stabilized and Efficient Catalyst for Electrochemical Water Splitting. *Electrochim. Acta* **2017,** *242*, 260.

131. Li, Z.; Niu, W.; Zhou, L.; Yang, Y., Phosphorus and Aluminum Co-doped Porous NiO Nanosheets as Highly Efficient Electrocatalysts for Overall Water Splitting. *ACS Energy Lett.* **2018,** *3*, 892.

132. Wang, A. L.; Xu, H.; Li, G. R., NiCoFe Layered Triple Hydroxides with Porous Structures as High-Performance Electrocatalysts for Overall Water Splitting. *ACS Energy Lett.* **2016,** *1*, 445.

133. Liang, H.; Gandi, A. N.; Xia, C.; Hedhili, M. N.; Anjum, D. H.; Schwingenschlogl, U.; Alshareef, H. N., Amorphous NiFe-OH/NiFeP Electrocatalyst Fabricated at Low Temperature for Water Oxidation Applications. *ACS Energy Lett.* **2017,** *2*, 1035.

134. Zhang, B.; Lui, Y. H.; Ni, H.; Hu, S., Bimetallic $(Fe_xNi_{1-x})_2P$ Nanoarrays as Exceptionally Efficient Electrocatalysts for Oxygen Evolution in Alkaline and Neutral Media. *Nano Energy* **2017,** *38*, 553.

135. Stevens, M. B.; Enman, L. J.; Batchellor, A. S.; Cosby, M. R.; Vise, A. E.; Trang, C. D. M.; Boettcher, S. W., Measurement Techniques for the Study of Thin Film Heterogeneous Water Oxidation Electrocatalysts. *Chem. Mater.* **2016,** *29*, 120.

136. Wang, J.; Ma, X.; Qu, F.; Asiri, A. M.; Sun, X., Fe-Doped Ni_2P Nanosheet Array for High-Efficiency Electrochemical Water Oxidation. *Inorg. Chem.* **2017,** *56*, 1041.

137. Qian, M.; Cui, S.; Jiang, D.; Zhang, L.; Du, P., Highly Efficient and Stable Water-Oxidation Electrocatalysis with a Very Low Overpotential Using FeNiP Substitutional-Solid-Solution Nanoplate Arrays. *Adv. Mater.* **2017,** *29*, 1704075

138. Smith, R. D.; Prevot, M. S.; Fagan, R. D.; Zhang, Z.; Sedach, P. A.; Siu, M. K.; Trudel, S.; Berlinguette, C. P., Photochemical Route for Accessing Amorphous Metal Oxide Materials for Water Oxidation Catalysis. *Science* **2013,** *340*, 60.

139. Chen, G.-F.; Ma, T. Y.; Liu, Z.-Q.; Li, N.; Su, Y.-Z.; Davey, K.; Qiao, S.-Z., Efficient and Stable Bifunctional Electrocatalysts Ni/Ni_xM_y (M = P, S) for Overall Water Splitting. *Adv. Funct. Mater.* **2016,** *26*, 3314.

140. Luo, Y.; Chen, G.-F.; Ding, L.; Chen, X.; Ding, L.-X.; Wang, H., Efficient Electrocatalytic N_2 Fixation with Mxene under Ambient Conditions. *Joule* **2019,** *3*, 279.

141. Tang, T.; Jiang, W. J.; Niu, S.; Liu, N.; Luo, H.; Chen, Y. Y.; Jin, S. F.; Gao, F.; Wan, L. J.; Hu, J. S., Electronic and Morphological Dual Modulation of Cobalt Carbonate Hydroxides by Mn Doping toward Highly Efficient and Stable Bifunctional Electrocatalysts for Overall Water Splitting. *J. Am. Chem. Soc.* **2017,** *139*, 8320.

142. Wu, Y. Y.; Li, G. D.; Liu, Y. P.; Yang, L.; Lian, X. R.; Asefa, T.; Zou, X. X., Overall Water Splitting Catalyzed Efficiently by an Ultrathin Nanosheet-Built, Hollow Ni_3S_2-Based Electrocatalyst. *Adv. Funct. Mater.* **2016,** *26*, 4839.

143. Menezes, P. W.; Indra, A.; Das, C.; Walter, C.; Göbel, C.; Gutkin, V.; Schmeiβer, D.; Driess, M., Uncovering the Nature of Active Species of Nickel Phosphide Catalysts in High-Performance Electrochemical Overall Water Splitting. *ACS Catal.* **2016,** *7*, 103.

144. Li, W.; Gao, X. F.; Xiong, D. H.; Wei, F.; Song, W. G.; Xu, J. Y.; Liu, L. F., Hydrothermal Synthesis of Monolithic Co_3Se_4 Nanowire Electrodes for Oxygen Evolution and Overall Water Splitting with High Efficiency and Extraordinary Catalytic Stability. *Adv. Energy Mater.* **2017,** *7*, 1602579.

145. Zhang, T.; Wu, M. Y.; Yan, D. Y.; Mao, J.; Liu, H.; Hu, W. B.; Du, X. W.; Ling, T.; Qiao, S. Z., Engineering Oxygen Vacancy on Nio Nanorod Arrays for Alkaline Hydrogen Evolution. *Nano Energy* **2018**, *43*, 103.

146. Deng, J.; Iniguez, J. A.; Liu, C., Electrocatalytic Nitrogen Reduction at Low Temperature. *Joule* **2018,** *2*, 846.

147. Suryanto, B. H. R.; Du, H. L.; Wang, D. B.; Chen, J.; Simonov, A. N.; MacFarlane, D. R., Challenges and Prospects in the Catalysis of Electroreduction of Nitrogen to Ammonia. *Nat. Catal.* **2019,** *2*, 290.

148. Zhang, L.; Ding, L. X.; Chen, G. F.; Yang, X.; Wang, H., Ammonia Synthesis under Ambient Conditions: Selective Electroreduction of Dinitrogen to Ammonia on Black Phosphorus Nanosheets. *Angew. Chem. Int. Ed. Engl.* **2019,** *58*, 2612.

149. Suryanto, B. H. R.; Kang, C. S. M.; Wang, D.; Xiao, C.; Zhou, F.; Azofra, L. M.; Cavallo, L.; Zhang, X.; MacFarlane, D. R., Rational Electrode–Electrolyte Design for Efficient Ammonia Electrosynthesis under Ambient Conditions. *ACS Energy Lett.* **2018,** *3*, 1219.

150. Andersen, S. Z.; Colic, V.; Yang, S.; Schwalbe, J. A.; Nielander, A. C.; McEnaney, J. M.; Enemark-Rasmussen, K.; Baker, J. G.; Singh, A. R.; Rohr, B. A.; Statt, M. J.; Blair, S. J.; Mezzavilla, S.; Kibsgaard, J.; Vesborg, P. C. K.; Cargnello, M.; Bent, S. F.; Jaramillo, T. F.; Stephens, I. E. L.; Norskov, J. K.; Chorkendorff, I., A Rigorous Electrochemical Ammonia Synthesis Protocol with Quantitative Isotope Measurements. *Nature* **2019,** *570*, 504.

151. Enhanced Electrocatalytic N_2 Reduction Via Partial Anion Substitution in Titanium Oxide–Carbon Composites. *Angew. Chem. Int. Ed.* **2019,** *58*, 2.

152. Zhao, J.; Chen, Z., Single Mo Atom Supported on Defective Boron Nitride Monolayer as an Efficient Electrocatalyst for Nitrogen Fixation: A Computational Study. *J. Am. Chem. Soc.* **2017,** *139*, 12480.

153. He, C.; Wu, Z.-Y.; Zhao, L.; Ming, M.; Zhang, Y.; Yi, Y.; Hu, J.-S., Identification of FeN_4 as An Efficient Active Site for Electrochemical N_2 Reduction. *ACS Catal.* **2019,** *9*, 7311.

154. Bao, D.; Zhang, Q.; Meng, F. L.; Zhong, H. X.; Shi, M. M.; Zhang, Y.; Yan, J. M.; Jiang, Q.; Zhang, X. B., Electrochemical Reduction of N_2 under Ambient Conditions for Artificial N_2 Fixation and Renewable Energy Storage Using N_2/NH_3 Cycle. *Adv. Mater.* **2017,** *29*, 1604799.

155. Lee, H. K.; Koh, C. S. L.; Lee, Y. H.; Liu, C.; Phang, I. Y.; Han, X.; Tsung, C. K.; Ling, X. Y., Favoring the Unfavored: Selective Electrochemical Nitrogen Fixation Using a Reticular Chemistry Approach. *Sci. Adv.* **2018,** *4*, eaar3208.

156. Hao, Y.-C.; Guo, Y.; Chen, L.-W.; Shu, M.; Wang, X.-Y.; Bu, T.-A.; Gao, W.-Y.; Zhang, N.; Su, X.; Feng, X.; Zhou, J.-W.; Wang, B.; Hu, C.-W.; Yin, A.-X.; Si, R.; Zhang, Y.-W.; Yan, C.-H., Promoting Nitrogen Electroreduction to Ammonia with Bismuth Nanocrystals and Potassium Cations in Water. *Nat. Catal.* **2019,** *2*, 448.

157. Wang, M.; Liu, S.; Qian, T.; Liu, J.; Zhou, J.; Ji, H.; Xiong, J.; Zhong, J.; Yan, C., Over 56.55% Faradaic Efficiency of Ambient Ammonia Synthesis Enabled by Positively Shifting the Reaction Potential. *Nat. Commun.* **2019,** *10*, 341.

158. Zhang, N.; Jalil, A.; Wu, D.; Chen, S.; Liu, Y.; Gao, C.; Ye, W.; Qi, Z.; Ju, H.; Wang, C.; Wu, X.; Song, L.; Zhu, J.; Xiong, Y., Refining Defect States in $W_{18}O_{49}$ by Mo Doping: A Strategy for Tuning N_2 Activation Towards Solar-Driven Nitrogen Fixation. *J. Am. Chem. Soc.* **2018,** *140*, 9434.

159. Wang, Z.; Gong, F.; Zhang, L.; Wang, R.; Ji, L.; Liu, Q.; Luo, Y.; Guo, H.; Li, Y.; Gao, P.; Shi, X.; Li, B.; Tang, B.; Sun, X., Electrocatalytic Hydrogenation of N_2 to NH_3 by MnO: Experimental and Theoretical Investigations. *Adv. Sci.* **2019,** *6*, 1801182.

160. Huang, L.; Gu, X.; Zheng, G., Tuning Active Sites of Mxene for Efficient Electrocatalytic N_2 Fixation. *Chem* **2019,** *5*, 15.

161. Legare, M. A.; Belanger-Chabot, G.; Dewhurst, R. D.; Welz, E.; Krummenacher, I.; Engels, B.; Braunschweig, H., Nitrogen Fixation and Reduction at Boron. *Science* **2018,** *359*, 896.

162. Ling, C.; Niu, X.; Li, Q.; Du, A.; Wang, J., Metal-Free Single Atom Catalyst for N_2 Fixation Driven by Visible Light. *J. Am. Chem. Soc.* **2018,** *140*, 14161.

163. Duca, M.; Cucarella, M. O.; Rodriguez, P.; Koper, M. T., Direct Reduction of Nitrite to N_2 on a Pt (100) Electrode in Alkaline Media. *J. Am. Chem. Soc.* **2010,** *132*, 18042.

164. Wang, J.; Yu, L.; Hu, L.; Chen, G.; Xin, H.; Feng, X., Ambient Ammonia Synthesis Via Palladium-Catalyzed Electrohydrogenation of Dinitrogen at Low Overpotential. *Nat. Commun.* **2018,** *9*, 1795.

165. Zhao, Y.; Qiao, J.; Yu, Z.; Yu, P.; Xu, K.; Lau, S. P.; Zhou, W.; Liu, Z.; Wang, X.; Ji, W.; Chai, Y., High-Electron-Mobility and Air-Stable 2D Layered $PtSe_2$ Fets. *Adv. Mater.* **2017,** *29*, 1604230.

166. Zhao, Y.; Qiao, J.; Yu, P.; Hu, Z.; Lin, Z.; Lau, S. P.; Liu, Z.; Ji, W.; Chai, Y., Extraordinarily Strong Interlayer Interaction in 2D Layered PtS_2. *Adv. Mater.* **2016,** *28*, 2399.

167. Chen, P.; Zhang, N.; Wang, S.; Zhou, T.; Tong, Y.; Ao, C.; Yan, W.; Zhang, L.; Chu, W.; Wu, C.; Xie, Y., Interfacial Engineering of Cobalt Sulfide/Graphene Hybrids for Highly Efficient Ammonia Electrosynthesis. *Proc. Natl. Acad. Sci. USA* **2019,** *116*, 6635.

168. Ohki, Y.; Uchida, K.; Tada, M.; Cramer, R. E.; Ogura, T.; Ohta, T., N_2 Activation on a Molybdenum-Titanium-Sulfur Cluster. *Nat. Commun.* **2018,** *9*, 3200.

169. Ma, W.; Xie, S.; Zhang, X. G.; Sun, F.; Kang, J.; Jiang, Z.; Zhang, Q.; Wu, D. Y.; Wang, Y., Promoting Electrocatalytic CO_2 Reduction to Formate Via Sulfur-Boosting Water Activation on Indium Surfaces. *Nat. Commun.* **2019,** *10*, 892.

170. Dembowski, J.; Marosi, L.; Essig, M., Platinum Sulfide by XPS. *Surf. Sci. Spectra* **1993,** *2*, 104.

171. Li, Y. H.; Xing, J.; Chen, Z. J.; Li, Z.; Tian, F.; Zheng, L. R.; Wang, H. F.; Hu, P.; Zhao, H. J.; Yang, H. G., Unidirectional Suppression of Hydrogen Oxidation on Oxidized Platinum Clusters. *Nat. Commun.* **2013,** *4*, 2500.

172. Chen, G. F.; Ren, S.; Zhang, L.; Cheng, H.; Luo, Y.; Zhu, K.; Ding, L. X.; Wang, H., Advances in Electrocatalytic N_2 Reduction-Strategies to Tackle the Selectivity Challenge. *Small Methods* **2018,** *3*, 1800337.

173. Liu, X.; Jiao, Y.; Zheng, Y.; Jaroniec, M.; Qiao, S. Z., Building up a Picture of the Electrocatalytic Nitrogen Reduction Activity of Transition Metal Single-Atom Catalysts. *J. Am. Chem. Soc.* **2019,** *141*, 9664.

174. Yang, X.; Nash, J.; Anibal, J.; Dunwell, M.; Kattel, S.; Stavitski, E.; Attenkofer, K.; Chen, J. G.; Yan, Y.; Xu, B., Mechanistic Insights into Electrochemical Nitrogen Reduction Reaction on Vanadium Nitride Nanoparticles. *J. Am. Chem. Soc.* **2018,** *140*, 13387.

175. Zhou, F. L.; Azofra, L. M.; Ali, M.; Kar, M.; Simonov, A. N.; McDonnell-Worth, C.; Sun, C. H.; Zhang, X. Y.; MacFarlane, D. R., Electro-Synthesis of Ammonia from Nitrogen at Ambient Temperature and Pressure in Ionic Liquids. *Energ. Environ. Sci.* **2017,** *10*, 2516.

176. Lindley, B. M.; Appel, A. M.; Krogh-Jespersen, K.; Mayer, J. M.; Miller, A. J. M., Evaluating the Thermodynamics of Electrocatalytic N_2 Reduction in Acetonitrile. *ACS Energy Lett.* **2016,** *1*, 698.

177. Abghoui, Y.; Garden, A. L.; Howalt, J. G.; Vegge, T.; Skúlason, E., Electroreduction of N_2 to Ammonia at Ambient Conditions on Mononitrides of Zr, Nb, Cr, and V: A DFT Guide for Experiments. *ACS Catal.* **2015,** *6*, 635.

178. Azofra, L. M.; Sun, C.; Cavallo, L.; MacFarlane, D. R., Feasibility of N_2 Binding and Reduction to Ammonia on Fe-Deposited MoS_2 2D Sheets: A DFT Study. *Chemistry* **2017,** *23*, 8275.

179. Li, Q. Y.; He, L. Z.; Sun, C. H.; Zhang, X. W., Computational Study of MoN_2 Monolayer as Electrochemical Catalysts for Nitrogen Reduction. *J. Phys. Chem. C* **2017,** *121*, 27563.

180. Roux, Y.; Duboc, C.; Gennari, M., Molecular Catalysts for N_2 Reduction: State of the Art, Mechanism, and Challenges. *Chemphyschem* **2017,** *18*, 2606.

181. Kastner, J.; Blochl, P. E., Towards an Understanding of the Workings of Nitrogenase from DFT Calculations. *Chemphyschem* **2005,** *6*, 1724.

182. Xu, H.; Cheng, D.; Cao, D.; Zeng, X. C., A Universal Principle for a Rational Design of Single-Atom Electrocatalysts. *Nat. Catal.* **2018,** *1*, 339.

183. Macleod, K. C.; Holland, P. L., Recent Developments in the Homogeneous Reduction of Dinitrogen by Molybdenum and Iron. *Nat Chem* **2013,** *5*, 559.

184. Tao, H. C.; Choi, C.; Ding, L. X.; Jiang, Z.; Hang, Z. S.; Jia, M. W.; Fan, Q.; Gao, Y. N.; Wang, H. H.; Robertson, A. W.; Hong, S.; Jung, Y. S.; Liu, S. Z.; Sun, Z. Y., Nitrogen Fixation by Ru Single-Atom Electrocatalytic Reduction. *Chem* **2019,** *5*, 204.

185. Ling, C.; Ouyang, Y.; Li, Q.; Bai, X.; Mao, X.; Du, A.; Wang, J., A General Two-Step Strategy-Based High-Throughput Screening of Single Atom Catalysts for Nitrogen Fixation. *Small Methods* **2018**, 1800376.